



Lecture Notes in Mechanical Engineering

Bijoy Bhattacharyya

Jose Mathew

N. Saravanakumar

G. Rajeshkumar *Editors*

Advances in Micro and Nano Manufacturing and Surface Engineering


Proceedings of AIMTDR 2021

 Springer

Lecture Notes in Mechanical Engineering


Series Editors

Fakher Chaari, National School of Engineers, University of Sfax, Sfax, Tunisia

Francesco Gherardini , Dipartimento di Ingegneria “Enzo Ferrari”, Università di Modena e Reggio Emilia, Modena, Italy

Vitalii Ivanov, Department of Manufacturing Engineering, Machines and Tools, Sumy State University, Sumy, Ukraine

Editorial Board

Francisco Cavas-Martínez , Departamento de Estructuras, Construcción y Expresión Gráfica Universidad Politécnica de Cartagena, Cartagena, Murcia, Spain

Francesca di Mare, Institute of Energy Technology, Ruhr-Universität Bochum, Bochum, Nordrhein-Westfalen, Germany

Mohamed Haddar, National School of Engineers of Sfax (ENIS), Sfax, Tunisia

Young W. Kwon, Department of Manufacturing Engineering and Aerospace Engineering, Graduate School of Engineering and Applied Science, Monterey, CA, USA

Justyna Trojanowska, Poznan University of Technology, Poznan, Poland

Lecture Notes in Mechanical Engineering (LNME) publishes the latest developments in Mechanical Engineering—quickly, informally and with high quality. Original research reported in proceedings and post-proceedings represents the core of LNME. Volumes published in LNME embrace all aspects, subfields and new challenges of mechanical engineering. Topics in the series include:

- Engineering Design
- Machinery and Machine Elements
- Mechanical Structures and Stress Analysis
- Automotive Engineering
- Engine Technology
- Aerospace Technology and Astronautics
- Nanotechnology and Microengineering
- Control, Robotics, Mechatronics
- MEMS
- Theoretical and Applied Mechanics
- Dynamical Systems, Control
- Fluid Mechanics
- Engineering Thermodynamics, Heat and Mass Transfer
- Manufacturing
- Precision Engineering, Instrumentation, Measurement
- Materials Engineering
- Tribology and Surface Technology

To submit a proposal or request further information, please contact the Springer Editor of your location:

China: Ms. Ella Zhang at ella.zhang@springer.com

India: Priya Vyas at priya.vyas@springer.com

Rest of Asia, Australia, New Zealand: Swati Meherishi at swati.meherishi@springer.com

All other countries: Dr. Leontina Di Cecco at Leontina.dicecco@springer.com

To submit a proposal for a monograph, please check our Springer Tracts in Mechanical Engineering at <https://link.springer.com/bookseries/11693> or contact Leontina.dicecco@springer.com

Indexed by SCOPUS. All books published in the series are submitted for consideration in Web of Science.

Bijoy Bhattacharyya · Jose Mathew ·
N. Saravanakumar · G. Rajeshkumar
Editors

Advances in Micro and Nano Manufacturing and Surface Engineering

Proceedings of AIMTDR 2021

 Springer

Editors

Bijoy Bhattacharyya
Department of Production Engineering
Jadavpur University
Kolkata, India

Jose Mathew
Department of Mechanical Engineering
National Institute of Technology
Calicut, Kerala, India

N. Saravanakumar
Department of Mechanical Engineering
PSG Institute of Technology and Applied
Research
Coimbatore, Tamil Nadu, India

G. Rajeshkumar
Department of Mechanical Engineering
PSG Institute of Technology and Applied
Research
Coimbatore, Tamil Nadu, India

ISSN 2195-4356

ISSN 2195-4364 (electronic)

Lecture Notes in Mechanical Engineering

ISBN 978-981-19-4570-0

ISBN 978-981-19-4571-7 (eBook)

<https://doi.org/10.1007/978-981-19-4571-7>

© The Editor(s) (if applicable) and The Author(s), under exclusive license to Springer Nature Singapore Pte Ltd. 2023

This work is subject to copyright. All rights are solely and exclusively licensed by the Publisher, whether the whole or part of the material is concerned, specifically the rights of translation, reprinting, reuse of illustrations, recitation, broadcasting, reproduction on microfilms or in any other physical way, and transmission or information storage and retrieval, electronic adaptation, computer software, or by similar or dissimilar methodology now known or hereafter developed.

The use of general descriptive names, registered names, trademarks, service marks, etc. in this publication does not imply, even in the absence of a specific statement, that such names are exempt from the relevant protective laws and regulations and therefore free for general use.

The publisher, the authors, and the editors are safe to assume that the advice and information in this book are believed to be true and accurate at the date of publication. Neither the publisher nor the authors or the editors give a warranty, expressed or implied, with respect to the material contained herein or for any errors or omissions that may have been made. The publisher remains neutral with regard to jurisdictional claims in published maps and institutional affiliations.

This Springer imprint is published by the registered company Springer Nature Singapore Pte Ltd.

The registered company address is: 152 Beach Road, #21-01/04 Gateway East, Singapore 189721, Singapore

AIMTDR 2021 Conference Core Organizing Committee

Chief Patron

Shri. L. Gopalakrishnan, Managing Trustee, PSG Institutions

Patrons

Dr. P. Radhakrishnan, Director, PSG Institute of Advanced Studies

Dr. P. V. Mohanram, Secretary, PSG Institute of Technology and Applied Research

Dr. K. Prakasan, Principal, PSG College of Technology

Dr. G. Chandramohan, Principal, PSG Institute of Technology and Applied Research

President (NAC-AIMTDR)

Shri. Vikram Mohan, Managing Director, Pricol Limited, Coimbatore

Vice President (NAC-AIMTDR)

Dr. Udhay Shankar Dixit, Professor, IIT Guwahati, India

Chairman

Dr. P. R. Thyla, Professor and Head, Department of Mechanical Engineering, PSG College of Technology

Organizing Secretary

Dr. V. Prabhu Raja, Professor, Department of Mechanical Engineering, PSG College of Technology

Co-Organizing Secretary

Dr. N. Saravanakumar, Professor and Head, Department of Mechanical Engineering, PSG Institute of Technology and Applied Research

Joint Organizing Secretaries

Dr. N. Mahendrakumar, Assistant Professor, PSG College of Technology
Dr. C. Shanmugam, Assistant Professor (Sr.Gr), PSG College of Technology
Dr. M. Kalayarasan, Assistant Professor (Sr.Gr), PSG College of Technology
Dr. P. Dhanabal, Assistant Professor (Sr.Gr), PSG College of Technology
Mr. S. Mohanraj, Assistant Professor (Sr.Gr), PSG College of Technology
Dr. V. Rajkumar, Associate Professor, PSG Institute of Technology and Applied Research
Dr. S. Nanthakumar, Assistant Professor, PSG Institute of Technology and Applied Research

Secretaries—Public Relations

Dr. A. Adhiyamaan, Assistant Professor (Sr.Gr), PSG College of Technology
Mr. A. Mohan, Assistant Professor, PSG College of Technology

Treasurer

Mr. D. Martin Suresh Babu, Assistant Professor, PSG College of Technology

Joint Treasurer

Mr. P. Govindaraj, Assistant Professor (Sr.Gr), PSG College of Technology

Members—PSG College of Technology

Dr. K. Ragu, Professor
Dr. N. Ramesh Babu, Professor
Dr. D. Rajenthirakumar, Professor
Dr. R. Jayachitra, Associate Professor
Dr. R. Sridhar, Assistant Professor
Dr. S. Udhayakumar, Assistant Professor
Mr. K. Sadesh, Assistant Professor
Dr. V. Vijayakumar, Assistant Professor (Sr.Gr)
Dr. A. S. Prasanth, Assistant Professor (Sr.Gr)
Mr. D. Shanmuga Sundaram, Assistant Professor
Mr. T. Anantharaj, Assistant Professor
Mr. S. Samsudeensadham, Assistant Professor
Ms. M. Gomathi Prabha, Assistant Professor

Members—PSG Institute of Technology and Applied Research

Dr. R. Ramesh, Professor
Dr. D. Elangovan, Professor
Dr. P. Manoj Kumar, Associate Professor
Dr. G. Rajeshkumar, Associate Professor
Mr. J. Nagarjun, Assistant Professor (Sr.Gr)
Mr. T. Prem Kumar, Assistant Professor (Sr.Gr)
Mr. M. Senthilvel, Assistant Professor
Mr. R. Avinash Kumar, Assistant Professor

National Advisory Committee

Prof. B. B. Ahuja, COEP, Pune
Prof. Amitabha Ghosh, IEST, Shibur
Dr. R. Balasubramaniam, BARC, Mumbai
Prof. Bijoy Bhattacharyya, Jadavpur University, Kolkatta
Prof. Biswanath Doloi, Jadavpur University, Kolkatta
Prof. A. K. Chattopadhyay, IIT Kharagpur
Dr. Dasharath Ram Yadav, DRDL, Hyderabad
Prof. V. K. Jain, IIT Kanpur
Prof. P. K. Jain, IIT Roorkee
Prof. Jose Mathew, NIT Calicut
Shri. P. Kaniappan, WABCO, Chennai
Prof. M. Kanthababu, Anna University, Chennai
Prof. N. K. Mehta, IIT Roorkee
Shri. P. J. Mohanram, IMTMA, Bengaluru
Prof. P. V. Mohanram, PSG Institute of Technology and Applied Research, Coimbatore
Dr. Nagahanumaiah, CMTI, Bengaluru
Prof. S. Narayanan, VIT University, Vellore
Shri. Neeraj Sinha, NITI Aayog, New Delhi
Prof. S. S. Pande, IIT Bombay, Mumbai
Dr. DR. Prasada Raju, MVGR COE, Vizianagaram
Prof. V. Radhakrishnan, IIST, Trivandrum
Prof. P. Radhakrishnan, PSG Institute of Advanced Studies, Coimbatore
Prof. N. Ramesh Babu, IIT Madras, Chennai
Prof. J. Ramkumar, IIT Kanpur
Prof. P. V. Rao, IIT Delhi
Prof. Santosh Kumar, IIT (BHU), Varanasi
Prof. H. S. Shan, IIT Roorkee
Prof. M. S. Shunmugam, IIT Madras, Chennai
Dr. V. Sumantran, Celeris Technologies, Chennai
Dr. V. K. Suri, BARC, Mumbai
Prof. Vinod Yadava, NIT Hamirpur

Foreword

8th International and 29th All India Manufacturing Technology, Design and Research Conference Proceedings (Volumes 1–5)

(Edited by Different Professors and Researchers)

First, I would like to congratulate the Editors of five different volumes of proceedings of 8th International and 29th All India Manufacturing Technology, Design and Research Conference (AIMTDR) proceedings being published by Springer. These volumes are very good collection of the research and review papers on the manufacturing processes like Modern Machining processes (Volume-1), Additive Manufacturing and Metal Joining (Volume-2), Simulation, Product Design and Development (Volume-3), Forming, Machining and Automation (Volume-4) and Micro and Nano Manufacturing and Surface Engineering (Volume-5). These five volumes are comprehensive collection of the research papers focusing on the most recent research and developments in the area of manufacturing processes. These subject areas continue to be dominant manufacturing technologies, say, the *technologies of future*, namely, 3-D printing (Additive Manufacturing) which generally lacks speed, surface finish and dimensional accuracy. To compensate these weaknesses of 3-D printing in the real life production, I could also see good papers on Micro-/nano-manufacturing and nano-finishing. Theoretical analysis, optimization and simulation of manufacturing processes would definitely provide the necessary insights into the physics and mechanisms of these processes, as well as their basic understanding. These five volumes would be invaluable to the researchers working in research laboratories and engineers in industrial organizations working on shop floors for learning, consulting and applying some of the findings deliberated in the conference by the authors of different research papers.

Such conferences encourage the interaction between the research scholars, faculty members and user industries' representatives from different parts of the world. Unfortunately, this could not happen in this hybrid conference to the desired extent due

to the pandemic effects across the globe. Apart from these contributed papers, there were many on-line and off-line keynote lectures delivered by the researchers from different countries including India. I am sure that these papers should be of great help to the readers of these proceedings. These proceedings/collection of the papers should be of great help to the academia and industries as well as reference books in different sub-fields of manufacturing processes.

I would like to congratulate the authors for their contributions to all these five volumes of the proceedings and the Editorial Committee Members for their untiring efforts made in bringing out these research papers' collections in five volumes. I will also like to thank the technical committee members in general and ex-vice-president of NAC, Prof. U. S. Dixit for inviting me to write this foreword.

Kanpur, India

Dr. V. K. Jain
Professor (Retired) I.I.T. Kanpur
Member, National Advisory
Committee, AIMTDR 2021

Contents

Prediction of Machining Quality and Tool Wear in Micro-Turning Machine Using Machine Learning Models	1
T. Rajesh Babu and G. L. Samuel	
Plasma Characterization in Ultrasonic Vibration-Assisted Micro-Electrical Discharge Machining (μ-EDM)	13
Leeba Varghese, Jerin George, and K. K. Manesh	
Effect of Process Parameters on Accuracy of Holes Drilled on Quartz by Micro-USM	23
Santosh Kumar, B. Doloi, and Bijoy Bhattacharyya	
Influence of Vibration in the Nozzle Frame on the Ribbon Characterization in Planar Flow Melt Spinning Process	31
Meenuga ShanthiRaju, Anil Kumar Birru, and Sowjanya Madireddi	
Experimental Investigation into Wire Electrochemical Micro-Machining for Reduction of MicroSparks and Overcut	41
Naresh Besekar and Bijoy Bhattacharyya	
Influence of Voltage Pulse on Machining Accuracy in Electrochemical Micromachining	53
Himadri Sekhar Panda and Bijoy Bhattacharyya	
A Study on the Influence of Cutting Tool Geometry on the Temperature of the Workpiece in Nanometric Cutting of Silicon	67
Prateek Gupta and Janakrajan Ramkumar	
Experimental and Dimensional Analysis of Planar Flow Melt Spinning Process	79
Sowjanya Madireddi	

Encapsulation of CNT Films on Silicon Wafer by DLC Synthesized by PECVD for Application as a Thermal Interface Material	95
Krishna Ankit, T. Gecil Evangeline, L. S. Aravinda, N. Sharath Kumar, Mamilla Ravi Sankar, Nagahanumaiah, K. Niranjan Reddy, and N. Balashanmugam	
Design and Analysis of High Sensitivity MEMS Microphone	107
Jins Abraham, Harsha Sanjeev, and K. Nisarga	
Dependency of Machining Forces on Process Parameters During Sustainable MQL-Based Micro-milling of D2 Steel	119
Suman Saha, Shauvik Sikdar, A. Sravan Kumar, Sankha Deb, and P. P. Bandyopadhyay	
Two-Dimensional Finite Element Simulation of Micro-Electric Discharge Machining of Ti-6Al-4 V	129
B. C. Karthik, P. K. Pradeesh Karun, P. Sanal, Ch. Surendra, and Basil Kuriachen	
Corrosion Studies on AA7075-T7352 Alloys Under Adverse Environments	143
N. R. Karthik Varma, Neeraj K. Namboodiri, Sandeep Justin, S. Sreegovind, and K. Manoj Kumar	
Surface Modification of Al-7075 Alloy by Electro-Discharge Coating Process Using SiC/Cu Green Compact Electrode	151
Lokesh Kumar Ranjan, Sujoy Chakraborty, Uttam Kumar Mandal, Vidyut Dey, and Kanishka Jha	
Effect of Heat Input on Corrosion Resistance of 316 Austenitic Stainless Steel Cladding on Low-Carbon Steel Plate	163
Soumak Bose and Santanu Das	
Surface Characterization of Miniature Structures for Electronic Device Manufacturing	177
Swarup Paul	
An Empirical-Statistical and Experimental Analysis of Direct Laser Metal Deposition of WC-12Co Mixed Powder on SS 304 Substrate	187
Anitesh Kumar Singh, Kalinga Simant Bal, Dilip Kumar Pratihar, and Asimava Roy Choudhury	
Experimental Investigation on AFF of FDM Printed Pattern for Extrusion Die Insert	199
Harlal Singh Mali, Abdul Wahab Hashmi, Manish Kumar Jangid, and Anoj Meena	

Experimental Study on Cylindrical Grinding of Bearing Bush to Improve Surface Finish 213
 M. S. Karthik, V. R. Raju, K. N. Reddy, N. Balashanmugam, and M. R. Shankar

Study of Correlation Between Areal Surface Parameters and CoF of Ti6Al4V 225
 M. Venkata Krishna Reddy, Jino Joshy, Basil Kuriachen, and M. L. Joy

Wear and Hardness Behavior of Duplex-Treated AISI 1045 and AISI 4142 Steels 235
 B. Vaishnavi, A. Adhiyamaan, D. J. Hiran Gabriel, and Vinoth Kanna Chandrasekar

Prediction of Mechanical Behaviour of AA 3003-O with Varying Volume Fractions of White Fly Ash and SiC 245
 P. Ilanthirayan, M. Kalayarasan, and S. Mohanraj

Development of Novel Low-Cost Sintered Magnetic Abrasive for Surface Finishing 257
 Yogendra Kumar and Harpreet Singh

Characterization and Optimization of Pistachio Shell Filler-Based Epoxy Composites Using TOPSIS 267
 Sandeep Gairola, Hitesh Sharma, and Inderdeep Singh

Effect of Ball Milling Mechanism on the Density and Hardness of Al Matrix Consolidated Through Pressure Less Sintering 283
 Kishor Kumar Sadhu, Nilrudra Mandal, and Rashmi R. Sahoo

Fabrication of Al/Al-Co Composites by Stir Casting Method 291
 Devara Srinu, K. Srinivasarao, and N. R. M. R. Bharagava

Effect of Low Volume Reinforcement of Graphene/B₄C Nano Particles in Aluminium 6061-T6 Alloy 299
 Saikiran Ammisetty, CH. R. Vikram Kumar, and K. Hemachandra Reddy

Evaluation of Chemical and Mechanical Properties of Al-Si-Mg Composite for Use in Boat Engine Bed 309
 N. Mathimurugan, R. Subramanian, S. Ajith Balaa, R. Manoj, and C. Sathish

Realizing the Application Potential of Graphene-Modified Bionanocomposites for Prosthesis and Implant Applications 323
 Devendra Kumar Singh and Rajesh Kumar Verma

**Sliding Wear Behavior of Cast, Cold Extruded,
and Precipitation-Hardened Al/TiC_p Metal Matrix Composite 337**

P. N. Siddappa, B. P. Shivakumar, M. Mruthunjaya,
and K. S. Anil Kumar

About the Editors

Dr. Bijoy Bhattacharyya is Professor of Production Engineering Department in Jadavpur University, Kolkata, India. He had completed his B.E. in the year 1983 from REC, Calicut, Kerala and his M.E. in the year 1985 and Ph.D. in 1991 from Jadavpur University. He is specialized in Advanced manufacturing technology, non-traditional machining, micromachining and production management. He has published 166 research papers in reputed journals and more than 350 research papers in conferences. Several Ph.Ds. have been completed under his guidance. He has completed several research projects and he is a recipient of various awards. Dr. Bhattacharyya served as a reviewer and editorial board member for various reputed national and international journals.

Dr. Jose Mathew is Professor and Ex-Dean (Research and Consultancy) of the National Institute of Technology Calicut, Kerala. He received his M.Tech. and Ph.D. from IIT Kanpur (1990) and IIT Bombay (1999), respectively. His research interests are micro and nano-machining process, precision and ultra-precision machining, modelling and analysis of machining of ‘difficult to machine’ materials, etc. He has published about 65 research papers in international journals and more than 100 research papers in international conferences. Several M. Tech and Ph.D. thesis have been completed under his guidance. He has also worked on a number of industry sponsored research and development projects and consultancy projects. He is a recipient of various awards from DST, ISTE and NITC.

Dr. N. Saravanakumar is Professor and Head in the Department of Mechanical Engineering, PSG Institute of Technology and Applied Research, Coimbatore. He obtained his B.E. (Mechanical Engineering) and M.E. (Engineering Design) from Bharathiar University, Coimbatore, and Ph.D. from Anna University, Chennai. His major areas of research include Tribology, Development of nano-particulate lubricants, Composites and Metal forming. He has published 15 papers in peer reviewed international journals and more than 25 conference publications. Dr. Saravanakumar received project fundings from various agencies like DST, DRDL, NPOL, etc., to carry out research.

Dr. G. Rajeshkumar obtained his B.E. (Mechanical Engineering) from Sri Ramakrishna Institute of Technology, Coimbatore in 2010 and his M.E (Engineering Design) at Kongu Engineering College in 2012 with a Gold Medal. He received his Ph.D. in Mechanical Engineering from Anna University, Chennai in 2017. He is serving in PSG iTech since 2017 and is presently an Associate Professor in the Department of Mechanical Engineering. He is presently carrying out research in Natural fibers, Polymer matrix composites, Mechanism of needle Insertion in Soft Tissues, Tribology and Vibration. He has published about 50 peer reviewed international journal papers, 15 book chapters, 40 international and national conference proceedings and a text book. He has also edited a book titled *Bast Fibers and their Composites*, as well as a proceedings titled *Materials, Design and Manufacturing for Sustainable Environment*, both of which were published by Springer Nature, Singapore.

Prediction of Machining Quality and Tool Wear in Micro-Turning Machine Using Machine Learning Models



T. Rajesh Babu and G. L. Samuel

1 Introduction

All the processes, including manufacturing, in today's world are being revolutionized due to the introduction of Industry 4.0. Industry 4.0 is being widely adapted as it exhibits outstanding results. Any machined product should meet stringent quality standards and have a better surface finish for precise outcomes. The vast range of applications for micro-components, such as aerospace, medical, electronics and logistics communications. [1] is driving up the demand. The tolerance for the micro-components is quite negligible. Hence, efficient in-process monitoring and control methods are necessary to manufacture a high-quality product without any rejection. The importance of micro-manufacturing technologies has become increasingly significant. As a matter of fact, miniaturized titanium alloys are vigorously used in many biomedical and aeronautical industries. As a result, it is critical to specialize in micro-manufacturing processes for titanium alloys [2]. Micro-turning is a manufacturing process wherein miniaturized components can be manufactured with high precision at the micrometer level. Titanium alloys possess superior strength to weight ratio, excellent wear and corrosion resistance. Due to the low elastic modulus, low thermal conductivity and high chemical reactivity with the cutting tool material, titanium alloys are machined using coated carbide cutting tools [3].

Titanium alloys are extremely hard to machine due to their remarkable chemical and mechanical characteristics. Hence, tool wears out rapidly during the machining of these materials resulting in chatter and poor surface finish [4]. The forecast of tool wear and surface roughness of the machined component is important to ensure the performance of the machine tool. PCD tools perform better for machining Ti alloys

T. R. Babu · G. L. Samuel (✉)

Manufacturing Engineering Section, Department of Mechanical Engineering, IIT Madras, Chennai 600036, India

e-mail: samuelgl@iitm.ac.in

as compared to NbC, TiC, VC, WC, ZrC, TiN, ZrO and TiB₂ as they do not form TiC layer which avoids diffusion of constituents from work materials [5].

Before a particular surface quality threshold is surpassed, necessary action should be taken to reduce the damage. Hence, it is vital to predict the cutting tool condition at any instant of time to avoid any damage to the workpiece and the tool. Recent research has shown that many Artificial Intelligence (AI) algorithms have been developed for the predictive analysis of the machine tool. Atluru et al. [6] introduced a smart machine supervisory system framework that incorporates individual process monitoring and control modules to achieve a globally optimal machining solution. A LabVIEW application that incorporates process planning, health monitoring and tool condition monitoring was used to demonstrate the system's decision-making mechanism. Cheng et al. [7] addressed four types of smart cutting tools for ultra-precision and micro-manufacturing applications, including a force-based smart cutting tool, a temperature-based internally cooled cutting tool, a fast tool servo (FTS) and smart collets. Ploughing rather than cutting occurs in high-speed micro-turning when the depth of cut and feed are less than the tool nose radius and edge radius [8].

Wu et al. [9] investigated and discussed the wear properties of the diamond tool and the micro-topography of the ultra-precision turned surface. Kumar [10] studied the measurement of cutting conditions, surface roughness and material removal rate of micro-turning process, and a Genetic Algorithm was developed to optimize the process parameters. Aslantas et al. [11] explored the multi-objective optimization of cutting parameters of micro-turning of Ti-6Al-4 V by response surface method (RSM). Agrawal et al. [12] developed multiple regression, random forest and quantile regression to estimate the surface roughness of machined components in hard turning of AISI 4340 steel based on the cutting parameters.

Liu et al. [13] proposed systematic steps to construct the Cyber Physical Machine Tool (CPMT) and an MTConnect-based CPMT prototype also has been developed. Aghazadeh et al. [14] proposed a condition monitoring smart machine tool based on the current signal of spindle motor as the fault indicator signal. Spectral Subtraction Algorithm and Artificial Intelligence methods like Gaussian Process Regression (GPR), Bayesian Ridge Regression, Nearest Neighbours Regression (KNN), Support and Decision Trees Regression are used to build the smart machine tool. Ridwan et al. [15] implemented a STEP-NC-enabled Machine Condition Monitoring system by real-time cutting power, vibration and feed-rate. Data from several sensors was broadcast in MTConnect format, and fuzzy logic was used to achieve self-contained in-process feed-rate optimization. Morgan et al. [16] described the design of an Industry 4.0-compliant framework implemented as an Internet-based client-server approach for monitoring and teleoperation of CNC machine tools.

This work presents AI-based models to predict the surface roughness of the machined component and the flank wear of the cutting tool based on multiple input parameters. This predictive analysis is based on the experimental data obtained from the micro-turning machine. A series of machine learning models, Random Forest (RF), Standard Multilayer Perception (MLP), Regression Trees and Radial-based functions are developed, and the comparisons have made among them for accuracy in prediction and tuning time.

2 Experimental Study

The experimental setup for micro-turning is shown in Fig. 1. It comprises of a cast iron machine base of size $600 \times 600 \times 20$ mm, X-axis and Z-axis linear slides. The machine base is mounted over four levelling anti-vibration screw jacks which absorb the vibrations from the ground. Levelling screws are used to flatten the machine base with the help of spirit level while mounting on the machine table.

Linear slideways are mounted over the base for Z and X-axis movement. A backlash-free ball screw and nut mechanism is used to convert rotary motion to linear motion for the Z-axis and X-axis. The ball screws are supported by contact angular bearing, which can withstand both axial and radial loads. The ball screw has a dynamic load capacity of 340 kg and a static load capacity of 740 kg. A micro-drive (make: VLT) regulates the spindle speed. A stepper motor with an integrated drive controls the feed action, while a dial indicator assisted micrometre controls the depth of cut. A vibration sensor module is attached near the cutting tool tip to measure the vibration of the cutting tool during machining.

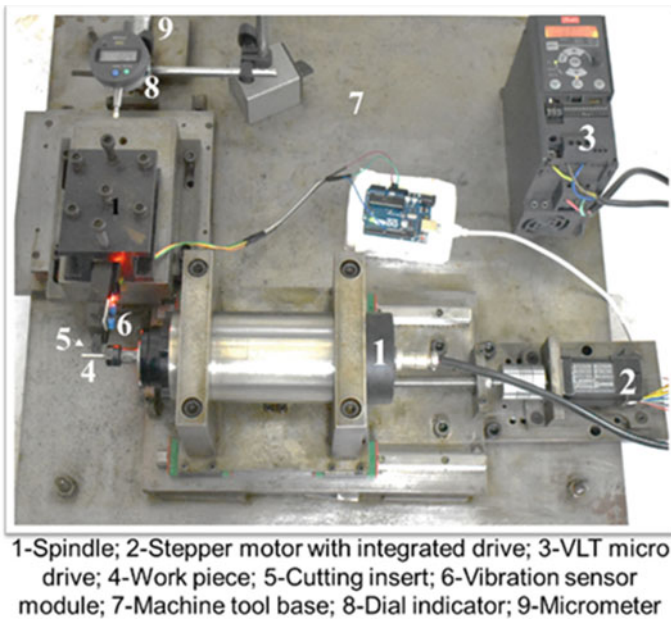


Fig. 1 Micro-turning machine

2.1 *Speed Control*

2.1.1 *Spindle*

The spindle is connected to the VLT micro-drive FC 51 to control the speed, and RPM of the spindle is calibrated with a non-contact digital type tachometer. This machine's spindle spins at a maximum speed of 24,000 rpm. With the help of a VLT drive, the spindle speed can be manually regulated in increments of 60 rpm. To hold the work piece, a 5 to 5.5 mm ER 11 collet is fitted to the spindle. The runout of the spindle is measured as 10 μ m.

2.1.2 *Feed*

A stepper motor with an integrated drive shaft is connected to the ball screw shaft through an aluminium based flexible coupling to regulate the feed. The microcontroller (Arduino UNO) is utilized to drive the stepper motor, which has a maximum speed of 500 rpm and a step angle of 1.8°. A non-contact type digital tachometer is used to calibrate the stepper motor speed. The ball screw integrated to the machine tool has a pitch of 2 mm. Hence, the feed motion resolution of 0.01 mm is achieved for the given step angle. The feed for revolution is the distance travelled by the spindle slide per one rotation of the spindle motor. The formula to calculate feed is shown in the Eq. (1)

$$\text{Feed (mm/rev)} = p \times \frac{N_m}{N_s} \quad (1)$$

where p = ball screw pitch, N_s = spindle speed and N_m = stepper motor speed.

2.1.3 *Depth of Cut*

The shaft of the ball screw mounted with tool post slideway is coupled with the anvil of screw gauge to regulate the depth of cut. A dial indicator is installed to track the cutting tool movement in the depth direction. With the use of a dial indicator and a micrometre, 1 μ m resolution is achieved in the depth direction.

2.2 *Cutting Tool*

The tool post is equipped with a tool holder. The tool holder is fastened to the coated carbide cutting inserts (CCMT060204LF KC5010). The cutting insert has a nose

radius of 0.4 mm, approach angle of 90° and 70° clearance angle. Each sample has been machined with new cutting insert.

2.3 *Vibration Measurement*

A vibration sensor module (SW-420) is attached near the cutting insert for measuring the vibration of cutting tool during machining. The vibration sensor sw-420 and comparator LM393 are used in this sensor module to detect any vibrations that exceeded the threshold. The vibration data is collected by a microcontroller (Arduino UNO) attached to the sensor module. SW-420 is a closed-type vibration sensor that provides a comparator output, a clean signal, a good waveform and a high level of capability. The sensor chip is damaged when the signal is reversed.

2.4 *Surface Roughness Measurement*

The surface roughness of the machined component is determined using a Wyko NT110 surface roughness 3D profilometer. This enables high-resolution three-dimensional surface assessments spanning from nanometre-scale roughness to millimetre-scale steps. Readings for each sample were taken at three locations, and the mean value was recorded as the surface roughness (R_a). Sample data is shown in Fig. 2.

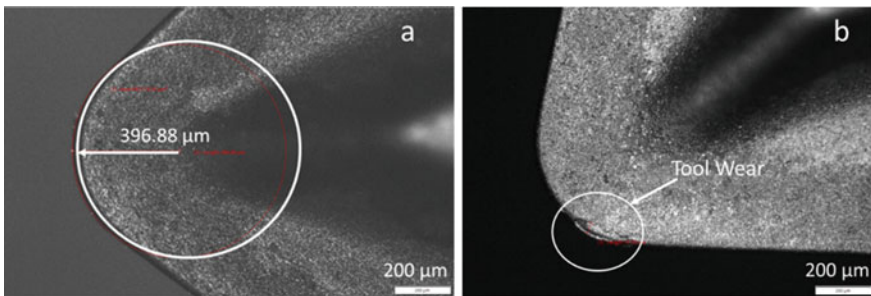


Fig.2 Cutting insert tool tip, **a** before machining, **b** after machining

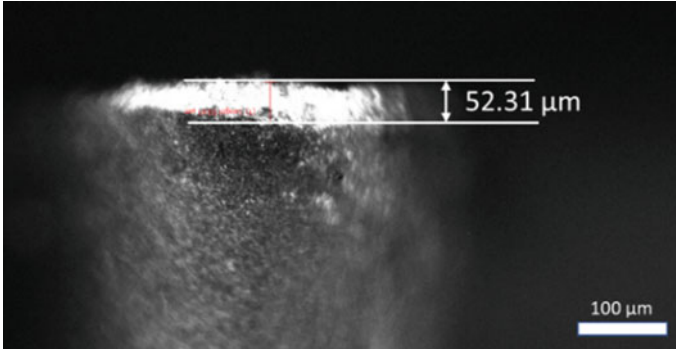


Fig. 3 Tool flank wear width after the Exp. no. 4

2.5 Tool Flank Wear Measurement

The width of the tool flank wear is measured by means of images collected with an Olympus inverted microscope. Figure 3 shows images taken by inverted microscope of the cutting tool tip before and after machining.

3 Machine Learning Models

Machine learning (ML) refers to the capability of computers to solve problems without being explicitly programmed to do so. Computational approaches that use the experience to improve performance or make accurate predictions are referred to as ML [17]. ML applications manufacturing industry includes cost reduction, less wastage, inventory control, operator safety enhancement, higher productivity, repair verification, overall profit and many more [18]. Multilayer perceptrons (MLPs), radial basis functions (RBFs), regression trees and random forest were used to assess ML regressors in this study (RF). In addition, linear regression was used as a baseline approach.

3.1 Multilayer Perceptron

The standard multilayer perceptron (MLP) is a torrent of single-layer perceptrons. This network contains a layer of input nodes, a layer of output nodes and one or more intermediate because the interior layers are not directly visible from the system's inputs and outputs, they are referred to as "hidden layers". An input layer of four nodes, an output layer of two nodes and three hidden layers of sixty nodes each were chosen and employed in this work on a trial-and-error basis.

3.2 *Random Forest (RF)*

A random forest is a collection of decision trees that have been trained using the “bagging” technique. The main idea of the bagging method is that combining many learning models enhances the total output [19]. In this study, the RF model is trained with 10 trees, mean squared error (MSE) as a criteria function to quantify the quality of a split and two sample splits with the rest of the parameters set to default.

3.3 *Regression Trees*

A regression tree is constructed using a technique known as binary recursive partitioning, which is an iterative operation that partitions data into partitions or branches and then divides each partition into smaller groups as the methodology continues up each branch. In this research, a decision tree algorithm with a cross entropy cost/loss function is devised, and tree pruning is used to reduce overfitting of the training data.

3.4 *Radial-Based Functions (RBF)*

RBF nets are extremely used many Gaussian curves to approximate the underlying functions. This network has only one hidden layer and fully connected with input layer and output of the hidden layer perform weighted some to get the output. This network only contains one hidden layer that is fully connected to the input layer, and the hidden layer’s output does a weighted sum to produce the output. The output neurons and weights are matrix since the RBF was designed for multiple output in this work.

4 **Results and Discussion**

Experiments are performed in an indigenously developed micro-turning machine. The three-level full factorial technique is used to design the experiments by altering the process parameters. The vibration sensor module installed at the tooltip collects vibration signals during machining, the surface roughness of the workpiece is measured with a Wyko 3D profilometer, and tool flank wear is computed from the images obtained with an Olympus inverted microscope. All the measured values are listed in Table 1.

Figures 3, 4 and 5 show the measured tool flank wear width, surface roughness measurement details and vibration data for Exp. No. 4. The data from the experiments is cleansed before being used to train the model. The models are trained with 80%

Table 1 Experimental results of micro-turning machine

Exp. No.	Speed (m/min)	Feed (μm)	Depth of cut (μm)	Cutting tool vibration (Hz)	Flank wear width (μm)	Surface roughness (R_a) (μm)
1	126	5	30	128	22.24	0.448
2	126	5	50	177	31.15	0.658
3	126	5	70	213	37.59	0.763
4	126	10	30	182	52.31	0.407
5	126	10	50	230	59.99	0.538
6	126	10	70	308	70.11	0.835
7	126	15	30	190	52.99	0.541
8	126	15	50	1196	100.5	2.142
9	126	15	70	387	65.5	0.942
10	157	5	30	137	26.23	0.542
11	157	5	50	211	42.88	0.607
12	157	5	70	314	70.98	0.732
13	157	10	30	430	31.45	0.684
14	157	10	50	511	34.17	0.712
15	157	10	70	608	43.92	0.775
16	157	15	30	485	33.47	0.652
17	157	15	50	512	48.42	0.688
18	157	15	70	611	56.64	0.774
19	188	5	30	327	22.6	0.638
20	188	5	50	385	36.45	0.688
21	188	5	70	450	57.97	0.774
22	188	10	30	297	36.45	0.652
23	188	10	50	347	50.6	0.714
24	188	10	70	512	60.84	0.817
25	188	15	30	334	42.93	0.707
25	188	15	50	401	57.97	0.817
27	188	15	70	487	70.8	0.831

of the obtained data that is randomly selected, and the remaining data has been used to test them. Speed, feed, depth of cut and vibration data are used as input data, while surface roughness and tool flank wear width are output data for developing the model.

Four machine learning models based on RF, MLP, Regression tree and Radial-based function were built to predict the machine tool condition. The MLP model is trained with four hidden layers, a learning rate of 0.01 and a momentum of 0.3, whereas the RBF, regression tree and random forest (RF) models use a ridge of 0.1, a minimum of 8 instances and 200 iterations.

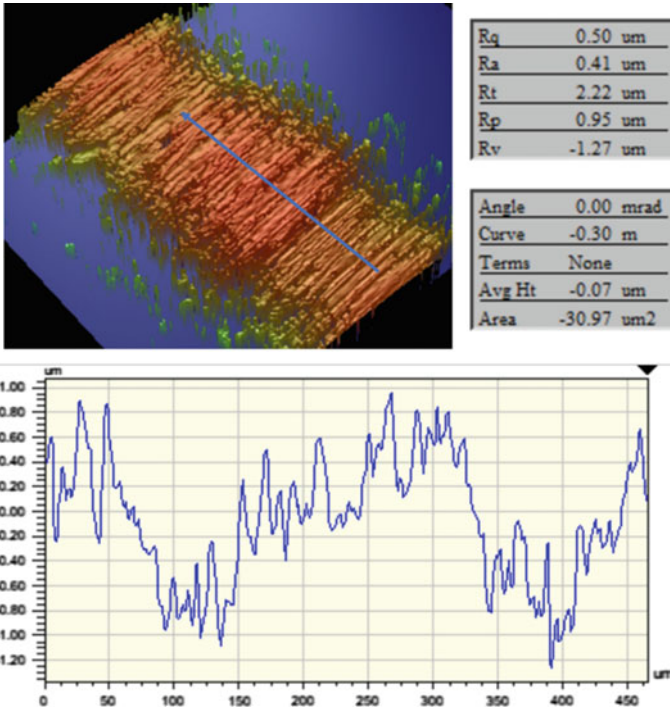


Fig. 4 Surface roughness measurement details of the machined component for the Exp. No. 4

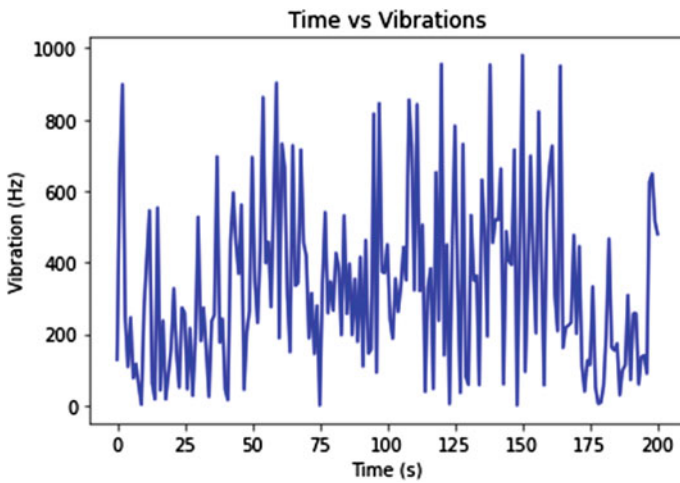


Fig. 5 Vibration of the cutting tool for the Exp. No.4

Table 2 Precision test results of machine learning models

ML model	Accuracy (%)	Tuning time (s)
Random forest	88	0.07
Regression tree	81	0.03
Multilayer perceptron	75	0.05
Radial-based Function	72	0.02

The prediction accuracies of all the models are low and the tuning time is quite short because the models are trained with little data. An Intel Core i5 2300 2.8 GHz processor was used to calculate the computation time. Table 2 shows the prediction accuracy and tuning time details for all of the produced models.

The prediction accuracy of RF models is 88%, which is higher than other models with a tuning time of 0.07 s, but the accuracy prediction of regression trees is 81% with a tuning time of 0.03 s, which is less than half the time of RF models. Because RF is composed of decision trees and trained with four trees, hence it has a longer tuning time with good prediction accuracy than a regression tree model. RBF model has lower prediction accuracy and takes less time to compute, as this model just contains one hidden layer. The performance of MLP depends significantly on the number of hidden layers and its associated neurons. The present study evaluates the MLP performance with varying hidden layers and nodes. It is found that three hidden layers with having six neurons each result in optimum performance. This MLP model has a prediction accuracy of 75, which is lower than both the RF and the Regression tree, and a tuning time of 0.05 s, which is slower than both the regression tree and the radial basis model. The computations take longer because the MLP was trained with three layers and 60 nodes in each layer. Figures 6 and 7 provide comparison graphs for predicting tool flank wear and surface roughness of the machined component using proposed ML models.

5 Conclusions

In this research, four common machine learning techniques, namely RF, MLP, Regression tree and Radial basis function, were used to predict tool wear of the cutting tool and surface roughness of machine components. The experiments are performed in a micro-turning machine. Vibrational data during machining, the surface roughness of the machined component and flank wear of the cutting tool were collected. The obtained data was used to train the model for predictive analysis of the machine tool. Vibrational data was recorded during the process, as well as the surface roughness of the machined component and flank wear of the cutting tool after each pass. The information gathered was utilized to develop a machine learning model that could predict machine tool performance.

From the analysis, it is seen that the RF model has more accuracy but takes a longer time to compute, whereas the Radial-based function has lower accuracy but takes

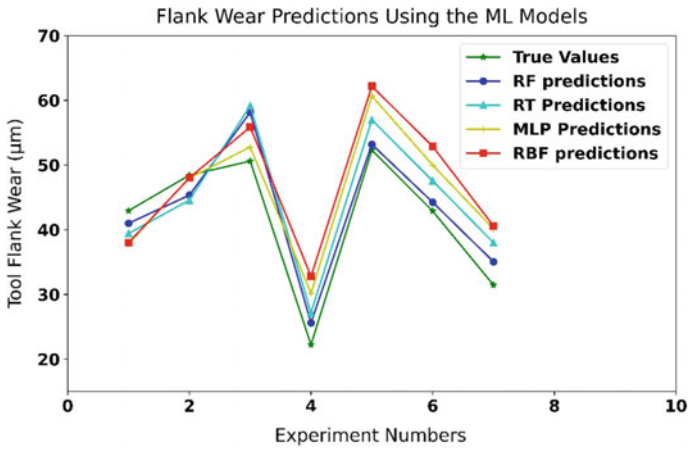


Fig. 6 Prediction of tool flank wear using ML models

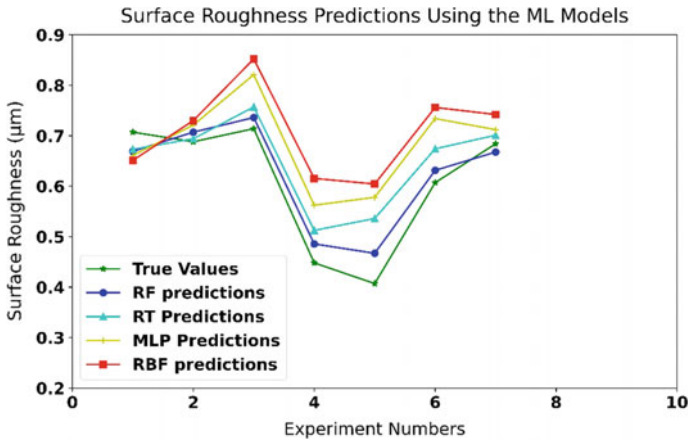


Fig. 7 Prediction of surface roughness using ML models

less time to compute. The accuracy of the Regression tree is 7% lower than the RF model, but it is two times faster. Considering the significance of computation time and accuracy associated with the various ML models, the Regression tree results in better performance to predict the machine tool condition. Tool wear and surface finish are primarily influenced by cutting parameters and cutting tool vibration. Lower feed rates and moderate depth of cut with high cutting speed result in less vibrations, minimum flank wear in cutting tool and good surface finish.

References

1. Jaffery SI, Driver N, Mativenga PT. Analysis of process parameters in the micromachining of Ti-6Al-4V alloy. In: Proceedings of the 36th international MATADOR conference vol 2010, pp 239–242. https://doi.org/10.1007/978-1-84996-432-6_55
2. Elias JV, Venkatesh NP, Lawrence KD, Mathew J (2021) Tool texturing for micro-turning applications—an approach using mechanical micro indentation. *Mater Manuf Process* 36(1):84–93. <https://doi.org/10.1080/10426914.2020.1813899>
3. Jagadesh T, Samuel GL (2014) Investigations into cutting forces and surface roughness in micro turning of titanium alloy using coated carbide tool. *Procedia Mater Sci* 5:2450–2457. <https://doi.org/10.1016/j.mspro.2014.07.496>
4. Özel T, Sima M, Srivastava AK, Kaftanoglu B (2010) Investigations on the effects of multi-layered coated inserts in machining Ti-6Al-4V alloy with experiments and finite element simulations. *CIRP Ann—Manuf Technol* 59(1):77–82. <https://doi.org/10.1016/j.cirp.2010.03.055>
5. Hartung PD, Kramer BM, von Turkovich BF (1982) Tool wear in titanium machining. *CIRP Ann—Manuf Technol* 31(1):75–80. [https://doi.org/10.1016/S0007-8506\(07\)63272-7](https://doi.org/10.1016/S0007-8506(07)63272-7)
6. Atluru S, Huang SH, Snyder JP (2012) A smart machine supervisory system framework. *Int J Adv Manuf Technol* 58(5–8):563–572. <https://doi.org/10.1007/s00170-011-3405-4>
7. Cheng K, Niu ZC, Wang RC, Rakowski R, Bateman R (2017) Smart cutting tools and smart machining: development approaches, and their implementation and application perspectives. *Chinese J Mech Eng (English Ed.,* 30(5):1162–1176. <https://doi.org/10.1007/s10033-017-0183-4>
8. Aslantas K, Çiçek A (2018) High speed turning of Ti6Al4V alloy in micro cutting conditions. *Procedia CIRP* 77:58–61. <https://doi.org/10.1016/j.procir.2018.08.213>
9. Wu D, Wang B, Fang F, (2019) Effects of tool wear on surface micro-topography in ultra-precision turning. *Int J Adv Manuf Technol*, pp 4397–4407. <https://doi.org/10.1007/s00170-019-03494-8>.
10. Kumar SPL (2019) Measurement and uncertainty analysis of surface roughness and material removal rate in micro turning operation and process parameters optimization. *Meas J Int Meas Confed* 140:538–547. <https://doi.org/10.1016/j.measurement.2019.04.029>
11. Aslantas K et al (2020) Investigations on surface roughness and toolwear characteristics in micro-turning of Ti-6Al-4V alloy. *Materials (Basel)* 13(13):1–20. <https://doi.org/10.3390/ma13132998>
12. Agrawal A, Goel S, Rashid WB, Price M (2015) Prediction of surface roughness during hard turning of AISI 4340 steel (69 HRC). *Appl Soft Comput* 30:279–286. <https://doi.org/10.1016/j.asoc.2015.01.059>
13. Liu C, Vengayil H, Zhong RY, Xu X (2018) A systematic development method for cyber-physical machine tools. *J Manuf Syst* 48:13–24. <https://doi.org/10.1016/j.jmsy.2018.02.001>
14. Aghazadeh F, Tahan A, Thomas M (2017) Tool condition monitoring using spectral subtraction algorithm and artificial intelligence methods in milling process. *Int J Mech Eng Robot Res* 6(6):30–34. <https://doi.org/10.18178/ijmerr.7.1.30-34>
15. Ridwan F, Xu X (2013) Advanced CNC system with in-process feed-rate optimisation. *Robot Comput Integr Manuf* 29(3):12–20. <https://doi.org/10.1016/j.rcim.2012.04.008>
16. Morgan J, O'Donnell GE (2018) Cyber physical process monitoring systems. *J Intell Manuf* 29(6):1317–1328. <https://doi.org/10.1007/s10845-015-1180-z>
17. Samuel AL (1988) Some studies in machine learning using the game of checkers. II—recent progress. *Comput Games I* 44(1):366–400. https://doi.org/10.1007/978-1-4613-8716-9_15
18. Peres RS, Rocha AD, Leitao P, Barata J (2018) IDARTS—Towards intelligent data analysis and real-time supervision for industry 4.0. *Comput Ind* 101, pp 138–146. <https://doi.org/10.1016/j.compind.2018.07.004>
19. Nouhi S, Pour M (2021) Prediction of surface roughness of various machining processes by a hybrid algorithm including time series analysis, wavelet transform and multi view embedding. *Meas J Int Meas Confed* 184. <https://doi.org/10.1016/j.measurement.2021.109904>

Plasma Characterization in Ultrasonic Vibration-Assisted Micro-Electrical Discharge Machining (μ -EDM)



Leeba Varghese , Jerin George, and K. K. Manesh 

1 Introduction

Micro-EDM is an advanced manufacturing process which has the capability to remove material in the sub-grain size range. It causes minimum damage to the material due to its non-contact nature and thus retains the properties of the material. This has made it a suitable choice for machining Nitinol shape memory alloy, widely used in biomedical and aerospace applications.

The material removal takes place due to a plasma generated in the gap between tool and workpiece, immersed in a dielectric. An electric potential is applied between the tool and workpiece electrodes by using a Resistance–Capacitance (RC) circuit. In the experimental set up, de-ionized water is used as dielectric. When breakdown potential of the dielectric is reached, it tends to break down into ions by releasing electrons. This breakdown process is initiated by primary electrons emitted by cathode, the tool electrode. Breakdown of the dielectric releases secondary electrons, through a series of chemical reactions and results in the formation of a plasma channel. The resulting avalanche of electrons is seen as the spark which will last only for a few microseconds. The bombardment of these ions and electrons on the surface of the tool and work piece, respectively, causes melting of corresponding electrodes and thereby material is removed from their surface. At the end of the discharge, the supply shutdown and plasma implodes under the external pressure applied by the surrounding dielectric. The dielectric flushes the molten metal along with the debris and leaving a crater at the work piece surface [1].

L. Varghese (✉) · J. George · K. K. Manesh
Department of Mechanical Engineering, Government Engineering College, Thrissur, India
e-mail: leebavarghese1982@gmail.com

K. K. Manesh
e-mail: maneshkk@gectcr.ac.in

2 Ultrasonic Vibration-Assisted EDM

The IEG of a μ EDM is below 10 μm , which itself reduce an effective dielectric flushing. This is one of the major reasons behind the reduced MRR and poor surface finish delivered by μ EDM. It is a proven fact that effective flushing of molten metal from melt pool causes increased crater depth and thereby crater volume. Also, an effective flushing at IEG will carry away the debris at IEG, which causes controlled spark and thereby reduces surface roughness. Hence, it is important to maintain an effective flushing at IEG for better output. For improving the flushing efficiency, researchers found that providing pulsating effect over the dielectric at IEG will produce cavitation bubbles and thereby micro jets, which effectively flushes the molten metal from the pool and debris at gap [2].

Ultrasonic vibration is applied to EDM in three different modes, vibration applied on tool, work piece, and on dielectric. In the present study, ultrasonic vibration is applied over the tool electrode. Shabgard et al., in 2018 conducted a numerical and experimental study on tool vibration of EDM. The study delivers an exact idea about the involvement of tool vibration over MRR and recast layer. The two advantages of providing ultrasonic vibration in micro-EDM are increased plasma energy density and effective flushing ability. In an ultrasonic vibration-assisted EDM tool, electrode moves up and down with a frequency greater than 20 kHz. During the downward movement of the tool, acoustic pressure is added to the surrounding dielectric pressure and thereby increases the hydro-static pressure at plasma channel. This confines the plasma channel expansion and thus increases the electron density (N_e). The increased electron density reduces the mean free path distance of electrons. The high frequency motion of tool electrode will accelerate the vertical velocity of electrons, ions, and neutral particles in plasma channel which increases the kinetic energy and thereby the temperature due to electron bombardments. This will increase the plasma temperature and thereby melting of more metal at work piece surface [3].

Increased MRR and reduced surface roughness offered by ultrasonic vibration-assisted μ EDM enables it to be a prominent non-conventional manufacturing operation in the machining of advanced materials. Shape memory alloys (SMA) are one of the most common advanced materials applicable in modern manufacturing industries. Nickel-titanium alloy or Nitinol is one of the most advanced SMA used in various industrial applications such as automotive, robotics, actuators, electronics, and biomedical [4].

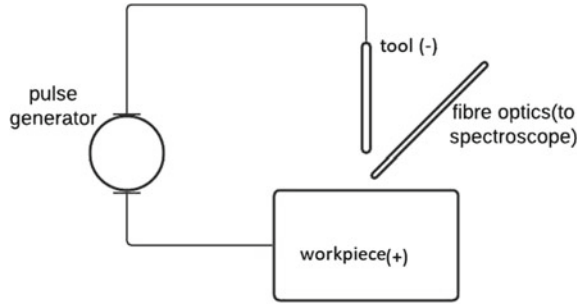
3 Experiment Performed

The experiment was performed on an in-house developed experimental set up. Nitinol was used as the work piece as well as tool material in order to reduce surface contamination. The work piece and tool were fixed on an XYZ stage controlled by servomotors having 1-micron resolution. The tool was made to move in the Z axis, which

Table 1 Micro-EDM process parameters

Process parameters	Level 1	Level 2	Level 3
Voltage (V)	40	100	110
Spark on time (μ s)	5	10	20
Amplitude	2	4	8
Frequency	20	40	60

Fig. 1 Setup for temperature and density measurement



was also equipped with an emergency stop triggering circuit-based feedback system, to set the spark gap. The ultrasonic vibration is given by a piezoelectric actuator with no load displacement at resonance varying between 165 and 247 μ m. The tool was given negative polarity and the work piece, positive polarity from the RC circuit-based pulse generator.

The levels of input parameters are given in Table 1. The tool is lowered using Mach3 Loader interface of the XYZ stage. Inter-electrode gap is maintained at a preset value with the help of feedback system. The process parameters are applied as per the L27 orthogonal array. Then, the triggering pulse is given after selecting the single pulse mode of pulse generating circuit. The capacitor of the RC circuit gets discharged for the specified pulse on time, creating a spark at the inter-electrode gap between the work piece and tool.

A 1500-micron dia, 1 m long UV–VIS optic fiber with collimation and focusing lens assembly is erected by using a holder in the inter-electrode gap as shown in Fig. 1. This captures the intensity of light emitted by the plasma and transfers it to the spectroscope via a slit. The Spectra G600 TSF spectroscope, with a wavelength range of 320–900 nm.

4 Plasma Temperature and Density

When the applied potential reaches a value equal to the breakdown potential of the dielectric, it breaks down into positive ions, negative ions, and electrons. A large number of chemical reactions are involved in the formation of plasma. These

are elastic, ionization, excitation, and dissociation reactions. These reactions have a significant influence on the evolution of plasma temperature and electron density. The energy released during this stage by the reactions is absorbed by the different species, and they get excited to a higher energy state. This happens during the initialization and expansion stage of the plasma. When plasma tends to come back to its equilibrium state, these species reach their initial energy stage. The emitted energy in the visible range is captured by the fiber optics connected to the spectroscope. The images captured by the spectroscope are processed by an in-line CCD camera, and the emission spectra are plotted.

4.1 Analysis of the Spectrum

4.1.1 Dark Data Subtraction

Dark data is the spectrum captured at the absence of light source. The spectroscopic parameters such as slit width and exposure were set according to the actual experimental requirements. Here, the light source is plasma and the dark data collected at the absence of plasma is processed. With dark data subtraction, noises are reduced.

4.1.2 Base Line Subtraction

As line ratio method is used for calculation of plasma characteristics, the value of intensity is not important. Hence, the base line of the whole spectrum is shifted toward X(0). Base line subtraction is executed in Origin Pro software.

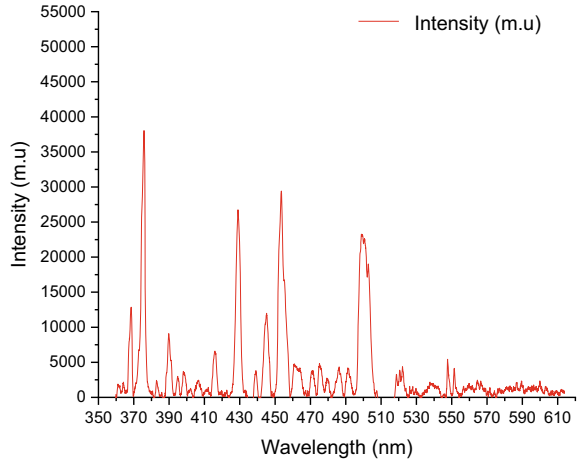
4.1.3 Smoothing

It is the signal processing technique used for noise cancelation. Smoothing of the spectrum is performed for better identification of peak and to fit Lorentz curve more effectively. Software used is Origin Pro 2018. Adjacent averaging method is used for this purpose.

4.1.4 Element Identification

De-ionized water is used as dielectric while performing actual experiments. Elements needed to be identified are titanium (Ti), nickel (Ni), hydrogen (H), and oxygen (O). These elements are identified from the values of wavelengths given in NIST (National Institutes of Standards and Technology) atomic spectrum database [5] (Fig. 2).

Fig. 2 Spectrum obtained after processing



4.2 Calculation of Plasma Temperature

The Atomic Spectra Database (NIST) contains data for observed transitions and energy levels in atoms and atomic ions. It also includes radiative transition probabilities, ground states and ionization energies, wavelengths, relative intensities, and energy levels.

The temperature is calculated assuming that plasma has reached a local thermodynamic equilibrium [6]. A pair of spectral peaks of same species is selected, and the values corresponding to the wavelength at those peaks are taken from NIST database [7].

$$T = \frac{|E_2 - E_1|}{\left(\ln \frac{I_1 \lambda_1 A_2 g_2}{I_2 \lambda_2 A_1 g_1} \right) k_b} \quad (1)$$

where,

E_1 is the excitation potential

A_1 is the transition probability

g_1 is the statistical weight of the excited level

I_1 is the measured intensity for the emission line at wavelength λ_1 .

E_2 , A_2 , g_2 , and I_2 are similar functions at wavelength λ_2 , and k_b is the Boltzmann constant.

The ratio I_1/I_2 is taken from the spectrum obtained.

4.3 Electron Density Calculation

In micro-EDM, Stark broadening is more dominant than Doppler broadening and Lorentz fit suits better for calculating FWHM. Here, hydrogen Balmer line (H_β) is used to calculate electron density [8].

$$N_e = C * \Delta\lambda_\beta^{\frac{3}{2}} \quad (2)$$

where,

N_e electron density in cm^{-3} .

C is excitation coefficient.

5 Results and Discussions

5.1 Plasma Temperature

The spectral lines for calculation of temperature are chosen in such a way that they belong to the same element and the relative intensity between them is maximum. Spectroscopic data corresponding to the selected lines is given in Table 2. Resonant spectral lines are not chosen as it will reduce the accuracy of temperature estimation due to their self-absorption effect [9].

Table 2 Spectroscopic data of selected emission lines

Atom/ion	Wavelength (nm)	Transition probability (A_{ki})(s^{-1})	Lower energy level (cm^{-1})	Upper energy level (cm^{-1})
Ti I	429.57	1.30E + 08	6556.833	29829.112
Ti I	453.32	8.83E + 07	6842.962	28896.059
Ti I	518.63	3.79E + 06	17075.258	36351.365
Ti II	390.05	2.76E + 07	9118.2849	34748.5062
Ti II	416.15	3.90E + 05	8744.3406	32767.1961
Ti II	439.10	3.02E + 05	9930.7766	32692.1022
Ni I	383.16	1.5E + 06	3409.937	29500.674
Ni I	547.69	9.5E + 06	14728.840	32982.260

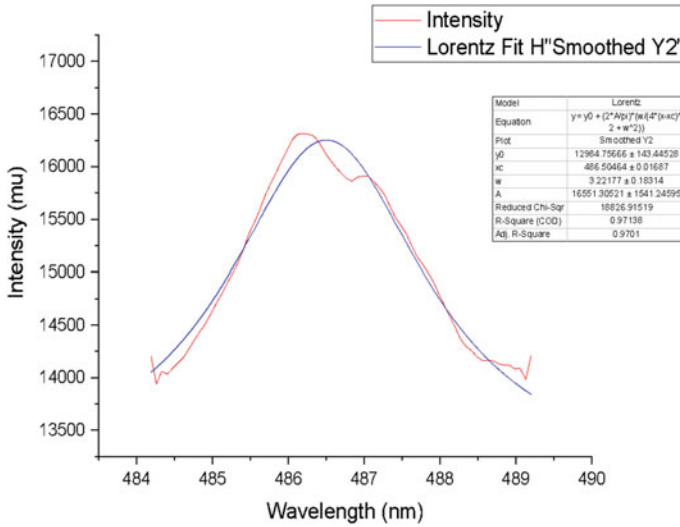


Fig. 3 Lorentz fit over hydrogen Balmer line

5.2 Electron Density

The shift and broadening of H_β (486.13 nm) spectral line is used to measure the electron density. In this case, the shift and broadening of spectral line occurs when collision takes place between charged particles. FWHM simulation of Lorentz curve fit method is used as shown in Fig. 3.

5.3 Effect of Ultrasonic Vibration

Ultrasonic vibration is given to the tool in the current experiment since its effect will not be completely obtained at the inter-electrode gap if the dielectric tank is vibrated. Vibration provided at the work piece may also give the same results. Table 3 shows the plasma temperature and electron density calculated for 27 experimental runs, using equation (1) and (2). It can be seen that the temperature obtained is higher compared to the referred experiment [2] and the electron density shows only a slight variation. From this, it can be inferred that implementation of ultrasonic vibration as a hybrid technology in micro-EDM is an appreciable approach as far as the plasma characteristics are concerned.

Table 3 Micro-EDM machining parameters and results

Run	Voltage	Spark ON time	Amplitude	Frequency	Plasma temperature	Electron density
	V	μ s	m.u	KHz	K	cm^{-3}
1	60	40	5	40	11283	8.4027E + 16
2	80	20	5	40	7754	6.16783E + 16
3	40	40	5	20	8430	9.35336E + 16
4	40	40	2	40	9200	6.78313E + 16
5	80	60	5	40	11710	9.72487E + 16
6	40	20	5	40	6890	8.1693E + 16
7	40	40	5	60	9522	6.57136E + 16
8	60	40	2	60	10318	5.36911E + 16
9	60	40	2	20	9118	7.42607E + 16
10	60	40	8	20	8339	1.18087E + 17
11	80	40	5	20	9202	7.68066E + 16
12	60	20	5	20	7220	8.25657E + 16
13	80	40	5	60	10080	6.41E + 16
14	40	60	5	40	8548	9.9101E + 16
15	40	40	8	40	9312	6.81591E + 16
16	60	40	5	40	11320	8.02454E + 16
17	60	40	5	40	10980	8.03554E + 16
18	60	20	8	40	7698	1.03468E + 17
19	80	40	2	40	9108	1.23567E + 16
20	60	40	8	60	9088	1.4689E + 17
21	60	60	2	40	9761	7.17435E + 16
22	60	20	2	40	8337	5.90792E + 16
23	60	60	8	40	9448	6.17047E + 16
24	60	60	5	20	8989	5.34388E + 16
25	80	40	8	40	9865	8.37341E + 16
26	60	60	5	60	9895	5.85587E + 16
27	60	20	5	60	9665	1.26894E + 17

6 Conclusions

This work was an attempt to find out if there is any improvement in the net heat generated at the plasma in a micro-EDM process by providing an ultrasonic vibration to the tool. The conclusions drawn are

- (1) In micro-EDM, increasing the rate of circulation of dielectric may not be an effective option for removal of debris since it might delay the ionization process and thus the formation of plasma. Providing ultrasonic vibration to the tool

can improve the flushing efficiency of the dielectric without increasing its flow rate. Also, the higher temperature is obtained at the plasma while providing ultrasonic vibration to the tool as the electrons accelerate and thus more energy is released on electron bombardments on the work piece surface. In this study, the temperature shows a definite improvement compared to the referred experiment [10] and electron density remains almost same.

- (2) The choice of the spectral lines is important as a different set of lines can give an entirely different value. Spectral lines should be chosen in such a way that relative intensity between them is maximum.
- (3) Optimization of these results is to be conducted, and a model has to be created to predict the characteristics of the plasma.

References

1. Mujumdar SS et al (2014) A model of micro-electro discharge machining plasma discharge in deionized water. *J Manuf Sci Eng* 136:031011–031021
2. Shabgard M et al (2011) Ultrasonic assisted EDM: effect of the work piece vibration in the machining characteristics of FW4 welded metal. *Front Mech Eng* 6:419–428
3. Shabgard M et al (2018) Numerical and experimental study of the effects of ultrasonic vibrations of tool on machining characteristics of EDM process. *Int J Adv Manuf Technol* 96:2657–2669
4. Jani M et al (2013) A review of shape memory alloy research, applications and opportunities. *Mater Des* 56:1078–1113
5. NIST atomic spectra database, <https://www.nist.gov/pml/atomic-spectra-database> last visited on 02/07/2021.
6. Safeen A et al (2019) Measurement of plasma parameters for copper using laser induced breakdown spectroscopy. *Dig J nanomater Bio Struct* 14:29–35
7. Mujumdar SS et al (2018) Effect of dielectric conductivity on micro-electrical discharge machining plasma characteristics using optical emission spectroscopy. *J Micro Nano Manuf* vol 6, 031001-1
8. Descoedres A et al (2004) Optical emission spectroscopy of electrical discharge machining plasma. *J Mater Process Technol* 149:184–190
9. Idris N et al (2018) Temperature estimation using Boltzmann plot method of many calcium emission lines in laser plasma produced on river clamshell sample. *IOP Conf Series* 11200:12098. <https://doi.org/10.1088/1742-6596/1120/1/012098>
10. Nagahanumaiyah et al (2009) Characterization of plasma in micro-EDM using optical spectroscopy. *J Manuf Process* 11:82–87

Effect of Process Parameters on Accuracy of Holes Drilled on Quartz by Micro-USM



Santosh Kumar , B. Doloi , and Bijoy Bhattacharyya

1 Introduction

Ultrasonic micro machining (USMM) is an abrasive-based method, which is applied to conductive and non-conductive hard and brittle materials like glass, quartz and advanced ceramics to create through holes and different micro features. Abrasive slurry is disbursed into the work surface, where micro tool tip is ultrasonically vibrated. When the free abrasive particles come at the tool–workpiece interface, they get energized through the aid of ultrasonic vibration in the down stroke of tool tip and ultimately remove materials through fatigue failure. Various micro machining technologies are available for producing micro features. But, other process like micro-EDM and micro-ECM is not appropriate for electrically non-conductive materials. Using micro laser beam machining method, hard and brittle materials can be machined but due to thermal process, it can source thermal spoil to machined features of the job material [1, 2]. Unlike laser beam machining, USMM neither thermally spoils the work material nor produces significant levels of stresses. USMM is therefore suitable in machining fragile components of hard and brittle materials, where it is essential to reduce stresses or thermal distortions. It is also not a chemical and electrical process; so there is no change in chemical or physical properties of the workpiece.

For watch making industry, microfluidic, optical applications, there is need of generation of micro 3D features on materials like glass, quartz, etc. Ultrasonic micro machining is a promise technique for these applications [3]. Technique for measurement and also theoretical model to estimate the micro tool wear had been proposed [4, 5]. The mechanism of material removal in micro-USM was in both ductile and brittle manner [6]. Tool wear is a major issue in USMM, because it has an impact on

S. Kumar (✉) · B. Doloi · B. Bhattacharyya
Production Engineering Department, Jadavpur University, Kolkata 700 032, India
e-mail: santosh14fiem@gmail.com

the precision of micro features. The depth is affected by longitudinal wear, while the taper imposed on micro holes is determined by lateral wear [7]. In USMM, micro features can be generated using complex or simply shaped tools [8–11]. In micro-USM, abrasive slurry concentration is more influenced parameter than power rating and tool feed rate for micro-hole drilling on quartz. [12]. EPAMUSM is a magnificent technique to generate micro hole in hard and brittle material [13].

The objectives of this paper are to analyze the accuracy of micro-hole drilling on quartz by USMM, using simple cylindrical-shaped tool. The overcut and taper angle variations have been analyzed and discussed.

2 Experimental Setup Details and Planning

In ultrasonic micromachining (USMM), electrical energy is transformed into mechanical vibration through transducer. It moves toward the horns through coupler. The horn increases the amplitude of the vibration and directs it to the micro tool. Now, micro tool vibrates along vertical axis at ultrasonic frequency, typically 20 kHz with low amplitude. The micro-USM has a maximum power rating of 1000 W and can operate with a constant static load. At the same time, the feed rate is applied vertically downward. Abrasive material is diverse in water and constantly flows across the machining zone. Figure 1 depicts a schematic representation of an ultrasonic micro machining system.

Micro tool fabricated as per design is shown in Fig. 2. Tool is designed as per required length and weight of tool. The tool material has been chosen as SS304 which is highly efficient tool material for USMM. Furthermore, stainless steel is a low-cost and easily available material. The fabricated tool is silver brazed to hexagonal

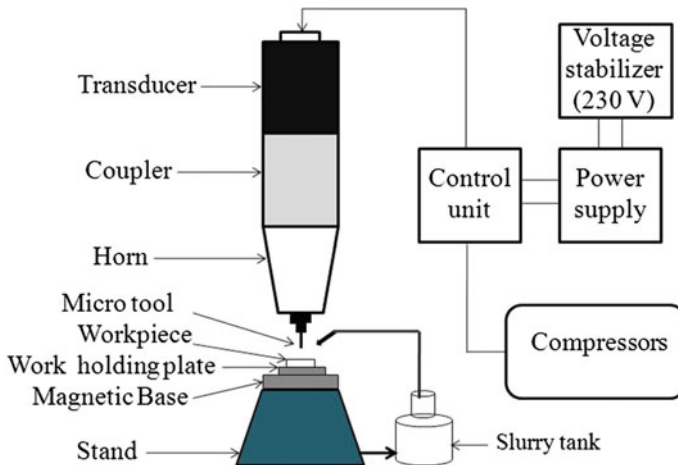
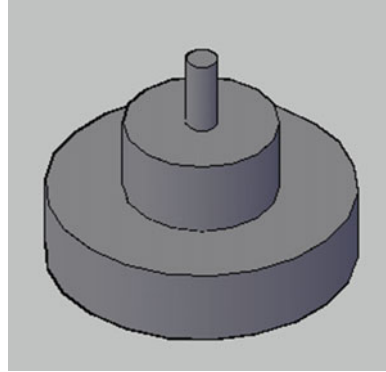


Fig. 1 Schematic representation of ultrasonic micro machining system

Fig. 2 Micro tool design for USMM



bolt and then mounted in horn. The quartz material of 1 mm thickness (Size 25 × 25 mm) put on the fixture made of conductive material which is placed on magnetic base. Abrasive particles such as boron carbide, silicon carbide and aluminum oxide combined with water at normal temperature were selected as abrasive slurry. The abrasive slurry concentration varies from 10 (10 gm per 100 cc of water) to 40% during experimentation. The slurry flow rate varies from 40 ml/sec to 55 ml/sec during experimentation.

3 Measurement of Responses

The micro-hole drilling experiments were executed by USM of Sonic-Mill Model AP-1000. Optical microscope (Leica DM 2500) is used to capture the images of drilled holes and for the measure of dimension of the holes. The optical images are captured for calculation of overcut at entrance, overcut at exit and taper angle.

3.1 Measurement of Overcut

After machining, the workpiece is cleaned using acetone. The overcut is the measure of increased diameter of machined hole. Diametrical overcut is measured as the difference in diameter of machined hole and the diameter of micro tool as given in Eq. (1).

$$D_o = D_h - D_t \quad (1)$$

where, D_o is diametrical overcut, D_h is diameter of machined hole and D_t is diameter of micro tool before machining.

3.2 Measurement of Taper Angle

At first, diameter at entrance and exit surface of micro hole produced on quartz were measured by optical microscope. For calculating the taper angle, as given in Eq. (2) is used.

$$\text{Half taper angle} = \tan^{-1} \frac{D_{\text{entry}} - D_{\text{exit}}}{2t} \quad (2)$$

where, D_{entry} Entrance diameter of micro hole,
 D_{exit} Exit diameter of micro hole, and
 t Workpiece thickness.

4 Results and Discussion

The investigational analysis has been done on quartz during USMM. Micro tool of SS304 of 330 μm was used. Three different type of abrasive (B_4C , SiC and Al_2O_3) of grain size 14 μm was used by changing abrasive concentrations and abrasive flow rate. μ -holes were generated successfully on Quartz using the USMM. The warmth of work material was equal to the slurry, because slurry was circulating around machining zone. The variables of major machining responses of USM μ -hole drilling, such as overcut and taper angle, were analyzed with respect to abrasive slurry concentration and slurry flow rate for different type of abrasive.

4.1 Variation of Overcut with Process Parameters

The variation of overcut with abrasive slurry concentration is shown in Fig. 3. Lower overcut of USM micro-hole drilling is obtained 28 μm , 34 μm and 37 μm for Al_2O_3 , SiC and B_4C abrasives, respectively, at low abrasive slurry concentration as 10%. Overcut varies in the same manner at higher abrasive slurry concentration for all three type of abrasive. As abrasive slurry concentration increases, overcut also increases since more number of abrasives are available during machining. Overcut is obtained as 34 μm , 40 μm and 46 μm for Al_2O_3 , SiC and B_4C abrasives, respectively, at higher abrasive slurry concentration (40% by weight).

The variation of overcut with slurry flow rate is shows in Fig. 4, while three different types of abrasive are used. The lower value of overcut is obtained as 27 μm , 29 μm and 37 μm for Al_2O_3 , SiC and B_4C abrasives, respectively, at 10% abrasive slurry concentration. At 10% abrasive slurry concentration overcut is less while using Al_2O_3 and SiC as compared to B_4C .

Fig. 3 Variation of overcut with abrasive slurry concentration

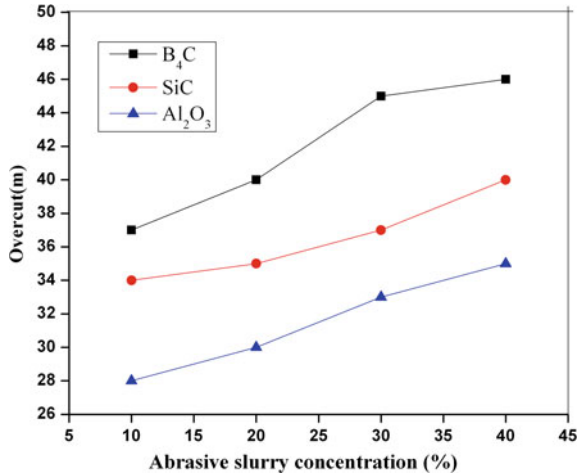
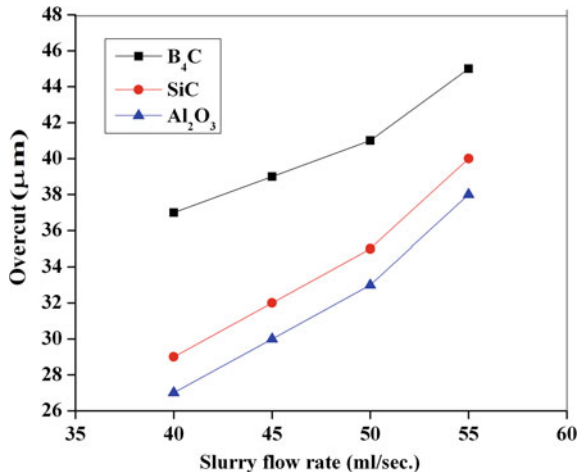


Fig. 4 Variation of overcut with slurry flow rate



4.2 Variation of Taper Angle with Process Parameters

Figure 5 shows that taper angle is a smaller amount when abrasive slurry concentration is low (10% by weight). The lower value of taper angle is 1.41 °, 1.70 ° and 2.14 ° for Al₂O₃, SiC and B₄C abrasives, respectively, at low abrasive slurry concentration (10% by weight). Taper angle increases with increasing abrasive slurry concentration. Taper hole is formed due to non-uniform machining as tool is gradually entered into the workpiece. The taper angles of 2.0 °, 2.23 ° and 2.87 ° are obtained for Al₂O₃, SiC and B₄C abrasives, respectively, at high abrasive slurry concentration (40% by weight).

Fig. 5 Variation between taper angle and abrasive slurry concentration

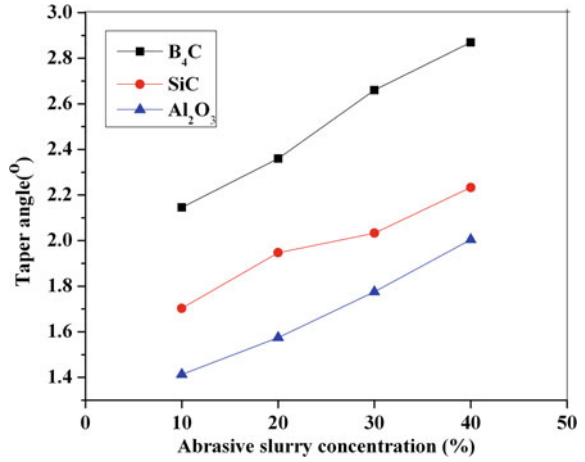


Fig. 6 Variation between taper angle and slurry flow rate

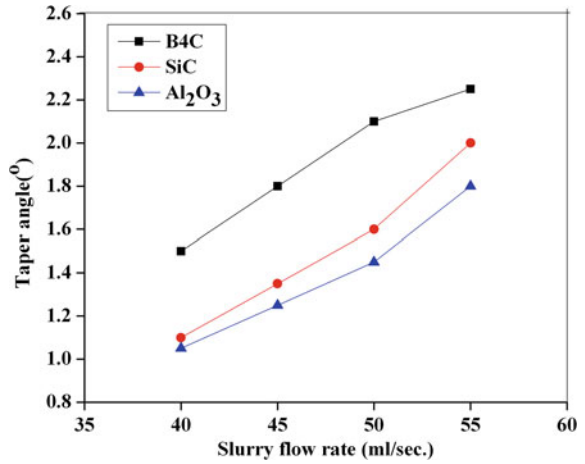
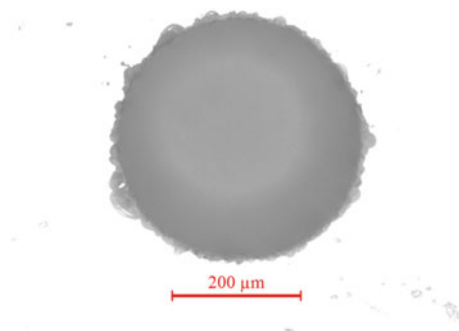


Figure 6 demonstrates the variant of taper angle with slurry flow rate. The taper angle of 1.05 °, 1.1 ° and 1.5 ° are obtained for Al₂O₃, SiC and B₄C abrasives, respectively, at lower slurry flow rate (40 ml/sec). Taper angle increases with increase in slurry flow rate, as fresh abrasive particle available in machining zone and erode more material also from the bottom part of the hole. The taper angles of 1.8 °, 2.0 ° and 2.25 ° are obtained for Al₂O₃, SiC and B₄C abrasives, respectively, at higher slurry flow rate (55 ml/sec).

Figure 7 shows the micro graph of micro-hole drilled on quartz by ultrasonic micro machining through developed circular cross section micro tool.

Fig. 7 Micro graph of micro hole on quartz



5 Conclusions

In this paper, ultrasonic micro machining method has been successfully utilized for making μ -hole on quartz by μ -tool of circular cross section. The results of the study show that process parameters such as abrasive slurry concentration and slurry flow rate have an effect on the overcut and taper angle of micro holes produced on quartz using different abrasives. From the experimental results, lower value of overcut and lower value of taper angle have been achieved as $27 \mu\text{m}$ and 1.05° , respectively. It is also concluded that for achieving lower overcut and lower taper angle, low value of slurry concentration and low slurry flow rate has been used. For achieving lower overcut and low taper angle, Al_2O_3 abrasive has been preferred during micro-hole generation on quartz.

Few research works on micro feature producing on quartz by USMM process have been reported till date, but more experimental work in the area of optimization during micro feature generation on quartz by USMM process is required.

References

1. Chen K, Yao YL (2000) Process optimization in pulsed laser micromachining with applications in medical device manufacturing. *Int J Adv Manuf Technol* 16(4):243–249
2. Kibria G, Doloi B, Bhattacharyya B (2010) Experimental analysis on Nd: YAG laser micro turning of alumina ceramic. *Int J Adv Manuf Technol* 150 (5–8):643–650
3. Egashira K, Masuzawa T (1999) Micro ultrasonic machining by the application of workpiece vibration. *Annals of CIRP; Annals of CIRP* 48 (1)
4. Jain V, Sharma AK, Kumar P (2012) Investigations on tool wear in micro ultrasonic machining. *Appl Mech Mater* vol 110–116, pp 1561–1566
5. Zuyuan Y, Chunshi M, Chengming A, Jianzhong L, Dongming G (2012) Prediction of tool wear in micro USM. *CIRP Anal Manuf Tech* 61(1):227–230
6. Zarepour H, Yeo SH (2012) Predictive modeling of material removal modes in micro ultrasonic machining. *Int J Mach Tools Manuf* 62:13–23
7. Cheema MS, Singh PK, Tyagi O, Dvivedi A, Sharma AK (2016) Tool wear and form accuracy in ultrasonically machined microchannels. *Measurement* 81:85–94

8. Egashira K, Taniguchi T, Tsuchiya H, Miyazaki M (2004) Micro ultrasonic machining using multitools. In: Proceedings of the 7th international conference on progress machining technology (ICPMT 04), pp 297–301
9. Yu ZY, Rajurkar KP, Tandon A (2004) Study of 3D micro-ultrasonic machining. *J Manuf Sci Eng* 126(4):727–732
10. Sun XQ, Masuzawa T, Fujino M (1996) Micro ultrasonic machining and its applications in MEM S. *Sens Actuators A: Phys* 57(2):159–164
11. Boy JJ, Andrey E, Boulouize A, Khan-Malek C (2010) Developments in micro ultrasonic machining (MUSM) at FEMTO-ST. *Int J Adv Manuf Technol* 47(1–4):37–45
12. Kumar S, Hansda B, Das S, Doloi B, Bhattacharyya B (2017) Micro hole fabrication on quartz using ultrasonic micromachining process. *Int J Precision Technol* 7:222–236
13. He JF, Guo ZN, Lian HS, Liu JW, Yao Z, Deng Y (2019) Experiments and simulations of micro-hole manufacturing by electrophoresis-assisted micro-ultrasonic machining. *J Mater Process Tech* 264:10–20

Influence of Vibration in the Nozzle Frame on the Ribbon Characterization in Planar Flow Melt Spinning Process



Meenuga ShanthiRaju , Anil Kumar Birru , and Sowjanya Madireddi 

1 Introduction

The PFMS process is a continuous casting approach for manufacturing thinner, wider, and continuous amorphous/nanocrystalline metal ribbons by rapid solidification technique [1–3]. This process has been enormously gain interest in industry and academic research because of the environmental and economic advantages of final casting product [4–6]. On the one hand, Fe-based amorphous ribbons have deficiency of long-range structural imperfection, exhibit large elastic strain restriction, excellence in strength, good wear, and corrosion resistance [7–10]. On the other hand, nanocrystalline ribbons have exclusive combination of enlarged physical, chemical, thermal, and mechanical properties [8, 9]. The effect of predominant process parameters such as quenching wheel speed (U), nozzle wheel gap (G), melt ejection pressure (P), and melting temperature (T) was studied on ribbon surface topography [10–12]. The foremost factors for formation of ribbon structure which are including characteristics of nucleation, kinetic crystal growth, internal readjustment of heat, and external heat extraction [13].

The defected casting lines appeared on the surface of the ribbon due to meniscus holding subjected to melt motion. Also, they mentioned cross lines were similar to the herringbone line but difference wavelength [14]. The dimples and striation lines are avoided within the specified range of Stefan number in the 50Pb-50Sn alloy. This criterion was not successful for all alloy systems. A continuous cross wave or herringbone defect lines were studied by correlating between the meniscus frequency and wave lines [15]. Theisen, Huang et al. [16, 17] observed that the

M. ShanthiRaju (✉) · A. K. Birru
National Institute of Technology, Manipur 795004, India
e-mail: shantimr@gmail.com

S. Madireddi
CVR College of Engineering, Hyderabad, Telangana 501510, India

herringbone defect occurred at lower over pressure than the cross wave line defects. In addition, they have scaled herringbone and cross wave lines with capillary frequency $(\sigma/\rho g^3)^{1/2}$, where σ is surface tension, g is the nozzle wheel gap, and ρ is density of liquid. Despite of above work, the mechanism of herringbone defect formation largely remained unclear.

Nevertheless, amorphous alloys can also failure by cavitation instabilities [10, 18, 19]. The shear bands affected to be nucleated in amorphous materials failure in microscopic level under dynamic and quasistatic loads [9, 19, 20]. The mechanism of cavitation inception in brittle materials is due to fluctuation of atomic density initiate at weak zones to reduce the yield strength [21]. The prognosis of void growth in cavitation instability explained through single spherical void model and the theory of free volume [10]. Further investigation has been carried out by [20] cavitation instability is remarkable decreased by the weak zones and it does not decreased at stress ratio reduced from unity. Also, they observed the spallation causes fracture in amorphous materials like micro dimple nucleation, porous, and equiaxed cellular growth on the surface of the ribbon. The formation of defects on solidified surface of the ribbon was due to dynamic variation in pressure distribution, density of melt, solidification temperature, and motion of the quenching wheel [22]. Moreover, the concentration has been taken to examination of cavitation instability on regular crystalline materials rather on amorphous alloys. In this present research, we focused on the influence of vibration at the liquid ejected nozzle frame, which is directly affected on the melt puddle morphology and solidified ribbon surface.

2 Experimental

The titular composition $\text{Fe}_{73.5}\text{Si}_{13.5}\text{B}_9\text{Nb}_3\text{Cu}_1$ of basic alloy has prepared in induction melting furnace at 1×10^{-5} mbar of vacuum level under complete control of argon gas. The alloy was prepared for 100 g weight percentage by using economically available materials. The alloy composition of Fe-B (15.37 wt. %), Fe-Si (12.69 wt. %), and (Fe-Nb 7.73 wt. %), pure Fe 62.94 wt. % and pure Cu 1.30 wt. % and additionally for evaporation loses an extra 10% Boron has added [22]. The chemical homogeneity test has been conducted to ensure the homogeneity of basic alloy. The atomic weight percentages of this fundamental nominal alloy are compare with the analyzed alloy. The results of nominal and analyzed atomic weight percentages are given in Table 1.

Table 1 The atomic weight percentages of analyzed and nominal alloy compositions [22]

Composition	Fe (at%)	B (at%)	Si (at%)	Nb (at%)	Cu (at%)
Analysis	72.84	9.52	13.6	3.03	1
Nominal	73.5	9	13.5	3	1

Table 2 The process parameters for experimentation

Exp. No.	Weight of alloy (g)	Wheel speed (U) (m/s)	Ejection pressure (P) (kpa)	Nozzle wheel gap (G) (mm)	Melt temperature (T) (K)
1	122	30	7	0.35	1575
2	104	30	14	0.35	1575
3	101	30	21	0.35	1575

The liquid is ejected nearly at critical temperature ($T_c = 1350^\circ\text{C}$) from the quartz crucible nozzle slit gap 0.3 mm. The quenching wheel speed $U = 30\text{ m/s}$, nozzle wheel gap $G = 0.35\text{ mm}$, and the melt temperature $T = 1575\text{ K}$ have taken constant throughout the experimentation, and ejection pressure varied as 7, 14, and 21 kPa. The process parameters for experimentation are given in Table 2.

The puddle formation was captured using the images obtained from the high speed videography at a rate 100 frames/sec (Falcon 1.4M100, Dalsa waterloo, Ontario, Canada). The length of the puddle which touched the wheel surface was measured by Imagepro plus software.

3 Results and Discussion

The predominant process parameters for Fig. 1 are $T = 1575\text{ K}$, $U = 30\text{ m/s}$, $G = 0.35\text{ mm}$, $P = 7\text{ kPa}$, and alloy weight is 122 g. The characteristics of the solidified ribbon for experiment 1 are given in Table 3.

Figure 1 shows the high speed images of puddle evolution in between nozzle wheel gap. The experiment starts from liquid ejection at 0 ms and ends at 600 ms. Figure 2a explains the stable length of the puddle on the rotating chilled copper wheel surface with time. A continuous ribbon is obtained at firmness of the puddle from 51 to 520 ms and the puddle length varies from 0.823 to 0.876 mm. Figure 2b gives the nozzle wheel gap (G) which also equal to height of the puddle is varied from 0.3768 to 0.3869 mm during the steadiness of the puddle. The actual maintained gap $G = 0.35\text{ mm}$ is varied due to vibration in the ejection nozzle slit. A continuous ejection of liquid on the rotating chilled wheel surface from the nozzle slit gap ($g = 0.3\text{ mm}$) causes the upthrust or buoyancy force and the surface tension of the liquid slightly lift the nozzle frame. Due to this vibrational effect, the fluctuation generates in puddle morphology. According to the fluid mechanism concepts the compressive stress in the puddle fluid medium between the rotating chilled substrate and nozzle bottom surface. When the fluid is subjected to rapid compression stress due to ejection pressure on the rotating chilled substrate, the internal resistance force of the fluid particles may increase during solidification at boundary layer. The solidified particles try to push up the nozzle frame slightly, and the fluid may undergo shear stress by the drag force of the quenching wheel. The upward resistance force of the fluid and shear stress due

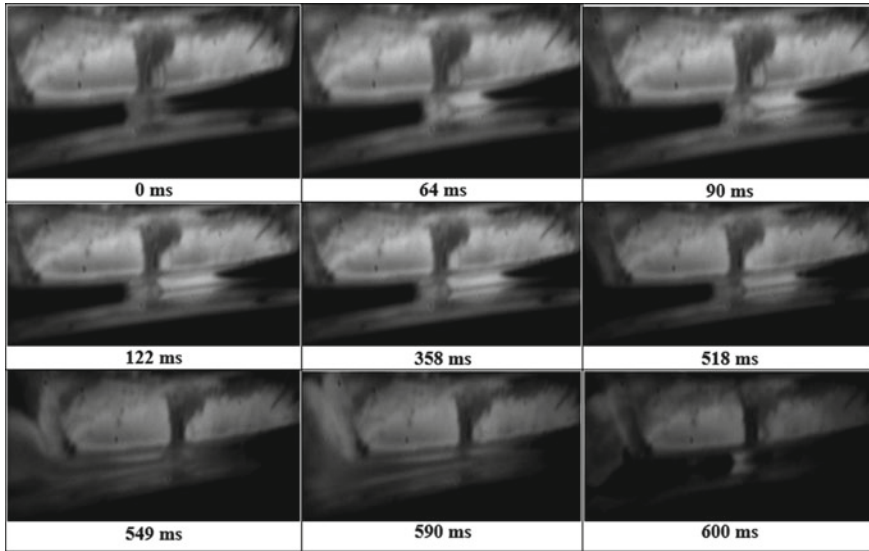


Fig. 1 High speed images of puddle evolution in between nozzle wheel gap for experiment 1

Table 3 The solidified ribbon morphology for experiment 1

Exp. No.	Structure	Length (m)	Average width (mm)	Average thickness (μm)	Surface roughness (μm)
1	Amorphous	9	17	37.3	1.21

to wheel drag causes a small vibration in the nozzle frame. When the fluctuation or vibration of the nozzle frame is at upper position, the pressure may drop at bottom and upper edges of the upstream meniscus (USM). The drag force of the quenching wheel speed entraps surrounded air into liquid puddle from the edges of downstream meniscus (DSM). The regular fluctuations in the puddle and entrapment of air act as thermal resistance at the boundary layer of the wheel substrate may exhibits the herringbone defect on the surface of the ribbon. Figure 3 shows a regular herringbone defect pattern on solidified ribbon surface, and its contour plot color mapping shows the single wavelength.

The two fundamental mechanisms have given [23] for any aspect with an attribute stream wise wave length on continuous casting product. In the first, the template transfer formation mechanism is simply doubling the wheel speed is not affected wave length. In the second, pulse transfer formation mechanism is simply doubling the wheel speed will double the wavelength of the aspect since, the wheel rotate twice then the impingement action. Moreover, the dependence or not of the wavelength but the wheel speed is key to determine the cross wave formation in physics.

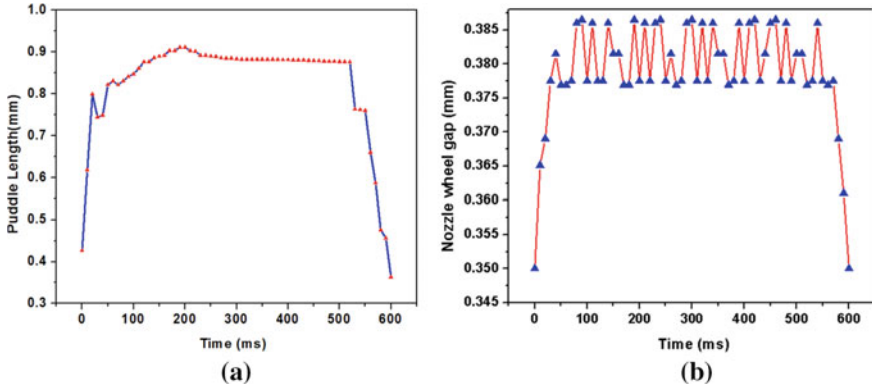


Fig. 2 a Length of the puddle verses to time, b nozzle wheel gap verses to time for experiment 1

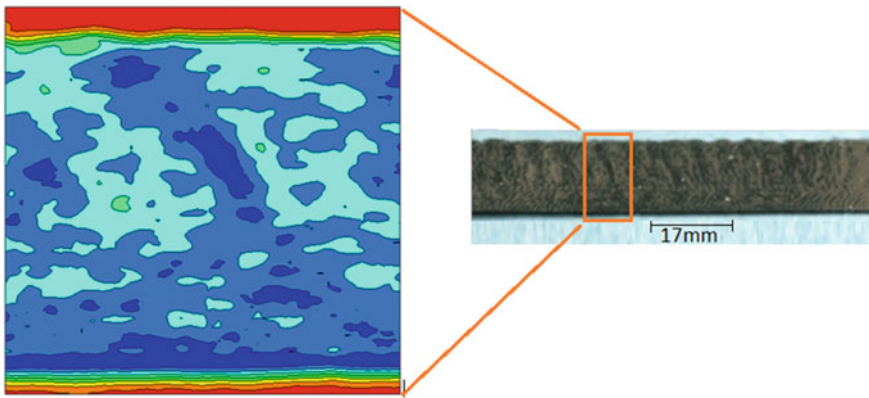


Fig. 3 Regular herringbone defect pattern on solidified ribbon surface and its contour plot color mapping shows the single wavelength

The process parameters for Fig. 4 are $T = 1575 \text{ K}$, $U = 30 \text{ m/s}$, $G = 0.35 \text{ mm}$, $P = 14 \text{ kPa}$, and alloy weight is 104 g. The characteristics of the ribbon for experiment 2 are given in Table 4.

Figure 4 shows the high speed images of puddle development in between nozzle quenching wheel gap for experiment 2. From Fig. 5a and b experiment starts from liquid ejection pressure at 0 to 461 ms. A continues ribbon obtained at firmness of the puddle from 163 to 407 ms and the puddle length varies from 0.883 to 1.05 mm. The nozzle wheel gap (G) or height of the puddle is varied from 0.385 to 0.3961 mm during the steadiness of the puddle.

The length and height of the puddle increased as increasing the ejection pressure from 7 to 14 kPa. The ribbon morphology is greatly affected by the ejection pressure and puddle geometry. By increasing the ejection pressure, both the length and height of the puddle increased. When the nozzle wheel gap or height of the puddle is high,

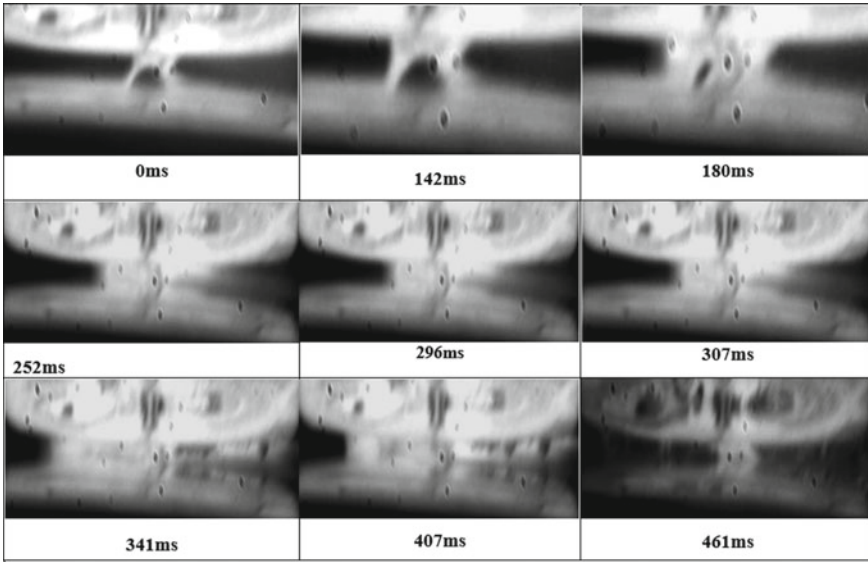


Fig. 4 High speed images of puddle evolution in between nozzle wheel gap for experiment 2

Table 4 Gives the ribbon morphology for experiment 2

Exp. No	Structure	Length (m)	Average width (mm)	Average thickness (μm)	Surface roughness (μm)
2	Amorphous and partial crystalline	12	18	60.6	1.24

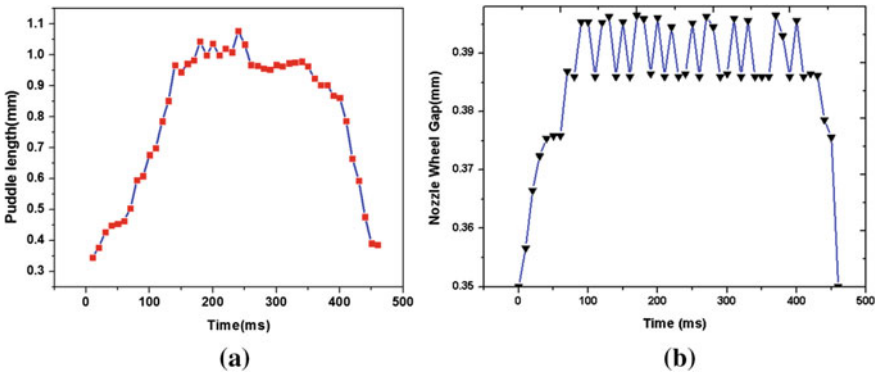


Fig. 5 **a** the length of the puddle verses to time, **b** nozzle wheel gap verses to time for experiment 2

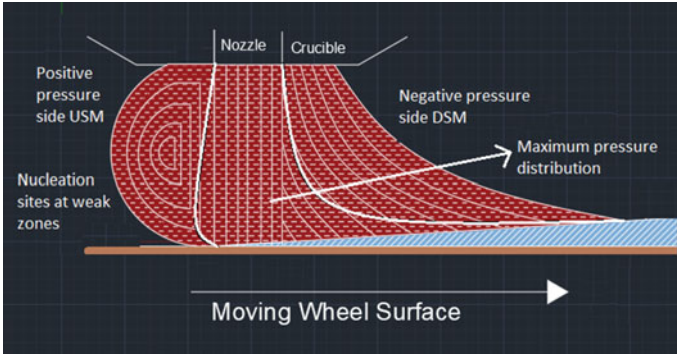


Fig. 6 Pressure distribution at nucleation sites weak zones USM and DSM and formation puddle

the entrapment of air is more from the USM. The simulation work [24] gives the maximum distribution of pressure in the puddle is about five times at lower ejection pressure, and not even doubled in case of higher ejection pressure. Consequently, a radical reduction of pressure at both sides DSM and USM with same magnitude of negative and positive sign. The maximum distribution of increased pressure irrespective of the ejection pressure is resolved only at mid portion of the puddle. The representation of the puddle formation in between the nozzle and on the quenching wheel surface in Fig. 6.

According to assumptions of classical thermodynamic theory predict the initiation of nucleation and kinetic crystal growth starts at weak zones where relatively low pressure, i.e., the bottom edge of USM. It is interesting to notify the formation of porosity at nearly micron level on surface of ribbon. This may be the cause of cavitation effect due to accelerated changes in pressure in the liquid puddle zone. Since the ejection of liquid is about to the critical temperature $T_c = 1350\text{ }^\circ\text{C}$, where the formation of vapor bubbles in liquid phase of the puddle [25]. The vapor bubbles get solidified near at the boundary layer of chilled wheel substrate and formed as

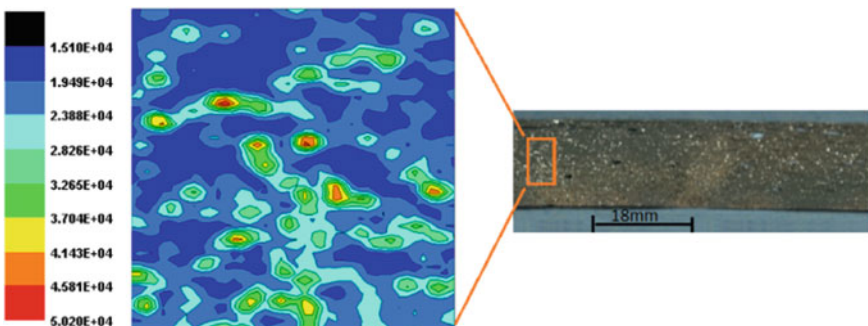


Fig. 7 Tiny porous formations on ribbon surface and contour plot color mapping

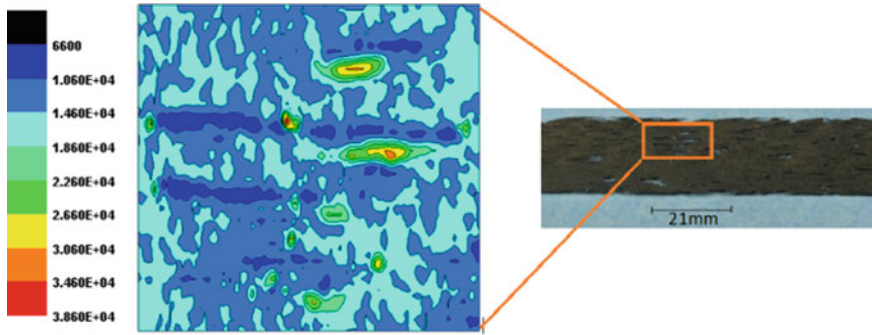


Fig. 8 Grooves and patches on ribbon formation and contour plot color mapping of the surface of the ribbon

Table 5 The ribbon morphology for experiment 3

Exp. No	Structure	Length (m)	Average width (mm)	Average thickness (μm)	Surface roughness (μm)
3	Crystal	6	21	85.3	1.52

tiny porous on the ribbon surface. Figure 7 shows the porous formation on ribbon surface.

The process parameters for Fig. 8 are $T = 1575 \text{ K}$, $U = 30 \text{ m/s}$, $G = 0.35 \text{ mm}$, $P = 21 \text{ kPa}$, and alloy weight is 101 g, and ribbon characteristics are shown in Table 3. The defect forms of small patches are appeared on the surface of the ribbon due to irregular profiled in the formation of puddle. The current results have confirmed to [26–28] at higher ejection pressure the thickness of the ribbon increased. At higher ejection pressure, the possibility of increment in viscosity of liquid flow on the moving wheel substrate may not be properly lingered. The formation of USM and DSM is broken due to surface tension of puddle and air interfaces which results the greater allure between the cohesion of fluid molecule and adhesion of air molecules. The imbalanced force between the fluid and air molecules the fluid become under tension. This behaves like elastic membranes so that the irregular contact of the puddle onto the quenching wheel during solidification process. Under these conditions, the formation of grooves and patches on the surface of the ribbon. The solidified ribbon has become fully crystalline and broken in nature. Table 5 gives the results of the third experiment.

4 Conclusion

1. The fluid is subjected to rapid compression stress due to ejection pressure on the rotating chilled substrate. The internal resistance (buoyancy) force of the fluid

- particles, surface tension, and shear stress due to wheel drag results vibration the nozzle frame. The regular fluctuation in the puddle and entrapment of surrounded air acts like thermal resistance at melt wheel contact may exhibits the herringbone defect on the ribbon surface.
2. The initiation of nucleation and kinetic crystal growth begins at the USM, where pressure is relatively low. The variation of pressure in the puddle accelerates may cause to formation tiny vapor bubbles due to cavitation inception. These vapor bubbles in the puddle get solidified at the boundary layer of the wheel substrate results porosity on the ribbon surface.
 3. At higher ejection pressure, the formation USM and DSM broke due to imbalanced force between the entrapped air and fluid molecules so that the puddle behaves like elastic membranes under tension. The irregular contact between the puddle and wheel substrate results patches and grooves on the ribbon surface.

Acknowledgements Authors would like to thankful to Defence Metallurgical Research Laboratory, Hyderabad, to carry out the current collaboration research work with NIT Manipur. Author 1 sincerely grateful Dr. Bhaskar Majumdar Sc. 'F' for all his technical backing and sparing time.

References

1. Narasimhan M (1979) Continuous casting method for metallic strips. U.S. Patent No. 4,142,571
2. Steen PH, Karcher C (1997) *Annu Rev Fluid Mech* 29:373–97
3. Altieri AL, Steen PH (2014) *J Thermal Sci Eng Appl* 6:1-9
4. Hasegawa R (2000) Present status of amorphous soft magnetic alloys. *J Magn Magn Mater* 215:240–245
5. Kumar K, Van Swygenhoven H, Suresh S (2003) Mechanical behavior of nanocrystalline metals and alloys. *Acta Mater* 51:5743–5774
6. Gleiter H (1989) Nanocrystalline materials. In: *Progress in materials science*, vol 33, Elsevier pp 223–315
7. Trudeau M, Ying J (1996) Nanocrystalline materials in catalysis and electrocatalysis: structure tailoring and surface reactivity. *Nanostruct Mater* 7:245–258
8. Suryanarayana C, Koch C (2000) Nanocrystalline materials—current research and future directions. *Hyperfine Interact* 130:5
9. Huang X, Ling Z, Zhang HS, Ma J, Dai LH (2011) How does spallation micro damage nucleate in bulk amorphous alloys under shock loading? *J Appl Phys* 110
10. Jiang MQ, Wang WH, Dai LH (2009) Prediction of shear-band thickness in metallic glasses. *Scripta Mater* 60:1004–1007
11. Majumdar B, Sowjanya M, Srinivas M, Babu DA, Kishen T, Reddy K (2012) *Trans Indian Inst Met* 65(6):841–847.
12. Clyne TW (1984) Numerical treatment of rapid solidification. *Metall Trans B* 15B:369–381
13. Carpenter J, Steen P (1992) Planar-flow spin-casting of molten metals: process behaviour. *J Mater Sci* 27(1):215–225
14. Byrne C, Theisen E, Reed B, Steen P (2006) Capillary puddle vibrations linked to casting-defect formation in planar-flow melt spinning. *Metall Mater Trans B* 37B:445–456
15. Praisner T, Chen J, Tseng A (1995) An experimental study of process behavior in planar flow melt spinning. *Metall Mater Trans B* 26(1):1199–1208

16. Theisen E (2007) Transient behavior of the planar-flow melt spinning process with capillary dynamics. Cornell University (Ph.D. thesis)
17. Huang X, Ling Z, Wang YJ, Dai LH (2016) Intrinsic structural defects on medium range in metallic glasses. *Intermetallics* 75:36–41
18. Huang X, Ling Z, Dai LH (2019) Influence of surface energy and thermal effects on cavitation instabilities in metallic glasses. *Mech Mater* 131:113–120
19. Huang X, Ling Z, Dai LH (2013) Cavitation instabilities in bulk metallic glasses. *Int J Solids Struct* 50:1364–1372
20. Singh I, Guo TF, Murali P, Narasimhan R, Zhang YW, Gao HJ (2013) Cavitation in materials with distributed weak zones: implications on the origin of brittle fracture in metallic glasses. *J Mech Phys Solids* 61:1047–1064
21. Murali P, Guo TF, Zhang YW, Narasimhan R, Li Y, Gao HJ (2011) Atomic scale fluctuations govern brittle fracture and cavitation behavior in metallic glasses. *American Phys Soc, PRL*. 215501 vol 107, pp 1–5
22. Meenuga S, Kumar BA, Kumar BP (2021) Effect of cavitation and spallation on ribbon morphology of Fe_{73.5}Si_{13.5}B₉Cu₁Nb₃ alloy in planar flow melt spinning process. *Mater Today: Proc* <https://doi.org/10.1016/j.matpr.2021.05.121>
23. Byrne CJ, Theisen EA, Reed BL, Steen PH (2006) *Metall Mater Trans B Process Metall Mater Process Sci* 37:445–456
24. Sowjanya M, Reddy TKK (2014) *J Mater Process Technol* 214:1861–1870
25. Gao H, Li Z, Zhou S, Zhang G, Cui N (2019) *Prog Nat Sci Mater Int* 29:556–560
26. Tkatch VI, Limanovskii AI, Denisenko SN, Rassolov SG (2002) The effect of the melt-spinning processing parameters on the rate of cooling. *Mater Sci Eng, A* 323(1–2):91–96
27. Srinivas M, Majumdar B, Phanikumar G, Akhtar D (2011) Effect of planar flow melt spinning parameters on ribbon formation in soft magnetic Fe_{68.5}Si_{18.5}B₉Nb₃Cu₁ alloy. *Metall Mater Trans B*, 42(2), 370–379
28. Bouchbinder E, Langer JS, Procaccia I (2007) *Phys Rev E—Stat Nonlinear Soft Matter Phys* 75:1–9

Experimental Investigation into Wire Electrochemical Micro-Machining for Reduction of MicroSparks and Overcut



Naresh Besekar and Bijoy Bhattacharyya

1 Introduction

Wire electrochemical micromachining (WECMM) is such an advanced machining process that dissolves material by required electrochemical reactions between cathode wire and anode workpiece dipped inside suitable electrolyte solution separated by a narrow inter-electrode gap (IEG). The WECMM is a transport-limited electrochemical dissolution process. The continuous removal of dissolved products and sludge becomes more difficult in the tiny IEG due to frequent microsparks and unstable machining [1]. Moreover, of the several research works for investigating the influence of various process parameters, no effort has been focused to control the effect of microsparks and reduction in overcut on wire electrochemical micromachining process considering most of the influencing parameters which is a primary requirement during machining. During the process, there may be a possibility of unusual sludge and dissolved products in narrow IEG causing microsparks which in turn reduces homogeneity and machining stability. Feed rate of tool wire has a great influence on corresponding micromachining criteria [2]. The machining stability and slot profile investigated with DP-WECMM are considerably better than those with traditional WECMM where frequent microsparks occur [3]. A proper combination of voltage and pulse period and pulse duration results in outstanding machining accuracy for a thick workpiece [4]. The axial and intermittent feed-direction vibrations combination are capable of improving the maximum feed rate [5]. A lower initial IEG can decrease the stray current results in a better entrance shape [6]. Proper feed rate leads to a small machined roughness surface without any microsparks [7]. High precision micro features can be achieved with the vibration of cathode wire [8]. Low frequency and small amplitude improve machining stability, accuracy, and

N. Besekar (✉) · B. Bhattacharyya
Department of Production Engineering, Jadavpur University, Kolkata 700032, India
e-mail: nareshwbesekar@gmail.com

improve overcut reduction [9]. The influence of voltage on wire feed rate was also investigated for achieving the maximum feed rate. Enhancement of mass transport and micro-vibration of wire improves the machining quality of WECMM [10]. The stray-current attack was identified to reduce stray current attack with wire insulating methods [11]. The effect of microspark and stray current on machining accuracy was experimentally investigated during electrochemical micromachining [12]. However, WECMM is still under investigation and microsparking in the IEG due to inappropriate flushing and accumulation of machining products, namely, sludge and gas bubbles and the effect of stray current deteriorates, degrades, and distorted homogeneity and stability of process as well as dimensional characteristics generated microfeatures which leads to increase in overcut.

The present experimental investigation is paying attention to the development of a proper WECMM for fabricating microfeatures for investigating the number of microsparks generation and overcut during micromachining. For this, a suitable axial flushing system has been implemented and the piezoelectric transducer (PZT) tool vibration has been used which results in a decrease in microsparks during machining. This paper, therefore, emphasizes finding out the effect of various controllable parameters such as feed rate, pulse voltage, pulse voltage frequency, and wire vibration frequency and amplitude with PZT on corresponding slit width for microspark effect as well as the formation of overcut. Numbers of micro-sparks are measured with the help of an oscilloscope. Also, after the experiments, the generated microslits have been carefully analyzed under the optical microscope. The influence of most influencing parameters on microspark generation and overcut is represented graphically to investigate the effect on the fabricated microslits by determining suitable ranges within which the WECMM process can get better control over the generation of microsparks and reduction in overcut which ultimately result in stable, accurate, and homogeneous micromachining.

2 Experimental Setup

An experimental setup for wire electrochemical micromachining (WECMM) is developed having various subsystems and mechanical machining units. The XYZ movement stage is power driven by three stepper motors. The XYZ movement represents three principle Cartesian axis directions of X, Y, and Z for positioning. It helps in workpiece location, holding the tool wire properly, and moving that wire precisely and accurately. Also, the power supply unit, electrolyte flow system; etc. along with various sub-systems like Perspex machining chamber, Perspex wire holding, and tensioning block and worktable connected to the stage. The position control unit is operated by a computer. The machining chamber is positioned on the stage during experiments. The worktable is used to hold the machining chamber and to restrict its movement during experimentations. A wire is held vertically straight with proper tension in the mentioned block. It has the arrangement to attach the PZT for introducing a small frequency and amplitude of wire vibration during machining. A

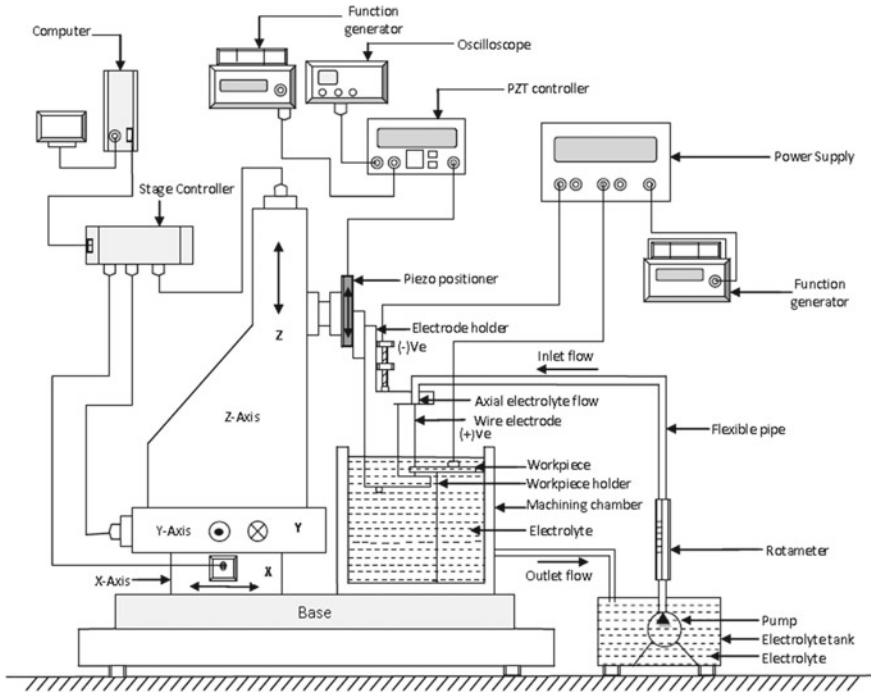


Fig. 1 Schematic diagram of the WECMM experimental setup

suitable axial electrolyte flow system has been developed for regulating proper flow. The flow system consists of a pump, electrolyte supply chamber, flow control valve, rotameter, etc., to control the flow. The DC pulse generator is used to generate different pulse nature of variable voltage, pulse period, and duty ratio. The oscilloscope has been used for monitoring different pulse power parameters during experiments and the measurement of micro-sparks. Also, multimeter, stereo zoom microscope, optical camera, and microscope, etc., have been used for carrying out the experiments. A schematic diagram of the WECMM experimental setup has been shown in Fig. 1.

3 Experimental Planning

In the present work, a tungsten wire of $\text{\O}50\mu\text{m}$ with a very thin layer of coating of synthetic enamel on a non-machining area is used as a tool electrode. The workpiece specimens were $15\text{ mm} \times 15\text{ mm} \times 0.1\text{ mm}$ stainless steel 304 sheets were used for better understanding the effect for micro sparks generation and overcut in machined slit width. The electrolyte used for experimentation was $0.1\text{ M H}_2\text{SO}_4$. Experimentations are done with a variable rectangular DC power supply. Microslits were

machined and the effect of micro-sparking and overcut were considered for experimental analysis. To investigate experimental results and to improve the machining quality, numbers of micro sparks are counted with the help of an oscilloscope at each stage of varying conditions of process parameters during machining of microslits and overcut measured with an optical microscope for each operating conditions by considering the mathematical model, as follows:

$$\text{Overcut} = 2\Delta s = 2\Delta b \sqrt{\frac{2d}{\Delta b} + 1} \tag{1}$$

where Δb , inter-electrode frontal gap; Δs , inter-electrode side gap; d , the diameter of wire electrode.

The experimental setup was prepared for microwire tool mounting and holding, workpiece mounting, and electrolyte flow system. All the experiments maintained the required amount of inter-electrode gap, i.e., $100\ \mu\text{m}$ by forwarding the motion of wire and checking the IEG with a continuity tester to avoid any contacts between wire and workpiece material. The process parameters have been set according to the planning and given the feed rates in the stage controller to move the wire electrode toward the workpiece. On completion of machining, switch off all the machine types of equipment in sequential order. The influence of various parameters on the generation of micro sparks and is responsible for the production of overcut while machining is considered for investigation. Sketch of side gap for overcut in WECMM machining process shown in Fig. 2.

In this experimental study, feed rate, pulse voltage, pulse voltage frequency, PZT tool vibration frequency, and amplitude were identified to carry out the experiments keeping other parameters fixed for all experiments, and working ranges were selected based on data given in the literature survey, review of experiences and trial experiments for microslits machining to understand the effect for generation of microsparks

Fig. 2 Sketch of side gap for overcut in WECMM process

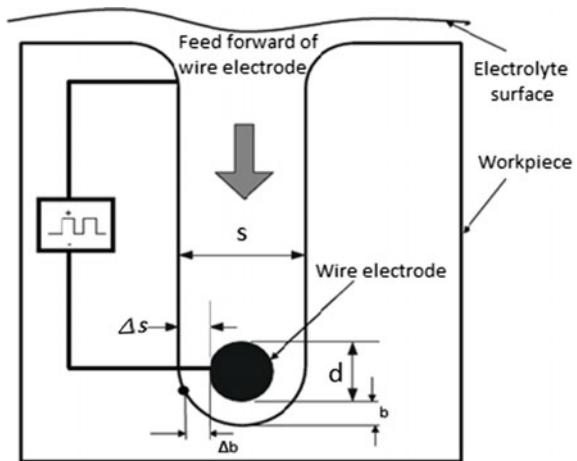


Table 1 Operating conditions

Working condition	Value
Workpiece material	Stainless Steel 304
Workpiece thickness	100 μm
Wire electrode Material	Tungsten
Diameter of wire Electrode	$\text{\O}50\mu\text{m}$
Applied pulse Voltage	4–12 V
Wire feed rate	1.0 $\mu\text{m}/\text{sec}$ to 1.8 $\mu\text{m}/\text{sec}$
Duty ratio	50%
Voltage pulse frequency	50 kHz to 500 kHz
Type and concentration of Electrolyte	0.1 M H_2SO_4
Electrolyte flow rate	35lph
IEG	100 μm
PZT tool vibration frequency	0–100 Hz
PZT tool vibration amplitude	0–50 μm
Insulating material for wire	Synthetic Enamel

and as well as the formation of overcut. Operating conditions for all the process parameters with their ranges used in experimentations are shown in Table 1.

4 Results and Discussion

4.1 Influence of Feed Rate on MicroSpark and Overcut

Experiments were conducted for the machining of microslits with 4 V applied voltage, 200 kHz voltage pulse frequency, 40 Hz PZT vibration frequency, 12.94 μm PZT vibration amplitude, and 1–1.8 $\mu\text{m}/\text{sec}$ ranges of feed rate. It is discovered that average current is increased with an increase in tool feed rate and micro sparks occur at higher currents, but overcut is reduced with an increase in feed rate. Microslits fabricated with lower feed rates are homogeneous as controlled dissolution occurred and due to the absence of a microsparks effect. If the wire feed rate was too high, it was difficult for the flow system to remove the sludge and dissolved product from narrow IEG, leading to microsparks. It is observed that wire feed rate in the range of 1.4–1.6 $\mu\text{m}/\text{sec}$ gives better control for the reduction of average current and overcut. Moreover, the average overcut is at a bit higher side regarding the fact that tungsten wire of diameter 50 μm and IEG of 100 μm have been used during experiments due to the application of such a low feed rate. To achieve better machining quality, as well as to prevent the occurrence of microsparks and to reduce overcut, the influence

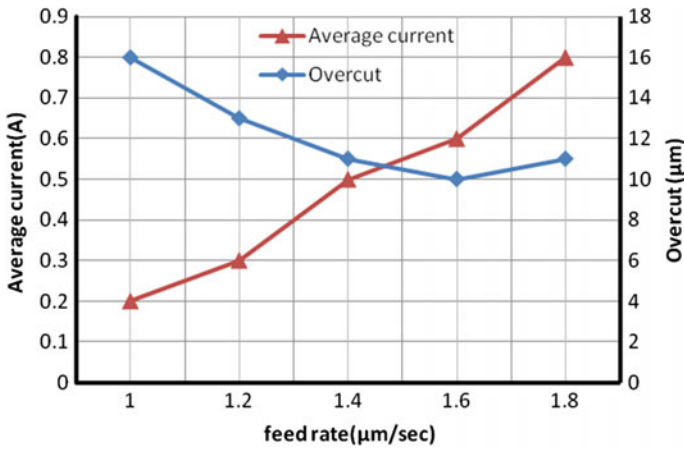


Fig. 3 Influence of tool feed rate on average current and overcut

of feed rate with quantity microsparks and overcut was investigated and plotted on a graph as shown in Fig. 3.

4.2 Influence of Machining Voltage on MicroSpark and Overcut

The effect of pulse voltage on overcut without vibration and with PZT tool vibration was investigated at 1.4 μm/sec tool feed rate, 50% duty ratio, 250 kHz voltage pulse frequency, 35lph electrolyte flow rate, 100 μm thick SS304 workpiece, Ø50μm tungsten wire electrode, 0.1 M H₂SO₄ and 60 Hz frequency with 12.94 μm amplitude of PZT vibration and with a range of 4–12 V applied voltage. It is observed that overcut is much less using PZT wire vibration during machining as shown in Fig. 4.

Further experimental trials are conducted to investigate the effect of applied voltage on overcut and the number of microsparks produced with the same above parametric conditions with PZT vibration. It is seen that when the applied voltage is on the lower side, the inter-electrode gap narrows and, micro-sparks occur more frequently due to poor removal of sludge and dissolved products from narrow IEG. It is eliminated with PZT vibration due to pressure created in the electrolyte. Also, it promotes the renewal of fresh electrolytes and the removal of dissolved products from the narrow IEG. It is again observed that the overcut and number of micro sparks increases with an increase in applied voltage and decreases with a decrease in applied voltage. A large voltage leads to a high current density, which induces a high material removing rate. Then a wide side gap is obtained which ultimately increases the overcut. Microsparks were observed during the initial machining process. As the machining process continued, microsparks vanished while the average current

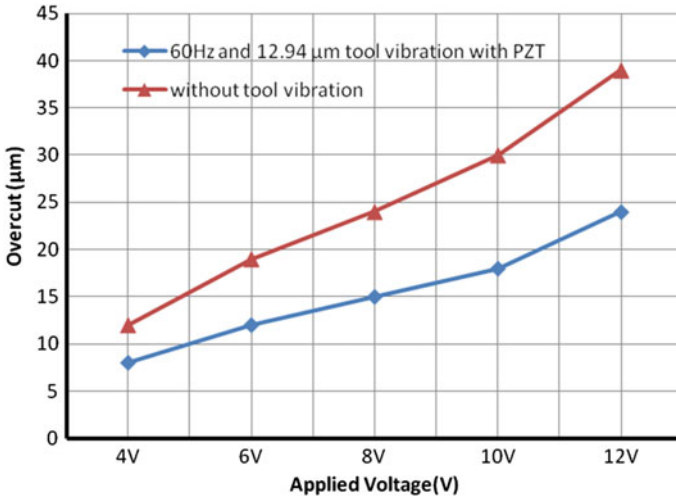


Fig. 4 Influence of applied voltage on overcut with and without PZT vibration

decreased. Furthermore, the wire loses its straightness and tension and resulting insufficient electrolyte flushing along the wire electrode in narrow IEG. As a result, the machining goal could not be accomplished. As per Faraday’s and Ohm’s laws, greater machining current into the machining gap created with higher applied voltage which increases the MRR leads to an increase in overcut and more number of micro-sparks which reduces homogeneity and accuracy of machining. It is found that applied voltage in the range of 4–6 V gives better control on the reduction of a number of microsparks and overcut. The applied pulse voltage effect on overcut and the number of micro-sparks are plotted graphically as shown in Fig. 5.

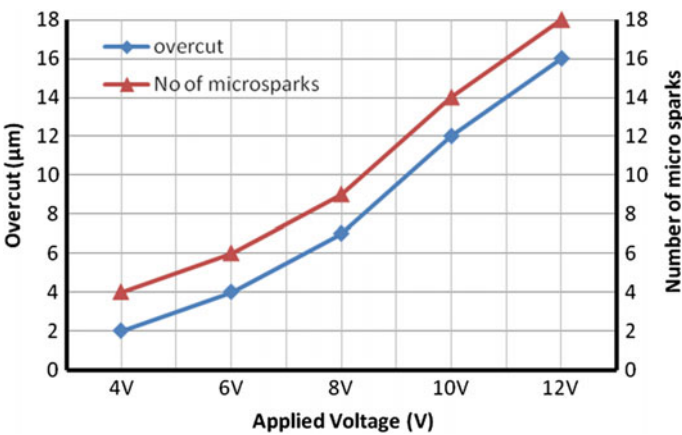


Fig. 5 Influence of applied voltage on overcut and number of microsparks

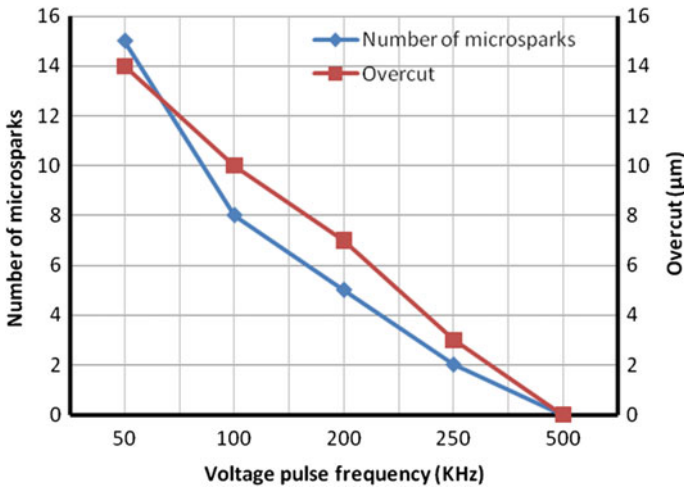


Fig. 6 Influence of voltage pulse frequency on overcut and number of micro sparks

4.3 Influence of Voltage Pulse Frequency on MicroSpark and Overcut

The experiments reveal the effect of applied voltage pulse frequency on overcut and a number of sparks produced during machining of microslits with 6 V applied voltage, 1.4 $\mu\text{m}/\text{sec}$ feed rate, 40 Hz PZT vibration frequency, 12.94 μm PZT vibration amplitude, and 50–500 kHz range of voltage pulse frequency. It is observed that the value of the overcut of the microslit decreases almost linearly with the increase in applied voltage pulse frequency. Moreover, with a further increase in frequency beyond 500 kHz, then no machining will occur. It is also observed that with a decrease in the frequency value which may be up to 50 kHz, generation of more heavy microsparks occurs and the machining product will fully block the narrow IEG. As a result, machining will stop after starting. A voltage pulse frequency of 250 kHz is optimal for the reduction of microsparks and overcut. The graph for the influence of voltage pulse frequency on overcut and number of microsparks is plotted as shown in Fig. 6.

4.4 Influence of PZT Tool Vibration Frequency on a Micro Spark

The influence of micro-tool vibration frequencies on a number of micro sparks generated is investigated by conducting experiments with 6 V applied voltage, 1.4 $\mu\text{m}/\text{sec}$ feed rate, 200 kHz voltage pulse frequency, and 12.94 μm PZT vibration amplitude. It is observed that for vibration frequencies of 0–5 Hz, it is not enough to remove

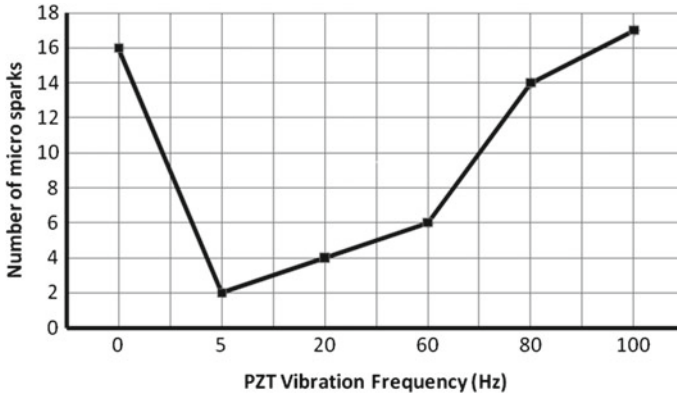


Fig. 7 Influence of PZT vibration frequency on a number of micro-sparks

the dissolved products from narrow IEG, and a number of micro spark generations are quite large which leads to unstable process stability. When the PZT frequency of vibration is higher than 40 Hz, the number of micro-sparks increases quickly due to wire electrode radial vibration which is more frequent at 80 Hz frequency. It is observed that vibration frequencies of 5–20 Hz have better control for the reduction of micro-sparks as shown in Fig. 7. Therefore, a proper range of PZT vibration frequency has a considerable effect on the better renewal of fresh electrolytes. It also improves the machining stability and accuracy.

4.5 Influence of PZT Vibration Amplitude on Micro-Sparks

An experimental trial has been conducted with 6 V applied voltage, 1.4 $\mu\text{m}/\text{sec}$ wire feed rate, and 200 kHz voltage pulse frequency, 20 Hz PZT vibration frequency with 0–50 μm range of PZT vibration amplitude of wire vibration. It is observed that when vibration amplitude is lower than 10 μm , renewal of electrolyte was difficult due to less pressure in narrow IEG. On the other hand, micro-sparks occur with high frequency with unstable machining. The range of 10–20 μm micro-tool vibration amplitudes generates quite fewer micro-sparks which leads to better processing stability during micromachining. However, At PZT amplitude higher than 20 μm , the number of micro-sparks increases due to the more wire electrode radial swing, resulting in unstable machining. The influence of PZT vibration amplitude on a number of micro-sparks was observed as shown in Fig. 8.

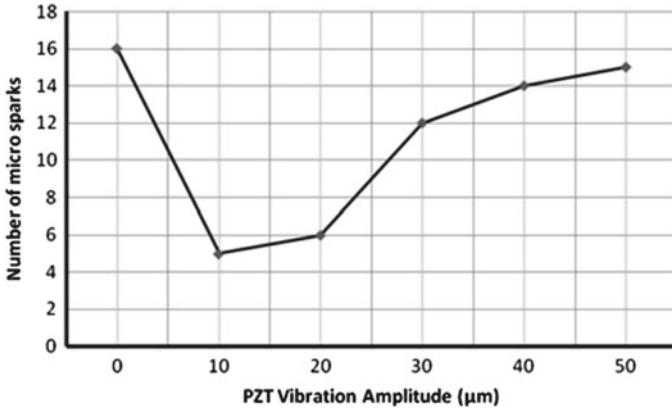
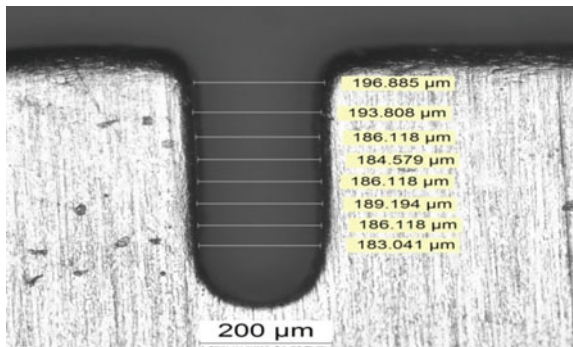


Fig. 8 Influence of PZT vibration amplitude on number of micro sparks

5 Controlled Parametric Micro-Slit Fabrication

After finding out the influence of various predominant machining parameters and using a controlled parametric combination of 6 V voltage, 1.4 $\mu\text{m}/\text{sec}$ feed rate, 250 kHz voltage pulse frequency, 20 Hz PZT vibration frequency, and 10 μm PZT vibration amplitude, micro-slit has been fabricated. As IEG is 100 μm which is quite large, it has taken a considerable amount of time to overcome the effect of micro sparks and to reduce the chances of overcut at the entry point of machining, but micro-slit is quite smooth and homogeneous as shown in Fig. 9.

Fig. 9 Micro-slit fabricated with controlled parametric condition



6 Conclusions

The present experimental investigation highlights that effect of micro-sparks and overcut on dimensional characteristics of the microslit during wire electrochemical micromachining is greatly influenced by the various influencing process parameters. The influence of different process parameters on the generation of a number of micro-sparks and overcut were exhibited through graphical plots. Based on the above graphical plot representations and observations, the following conclusion has been drawn.

- (i) Experiments with increasing feed rate have resulted in a decrease in overcut and with higher value of feed rate started showing abrupt change and increasing trend in overcut problem due to coagulation of reaction products in the IEG due to uncontrolled micromachining process. Average current increases with an increase in feed rate and micro-sparks occur at higher currents. It is observed that wire feed rate in the range of 1.4–1.6 $\mu\text{m}/\text{sec}$ gives better control for the reduction of average current and overcut.
- (ii) The overcut and a number of micro-sparks increase as applied voltage increases. Again it is observed that overcut is less when the micromachining operation is performed with a tool vibration PZT system. It is found that applied voltage in the range of 4–6 V gives better control on the reduction of a number of microsparks and overcut.
- (iii) Experimental results reveal that with the increase in applied voltage pulse frequency, the value of the overcut of the micro-slit decreases almost linearly but at the very low frequency, the number of micro-sparks increases which reduces the process stability and homogeneity. A voltage pulse frequency of 250 kHz is optimal for the reduction of micro-sparks and overcut.
- (iv) It can be concluded that low frequency and small amplitude vibration of wire electrodes with PZT significantly improves processing stability by reducing the generation of micro sparks and overcut. It is observed that vibration frequencies of 5–20 Hz with 10–20 μm micro-tool vibration amplitudes of wire vibration with PZT has better control over the reduction of microsparks.

WECMM plays a crucial role in machining desired complex microfeatures. However, an in-depth research is still required to improve the potential and effectiveness of the process by determining suitable machining conditions as well as strict control of operating parameters in the future.

References

1. Bhattacharyya B (2015) Electrochemical micromachining for nanofabrication, MEMS and nanotechnology, William Andrew applied science publishers. Imprint of Elsevier Inc., Massachusetts, USA
2. Debnath S, Kundu J, Bhattacharyya B (2019) Influence of wire feed rate on micro-slit width fabricated by wire ECM process. *Int J Precision Technol* vol.8, Nos.2/3/4
3. Gao C, Qu N, He H, Meng L (2019) Double-pulsed wire electrochemical micro-machining of type-304 stainless steel. *J Mater Process Technol* 381–387:266
4. Gao C, Qu N (2018) Wire electrochemical micromachining of high-aspect-ratio microstructures on stainless steel 304 with 270 μ m thickness. *Int J Adv Manuf Technol* 263–272:100
5. He H, Zhang X, Qu N, Zeng Y, Zhong B (2019) Wire electrochemical micromachining assisted with coupling axial and intermittent feed-direction vibrations. *J Electrochem Soc* 166(6):E165–E180
6. Wang S, Zeng Y, Liu Y, Zhu D (2012) Microwire electrochemical machining with an axial electrolyte flow. *Int J Adv Manuf Technol* 25–32:63
7. Xu K, Zeng Y, Li P, Fang X, Zhu D (2016) Effect of wire cathode surface hydrophilia when using a traveling wire in wire electrochemical micromachining. *J Mater Process Technol* 68–74:235
8. Zeng YB, Yu Q, Wang S, Zhu D (2012) Enhancement of mass transport in microwire electrochemical machining. *CIRP Ann—Manuf Technol* 61:195–198
9. Wang S, Zhu D, Zeng Y, Liu Y (2011) Micro wire-electrode electrochemical cutting with low frequency and small amplitude tool vibration. *Int J Adv Manuf Technol* 535–544:53
10. Debnath S, Kundu J, Bhattacharyya B (2018) Modeling and influence of voltage and duty ratio on wire feed in WECM: possible alternative of WEDM. *J Electrochem Soc* 165:E35–E44
11. Zeng Y, Ji H, Fang X, Wang Y, Ningsong Q (2014) Analysis and reduction of stray-current attack in reciprocated traveling wire electrochemical machining. Hindawi publishing corporation. *Advances in Mech Engg* 2014:505932
12. Munda J, Malapati M, Bhattacharyya B (2007) Control of micro-spark and stray-current effect during EMM process. *J Mater Process Technol* 151–158:194

Influence of Voltage Pulse on Machining Accuracy in Electrochemical Micromachining



Himadri Sekhar Panda  and Bijoy Bhattacharyya

1 Introduction

Nowadays, the miniaturizations of various ultra-precision items are very essential because it has been producing high-precision machine products and various types of equipment that are widely used in micro-manufacturing activities. Electrochemical micromachining (EMM) has been researched for the last decade due to industrial interest, and researchers have discovered that it has so many advantages, such as high machining accuracy, high MRR, no tool wear, smooth surface product, stress-free, machining ability of complex shapes, rapid machining, and environmental acceptability. Chemical micromachines are now used in the electronic industry to fabricate semiconductor devices. But, in the micromachining application range, EMM can produce better ultra-precision shapes of products than chemical micromachines.

EMM has some operational requirements such as machining dimensions should be in-between 1–999 μm and chemically resistant materials, i.e., copper alloys, super-alloys, titanium, and stainless steel, etc., are applicable for it [1]. To improve the machining accuracy of EMM, many researchers have been studying various parameters and operating conditions, such as micro-tool design, MRR control, elimination of micro sparks, electrolyte selection, IEG control, tool feed rate control, and power supply waveform. Bhattacharyya et al. developed an EMM setup and analyzed the machining process parameters, i.e., MRR, stray current, and overcut, to improve machining accuracy [2]. When electrochemical dissolution starts for the electrical conductivity of the electrolyte, then by-products of electrolysis, i.e., gas bubbles and heat, are generated. By utilizing the flow of electrolyte, it can be removed from the machine area, but some problems may arise that machine tool and workpiece are vibrating. Due to it, the electrolyte cannot be located properly in the machine

H. S. Panda (✉) · B. Bhattacharyya
Department of Production Engineering, Jadavpur University, Kolkata 700032, India
e-mail: himadrispanda26@gmail.com

zone, which produces an obstacle to designing an ultra-precision shape for machined products. The micro-tool surface is covered by electrolysis products for using a constant DC or unipolar voltage pulse. Then this micro-tool surface coating behaves as an electrical non-conducting insulator, which creates the shot circuit and stops the anodic dissolution. Gao et al. introduced a bipolar voltage pulse that can overcome the above-discussed problem because, in one pulse duration time, the polarity of electrodes changes alternatively [3]. But, it has two big problems, such as tool diameter being reduced and the shape of the product not being uniform in diameter as concerning target level. Another one is that the machining rate is reduced significantly because the consumed charges of the electric double layer are neutralized due to reverse pulse voltage. Sidek et al. studied the effect of triangular, sinusoidal, and rectangular voltage waveforms on increasing the machine accuracy of EMM [4]. Recently, Patel et al. analyzed the overcut by altering the energy of sinusoidal and triangular waveforms [5]. In the above waveform study, it is noticed that except for the rectangular pulse, the other two waveforms have no pulse off time and duty ratio. Two types of obstacles arise during machining, such as discharging phenomena of an electrical double layer and the sludge removal problem from the machine zone.

Previous research has discovered that using triangular and sinusoidal voltage pulse waveforms can improve machining accuracy. But many difficulties occurred during machining, which is discussed above. In this paper, the effect of the step pulse wave and the micro-tool feed rate control on machining accuracy has been investigated during microhole drilling. Simultaneously, overcut, stray current effect, machining time, the possibility of higher micro-tool feed rate, microhole shape accuracy, and generation of short circuits have been investigated by using different voltage pulse waveforms. Here, it has also been analyzed that the relationship between current and voltage during machining plays a significant role in the improvement of machining accuracy. The main objective of this paper is to develop a comparison study on machining accuracy utilizing traditional square pulse and a new technique, i.e., modifying traditional pulse patterns into a bunch of short square pulses mixed with different amplitudes.

2 Influence of Voltage Pulse on Machining Accuracy

Naturally, two types of electrical waves are used in EMM for machining, i.e., full-wave ripple-free rectified direct current (D.C.) and pulsed D.C. Due to the use of D.C. in a narrow electrode gap, a serious problem arises, such as generating an enormous amount of sludge on the micro tool, which behaves as an electrical non-conducting insulator and generates the shot circuit.

Pulse waves can improve the machining accuracy more than DC. Using pulse DC, initial IEG may be recovered during pulse off time because the workpiece dissolution process is controlled by pulse current. The dissolution product can be flushed away from the machine zone during relaxation time, i.e., pulse off time. The short pulse wave can enhance the current density so that machining accuracy can be increased

and anodic dissolution may be localized. Several investigations have been carried out on the effects of short pulses and ultrashort pulses. It was observed that the overcut can be minimized by utilizing a short pulse with a low tool feed rate rather than a large pulse with a high tool feed rate [6]. In this case, a serious issue arises from the use of a short pulse in EMM. If the pulse on-time is shorter than the short pulse cycle time, minor charges are stored at the double layer during the pulse on time and completely discharged between pulse off times. Hence, material removal may not take place from the workpiece during no charge accumulation time or Faradic time [7]. For this reason, the duty ratio cannot be forced below the threshold level for stable machining. If a high-frequency voltage pulse is used, then an issue arises that a large peak voltage is required to reduce the double layer charging time. As a consequent result, the energy requirement of the short pulse wave is increasing during machining [8]. In other cases, if pulse on time is extended, then MRR also increases immediately, but as a result, the side gap is not increased uniformly [9].

To improve machining accuracy, the utility of step pulse voltage waveforms is an alternative best solution. The pulse width of a step pulse wave is divided during one pulse on time. Hence, the peak-to-peak voltage of both voltage pulses, i.e., square pulse and step pulse, are equal, but their root mean square (RMS) values are not. The energy transfer capacity of the voltage pulse depends on its RMS value. For this reason, the total energy transfer capacity of a step pulse wave is less than the square pulse wave during one pulse on time. For power transmission calculations, the peak-to-peak voltage of a voltage pulse power supply is selected. But, the peak value duration time of different waveforms is not the same because the curvature of the waveform changes with the corresponding time. The nature of the peak value duration time of two types of voltage pulses is shown in Fig. 1.

From the above figure, it is noticed that the area of the half-cycle square wave is greater than the step pulse wave, but the half-cycle base is equal.

$$R.M.S. \text{ Value} = \sqrt{\frac{\text{Area of half - cycle of square wave}}{\text{Half - cycle base}}} \tag{1}$$

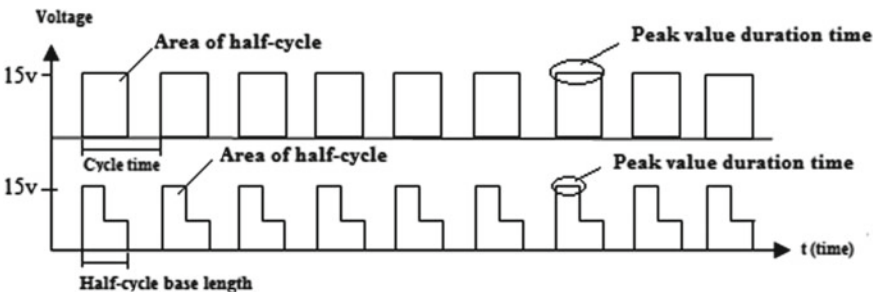


Fig. 1 Nature of square pulse and step pulse during same pulse on-time

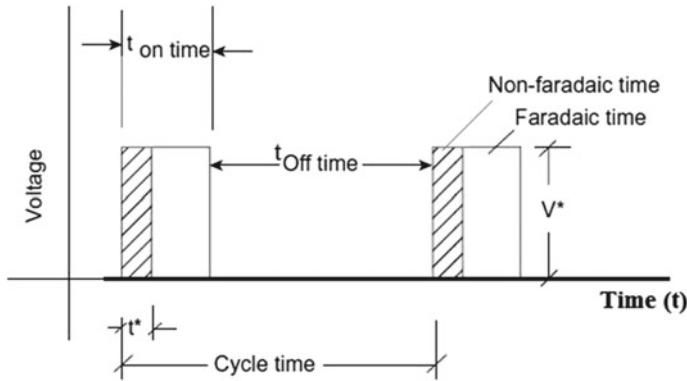


Fig. 2 Influence of square pulse charging and discharging effect on a double layer during EMM operation

Voltage can be gradually reduced after a non-Faradic time (charging time). Hence, the stray current and overcut can be reduced using a step pulse wave. As a consequence, the side gap can be reduced and the proper shape of the microhole may be obtainable. Using the step pulse, the problems of short pulse and large pulse may be removed because it has an option to set the pulse on-time properly. For this reason, the requirement for high frequency may be minimized. The effect of Faradic time and non-Faradic time on the voltage pulse is shown in Fig. 2.

2.1 Control of Micro-Tool Feed Rate

Machining accuracy can be improved by maintaining a linear relationship between micro-tool feed rate and MRR. If the tool feed rate is greater than the material removal rate, then there is a possibility that the tool will touch the workpiece. It is a dangerous situation for machining, which may damage the micro tool. Another problem is that a short circuit and sparks may be generated immediately. During machining time, sparks have a significant role in the improvement in overcut.

If micro-tool movement is continued with a constant feed rate, the above-discussed problem may be generated. This problem can be solved by using discontinue tool movement, which means that the micro-tool feed rate can be constant at first, then interrupted for a short period, and then returned to constant. This process may be continued until the tool reaches the absolute target as shown in Fig. 3. Employing this strategy, the short circuit effects may be eliminated, which improves machining accuracy because there is a chance to maintain a linear relationship between micro-tool feed rate and MRR.

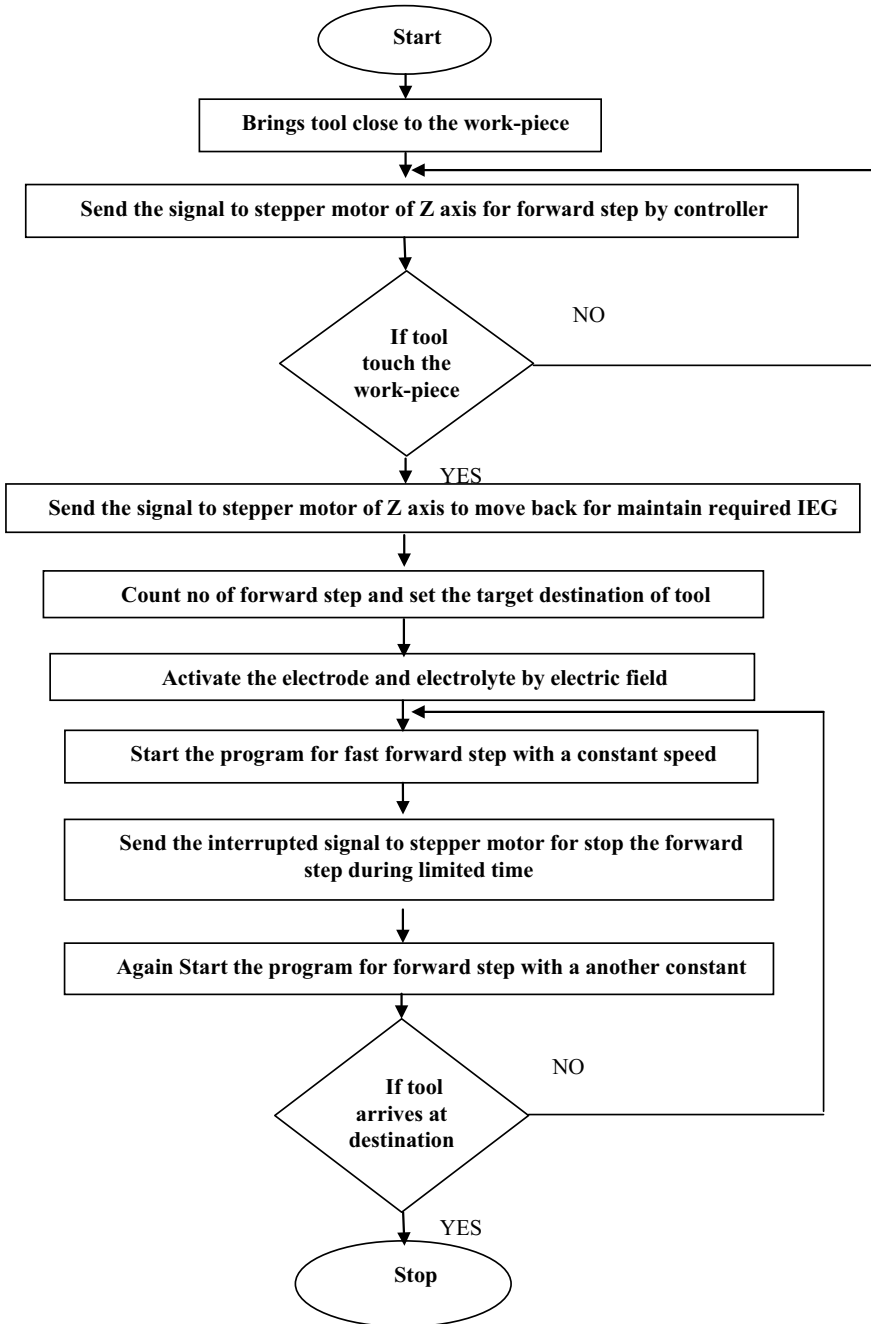


Fig. 3 Flow diagram of discontinues micro-tool feed rate control pattern

3 Experimental EMM SetUp

The EMM system setup has been established for the experiment, which consists of various subsystems such as the mechanical machining system, pulsed power supply, controller unit, electrolyte flow system, and machining chamber as shown in Fig. 4.

The precision movement of a micro-tool can be handled by a mechanical machining unit, which consists of three components as XYZ stages, a machining chamber, and a worktable. Due to the axis arrangement preference, the mechanical machine unit is designed as a gantry structure. In this arrangement, there is more working space, which is most advantageous for a sufficient store of fresh electrolytes. For this reason, heat and sludge can be easily removed from the machine zone into fresh ions during the chemical reaction. Here, in particular, the X-axis is mounted on the worktable. The machine chamber is made of perspex, and the workpiece holder is attached to it. The remaining two axes, Y and Z, are constructed for minimum load-bearing capability and are comparatively free. The controller unit interfaces with the computer and it controls the XYZ stages. The micro tool is always attached to the Z-axis, whose movement is along with the vertical axis. A programmable power supply unit is used to generate the pulse waveform. A pulse DC bipolar (20 V-100A) with a high-frequency range (100 mHz–20 kHz) power supply has been used for this experiment. A digital storage oscilloscope is used for data collection. This experimental setup is developed as a classic model and is less cost-effective.

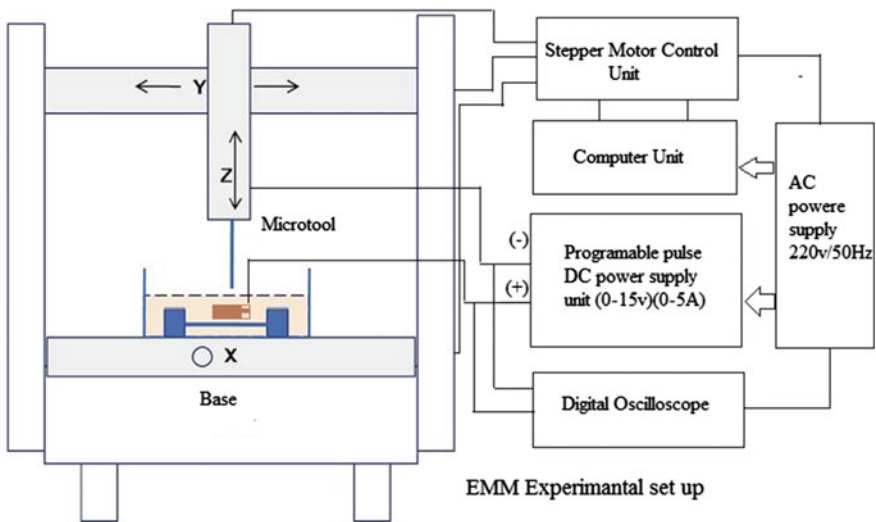


Fig. 4 Different subsystem of developed EMM setup is shown as a schematic view

4 Experimental Planning

Utilizing various voltage pulse waveforms, micro-holes can be drilled by the developed EMM setup to analyze performance aspects such as overcut, the shape of the hole, stray current effect, machining time, high tool feed rate, short circuit effect, current–voltage characteristics during machining, and comparison of machining accuracy for two types of voltage pulse waveforms, i.e., square pulse and step pulse. Here, a micro tool of Φ 200 μm in diameter made of tungsten material was used for experiments. For microhole drilling, a stainless steel sheet (SS304) of 100 μm thickness was chosen. Electrolyte selection for micromachining is an important decision for this experiment. As electrolyte flashing is not acceptable for micromachining because it can hamper the machining process, so that H_2SO_4 electrolyte was selected as a stagnant electrolyte. Experimentally, it was investigated that sludge is dissolved in the electrolyte during micromachining. The low concentration of H_2SO_4 electrolyte can reduce the side gap and enhance the surface quality [10, 11]. Hence, 0.1 mol/L concentrated H_2SO_4 electrolyte was selected for experimentation. A programmable D.C pulsed power supply was chosen for experimentation because square pulse and step pulse waveforms can be generated without a function generator. Another research objective is to design an EMM setup using a minimum subsystem to reduce the complexity of setup and cost-effectiveness. Previous research has shown that machining accuracy can be improved by using machining conditions such as a voltage range of 4–10 V, a current rating of up to 5A, a pulse frequency range of 217 kHz–10 MHz, and a duty ratio of no more than 60% [2, 10]. Hence, the operating R.M.S. voltage of the square pulse wave was 10.62 and 8.38 V for the step pulse was selected for the experiment. However, pulse frequency, i.e., 500 Hz, and duty ratio, i.e., 50%, were chosen for the above two voltage pulse waveforms. Here, micro-tool feed rate, i.e., 0.5 $\mu\text{m}/\text{sec}$, and IEG, i.e., 20 μm were selected to improve machine accuracy, eliminate micro sparks, and reduce the machining time. Overcut, stray current effect, and shape of the hole were analyzed by the image of the microhole observed by a digital microscope (Leica). For the experimental study, other parameters, i.e., voltage RMS, voltage peak duration time, output current, and voltage characteristics were measured by a digital oscilloscope. All machining conditions are listed in Table 1.

5 Experimental Result Analysis

Several microhole structures have been designed using the developed EMM setup and the best results are discussed here. After fabrication of microholes utilizing the developed EMM setup, experimental results have been analyzed, which are plotted in the graph. Figures 5 and 6 exhibit the characteristics of waveforms, respectively, square pulse and step pulse, which were measured by a digital oscilloscope. Here, the RMS voltage of a square pulse is 10.62 V and a step pulse is 8.38 V, but the

Table 1 Operating conditions for micro-hole fabrication

Condition	Description
Micro tool (Tungsten)	Φ 200 μm
Electrolyte (H_2SO_4) V peak-to-peak	0.1 mol/L 15 V
V_{rms} (step pulse wave)	8.38 V
V_{rms} (square pulse wave)	10.62 V
Pulse frequency	500 Hz
Duty ratio (%)	50%
Feed rate of micro tool	0.5 $\mu\text{m}/\text{sec}$
IEG	20 μm

peak-to-peak voltage is 15 V for both voltage pulse waves. So, it can be said that the energy transmitting capacity of the step pulse wave is less than square pulse because it depends on the RMS value. Another significant part is that the voltage peak duration time is different during one pulse on time. It plays an important role in energy transmission to a load.

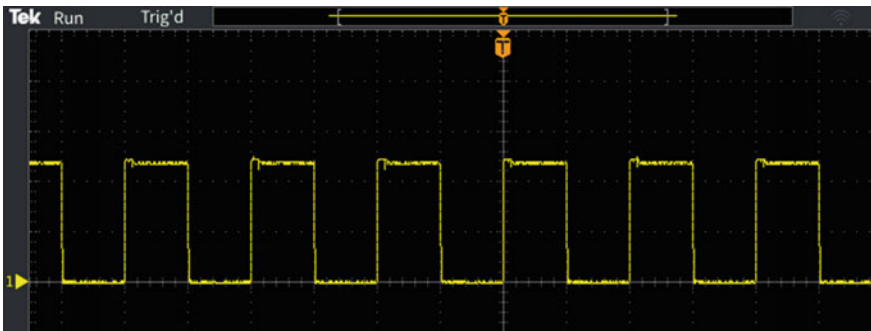


Fig. 5 Operational square pulse was measured by a digital oscilloscope

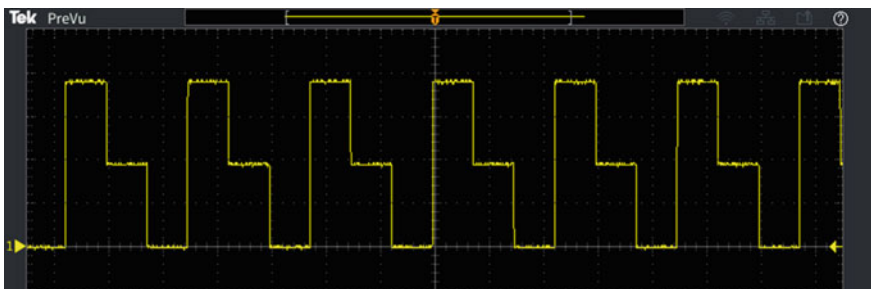


Fig. 6 Operational step pulse was measured by a digital oscilloscope

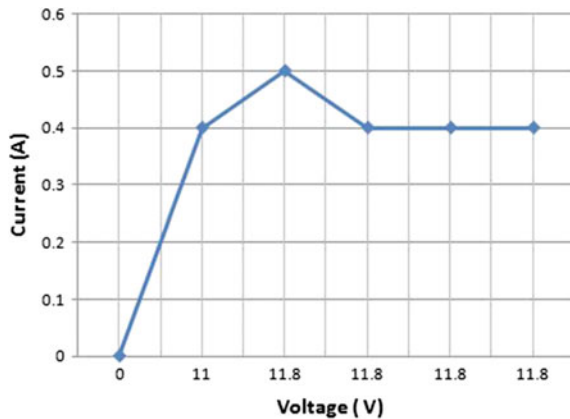
In square pulse, it is observed from current and voltage characteristic that initially current increases rapidly up to 0.5A, after that it is constant at 0.4A. The influence of square pulse inter-electrode current is saturated during machining. It has no significant impact on machining accuracy because MRR is directly controlled by current flux density. As a result, overcut increases during micro-hole drilling. Figure 7 shows that during machining, the voltage rises from 0 to 11.8 V as a result of the square pulse. During one half-cycle of a square pulse, the voltage varies such as 0, 15, and 0 V. Another observation is that peak value duration time is nearly equal to pulse on-time. From the result, it can be analyzed that after double layer charging time, the current is constant up to the end of the machining. It is observed that the influence of constant current, overcut, and stray current effects have increased.

As shown in Fig. 8, the current initially rises linearly up to 0.4A, then decreases linearly up to 0.2A, while voltage remains constant at 5.6 V. From this observation, it can be analyzed that the nature of the current is not constant during machining. In this case, the peak voltage duration time is very small compared to a square pulse. Voltage changes during one half-cycle of step pulse are as follows: 0, 15, 7.5, and 0 V. Hence, it can be said that the current flow rate of a step pulse is better for micromachining than a square pulse. It is analyzed that the discontinued tool feed rate is suitable for this type of current pattern.

A comparison result of the overcut influence of two types of the waveform is shown as a bar chart in Fig. 9. Experiment results show that overcut is generated at 435.24 μm in the horizontal axis for square pulses and 42.96 μm for step pulses. Hence, the influence of step pulse wave overcut can reduce by 90.13% than the conventional square pulse.

From microscopic image analysis, it is observed that the difference between the vertical and horizontal diameter of the microhole is 94.07 μm for square pulse wave as shown in Fig. 10. So, it can be said that the shape of the microhole is not accurate. The shallow portion around the microhole is generated because of the higher stray current effect, which creates uncontrolled dissolution.

Fig. 7 Current and voltage characteristics of square pulse wave



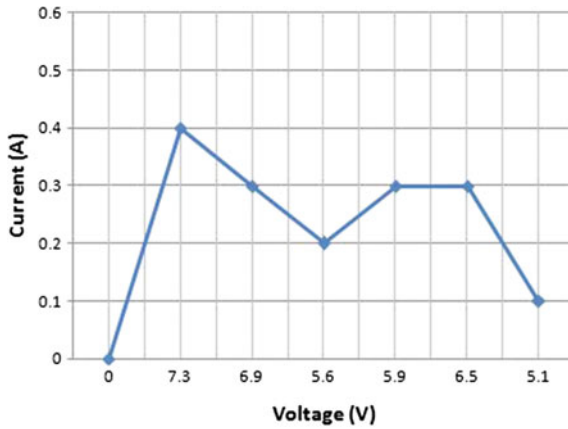


Fig. 8 Current and voltage characteristics of step pulse wave

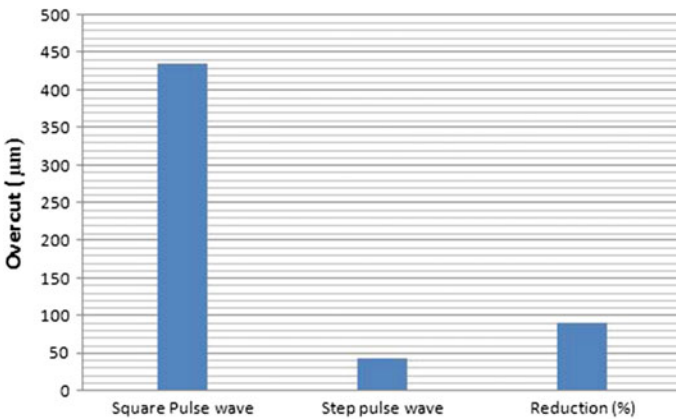


Fig. 9 Variation of the overcut with a different voltage pulse

The microscopic image as shown in Fig. 11 shows that the difference between the vertical and horizontal diameter of the microhole is $9.43 \mu\text{m}$ for step pulse, which represents the proper shape of the micro-hole. A few stray current affected areas around machined microholes are observed, which are generated due to 0.1A current increased after 0.2A arrives.

During machining, the total machining time was required for a square pulse was 4.48 min but for a step pulse, it was 3.39 min, while the tool feed rate was the same for both cases, i.e., $0.5 \mu\text{m}/\text{sec}$. Machining time can also be reduced by 24.33% due to the proper current flow rate.

Fig. 10 Micrograph of machined microhole at a particular machining condition, i.e., $V_{peak}, 15v$; $V_{rms}, 10.62v$; square pulse wave

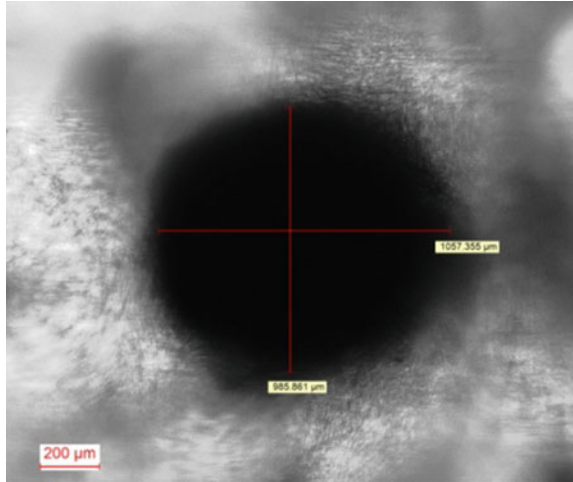
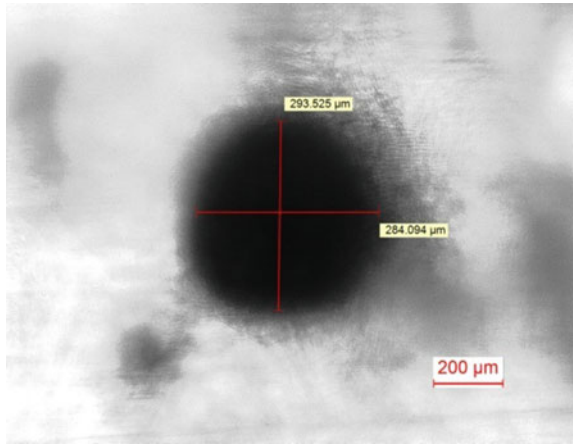


Fig. 11 Micrograph of machined microhole at a particular machining condition, i.e., $V_{peak}, 15v$; $V_{rms}, 8.38v$; Step pulse wave



6 Conclusions

In the present study, overcut, the shape of the machined microhole, stray current effect, machining time, possibilities of high feed rate, short circuit effect, and current-voltage characteristics during machining are investigated. After analyzing machined microhole experimental results, it can be concluded as follows:

- (i) The step pulse wave can improve machining accuracy more than the square pulse wave. Machining accuracy was measured in terms of overcut, stray current effect, short circuit effect, the shape of the hole, and machining time using two types of pulse waveforms.

- (ii) From experimental analysis, it is concluded that the current flow rate has a significant effect on overcut. From another analysis of test results, it can be concluded that tool feed rate control impacts on overcut. Hence, from the experimental result, it can be said that by utilizing step pulse wave, overcut can be reduced by 90.13% over square pulse wave.
- (iii) After observation of test results, it can be concluded that microhole shape accuracy of 89.98% can be improved by the step pulse wave. Experimentally, it is observed that low concentration electrolyte is used for both voltage pulse waves, but the stray current effect is not similar. So, it can be said that the current flow nature of a step pulse wave has a beneficial impact on stray current, while a square pulse wave cannot be significantly reduced.
- (iv) It can be concluded from the analyzed results that by utilizing step pulse waves, total machining time can be reduced by 24.33% over square pulses. This machining time can be analyzed, while the tool feed rate is the same for both experiments, but during the application of the step pulse wave, it is noticed that a high tool feed rate can be successfully applied. So, it can be concluded that machining time can be reduced more by step pulse.

Many challenging possibilities will open up for further research, such as monitoring of pulse time duration of the voltage pulse, use of the medium range of frequency, applying low duty ratio, use of high tool feed rate, the effect of different concentrations of electrolyte, and enhancing the accuracy of EMM. Hence, it is concluded from the present investigation that step pulse wave application is an innovative technique to improve the machining accuracy of electrochemical micromachine.

References

1. Rajurkar KP, Zhu D, McGeough JA, Kokaz J, De Silva A (1999) New development in electrochemical machining. *Ann CIRP* 48(2):567–579
2. Bhattacharyya B, Munda J (2003) Experimental investigation on the influence of electrochemical machining parameters on machining rate and accuracy in micromachining domain. *Int J Machine Tools Manufacture* 43:1301–10
3. Gao C, Qu N, He H, Meng L (2019) Double-pulsed wire electrochemical micro-machining of type-304 stainless steel. *J Mater Process Technol* 266:381–387. <https://doi.org/10.1016/j.jmptotec.2018.11.018>
4. Sidek RM, Hongrui C, Shiping L (2018) Effect of power signal waveform on shape accuracy in electrochemical drilling In: *IOP conference series: materials science and engineering* 392. <https://doi.org/10.1088/1757-899X/392/3/032015>
5. Patel DS, Agrawal V, Ramkumar J, Jain VK (2020) Reducing overcut in electrochemical micromachining process by altering the energy of voltage pulse using sinusoidal and triangular waveform. *Int J Mach Tools Manuf* 151:103526
6. Maeda R, Chikamori K, Yamamoto H (1984) Feed rate of wire electrochemical machining using pulsed current. *Precis Eng* 6:193–199
7. Hotoiu EL, Van Damme S, Albu C, Deconinck D, Demeter A, Deconinck J (2013) Simulation of nanosecond pulsed phenomena in electrochemical micromachining processes—effects of the signal and double layer properties. *Electrochim Acta* 93:8–16

8. Stojek Z (2010) The electrical double layer and its structure. In: Scholz F (ed) *Electroanalytical methods*, Springer, Berlin, Heidelberg. https://doi.org/10.1007/978-3-642-02915-8_1
9. Mithu MAH, Fantoni G, Ciampi J (2011) The effect of high frequency and duty cycle in electrochemical micro-drilling. *Int J Adv Manuf Technol* 55:921–933
10. Ghoshal B, Bhattacharyya B (2004) Shape control in micro borehole generation by EMM with the assistance of vibration of a tool. *Precis Eng* 38:127–137
11. Ryu SH (2009) Micro fabrication by the electrochemical process in citric acid electrolyte. *J Mater Process Technol* 209:2831–7

A Study on the Influence of Cutting Tool Geometry on the Temperature of the Workpiece in Nanometric Cutting of Silicon



Prateek Gupta  and Janakrajan Ramkumar 

1 Introduction

Silicon is the backbone of the semiconductor industry. Apart from building transistors for electronics, the optical properties of single-crystal silicon make it one of the most suited choices for developing infrared light-based devices. Therefore, manufacturing techniques are required which can machine silicon with nanometric accuracy. The development of several techniques such as electron beam lithography (EBL), focused ion beam (FIB) milling [1] and femtosecond laser machining [2] has opened up a new research field known as ultra-precision machining. The modeling of these processes at a nanometric scale possess a challenge due to the breakdown of the assumption of the continuum and this is where molecular dynamic simulations (MDS) provide a solution. Several software tools that use this technique have come up in the last decade. These tools include GROMACS [3], AMBER [4], DL-POLY [5] and LAMMPS [6]. Different tools have a different user community and are often specialized for a specific type of research. In this work, we have used LAMMPS as the primary tool of analysis.

Single-point diamond turning (SPDT) is a promising approach for the fabrication of micro/nanostructures by machining the desired structure directly on the surface of the workpiece. Using a single-point diamond turning tool [2] to remove material to obtain flat surface up to a certain surface roughness [7–9]. SPDT gives mirror-finish on most materials and is preferred over other ultra-precision manufacturing methods. Silicon is the backbone of the semiconductor industry [10]. Almost all the electronic devices in use today employ at least some kind of silicon-based semiconductors.

P. Gupta (✉) · J. Ramkumar
Indian Institute of Technology, Kanpur 208016, India
e-mail: ptkiitk@gmail.com

J. Ramkumar
e-mail: jrkumar@iitk.ac.in

SPDT was invented in the 1980s to obtain the desired surface finish on silicon. Such precision is required in applications, where the optical properties of silicon have a considerable role to play, for example, infrared light-based devices and has the potential to reduce the size of transistors which has been a constant source of progress in the electronics industry. Moore's law is the observation that the number of transistors in a dense integrated circuit (IC) doubles about every two years. However, it has been estimated that Moore's law would no longer be valid by 2025 since the development of technology to reduce the size of transistors is not progressing at the required rate [11].

Several studies have used MD simulations to study the nanometric cutting process for different material-tool combinations. The studies use different types of interatomic potentials, temperature conditions, software and models. LAMMPS is most extensively used for the simulation of nanometric cutting.

In work presented by Goel et al. [9], MDS performed using LAMMPS was used to simulate SPDT. The work aimed at investigating the wear of the diamond tool for different crystal orientations. ABOP potential functions were used. Results showed the strong influence of crystal orientation on the wear resistance of a diamond tool. The formation of SiC due to the high temperature, and pressure due to high-pressure phase transformation (HPPT) was also observed.

An essential contribution in the field of nanometric cutting was made by Goel et al. [8]. In this work, the mechanism of wear for the diamond tool in nanometric cutting of silicon was presented. The study found the formation of *SiC* on the surface of the workpiece and the tool. This was also explained using the stress and the radial distribution of silicon carbide concerning simulation time. The work was in excellent agreement with experimental data obtained through the X-ray photoelectron spectroscopy and the stresses involved in the simulation, and the stress data obtained in the simulations.

In work reported by Cai et al. [12], a new silicon cutting mechanism at the nanoscale was presented. The study used LAMMPS as the software tool for the simulation, and an infinitely hard tool was modeled. Tersoff potentials were used to model the interactions. The forces and the stresses during the cutting process were observed. The study focused on crack formation during the cutting process and the mode of failure during the cut that leads to chip formation. The study also investigated the effects of various deformed/undeformed chip thickness ratios and the corresponding mechanism of cutting.

In Zhang et al. [13], nanometric cutting of copper was studied in terms of the subsurface damage caused by the cutting process at different depths of cut and at different cutting speeds. The deformations of the crystal structure of copper was reported. It was reported that the cutting speed of the process makes little difference to the proportion of the BCC atoms in the region of cut. The different types of dislocation observed with different cutting depths was also reported.

In work reported by Fang et al. [14], nanometric cutting of monocrystalline silicon was simulated. The study aimed to identify the mechanism of chip formation in the cutting process and presented a model that used extrusion to explain chip formation instead of shearing used in conventional machining. Nanoindentation experiments

were found to be in good agreement with the simulation data. Tersoff potentials were used to model the interaction between the atoms, and the tool was assumed to be infinitely hard.

In a work presented by Kalkhoran et al. [15], nanometric cutting using a blunt tool was studied. A parameter called relative tool sharpness (RTS), defined as the ratio of undeformed chip thickness and tool radius, was used to characterize the cutting process. The cutting process was simulated using LAMMPS. The machining forces for different RTS were reported, along with the force ratios and the effective tool rake angles. The study used an infinitely hard tool, and the workpiece was modeled as single-crystal silicon. Tersoff potentials were used to model the interactions between different atoms.

In the work presented by Lie et al. [16], molecular dynamic simulations were performed using a grooved diamond cutting tools were used to manufacture structures on a silicon workpiece. ABOP potentials were used to model the interactions between the atoms. The cutting forces on the tool and workpiece along with the temperature distribution of the tool were reported. The geometry of the groove was varied, and the tool was assumed to be blunt or the study.

In the study by Lianfenga et al. [17], the effect of tool radius was studied on the cutting of skiving monocrystalline silicon was studied using molecular dynamic simulations. The work studied the mechanisms of cut for the material with different roundness of the tool and concluded that while in the case of a sharp tool, the mechanism of material removal is predominantly shear, as the roundness of the tool increases, the mechanism of cut tends to move toward extrusion accompanied by shearing. However, for the purposes of this study, the tool has been assumed to be sharp.

In this study, the process of cutting monocrystalline silicon using single-point diamond cutting tools has been studied at nanometric scale using molecular dynamic simulations. In this work, process of nanometric cutting has been simulated, and the temperature of the region of cut has been observed. The forces on the tool have also been reported. The simulations have been run for different depths of cut and tools including positive and negative rake angle tools. A brief mathematical overview of MDS has been discussed in Sect. 2. The various parameters used for modeling the process and the respective configurations have been discussed in Sect. 3. The results have been discussed in Sect. 4. The conclusions of this work have been discussed in Sect. 5.

2 MD Simulation

MDS provides the numerical solution of Newton's laws of motion for an ensemble of atoms [18]. It is used to observe phenomena at very small-time steps ($10^{-10}s$) and at an enhanced resolution. MDS uses the position, velocity and acceleration of various atoms in the system under consideration to calculate the desired properties of the system. The atoms/molecules in MDS are modeled as individual spring mass

systems with a dynamic spring constant. These spring constants are modeled using the potential functions. The choice of potential function is an essential part of any MDS study since it is the primary bridge between the simulation and real-world interaction between the atomic entities. The potential functions and the parameters of these functions are selected such that they satisfy the basic physical properties of the system, and the model is stable. There are several different potential functions used to model different types of systems. These potential functions include Lennard–Jones (LJ) potentials [19], analytical bond-order potential (ABOP) [20], Morse potentials [21] and pair-wise Morse potentials, embedded atom model (EAM) potentials [22], Bolding-Anderson potential and Tersoff potentials [23, 24] each of which has its own merits and demerits. In most of these potential functions, the distance between two atoms is used as an input, and the potential energy of the two atoms due to their proximity with each other is calculated.

In MDS, the motion of atomic bodies is realized by calculating the resultant forces for each atom and integrating them to calculate their trajectory according to the Newton's laws of motion [25]. This is mathematically described in Eq. (1):

$$m \frac{d^2 r_i}{dt^2} = \frac{d(mv_i)}{dt} = \frac{dp_i}{dt} = F_i \quad (1)$$

where m is the mass of the atom and r_i , v_i , p_i and F_i are the position vector, velocity vector, momentum vector and the force acting on the i th atom, respectively. t is the time in the simulation at which the position, velocity and acceleration of the atoms are calculated. F_i is calculated as the gradient of the potential energy (PE) with respect to the position of the i th atom as given in Eq. (2):

$$F_i = -\nabla_i V(r_1, r_2, r_3, \dots, r_N) \quad (2)$$

where V is the potential energy function. N is the number of atoms and ∇_i is the gradient operator for the i th atom $\nabla_i = \frac{\partial}{\partial x_i} \hat{i} + \frac{\partial}{\partial y_i} \hat{j} + \frac{\partial}{\partial z_i} \hat{k}$. Each time, step of MD simulation has a length of the order of femtoseconds. It should be noted that if the number of atoms in the system is N , then the number of differential equations solved in each time step is $6N$, and hence, the process is computationally expensive, thus the need for the high-performance computational resources for such a study [25].

For each time step, the force on each atom is calculated, and the force is then integrated to obtain the displacement of the atoms. There are a few algorithms that are most commonly used for this integration, e.g., Leapfrog integration [26] and Verlet integration [27].

The velocity of the atoms is also used to calculate the temperature of a given region in the simulation box. This is accomplished by using the relationship between the kinetic energy of the atoms, and the temperature is obtained from the kinetic theory of gases in Eq. (3) [9].

$$\frac{1}{2} \sum_i m_i |v_i|^2 = \frac{3}{2} N k_b T \tag{3}$$

where k_b is the Boltzmann constant ($1.3806503 \times 10^{-23} \text{ J/K}$) and T is the atomistic temperature.

3 Modeling

Several methods for modeling this process have been mentioned in the literature, which differ in the use of potential functions, boundary conditions, parameters of the tool (for example, tool radius, rigid tool, deformable tool) and the nature of the atoms used. In this work, Tersoff potentials have been used to model the behavior of silicon atoms and their interaction with carbon atoms in the diamond tool. The parameters for Tersoff potentials are readily available in LAMMPS [23, 24]. The time step for the simulation has been kept at 0.5 fs. Figure 1 shows a schematic diagram of the simulated system. The details of the simulation parameters are given in Table 1. The movement of the workpiece is constrained on one side by a group of rigidly fixed atoms and unconstrained on the other side. This has been described by Komanduri et al. as an elastic boundary condition [25]. A description of the four types of atoms used in this study is given as follows.

1. Boundary atoms: These atoms have been fixed and modeled as perfectly rigid to simulate the bulk of the workpiece away from the cut region.
2. Peripheral atoms: These atoms have been used to simulate the thermodynamics of the system. NVT ensemble has been used to simulate these atoms. This is used

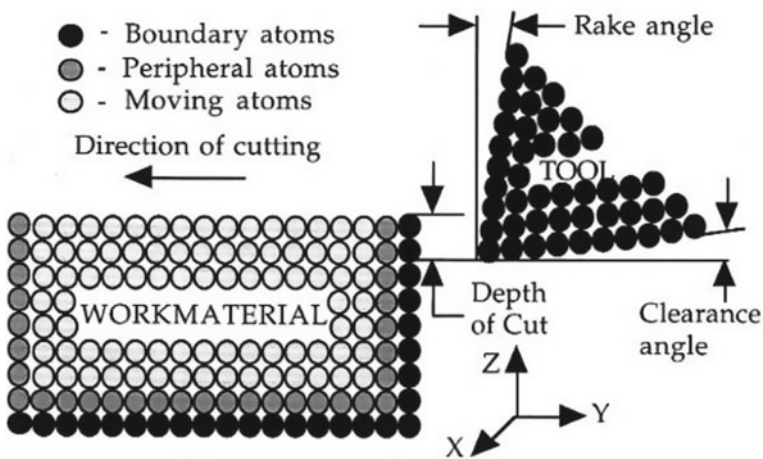


Fig. 1 Diagram of the atomic system studied

Table 1 Parameters used in the simulation with the lattice parameters of silicon $a = 5.431 \text{ \AA}$

Parameter	Value
Configuration	3D
Potentials used	Tersoff
Work material	Single-crystal silicon (diamond cubic)
Tool material	Perfectly rigid
Lattice parameter of workpiece	$a = 5.431 \text{ \AA}$
Velocity of cut	10 m/s
Relief angle	15°
Rake angle	$-30^\circ, -15^\circ, 0^\circ, 15^\circ, 30^\circ$
Depth of cut (DOC)	0a, 1a, 2a, 5a, 10a
Width of cut	5a
Dimensions of workpiece	$5a \times 70a \times 50a$

to simulate heat transfer in the system from the region of cut to the bulk of the workpiece. This layer has been kept to 2–3 atom thick as done in literature [25].

3. Tool atoms: The tool has been modeled to be rigid and sharp, the rake angle has been varied, and the tool velocity has been kept constant.
4. Workpiece atoms: These are atoms that have been modeled as following Newtonian physics. These atoms can be displaced and oscillate about their mean positions as dictated by Eq. (1).

4 Results and Discussion

All the simulations in this work have been performed using LAMMPS [6]. The data that was obtained from LAMMPS was processed and handles using Jupyter Notebooks [28] coded in Python and using NumPy, pandas and SciPy [29]. OVITO has been used to visualize the results obtained from the simulations and to supply all the snapshots that have been reported in this work [30]. The results related to the temperature of the workpiece during the cutting process have been discussed in Sect. 4.1, and the forces experienced by the tool during the cutting process have been discussed in Sect. 4.2.

4.1 Analysis of Temperature During Machining

The temperature of the workpiece during the machining process for each rake angle simulated has been plotted in Fig. 2. As expected, the temperature of the workpiece increases monotonically as the DOC of the process is increased. Oscillations observed

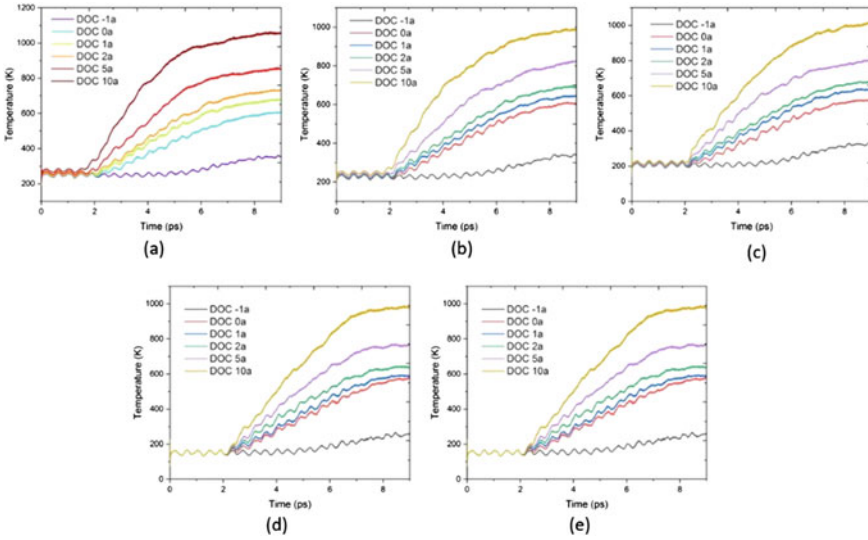


Fig. 2 Temperature of the workpiece for rake angles **a** -30° , **b** -15° , **c** 0° , **d** 15° and **e** 30°

in the plots are a common feature of the data obtained using MDS. The layer used to simulate the heat transfer of the region of cut with the bulk of the material is modeled using NVT ensemble. The NVT ensemble is used to define groups of atoms that conduct heat, but the velocity of the atoms is rescaled to keep the temperature of the system constant. The oscillations arise from the rescaling of the velocities of the atoms and have been observed in literature [9, 31]. The overall profile of the temperature with respect to time also agrees with the previous works. In addition to the profiles, we have also plotted data for the DOC of $-1a$. A negative depth of cut implies that the tool is not in cut but is simply gliding over the workpiece at a distance 1 atomic layer. This has been done to have an insight of the sensitivity of the interactions between the tool and the workpiece atoms. As far as the temperature is concerned, the interaction between the tool and workpiece when the tool is not in cut does not have much impact on the temperature of the process [18].

4.2 Analysis of Temperature During Machining

The force experienced by the tool of different rake angles with respect to time for different depths of cut is shown in figure Fig. 3. A plot for DOC $-1a$ have been added to the data for reasons similar to Fig. 2. Since the simulations are governed by potential functions this action itself (even when the tool is not in cut) would cause some force on the tool and the workpiece which has been plotted as DOC as $-1a$. As observed from the graphs, the force profile for the DOC as $-1a$ displays the same

profile for all rake angles and is hence also acts as a control for the experiments. It should be noted that large oscillations are observed in the force data obtained directly from LAMMPS. Hence, the data needs to be filtered before the presentation which has been accomplished using a moving average filter of window size 50. The scale of the oscillations has been reported in the graphs plotted by Goel et al. [8], where it can be seen that for small depth of cuts the oscillations can also cause the force to change the direction. The overall force profile is similar to the ones seen in the field of conventional manufacturing in the macro-domain. The force increases as the tool engages with the cut. There are oscillations similar to the oscillations cause in micro-machining due to chip breaking and then stabilizing while oscillating at a constant magnitude. However, it should be noted that in the simulations performed, no chip breakage was observed. The chip preferred to stick to the tool instead.

It was observed that among all the rake angles simulated, the forces with the -30° rake angle tool are most sensitive to the change in the depth of cut. This is as expected as the forces at DOC $0a$ are predominantly friction forces which are not expected to vary much with the DOC while the cutting forces are sensitive to the DOC. It was also observed that the forces for the higher rake angles are the most sensitive to the depth of cut. It can be hypothesized that while the positive rake angle of the tool removes material using a shearing process similar to macro-machining, the mechanism of cutting for negative rake angle tools tends to be extrusion [14]. It was also observed that on average, the tool with 0° experiences the least machining force. At a DOC of $0a$, the forces experienced by the various tools studied show a statistical range of $0.54\text{Ev}/\text{\AA}$ which increases to $2.15\text{Ev}/\text{\AA}$ for DOC $10a$. It observed that as the forces increase with the DOC, the average of the standard deviation remains

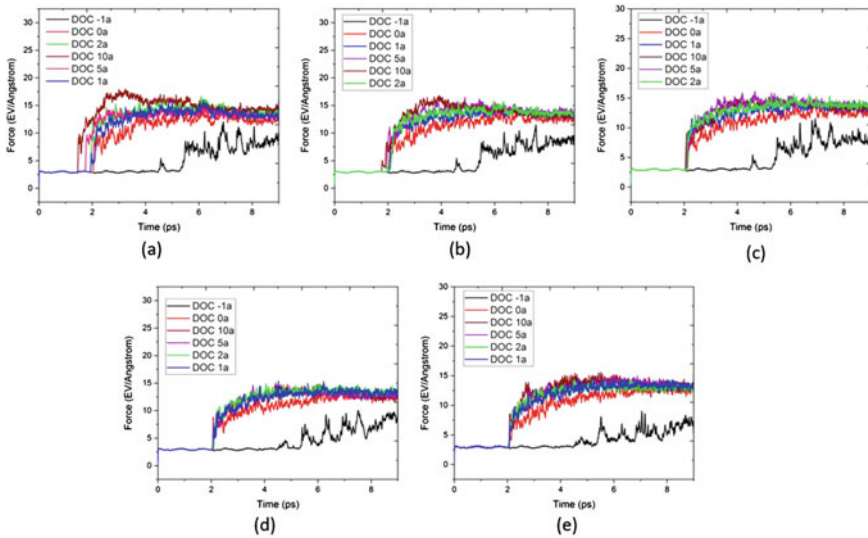


Fig. 3 Magnitude of force experienced by the tool for rake angles **a** -30° , **b** -15° , **c** 0° , **d** 15° and **e** 30°

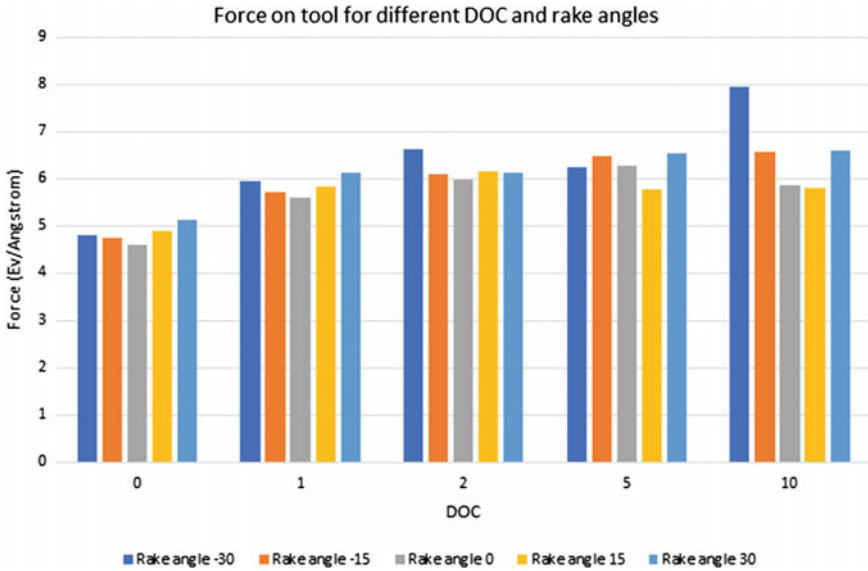


Fig. 4 Mean force experienced by tools (Y-axis) of different rake angles at different depths of cut (DOC) (X-axis)

fairly constant which indicated that the oscillations in the data are fairly constant. Compared to the neutral tool, the tool for rake angle -30° shows a $\approx 11.5\%$ increase in force, and the positive 30° rake angle tool shows a $\approx 7\%$ increase in force (Fig. 4).

5 Conclusions

The nanometric cutting process using single-point diamond cutting tool was simulated using LAMMPS. The temperature of the workpiece and the force experienced by the tool was observed. Tools for rake angle -30° , -15° , 0° , 15° and 30° were simulated, and the cutting process was observed for depths of cut $-1a$, $0a$, $1a$, $2a$, $5a$ and $10a$. It was observed that the tool for rake angle -30° was the most sensitive to change in the depth of cut in terms of the magnitude of force experienced. It was concluded that compared to a neutral rake angle, a negative rake angle can result in up to 11.5% increase in force, while a positive rake angle can result in up to 7.9% increase in force. Using negative rake angle, tools result in a greater heat evolution in the region of cut compared to +ve rake angle tool and the temperature increases monotonically with a decrease in the rake angle. The difference observed was 100 K from $+30^\circ$ to -30° .

References

1. Picard Y, Adams D, Vasile M, Ritchey M (2003) Focused ion beam-shaped microtools for ultra-precision machining of cylindrical components. *Precis Eng* 27(1):59–69
2. Tong Z, Luo X, Sun J, Liang Y, Jiang X (2015) Investigation of a scale-up manufacturing approach for nanostructures by using a nanoscale multi-tip diamond tool. *Int J Adv Manuf Technol* 80(1–4):699–710
3. Abraham MJ, Murtola T, Schulz R, Páll S, Smith JC, Hess B, Lindahl E (2015) GROMACS: high performance molecular simulations through multi-level parallelism from laptops to supercomputers. *SoftwareX* 1–2:19–25
4. Case DA, Darden TA, Cheatham TE, Simmerling CL, Wang J, Duke RE, Luo R, Crowley M, Walker RC, Zhang W (2008) Amber 10
5. Smith W, Forester TR, Todorov IT, Leslie M (2006) The DL poly 2 user manual. CCLRC, Daresbury Laboratory, Daresbury, Warrington WA4 4AD, England, vol 2
6. Plimpton S (1995) Fast Parallel algorithms for short-range molecular dynamics. *J Comput Phys* 117(1):1–19
7. Goel S, Haque Faisal N, Luo X, Yan J, Agrawal A (2014) Nanoindentation of polysilicon and single crystal silicon: molecular dynamics simulation and experimental validation. *J Phys D Appl Phys* 47(27):275304
8. Goel S, Luo X, Reuben RL (2013) Wear mechanism of diamond tools against single crystal silicon in single point diamond turning process. *Tribol Int* 57:272–281
9. Goel S, Luo X, Reuben RL, Pen H (2012) Influence of temperature and crystal orientation on tool wear during single point diamond turning of silicon. *Wear* 284–285:65–72
10. Mathews JA (1997) A silicon valley of the east: creating Taiwan's semiconductor industry. *Calif Manage Rev* 39(4):26–54
11. Shalf J (2020) The future of computing beyond Moore's Law. *Philos Trans Royal Soc A: Math Phy Eng Sci* 378(2166):20190061
12. Cai MB, Li XP, Rahman M (2007) Study of the mechanism of nanoscale ductile mode cutting of silicon using molecular dynamics simulation. *Int J Mach Tools Manuf* 47(1):75–80
13. Zhang P, Cao X, Zhang X, Wang Y (2021) Effects of cutting parameters on the subsurface damage of single crystal copper during nanocutting process. *Vacuum* 187:109420
14. Fang FZ, Wu H, Liu YC (2005) Modelling and experimental investigation on nanometric cutting of monocrystalline silicon. *Int J Mach Tools Manuf* 45(15):1681–1686
15. Ameli Kalkhoran SN, Vahdati M, Yan J (2019) Molecular dynamics investigation of nanometric cutting of single-crystal silicon using a blunt tool. *Jom* 71(12):4296–4304
16. Liu C, Zhang J, Zhang J, Chen X, He W, Xiao J, Xu J (2020) Influence of micro grooves of diamond tool on silicon cutting: a molecular dynamic study. *Mol Simul* 46(2):92–101
17. Lianfeng L, Qinchuan N, Minglin L (2020) Analysis of the influence of tool radius on mechanical state of monocrystalline silicon during nano-cutting. *Mech Adv Mater Struct* vol 0(0):1–15
18. Komanduri R, Raff LM (2001) A review on the molecular dynamics simulation of machining at the atomic scale. *Proc Inst Mech Eng Part B: J Eng Manuf* 215(12):1639–1672
19. Smit B (1992) Phase diagrams of Lennard-Jones fluids. *J Chem Phys* 96(11):8639–8640
20. Erhart P, Albe K (2005) Analytical potential for atomistic simulations of silicon, carbon, and silicon carbide. *Phys Rev B* 71(3):35211
21. Girifalco LA, Weizer VG (1959) Application of the morse potential function to cubic metals. *Phys Rev* 114(3):687
22. Becquart CS, Decker KM, Domain C, Ruste J, Souffez Y, Turbatte JC, Van Duysen JC (1997) Massively parallel molecular dynamics simulations with EAM potentials. *Radiat Eff Defects Solids* 142(1–4):9–21
23. Tersoff J (1986) New Empirical model for the structural properties of silicon. *Phys Rev Lett* 56(6):632–635
24. Tersoff J (1994) Chemical order in amorphous silicon carbide. *Phys Rev B* 49(23):16349–16352

25. Komanduri R, Chandrasekaran N, Raff LM (1999) Orientation effects in nanometric cutting of single crystal materials: an MD simulation approach. *CIRP Ann Manuf Technol* 48(1):67–72
26. Van Gunsteren WF, Berendsen HJC (1988) A leap-frog algorithm for stochastic dynamics. *Mol Simul* 1(3):173–185
27. Grubmüller H, Heller H, Windemuth A, Schulten K (1991) Generalized verlet algorithm for efficient molecular dynamics simulations with long-range interactions. *Mol Simul* 6(1–3):121–142
28. Kluyver T, Ragan-Kelley B, Pérez F, Granger B, Bussonnier M, Frederic J, Kelley K, Hamrick J, Grout J, Corlay S, Ivanov P, Avila D, Abdalla S, Willing C (2016) Jupyter notebooks—a publishing format for reproducible computational workflows. Positioning and power in academic publishing: players, agents and agendas. Loizides F, Schmidt B (eds)
29. McKinney W (2010) Data structures for statistical computing in python. In: Proceedings of the 9th python in science conference. Van der Walt S, Millman J (eds)
30. Stukowski A (2010) Visualization and analysis of atomistic simulation data with OVITO—the open visualization tool. *Model Simul Mater Sci Eng* (1)
31. Chavoshi SZ, Goel S, Luo X (2016) Influence of temperature on the anisotropic cutting behaviour of single crystal silicon: a molecular dynamics simulation investigation. *J Manuf Process* 23:201–210

Experimental and Dimensional Analysis of Planar Flow Melt Spinning Process



Sowjanya Madireddi

Nomenclature

C_p	Specific heat J/kgK
G	Nozzle-wheel gap mm
h	Convective heat transfer coefficient W/m ² K
k	Thermal conductivity W/mk
l	Length of the nozzle mm
P	Pressure kPa
Pr	Prandtl number
R_a	Surface roughness μm
Re	Reynolds number
t	Ribbon thickness μm
T	Ejection temperature °C
T_g	Glass transition temperature K
U	Wheel speed m/s
w	Nozzle-slit width mm
μ	Viscosity Pa.s
δ_{Tx}	Thickness of thermal boundary layer
x	Distance from slit center mm

S. Madireddi (✉)
CVR College of Engineering, Hyderabad 501510, India
e-mail: madireddisowjanya@gmail.com

© The Author(s), under exclusive license to Springer Nature Singapore Pte Ltd. 2023
B. Bhattacharyya et al. (eds.), *Advances in Micro and Nano Manufacturing and Surface Engineering*, Lecture Notes in Mechanical Engineering,
https://doi.org/10.1007/978-981-19-4571-7_8

1 Introduction

Core losses in the distribution transformer attribute to the material structure (amorphous/crystalline) and thickness of the lamina. Eddy current losses are directly proportional to the thickness of the lamina, and hysteresis losses depend on the structure of the material. Good quality amorphous ribbons produced by planar flow melt spinning process (PFMS) reduce these losses by 75% if used as core material. Hence, the present work focuses on the analysis and prediction of the conditions to obtain a higher quality ribbon during PFMS process for $\text{Fe}_{73.5}\text{Nb}_3\text{Cu}_1\text{Si}_{13.5}\text{B}_9$ alloy. As many investigators presented work on different materials and process conditions, the process is generalized using dimensional analysis for any material-parameter combination.

Some experimental studies reported earlier considered the effect of process conditions on the thickness of the ribbons. Some investigators focused on obtaining improved soft magnetic properties in the ribbon and some others reported various topographies of the ribbons and few others on numerical models [9]. Investigators [12] performed a parametric study of the effect of process variables on ribbon thickness for Pb–Sn ribbons and defined a process window for this material. Thickness of the ribbons with jetting temperature was observed to [7] decrease due to viscosity, which may also vary with alloy composition. Carpenter et al. [3] presented ribbons with various surface defects, viz. dimple, streak and herringbone obtained during PFMS process at various process conditions. Heat transfer between cooling wheel and melt puddle influences the ribbon formation [17, 23], and quench rates [21] influence the crystallization of $\text{Fe}_{73.5}\text{Nb}_3\text{Cu}_1\text{Si}_{13.5}\text{B}_9$ alloy. Matsuki et al. [10] observed a decrease in iron and hysteresis losses of Fe–Si–B alloy ribbons with decrease in surface roughness. Szewieczek et al. [19] studied the corrosion properties of Metglas alloy at various conditions. They also studied its effect on the magnetic properties of Finemet alloy and found that surface roughness [20] of the ribbons greatly influences these properties. Wu et al. [22] observed air entrainment and formation of air pockets affecting the magnetic properties of the ribbons. Induced air pockets were observed on the wheel side of the ribbon while casting in air, whereas these pockets were absent during the vacuum casting of $\text{Ni}_{78}\text{Si}_8\text{B}_{14}$ ribbons. Cox et al. [4] reported the herringbone defect due to translator motion of the cooling wheel. Byrne et al. [1, 2] observed cross-wave defect due to vibration of the puddle. All of the investigations differ with each other in terms of material or process condition. This makes it difficult to apply and use the results obtained by one investigator directly by the other investigator.

The present work compares thickness, surface roughness, topography and amorphous structure of the ribbons obtained at various process conditions. The equations hence obtained through non-dimensionalization (dimensional analysis) will be useful for the experimentalists to predict the variation in thickness and surface roughness of the product at a given process condition for any material-parameter combination prior to experiment. Thereby, reduce the cost of experimental investigation to

predict optimum condition to produce higher quality ribbons for the existing or new materials.

2 Experimental

Finemet alloy ($\text{Fe}_{73.5}\text{Si}_{13.5}\text{B}_9\text{Nb}_3\text{Cu}_1$) which possesses ultra-soft magnetic properties was used for the experimentation. Crucibles made of quartz having rectangular slit with length (l) and width (w) and with circular lobes at the end were employed to hold the material for induction heating. Material samples of approx. 150–200 g were used for each experiment. The sample was melted in the crucible using an induction heater. The crucible was brought down to the preset nozzle-wheel gap (G) when the melt reached to the required temperature (T). The melt was ejected by applying inert gas pressure (P) on to a rotating cooling wheel at a set speed (U). Solidified melt in the form of a ribbon was ejected from the under cooled puddle due to wheel rotation. Figure 1a shows the schematic of the puddle formation and ejection of ribbon from the under cooled puddle. USM and DSM represent upstream and downstream meniscus, respectively. Table 1 gives the process conditions at which parametric study was performed using Finemet alloy $\text{Fe}_{73.5}\text{Si}_{13.5}\text{B}_9\text{Nb}_3\text{Cu}_1$. Thickness and surface roughness were measured, and XRD analysis was performed on the as-spun ribbons.

3 Results and Discussion

The melt, which comes out through the rectangular slit upon ejection by gas pressure, accumulates in the form of a puddle in the nozzle-wheel gap. Heat transfer from the melt to the cooling wheel initiates the rapid solidification (freezing) of melt at its glass transition temperature T_g (point A) as shown in Fig. 1a. The thickness of the solidified material grows in the puddle until the downstream meniscus (DSM). The intersection point of solidified material, molten alloy and DSM (Fig. 1a, point B) determines the ribbon thickness. The condition of the melt at this point influences the surface quality of the ribbon.

In the present work, the reasons for the surface quality of the ribbon at various process conditions are analyzed for the first time using the boundary layer theory. For liquid metal flows, thickness of thermal boundary layer is higher than that of velocity boundary layer. As the melt solidifies at T_g and comes out of the puddle at point B (Fig. 1a), thickness of the ribbon can be assumed as the thickness of thermal boundary layer at T_g of the alloy. On the other hand, the laminar or turbulent flow condition of the melt at point B can be predicted using the non-dimensional form of velocity represented by Reynolds number for various process conditions. As the flow of melt depends on velocity and viscosity, calculation of Reynolds number (ratio of inertia to viscous forces) helps to analyze the surface quality.

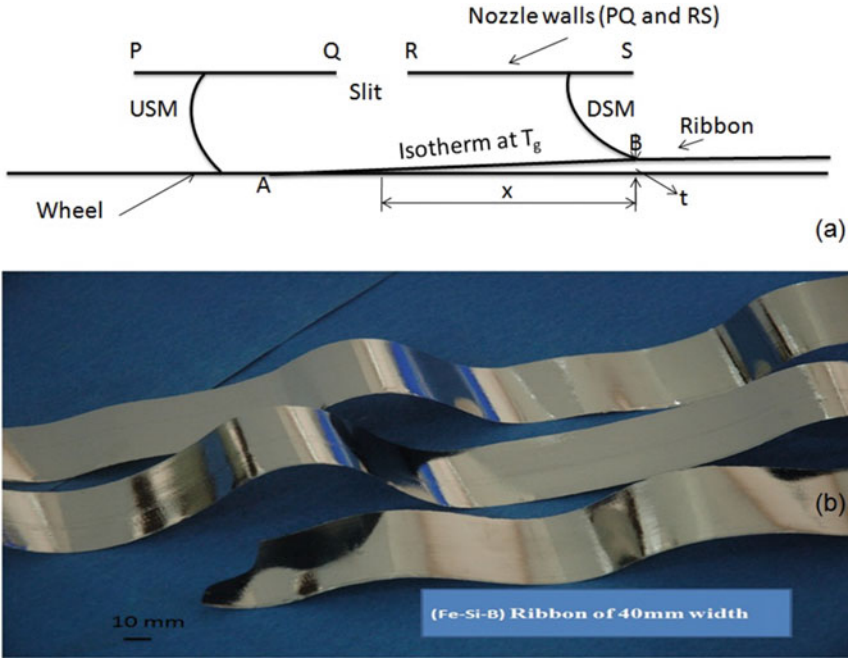


Fig. 1 a Schematic of ribbon formation during PFMS process, b sample ribbon (Fe-Si-B)

Schlichting [14] stated that there exists both laminar and turbulent flows for $2 \times 10^5 < Re < 6 \times 10^5$, where 2×10^5 is the subcritical Reynolds number. Ozisik [11] affirmed that the flow transforms within the boundary layer from laminar to turbulent when the Reynolds number is above 2×10^5 . However, it is difficult to find the Reynolds number in the puddle, as the properties of the melt changes rapidly. Hence, an equation to predict the thickness of thermal boundary layer can be employed to calculate the Reynolds number (Re). The following Eq. (1) is obtained from the equations for thickness of velocity and thermal boundary layer for $Re < 5 \times 10^5$ [8].

$$Re = \left[\frac{\delta_{Tx} Pr^{0.333}}{5x} \right]^2 \tag{1}$$

where δ_{Tx} is the thickness of thermal boundary layer and x is the position on the wheel in the direction of rotation. Thickness of the ribbon is taken as the thickness of the thermal boundary layer δ_{Tx} and x as 5 mm, as the nozzle walls (Fig. 1a PQ and RS) are of 5 mm each. Pr is the Prandtl number, defined as the ratio of molecular diffusivity of momentum to molecular diffusivity of heat and is given by.

$$Pr = \frac{\mu(T)C_p}{k} \tag{2}$$

Table 1 Experiments conducted using Fe_{73.5}Si_{13.5}B₉Nb₃Cu₁ alloy

Expt. no.	Pressure (kPa)	Temp (°C)	Wheel speed (m/s)	Slit length and width (mm × mm)	Gap (mm)	Material weight (g)
1	13.78	1100	18.9	50 × 0.5	0.3	150
2	15.51	1100	18.9	50 × 0.5	0.3	150
3	17.23	1100	18.9	50 × 0.5	0.3	150
4	18.96	1100	18.9	50 × 0.5	0.3	150
5	20.68	1100	18.9	50 × 0.5	0.3	130
6	13.78	1100	25.14	50 × 0.5	0.3	128
7	13.78	1125	25.14	50 × 0.5	0.3	150
8	13.78	1150	25.14	50 × 0.5	0.3	150
9	13.78	1175	25.14	50 × 0.5	0.3	150
10	13.78	1200	25.14	50 × 0.5	0.3	140
11	13.78	1100	18.9	50 × 0.5	0.3	170
12	13.78	1100	20.43	50 × 0.5	0.3	150
13	13.78	1100	22.05	50 × 0.5	0.3	130
14	13.78	1100	23.57	50 × 0.5	0.3	140
15	13.78	1100	25.14	50 × 0.5	0.3	145
16	13.78	1100	22.05	50 × 0.3	0.32	150
17	13.78	1100	22.05	50 × 0.4	0.32	150
18	13.78	1100	22.05	50 × 0.5	0.32	140
19	13.78	1100	22.05	50 × 0.6	0.32	140
20	13.78	1100	22.05	50 × 0.7	0.32	

The show the change in the respective parameter values keeping the rest constant

where C_p is the specific heat, k is the thermal conductivity and $\mu(T)$ is the viscosity at T_g of the alloy (Table 2).

To generalize the phenomenon, the dimensional quantities are to be represented in non-dimensional form. This helps to use the information obtained in the present study for any material and process parameter conditions [5]. All the critical process

Table 2 Material properties

Designation	Parameters	Values
ρ	Density	7180 kgm ⁻³
C_p	Specific heat	544 Jkg ⁻¹ K ⁻¹
k	Thermal conductivity	8.99 W/mK
μ	Viscosity	$\mu(T)$
σ	Surface tension	1.2 N/m
T_g	Glass transition temperature	873 K

parameters, properties of the material, heat transfer parameters and the resulting ribbon dimensional parameters are listed, and the dimensional analysis is applied. The non-dimensional groups derived for the PFMS process using Buckingham π theorem are as given below:

$$\frac{t}{G} = \emptyset \left[\frac{\rho P G^2}{\mu^2}, \frac{\mu C_p}{k}, \frac{\rho U G}{\mu}, \frac{h G}{k}, \frac{w}{G}, \frac{G^2 \rho^2 k T}{\mu^3}, \frac{R_a}{G} \right] \quad (3)$$

Where \emptyset is a function determined experimentally. The groups: $\left[\frac{\rho P G^2}{\mu^2} \right]$, $\left[\frac{\rho U G}{\mu} \right]$, $\left[\frac{w}{G} \right]$ and $\left[\frac{G^2 \rho^2 k T}{\mu^3} \right]$ represent non-dimensional form of pressure, wheel speed, slit width and temperature, respectively. Whereas the groups $\left[\frac{t}{G} \right]$ and $\left[\frac{R_a}{G} \right]$ represent non-dimensional thickness and surface roughness of the ribbon. Group $\frac{\mu C_p}{k}$ represents Prandtl number and $\left[\frac{h G}{k} \right]$ represents Nusselt's number.

3.1 Effect of Process Parameters on the Quality of the Ribbons

The ribbons obtained during the experiments using Finemet alloy at various process conditions show topographies of streak, wavy, dimple and polished. Ribbon obtained is made into 20 equal parts, and the measurement of thickness and roughness is performed on each sample. The error bars shown (Figs. 2, 3, 4 and 5) are 5% for thickness and 3% for surface roughness. Roughness measured on the wheel side for all the ribbons is less than 0.8 μm . Hence, the comparison of roughness as a measure of quality at various process conditions was performed on the airside.

Wheel Speed. Figure 2a–d shows ribbons obtained by varying the wheel speed from 18.9 m/s to 25.1 m/s and the corresponding roughness variations, respectively. Other

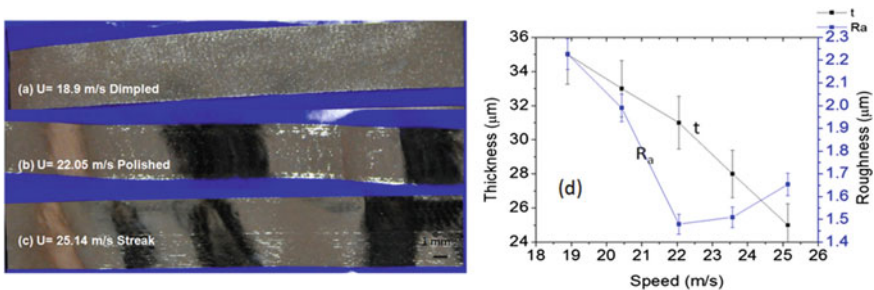


Fig. 2 Ribbons obtained at wheel speeds: **a** 18.9 m/s, **b** 22.05 m/s, **c** 25.14 m/s, **d** effect of speed on thickness and surface roughness

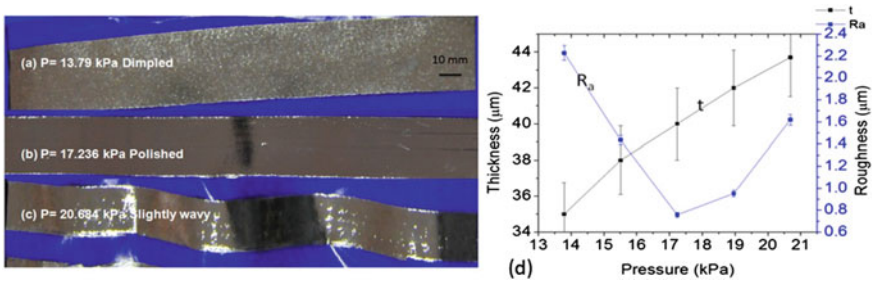


Fig. 3 Ribbons obtained at ejection pressures **a** 13.79 kPa **b** 17.23 kPa **c** 20.68 kPa **d** surface roughness at various ejection pressures

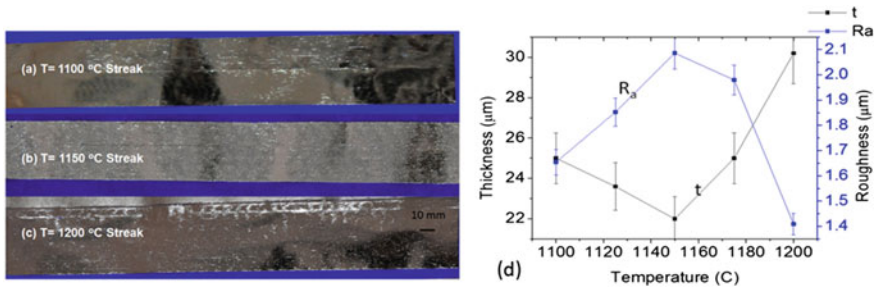


Fig. 4 Ribbons obtained at ejection temperatures **a** 1100 °C **b** 1150 °C **c** 1200 °C **d** surface roughness at various ejection temperatures

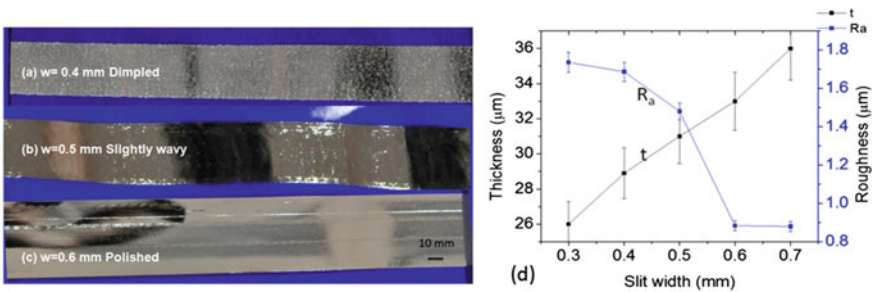


Fig. 5 Ribbons obtained at nozzle-slit width **a** 0.4 mm **b** 0.5 mm **c** 0.6 mm **d** surface roughness at various slit width

process conditions were kept at $P = 13.78$ kPa, $T = 1100^\circ\text{C}$, $G = 0.3$ mm and $w = 0.5$ mm. Dimpled, polished and streak patterns were observed for lower, medium and higher wheel speeds, respectively. Carpenter and Steen [3] predicted that the dimpled pattern was due to non-uniform heat transfer between the wheel and the melt at the meniscus side while streak pattern was due to non-contact of the melt with the wheel at higher speeds.

In the present experiments, the quality of the ribbons is compared using the Reynolds number (Re) and surface roughness. The value of Re calculated using Eq. (1) is in the range 1.5×10^5 – 3×10^5 and shows interesting comparison with roughness as discussed below. With increase in wheel speed from 18.9–22 m/s, the value of Reynolds number is less than 2×10^5 and roughness decreased from 2.2–1.45 μm . With further increase in speed to 25.1 m/s, Reynolds number increased above 2×10^5 and the surface roughness increased to 1.65 μm . The ribbon with polished surface obtained at wheel speed of 22.05 m/s exhibits lowest surface roughness of 1.45 μm for Re nearly 2×10^5 .

The thickness and surface roughness in the dimensional form for various wheel speeds (Fig. 2d) are as given below.

$$t = 22.78 + 2.33U - 0.089 U^2 \quad (4a)$$

$$R_a = 1.47 + 1.117 U - 0.095 U^2 + 0.002 U^3 \quad (4b)$$

The thickness and surface roughness derived in the non-dimensional form for various wheel speeds areas are given below.

$$\frac{t}{G} = 114 \left[\frac{\rho G U}{\mu} \right]^{-1.11} \quad (5a)$$

$$\frac{R_a}{G} = 3 \times 10^{-7} \left[\frac{\rho G U}{\mu} \right]^2 + 0.075 \quad (5b)$$

$$\left(\frac{R_a}{G} \right) \left(\frac{t}{G} \right) = 2 \times 10^{-6} \left[\frac{\rho G U}{\mu} \right]^2 - 0.002 \left[\frac{\rho G U}{\mu} \right] + 0.728 \quad (6)$$

Equation (4a) and (4b) are obtained by curve fitting the values for thickness t and surface roughness R_a measured for change in wheel speed U . Equation (5a), (5b) and (6) is obtained, by curve fitting the values for the dimensionless thickness t/G , dimensionless roughness R_a/G and for the ratio $(R_a/G)/(t/G)$ for change in dimensionless speed $[\rho G U/\mu]$. The non-dimensional thickness and wheel speed in Eq. (5a) show inverse proportionality. Equation (5b) shows increase in roughness with wheel speed. However, the value of coefficients in Eq. (6) shows that the roughness decreases with increase in speed and increases with further increase in speed. Figure 2d obtained from the experimental results also shows the similar trend for dimensional thickness and roughness with increase in wheel speeds. Thickness decreases with wheel speed due to faster melt removal rates as increase in Reynold's number means increase in flow velocity. Wheel speed and flow velocity if balance at DSM, the ribbon obtained may be of higher quality (Re nearly equal to 2×10^5). However, transitional flow ($\text{Re} > 2 \times 10^5$) amplifies the turbulence in the melt, resulting in increase in surface roughness at higher wheel speeds.

Ejection Pressure Figure 3a–d shows the ribbons obtained by varying the ejection pressure from 13.78 kPa to 20.68 kPa and the corresponding roughness variations, respectively. Other process conditions were kept at $U = 18.9$ m/s, $T = 1100^\circ\text{C}$, $G = 0.3$ mm and $w = 0.5$ mm. Dimpled, polished and wavy ribbons are obtained at lower, medium and higher pressures, respectively. Reynolds number calculated from Eq. (1) is less than 2×10^5 at all the pressures. For increase in pressure from 13.79 to 17.23 kPa, roughness decreased from 2.2 to 0.7 μm and Reynolds number decreased from 1.5×10^5 to 1.1×10^5 . With further increase in pressure to 20.68 kPa, roughness increased to 1.6 μm and Reynolds number further decreased to less than 1×10^5 . As the viscous force increases with higher melt flow rate, Reynolds number decreases with increase in pressure.

The thickness and surface roughness in the dimensional form for various ejection pressures (Fig. 3d) are given below.

$$R_a = 29.62 - 3.239 P + 0.091 P^2 \tag{7a}$$

$$t = 0.1148 + 3.39 P - 0.062 P^2 \tag{7b}$$

The thickness and surface roughness derived in the non-dimensional form for various ejection pressures are given below.

$$\frac{t}{G} = 0.003 \left[\frac{\rho P G^2}{\mu^2} \right]^{0.54} \tag{8a}$$

$$\frac{R_a}{G} = 7 \times 10^{-8} \left[\frac{\rho P G^2}{\mu^2} \right]^2 - 0.001 \left[\frac{\rho P G^2}{\mu^2} \right] + 0.098 \tag{8b}$$

$$t = 0.1148 + 3.39 P - 0.062 P^2 \tag{9}$$

Equations (7a) and (7b) are obtained by curve fitting the values t and R_a measured for change in pressure P . Equations (8a), (8b) and Eq. 9 are obtained by curve fitting the values for the ratios t/G , R_a/G and $(R_a/G)/(t/G)$ for change in dimensionless pressure $[\rho P G^2/\mu^2]$. The non-dimensional thickness is proportional to the dimensionless pressure (Eq. 8a) and increases with increase in pressure. However, the surface roughness (Eq. 8b) initially decreases and the positive intercept shows increase in its value with further increase in pressure. This increase in surface roughness is much higher with increase in thickness with pressure as evident from Eq. (9). Figure 3d obtained from the experimental results shows similar trend for both dimensional thickness and roughness. With increase in pressure, more amount of melt accumulates in the gap and increases the residence time of melt in the puddle leading to increase in thickness. The imbalance in flow velocity and wheel speed at low ejection pressures leads to dimple surface on the free side of the ribbon. However, increase in melt flow with increase in pressure suppresses the uneven surface (dimple) and the ribbon

attains polished topography. For pressures higher than 18.96 kPa, Reynolds number is less than 1×10^5 and the ribbon shows wavy topography due to resistance to flow caused by higher viscous force. This wavy surface increases the surface roughness. Present author [15] has observed from the numerical analysis that, higher pressures at lower wheel speeds cause puddle vibration and forms wavy topography, which is suppressed by thinner melts obtained at higher ejection temperatures. However, power consumption increases and more cooling rate is required for higher superheats. Hence, moderate ejection pressures employed at lower superheats (Re near to 2×10^5) may result in higher quality ribbon.

Ejection Temperature. Figure 4a–d shows ribbons and surface roughness variations with change in ejection temperature from 1100 to 1200°C. Other process conditions were kept at $U = 25.14$ m/s, $T = 1100^\circ\text{C}$, $G = 0.3$ mm and $w = 0.5$ mm. The surface topography of all the ribbons is streak pattern. The thickness and surface roughness in the dimensional form for various ejection temperatures (Fig. 4d) are given.

$$R_a = -288.43 + 0.507 T - 2.21 \times 10^{-4} T^2 \quad (10a)$$

$$t = 2658.7 - 4.63T + 0.002 T^2 \quad (10b)$$

The thickness and surface roughness derived in the non-dimensional form for various ejection temperatures are given below.

$$\frac{t}{G} = 13.58 - 5 \times 10^{-7} \left[\frac{G^2 \rho^2 k T}{\mu^3} \right] \quad (11a)$$

$$\frac{R_a}{G} = 5 \times 10^{-8} \left[\frac{G^2 \rho^2 k T}{\mu^3} \right] - 1.435 \quad (11b)$$

$$t = 2658.7 - 4.63T + 0.002 T^2 \quad (12)$$

Equations (10a) and (10b) are obtained by curve fitting the values t , R_a measured for change in melt ejection temperature T . Equation (11a) and (11b) and Eq. (12) are obtained, by curve fitting the non-dimensional terms t/G , R_a/G and $(R_a/G)/(t/G)$ for change in non-dimensional temperature $[G^2 \rho^2 k T / \mu^3]$. Thickness initially decreased and then increased with temperature (Fig. 4d). However, the surface roughness increased initially and then subsequently decreased with further increase in temperature. Equations (11a), (11b) and Eq. (12) show the similar trend for non-dimensional thickness and roughness with increase in temperature.

Reynolds number obtained at various temperatures is higher than 2×10^5 . But it is interesting to observe that the value of Re is initially increased from 3×10^5 to 3.8×10^5 with increase in temperature from 1100 to 1150 °C and then decreased to nearly 2×10^5 at 1200 °C at which the lowest surface roughness of the ribbons is observed. Decrease in viscosity with increase in temperature increases the flow ability of melt and hence increases the Reynolds number and decreases the thickness.

With further increase in temperature, decrease in viscosity leads to spread of melt on the wheel surface causing bigger puddles. This increases the residence time of melt in the puddle and increases the thickness. However, the increase in thickness reduces the flow velocity of melt and hence reduces the Reynolds number. As the value is near to the subcritical value, surface roughness is relatively less.

Ribbons obtained at very high superheats observed to possess dimple pattern due to air entrainment [13, 16]. However, all the ribbons obtained during the present set of experiments show streak pattern. The reason for streak pattern may be the higher wheel speed (25 m/s) selected in all the experiments as on the other hand, the ribbon obtained at 22 m/s and 1100 °C (Fig. 2b) is of polished surface. It infers that the wheel speed is instrumental in obtaining quality ribbon, and the influence of temperature is negligible at higher wheel speeds.

Nozzle-slit width. Figure 5a–d shows ribbons obtained and the surface roughness by varying the nozzle-slit width from 0.3 mm to 0.7 mm. Other process conditions were kept at $U = 22.05$ m/s, $T = 1100^\circ\text{C}$, $G = 0.32$ mm and $P = 13.78$ kPa. Dimple, slightly wavy and polished topographies are observed with low, medium and larger slit width, respectively.

The thickness and surface roughness in the dimensional form for various slit widths (w) (Fig. 5d) are given below.

$$R_a = 0.0938 + 9.535 w - 13.66 w^2 \tag{13a}$$

$$t = 19.1 + 23.38 w + 0.71 w^2 \tag{13b}$$

The thickness and surface roughness derived in the non-dimensional form for various slit widths are given below.

$$\frac{t}{G} = 0.024 \left[\frac{w}{G} \right] + 0.059 \tag{14a}$$

$$\frac{R_a}{G} = 0.006 \left[\frac{w}{G} \right]^3 - 0.038 \left[\frac{w}{G} \right]^2 + 0.44 \left[\frac{w}{G} \right] - 0.014 \tag{14b}$$

$$\left(\frac{R_a}{G} \right) / \left(\frac{t}{G} \right) = 0.057 \left[\frac{w}{G} \right]^3 - 0.268 \left[\frac{w}{G} \right]^2 + 0.36 \left[\frac{w}{G} \right] - 0.082 \tag{15}$$

Equation 13a and 13b is obtained by curve fitting the values t , R_a measured for change in slit width w . Equations (14a), (14b) and (15) are obtained, by curve fitting the values for the non-dimensional terms t/G , R_a/G and $(R_a/G)/(t/G)$ for change in non-dimensional slit width $[w/G]$. Increase in slit width increases the thickness and decreases the surface roughness as interpreted using Equations (14a), (14b) and (15). Similar trend is observed for dimensional thickness and roughness as shown in Fig. 5d. Reynolds number calculated from Eq. (1), for $w = 0.3$ mm to

0.7 mm decreased from 2.7×10^5 to 1.4×10^5 . This is because with increase in slit width the amount of melt flow increases resulting in bigger melt puddle. Hence, the puddle supplies more material and the residence time of melt increases in the puddle, resulting in thicker ribbons. With increase in thickness, the irregularities on the surface are suppressed decreasing the roughness. Of the two big nozzle-slit dimension, 0.6 mm is preferred as the roughness is nearly same but the thickness is much higher for nozzle with slit width of 0.7 mm. The Reynolds number for the nozzle with $w = 0.6$ mm is within the limit of 1.5×10^5 – 2×10^5 resulting polished surface.

3.2 X-Ray Diffraction Analysis

The melt in contact with the cooling wheel freezes at the glass transition temperature T_g of the alloy. The material near to the wheel cools to lower values due to the no slip boundary at the melt-wheel contact. The cooling effect is much higher near the wheel and decreases with the distance away from the cooling surface. The isotherm of T_g grows from point A to B as shown in Fig. 6. Hence, at point B, there exists a temperature gradient across the thickness of the ribbon. The difference in temperature across the ribbon decreases with decrease in thickness. Furthermore, the projections due to roughness (Fig. 6b) behave as extended surface and enhance the rate of heat transfer leading to difference in temperature on the surface. Hence, thickness and roughness cause temperature gradients across and on the surface of the ribbon, respectively. This gradient in turn defines the amorphous or crystalline nature of the ribbon on the free/airside. Figure 6c shows the roughness visible on the ribbon surface.

Figure 7 presents the XRD analysis performed on both sides of the ribbons. Wheel side represents the contact side of the ribbon with the wheel, and airside represents the

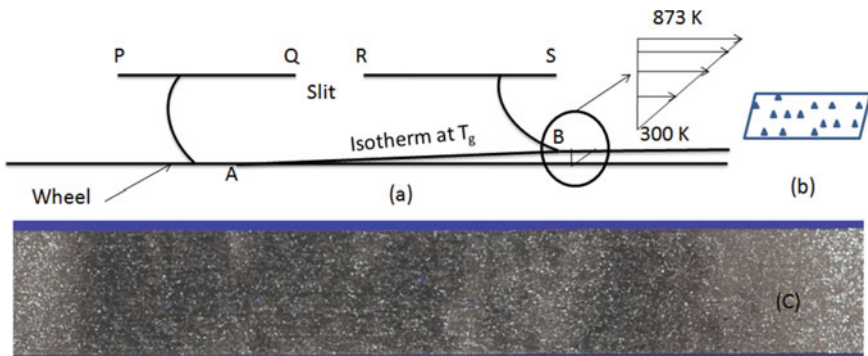


Fig. 6 **a** Schematic of temperature gradient across the ribbon thickness, **b** schematic of surface with roughness, **c** ribbon with high roughness

free side of the ribbon exposed to atmosphere. The wheel side surface of the ribbons shows amorphous nature by a broad hump between 40° and 50° diffraction angle and also show low roughness ($<1 \mu\text{m}$), for all the process conditions. The temperature of the melt in contact with the wheel will always be at the lowest value. Hence, the nature of the ribbon on the wheel side is amorphous for all the process conditions. However, iron peaks on the airside show crystalline nature. The crystalline/amorphous nature on the airside depends on the thickness and roughness of the ribbon. With increase in pressure from 13.78 to 20.68 kPa, both thickness and roughness increased leading to crystalline ribbons (Fig. 7a). For moderate pressures 17.23 kPa, even though roughness is less, higher thickness resulted into crystalline ribbon. Hence, we can infer that, to obtain an amorphous ribbon, lower ejection pressures are sufficient. With increase in wheel speed, even though there is a decrease in thickness, higher surface roughness resulted in to crystalline nature (Fig. 7b). With increase in slit width from 0.3 mm to 0.7 mm, although roughness decreased, increase in thickness and the temperature gradient across the ribbon led to non-amorphous nature on the surface (Fig. 7c).

It was observed by few investigators that the wheel temperature increases during planar flow melt spinning process [6] and wheel may also expands at high temperatures [18]. Present author [17] has observed an increase in wheel temperature leading to crystalline ribbons after a period of casting time. Further, wheel has to absorb more amount of heat with increase in ejection temperature. The effect of temperature on thickness and roughness of the ribbons is opposite. Lowest thickness obtained at 1150°C resulted in to amorphous nature suppressing the effect of roughness on the surface. Hence, super heats less than 100°C are preferred to obtain amorphous nature on the ribbon surface. Hence, we can infer that the temperature gradient across the ribbon and on the surface of the ribbon exists and is the reason for the ribbon being amorphous on the wheel side and crystalline on the free side.

4 Conclusions

Non-dimensional groups derived for the process help to estimate the change in thickness and surface roughness for any change in process parameters. During rapid solidification, the thickness of the ribbon is at the thermal boundary layer formed at the glass transition temperature of the alloy. Amorphous structure depends on the thickness of the ribbon. Hence, Reynolds number calculated from the equation for thermal boundary layer thickness is used for the parametric analysis of the ribbon quality. The inferences drawn are as follows:

- Polished surface topography is observed for $1 \times 10^5 < \text{Re} < 2 \times 10^5$ at the intersection point of melt, ribbon and downstream meniscus.
- Wavy surface is observed for $\text{Re} < 1 \times 10^5$ and streak or dimple topography for $\text{Re} > 2 \times 10^5$

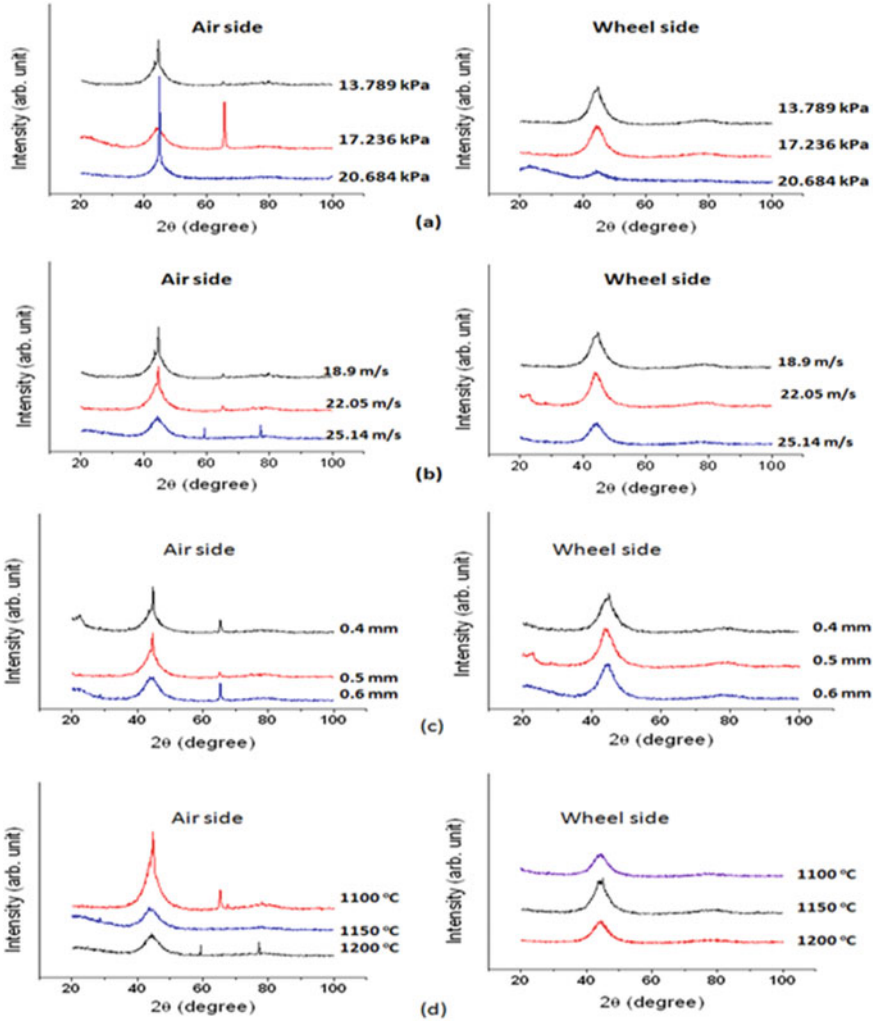


Fig. 7 XRD pattern of the ribbons at various, **a** ejection pressures, **b** wheel speeds, **c** nozzle-slit width, **d** ejection temperature [23].

- Nozzles with larger slit width produced polished ribbons due to unrestricted flow leading to smooth surface on the free side.
- Wheel speed dominates the effect of temperature on the ribbon topography.
- Surface roughness on the wheel side is less than 1 μm for all the ribbons, while varied on the airside with process conditions.
- Polished ribbons show lowest surface roughness on airside.
- Roughness enhances the heat transfer rate on the airside leading to local crystallization.

- Low temperatures near the wheel surface and a gradient across the ribbon result into amorphous and crystalline structure, respectively. Maintaining the wheel at lower temperatures may reduce the crystalline structure on the airside.

Acknowledgements The work is an extension of the research work performed by the author at Defence Metallurgical Research Laboratory (DMRL), Hyderabad (2011–14). The author is thankful to the organization for permitting to perform the research work.

Appendix A

As the properties of FINEMET are not available, the properties of similar alloy (Fe-Si-B) available in the literature (2009) taken for the calculations are as given below.


References

1. Byrne CJ, Theisen EA, Reed B, Steen PH (2006) Capillary puddle vibrations linked to casting-defect formation in planar-flow melt spinning. *Metll. Meterl. Trans. B (37B)*, 445–456 (2006).
2. Byrne CJ (2007) Planar-flow melt spinning: process stability and microstructure control, PhD dissertation, Cornell University
3. Carpenter JK, Steen PH (1992) Planar flow spin casting of molten metals process behavior. *J Mater Sci* 27:215–225
4. Cox BL, Steen PH (2013) Herringbone defect formation in planar-flow melt spinning. *J Mater Proc Tech* 213:1743–1752
5. Ede AJ (1967) An introduction to heat transfer principles and calculations, Int. Pergamon Press, London, pp 9–14
6. Karpe B, Kosec B, Bizjak M (2011) Modeling of heat transfer in the cooling wheel in the melt-spinning process. *J Achiev Mater Manuf Engg* 46:88–94
7. Nakagawa K, Kanadani T, Mori Y, Ishii Y (2011) The effect of jetting temperature on the fabrication of rapidly solidified Fe-Si-B systems alloys using single-roller melt spinning mater. *Trans* 52(2):196–200
8. Kothandaraman CP, Subramanyan S (2008) Heat and mass transfer data book, edn 6. New Age, New Delhi
9. Liu H, Chen W, Qiu S, Liu G (2009) Numerical simulation of initial development of fluid flow and heat transfer in planar flow casting process. *Metall Trans B (40B)*:411–429
10. Matsuki K, Kogiku F, Morito N (1998) Influence of surface roughness on magnetic properties of Fe-Si-B amorphous alloy. *IEEE Trans on Magn* 34(4):1180–1182
11. Ozisik MN (1985) Heat transfer a basic approach int. ed., McGraw-Hill, Singapore, pp 370–372
12. Praisner TJ, JSJ Chen, Tseng AA (1994) An experimental study of process behavior in planar flow melt spinning. *Metl Mater Trans B* 26B:1995–1996
13. Seino R, Yuichi S (2014) Observation of melt puddle behavior in planar flow casting in air. *J Alloy Comps* 586:5150–5152
14. Hermann S (1979) Boundary-layer theory int. ed., Mc-Graw Hill Inc., edn 4, 142–143
15. Sowjanya M, Reddy KKT (2014a) Wavy ribbon formation during planar flow melt spinning process—a 3D CFD analysis. In: 10th international conference on heat transfer, fluid mechanics and thermodynamics, Florida, 14–16

16. Sowjanya M, Reddy KKT, Srivastha B, Majumdar B (2014b) Simulation of initial ribbon formation during planar flow melt spinning process. *Appl Mech Mater* 446–447:352–355
17. Sowjanya M, Reddy KKT (2014c) Cooling wheel features and amorphous ribbon formation during planar flow melt spinning process. *J Mater Proc Tech* 214:1861–1870
18. Sundararajan A, Thomas BG (2008) Heat transfer during melt spinning of Al-7%Si alloy on a Cu-Be wheel. *TMS The Minerals Met Mat Soc*, pp 793–810
19. Szewieczek D, Baron A (2004) Electrochemical corrosion properties of amorphous Fe₇₈ Si₁₃ B₉ alloy. *J Mater Proc Tech* 157–158:442–445
20. Szewieczek D, Baron A (2005) Electrochemical corrosion and its influence on magnetic properties of Fe_{75.5} Si_{13.5} B₉Nb₃Cu₁ alloy. *J Mater Proc Tech* 164–165:940–946
21. Tiberto P, Stantero A, Baicco M, Matko I, Duhaj P (1996) Formation of nano-crystals in amorphous Fe_{73.5} Nb₃ Cu₁ Si_{13.5} B₉ ribbons produced with different quenching rate. *J Nanostruc Mater* 7(6):619–628
22. Chung-Yung W, Kuan-Ju L, Vheng Y-T, Huang C-K, Pan C-N, Li W-C, Chiang L-K, Yeh C-N, Fong S-C (2014) Development of amorphous ribbon manufacturing technology. *China Steel Tech Rep No* 27:28–42
23. Madireddi S (2020) Effect of heat transfer between melt puddle and cooling wheel on amorphous ribbon formation. *Eng Sci Technol Int J* 23(5):1162–1170

Encapsulation of CNT Films on Silicon Wafer by DLC Synthesized by PECVD for Application as a Thermal Interface Material



Krishna Ankit , T. Gecil Evangeline, L. S. Aravinda, N. Sharath Kumar, Mamilla Ravi Sankar, Nagahanumaiah, K. Niranjana Reddy, and N. Balashanmugam

1 Introduction

Sumio Iijima's discovery of CNTs opened up research in innovative materials [1]. CNTs are a boon to several capital goods sectors like microelectronics, nanotechnology, biomedical, etc., as they are known to have excellent physical properties.

CNTs are deposited using various chemical vapour deposition techniques. Plasma-enhanced chemical vapour deposition (PECVD) is one technique to synthesize CNTs at a lower substrate temperature than a conventional chemical vapour deposition (CVD). Based on the source of plasma used, PECVD is categorized into radiofrequency (RF), direct current (DC) and microwave (MW) PECVD [2–4]. CNTs with low amorphous carbon content have been deposited using the RF-PECVD technique with parallel plates. This modification effectively reduces the undesirable damage induced by plasma [5]. The growth of CNTs is promoted by factors like pretreatment of the catalyst, vacuum pressure and substrate temperature. In the absence of

K. Ankit (✉) · L. S. Aravinda · Nagahanumaiah · K. N. Reddy · N. Balashanmugam
Central Manufacturing Technology Institute (CMTI), Tumkur Road, Bangalore 560022, India
e-mail: ankit@cmti.res.in

Nagahanumaiah
e-mail: director@cmti.res.in

K. N. Reddy
e-mail: niranjana@cmti.res.in

T. G. Evangeline
Vellore Institute of Technology, Vellore 600097, India

K. Ankit · N. S. Kumar · M. R. Sankar
IIT Tirupati, Tirupati 517506, India
e-mail: evmrs@iittp.ac.in

a plasma, CNTs require to be synthesised at very high temperatures greater than 1000 °C. The presence of plasma facilitates the synthesis of CNTs [3].

CNTs have favourable thermal conduction properties [6]. Microelectronics comprise thin film coatings of AlN over CNTs to enhance thermal conductivity that may help in thermal dissipation [7]. Ion fluids comprising lowered percentages of MWCNTs in an electrochemical cell has improved the power of a thermochemical cell up to 30% [8]. Authors have demonstrated a nine times manifold decrease in thermal resistance when MWCNTs had their surface modified using pyrenylpropylphosphonic acid [9]. Authors have shown a resultant three times higher Carnot efficiency by using MWCNTs. This required the improvement of the cell's Carnot efficiency [10]. Covalent bond-based organic molecules improved adhesion of CNTs with the interfaces and has decreased thermal resistivity by six orders [11]. Some research groups have used photo acoustic technique for calculating total thermal resistance of the system for various CNT matrices [12].

Diamond-like carbon (DLC) is amorphous carbon [13] in its form of metastability and has a high number of sp³ bonds. DLC can have up to 70% of sp³ content [14]. The toughness of DLC is improved by incorporating CNTs over DLC which can be used in practical application for imparting hardness [15].

Depositing DLC over CNTs enhances the field emission properties by improving current density and field threshold forming a potential material in the fabrication of field emission devices [16, 17]. DLC deposited over CNTs was reported as the best candidates for field emission applications since they possess combined properties of both CNTs and DLC contributing to its long lifetime, stability and performance [18].

A lot of current global research is focused on usage of CNTs as a thermal interface material (TIM). CNTs offer a poor reliability at 200 μm height with thin film Cu deposited on the former imparting a mismatch in coefficient of thermal expansion [19]. CNTs are also known degrade faster although they have excellent thermal conductivities [20]. CNTs mixed with epoxy offer about 12.2 W/mK of thermal conductivity [21]. High performance vertically aligned CNTs (VACNT) offer potential as a TIM and many companies are trying to incorporate it as heat sinks [22]. Cu foil on plasma modified VACNT offered promise as thermal interface material [23]. TiN, SiO₂, Ni and Ti have also been deposited on nearly VACNTs and thermal conductivities up to 20 W/mK have been achieved experimentally [24, 25].

It is known that DLC has good thermal conductivity. The current research focuses on the development of DLC/CNT composite by depositing a thin film of DLC over PECVD-based synthesized CNTs for a different flow rate of acetylene. These nanocomposites are evaluated using characterization tools like scanning electron (SEM), transmission electron microscope (TEM), raman spectroscopy, and nanoindentation.

This research aims at development of CNT based DLC nano sandwich which not only enhances the adhesion of CNTs, but also offers a stable thermal interface material. As they are carbon-carbon nanocomposite, thermal mismatch is also avoided as mentioned in prior literature. This method is easily scalable on a wafer and hence can be used directly while fabricating devices in semiconductor fabs. This approach is being taken up as it seems to be one of the practical and industrially viable options

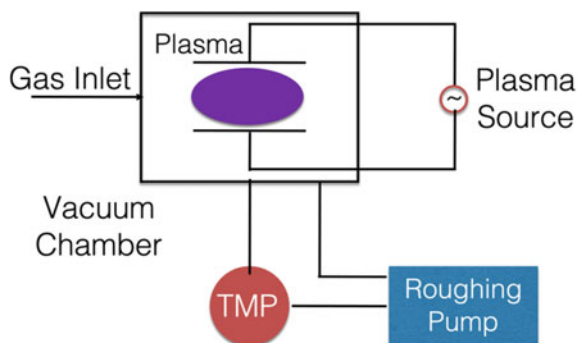
of developing efficient thermal interface materials for electronics and semiconductor applications. DLC of about 500 nm was deposited with flow rates of 300 and 100 sccm to encapsulate CNTs. The method for encapsulation of CNTs has been given in [25].

2 Experimental Details

2.1 Synthesis of CNTs

Silicon substrates of 10 mm^2 are cleaned in mild soap solution to separate impurities and then rinsed again in triple distilled water to eliminate alkali remnants of the soap solution. The wafers are rinsed in isopropyl alcohol which is subjected to a 10 min ultrasonication. The substrates undergo re-rinsing using distilled water to eliminate the alcohol traces. They are later dried in inert argon atmosphere. nickel (Ni) is sputtered using a DC magnetron on the Si substrate and acts as a catalyst for the growth of CNTs. The thickness of Ni is maintained at 5 nm using a calibrated quartz film thickness monitor. The thin layer of nickel anneals in the presence of hydrogen plasma with a flow rate of 200 sccm. The synthesis of CNTs succeeds in the nucleation process of Ni using a radiofrequency plasma-enhanced chemical vapour Deposition (RF-PECVD) (Roth & Rau, Model: HBS-500) system. The radiofrequency is set to 13.56 MHz on the system which is a typical IEEE standard. The ratio of carbon precursor to dilution gas is maintained at 1:8 during the deposition. Vertically aligned CNTs are synthesized for an $\text{C}_2\text{H}_2 / \text{H}_2$ flow rate of 25/200 sccm for a deposition time of 30 min at 600°C (Fig. 1).

Fig. 1 Schematic of the PECVD used for the experimentation



2.2 Deposition of DLC Thin Films

Diamond-like carbon is synthesized on CNT samples using the PECVD technique at 1.17×10^{-3} mbar for the C_2H_2 flow rates of 100 sccm and 300 sccm. A temperature of 350°C is maintained for the deposition of a 500 nm thin film of DLC over the CNT sample. The growth rate of DLCs has already been established and measurement techniques have been calibrated as stated in our previous experimentations [26–30].

Method of measurement of DLC. As mentioned above, in our previous experiments [26–30], the procedure was established by using time based deposition for each parameter calibrated for thickness with a spectroscopic ellipsometer (J A Woolam) using a specially developed B-Spline model which has undergone inter laboratory comparison with various other techniques at University of Chemnitz, Germany. Also, the thickness has been calibrated using the in-house surface profiler (Ametek Taly-surf) for step height measurement which has a resolution of 1 nm and is accredited by NABL. A non-contact optical profiler (Veeco NT9100) with a resolution of 0.1 nm has also been used to measure the step height for deposition based on time. These experiments have undergone hundreds of repeatability experiments to measure the deposition. The rate of deposition required to deposit DLC is noted, and 500 nm is deposited in the system. A similar comparative based methodology is also used in our previous work [24, 25].

2.3 Characterization

The synthesized 2D-nanocomposites are characterized using SEM, TEM, Raman and nano indentation. A Neon-40 Crossbeam (Carl Zeiss), FESEM was used to observe the surface morphology of the deposited 2D material. The crystal nature of the DLC/CNT composite is investigated using the Titan G2 60–300 transmission electron microscope (TEM). Raman spectroscopy (SEKI Technotron Corp, STR-300) was used to study the molecular fingerprint and determine the sp^3 and sp^2 content. Ansys software is used to model the thermal simulations.

3 Results and Discussion

3.1 Electron Microscopy

Figure 2 comprises of an SEM image of CNTs having a diameter ranging from 30 to 50 nm. Here 3.a. and 3.b. depict DLC synthesized on CNTs at a temperature of 350 °C for different C_2H_2 flow rates of 100 and 300 sccm. The high-resolution SEM image magnified up to 100Kx reveals the nature of 500 nm thick DLC layer deposited over CNTs thereby forming clusters of DLC layer on top of CNTs. A similar morphology

is observed in DLC deposited over CNTs at a C_2H_2 flow rate of 300 sccm. Hence, for different flow rates, the morphology observed is similar and shows no much variation. However, for the same contrast used for both the imaging, we can notice that there is a dense core region at the centre for the 300 sccm deposition of DLC and that is reflected in the z-contrast of SEM imaging (Fig. 3).

Figure 4a shows the high-resolution TEM image of DLC coated over CNTs where CNTs are identified by the presence of walls. The SAED pattern in Fig. 4b reveals the presence of both DLC and CNTs which are amorphous. The spots indicate that there is a good amount of crystalline DLC similar to cubic zirconia [29, 31].

Similar results can be observed for DLC deposited over CNTs at a C_2H_2 flow rate of 300 sccm. Figure 5a elucidates the high-resolution TEM image where CNTs are marked by the presence of multiple walls. Figure 5b shows the SAED pattern indicating the presence of both DLC and CNTs which are amorphous. The spots

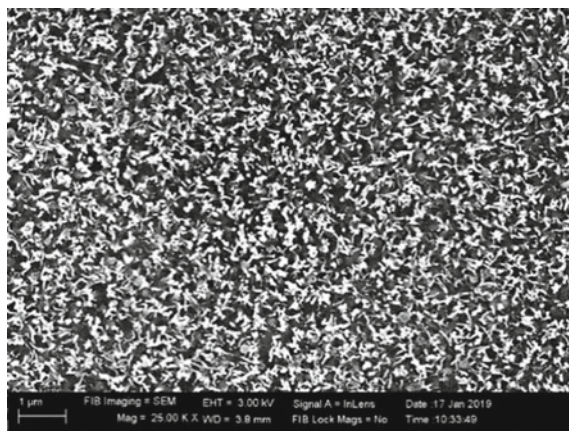


Fig. 2 SEM image of CNTs synthesized for deposition of DLC films

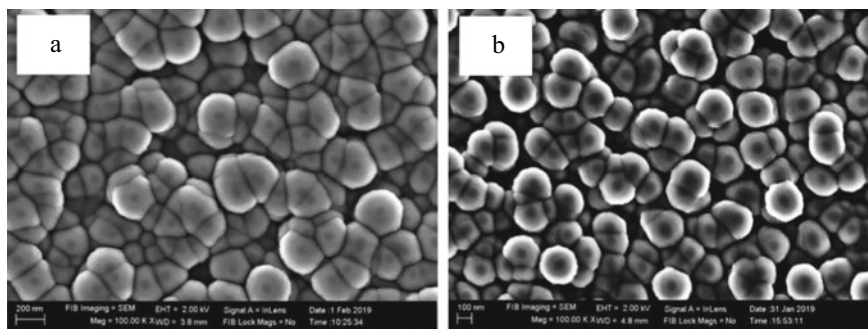


Fig. 3 a DLC coated over CNTs at 100 sccm at 350 °C b DLC coated over CNTs at 300 sccm at 350 °C

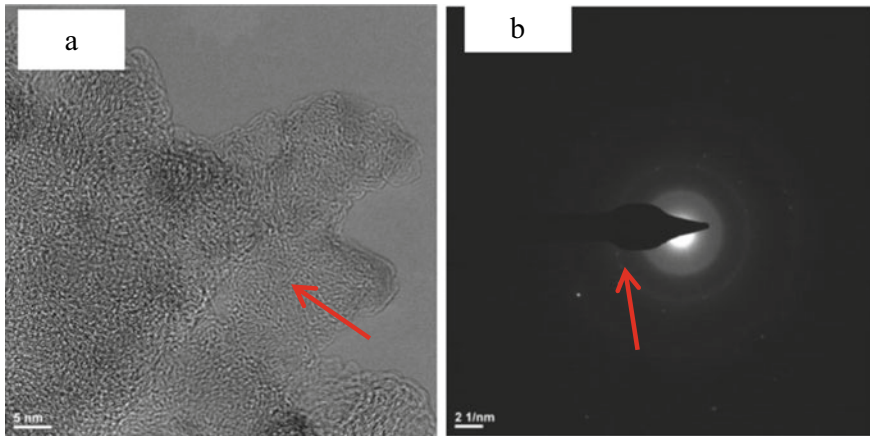


Fig. 4 **a** High-resolution TEM image of DLC coated over CNTs at 100 sccm **b** SAED of DLC coated over CNTs

represent crystalline DLC that exhibits structure similar to cubic zirconia [29, 31]. Region 1 in Fig. 5a shows the crystalline nickel from which CNTs have grown indicating the tip growth mechanism of CNT [32, 33].

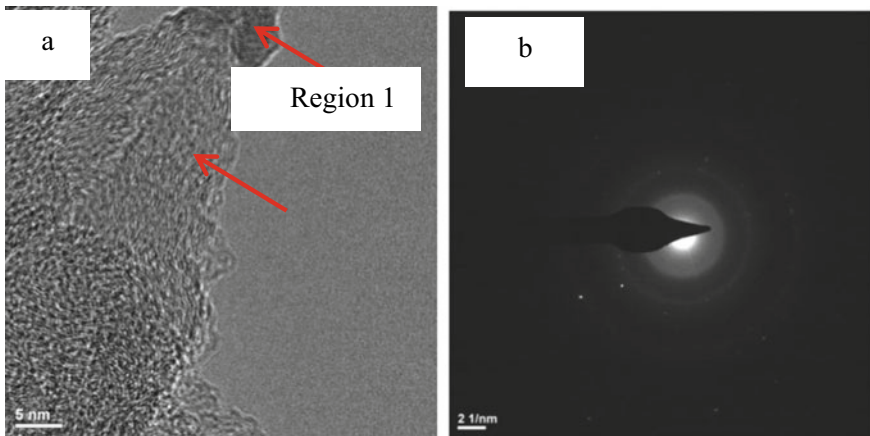
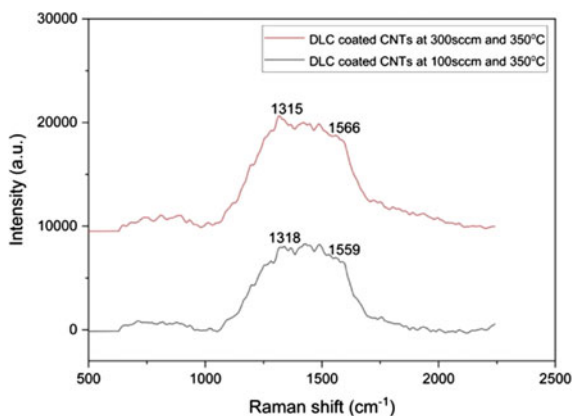


Fig. 5 **a** High-resolution TEM image of DLC coated over CNTs at 300 sccm **b** SAED of DLC coated over CNTs

3.2 Raman Spectroscopy

Carbon films exhibit similar features in their Raman spectra, hence both DLC and CNTs possess common features in the spectrum. DLC is a mixture of amorphous carbon that consists of both sp^3 and sp^2 hybridizations [34]. Figure 6 represents the Raman spectra of DLC/CNT composite for DLC deposition at 350°C for C_2H_2 flow rate at 100 sccm and 300 sccm. DLC/CNT for C_2H_2 flow rate at 100 sccm exhibiting peaks at positions 1318 cm^{-1} and 1559 cm^{-1} corresponding to D peak and G peak, respectively. DLC has an average G peak position ranging from 1581 cm^{-1} to 1600 cm^{-1} which is due to phonon confinement in graphitic domains. In this case, a decrease in G peak shift at 1559 cm^{-1} is observed owing to weaker sp^2 bonds which weaken vibrational modes [35]. Also, the G peak caters to the MWCNTs graphite frequency corresponding to the tangential vibration of carbon atoms [36]. A rise in D peak at position 1318 cm^{-1} corresponds to sp^3 hybridization due to the amorphous nature of DLC deposited over CNTs [16]. In the case of DLC deposited at 300 sccm and for a temperature of 350°C , the Raman spectra show the same characteristics features as that of DLC deposited at 100 sccm. However, it may be noted that for C_2H_2 flowrates of 100 sccm and 300 sccm, the synthesized DLC has a G peak at 1559 cm^{-1} and 1566 cm^{-1} which is close to the a-t:C type of DLC [37]. Although G peak arising at 1515 cm^{-1} corresponds to a-C: H type of DLC [37], it can be safely assumed that the crystalline graphitic content is higher in the current DLC subjected to study and closer to a-t:C DLC. It may also be noted that most of the vibrational signatures arising from the 2D material will be from DLC as it is 500 nm thick.

Fig. 6 Raman spectra of DLC coated over CNTs for C_2H_2 flow rate at 100 sccm and 300 sccm



3.3 Simulation of Heat Transfer

Computer simulations are cost effective methods to study and analyse the thermal properties of the nano sandwich in contention. Simulations are cost-effective to estimate rough thermal conductivities [38]. CNTs are proposed to be advanced material for thermal interfacing in the electronic industry [39]. Experimentally, thermoreflectance methods have been used to measure the thermal conductivity for MWCNTs and have been found to be about 13–17 W/m K [38].

Thermal flux and thermal distribution are analysed and predicted using Ansys software. The following are assumed (1) material is in steady state, (2) heat dissipates from the silicon side to DLC, (3) CNTs are vertically aligned, and (4) Homogeneity in material.

Model of the Si/CNT/DLC 2D nanomaterial was created using solidworks. Although the actual details of the composite are comprised of a Si substrate of 10 mm × 10 mm having a thickness of about 820 μm, CNTs having a length of about 800 nm.

Following are the assumptions taken in solidworks to model: (1) Substrate area: 10 mm² (2) thickness: 825 μm (3) CNT diameter: 100 nm (5) CNT height: 800 nm (6) DLC thickness: 500 nm. Although the diameter of CNT was 40 nm when measured using an SEM, the least diameter of the CNT was 100 nm when modelled using solidworks due to its limitation in modelling very low dimensional features. It can be noted that the results would be slightly coarser, however does not impede any inferences. The thermal analysis of the material considered at steady state was simulated using Ansys software. The boundary conditions fixed for the simulation were the temperature of base substrate Si area was fixed at 80 °C and CNT/DLC thin film matrix was maintained as 26 °C (sink temperature) which is roughly the average room temperature in India. Typically, semiconductors are interlocked to shut down by 80 °C. Hence, this upper cut off temperature is selected. Figure 7. shows the boundary conditions used for the simulation of the 2D-2D nanocomposite material.

R_M is the total resistance of the material, i.e. DLC. R_{CNT} is the total resistance of the CNT, and R_{Si} is the resistance of Silicon wafer.

Thermal resistance is the heat property of a material by which it resists the heat flow. This can be simplified by an equivalent resistance of individual material

$$Re_y = \frac{l_y}{A_y \lambda_y} \quad (1)$$

where

y = Numerical designation to each of the material in contention, i.e. Si, CNT and DLC.

Re = Total resistance of the material, K/W.

l = Length of respective materials, m

λ = Thermal conductivities of the materials, W/mK.

A = Area of the materials, m².

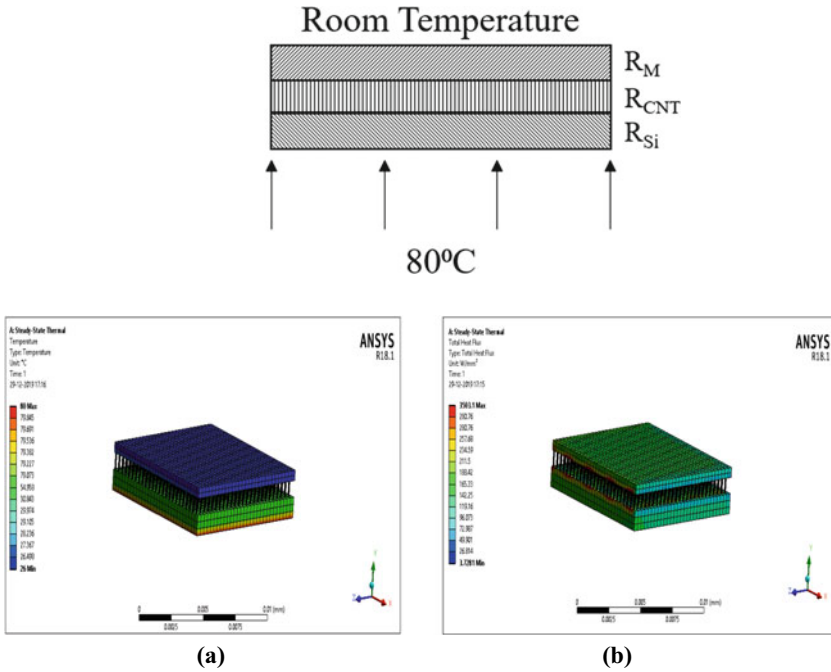


Fig. 7 Modelling of 2D nano composite for thermal simulation **a** Thermal distribution in the matrix **b** thermal flux in the Si/CNT/DLC matrix

Equivalent resistance of CNTs are given by (considered to be in parallel as they are multi-walled vertically aligned):

$$\frac{1}{Re_2} = \sum_{i=1}^n \frac{1}{Re_i} \tag{2}$$

CNT Area:

$$A_{CNT} = \pi dt \tag{3}$$

From the Raman results obtained above, the DLC coating is similar to a:t-C [37]. Hence, the approximate thermal conductivity of the DLC coating considered for calculating the equivalent resistance is 2.2 W/mK at room temperature [39, 40].

The equivalent resistance of the nanocomposite when in series is given by

$$Re_q = Re_1 + Re_2 + Re_3 \tag{4}$$

where

Re_q = Equivalent thermal resistance of the material matrix, K/W.

$t = 0.34$ nm, one carbon atom thickness.

$d =$ CNT Dia, m

$n =$ total CNTs.

Equivalent resistance of the Si/CNT/DLC matrix is determined by the aforementioned mathematical model. This is determined to be 2418.54 K/W. Thermal flux of the material matrix is determined by Ansys simulation using the calculations above which has an equivalent resistance of 73.59 W/mK.

Numerical Simulations. one dimensional heat transfer equation (without considering heat generation) is solved to obtain thermal distribution and total thermal flux of the nano material matrix of the nano sandwich. From simulations, the obtained thermal flux for this matrix is about 245 W/mm² (Fig. 7b).

4 Conclusions

DLC layer of 500 nm thickness was successfully coated over CNTs using the PECVD system at 350 °C for C₂H₂ flow rates of 100 sccm and 300 sccm. There is no substantial change in the thermal flux or dissipation with the change of flowrate, however, 300 sccm comprises larger content of amorphous carbon. SEM image highlights globular structures only encapsulating the top of the CNTs. TEM images show the polycrystalline nature of DLC with CNT in the matrix. The TEM results also give a detailed insight into the phases of the composite through SAED analysis. The Raman spectroscopy of DLC coated CNTs indicate the presence of DLC over CNTs by identifying the corresponding peaks. The Raman spectroscopy peaks provide the presence of DLC and CNTs with Raman Number for D peaks in the range of 1315–1318 cm⁻¹ and G peaks in the range of 1559–1566 cm⁻¹ showing the regime of t-aC:H and a-C:H. From a simulated thermal analysis of the material matrix, it was noted that the thermal flux is 245 W/mm² and the thermal conductivity is 73.59 W/mK.

Acknowledgements The authors thank Mr. Murugan A, Mrs. Sarmistha Dhan, and Mr. Basavaraju, CMTI for assisting in characterization.

References

1. Iijima S (1991) Helical microtubules of graphitic carbon. *Nature* 354:56–58. <https://doi.org/10.1038/354056a0>
2. Meyyappan M, Delzeit L, Cassell A, Hash D (2003) Carbon nanotube growth by PECVD: A review. *Plasma Sources Sci Technol*. <https://doi.org/10.1088/0963-0252/12/2/312>
3. Sato, Hideki & Hata K Growth of carbon nanotubes by plasma-enhanced chemical vapor deposition. *New Diam Front Carbon Technol* 16:163–176
4. Szabó A, Perri C, Csató A et al (2010) Synthesis methods of carbon nanotubes and related materials. *Materials (Basel)* 3:3092–3140. <https://doi.org/10.3390/ma3053092>

5. Yabe Y, Ohtake Y, Ishitobi T, et al (2004) Synthesis of well-aligned carbon nanotubes by radio frequency plasma enhanced CVD method. 13:1292–1295. <https://doi.org/10.1016/j.diamond.2003.11.067>
6. Hone J, Llaguno MC, Biercuk MJ et al (2002) Thermal properties of carbon nanotubes and nanotube-based materials. *Appl Phys A Mater Sci Process* 74:339–343. <https://doi.org/10.1007/s003390201277>
7. Tailleux A, Achour A, Djouadi MA et al (2012) PECVD low temperature synthesis of carbon nanotubes coated with aluminum nitride. *Surf Coatings Technol.* <https://doi.org/10.1016/j.surfcoat.2011.09.048>
8. Salazar PF, Stephens ST, Kazim AH et al (2014) Enhanced thermo-electrochemical power using carbon nanotube additives in ionic liquid redox electrolytes. *J Mater Chem A* 2:20676–20682. <https://doi.org/10.1039/c4ta04749d>
9. Taphouse JH, Smith OL, Marder SR, Cola BA (2014) A pyrenylpropyl phosphonic acid surface modifier for mitigating the thermal resistance of carbon nanotube contacts. *Adv Funct Mater* 24:465–471. <https://doi.org/10.1002/adfm.201301714>
10. Hu R, Cola BA, Haram N et al (2010) Harvesting waste thermal energy using a carbon-nanotube-based thermo-electrochemical cell. *Nano Lett* 10:838–846. <https://doi.org/10.1021/nl903267n>
11. Kaur S, Ravivikar N, Helms BA et al (2014) Enhanced thermal transport at covalently functionalized carbon nanotube array interfaces. *Nat Commun* 5:1–8. <https://doi.org/10.1038/ncomms4082>
12. Cola BA, Xu J, Cheng C, et al (2007) Photoacoustic characterization of carbon nanotube array thermal interfaces. *J Appl Phys* 101. <https://doi.org/10.1063/1.2510998>
13. Robertson J (2002) Diamond-like amorphous carbon. *Mater Sci Eng R Reports* 37:129–281. [https://doi.org/10.1016/S0927-796X\(02\)00005-0](https://doi.org/10.1016/S0927-796X(02)00005-0)
14. Casiraghi C, Ferrari AC, Robertson J (2005) Raman spectroscopy of hydrogenated amorphous carbons. *Phys Rev B-Condens Matter Mater Phys* 72:1–14. <https://doi.org/10.1103/PhysRevB.72.085401>
15. Kinoshita H, Ippai I, Sakai H, Ohmae N (2007) Synthesis and mechanical properties of carbon nanotube/diamond-like carbon composite films 16:1940–1944. <https://doi.org/10.1016/j.diamond.2007.08.004>
16. Hea F, Lib Z, Lib C, et al Enhanced Field Emission properties of Carbon Nanotubes by coating Diamond-like Carbon layer, 3–5
17. Li Y, Yan X, Wei J et al (2020) Dependence of optimum thickness of Ultrathin Diamond-like carbon coatings over carbon nanotubes on geometric field enhancement factor. *ACS Appl Electron Mater* 2:84–92. <https://doi.org/10.1021/ACSAELM.9B00561>
18. Zanin H, May PW, Hamanaka MHMO, Corat EJ (2013) Field Emission from Hybrid Diamond-like Carbon and Carbon Nanotube Composite Structures
19. Nylander A, Hansson J, Nilsson T et al (2021) Degradation of carbon nanotube array thermal interface materials through thermal aging: Effects of bonding, array height, and catalyst oxidation. *ACS Appl Mater Interfaces* 13:30992–31000. https://doi.org/10.1021/ACSAMI.1C05685/SUPPL_FILE/AMIC05685_SI_001.PDF
20. Nylander A, Hansson J, Samani MK et al (2019) Reliability investigation of a carbon nanotube array thermal interface material. *Energies* 12:1–10. <https://doi.org/10.3390/en12112080>
21. Mohamed M, Omar MN, Ishak MSA et al (2020) Comparison between CNT Thermal Interface Materials with Graphene Thermal Interface Material in Term of Thermal Conductivity. *Mater Sci Forum* 1010:160–165. <https://doi.org/10.4028/WWW.SCIENTIFIC.NET/MSF.1010.160>
22. Ping L, Hou PX, Liu C, Cheng HM (2019) Vertically aligned carbon nanotube arrays as a thermal interface material. *APL Mater* 7:020902. <https://doi.org/10.1063/1.5083868>
23. Zhang Q, Calderon A, Ebbing BR, et al (2020) Thermal properties enhancement of vertically aligned carbon nanotubes-based metal nanocomposites as thermal interface materials. *Front Mater* 7:359. <https://doi.org/10.3389/FMATS.2020.572956/BIBTEX>

24. Krishna A, Gecil Evangeline T, Aravinda LS et al (2020) Synthesis and thermal simulations of novel encapsulated CNT multifunctional thin-film based nanomaterial of SiO₂-CNT and TiN-CNT by PVD and PECVD techniques for thermal applications. *Diam Relat Mater* 109:108029. <https://doi.org/10.1016/J.DIAMOND.2020.108029>
25. Krishna A, Aravinda LS, Murugan A, et al (2021) A study on wafer scalable, industrially applicable CNT based nanocomposites of Al-CNT, Cu-CNT, Ti-CNT, and Ni-CNT as thermal interface materials synthesised by thin film techniques. *Surf Coatings Technol* 127926. <https://doi.org/10.1016/J.SURFCOAT.2021.127926>
26. Varade A, Niranjan Reddy K, Sasen D, et al (2014) Detailed Raman study of DLC coating on Si (100) made by RF-PECVD. In: *Procedia Engineering*
27. Varade A, Krishna A, Reddy KN et al (2014) Diamond-like carbon coating made by RF plasma enhanced chemical vapour deposition for protective antireflective coatings on Germanium. *Procedia Mater Sci* 5:1015–1019. <https://doi.org/10.1016/j.mspro.2014.07.390>
28. Niranjan Reddy K, Varade A, Krishna A, et al (2014) Double side coating of DLC on silicon by RF-PECVD for AR application. In: *Procedia Engineering*
29. Ankit K, Varade A, Reddy N et al (2017) Synthesis of high hardness, low COF diamond-like carbon using RF-PECVD at room temperature and evaluating its structure using electron microscopy. *Diam Relat Mater* 80:108–112. <https://doi.org/10.1016/j.diamond.2017.09.005>
30. Ankit K, Varade A, Niranjan Reddy K et al (2017) Synthesis of high hardness IR optical coating using diamond-like carbon by PECVD at room temperature. *Diam Relat Mater* 78:39–43. <https://doi.org/10.1016/j.diamond.2017.07.008>
31. Kozlov ME, Yase K, Minami N et al (1996) Observation of diamond crystallites in thin films prepared by laser ablation of hard fullerene-based carbon. *J Phys D Appl Phys* 29:929–933. <https://doi.org/10.1088/0022-3727/29/3/062>
32. Sinnott SB, Andrews R, Qian D et al (1999) Model of carbon nanotube growth through chemical vapor deposition. *Chem Phys Lett* 315:25–30. [https://doi.org/10.1016/S0009-2614\(99\)01216-6](https://doi.org/10.1016/S0009-2614(99)01216-6)
33. Danafar F, Fakhru'l-Razi A, Salleh MAM, Biak DRA (2009) Fluidized bed catalytic chemical vapor deposition synthesis of carbon nanotubes-A review. *Chem Eng J* 155:37–48. <https://doi.org/10.1016/j.cej.2009.07.052>
34. Ferrari AC, Robertson J (2004) Raman spectroscopy of amorphous, nanostructured, diamond like carbon, and nanodiamond. *Philos Trans R Soc, A* 362:2477–2512. <https://doi.org/10.1098/rsta.2004.1452>
35. Ferrari AC (2002) Determination of bonding in diamond-like carbon by Raman spectroscopy. *Diam Relat Mater* 11:1053–1061. [https://doi.org/10.1016/S0925-9635\(01\)00730-0](https://doi.org/10.1016/S0925-9635(01)00730-0)
36. Costa S, Borowiak-Palen E, Kruszyńska M et al (2008) Characterization of carbon nanotubes by Raman spectroscopy. *Mater Sci* 26:1–9. <https://doi.org/10.1155/2010/603978>
37. S. Kurtz, Tallant, R. Simpson, K. McCarty, L Bemardez DD and PM (1996) Diamond and Diamond-Like Carbon Films. *Adv Electronic Appl* 46
38. Kumaneck B, Janas D (2019) Thermal conductivity of carbon nanotube networks: a review. *J Mater Sci* 54:7397–7427. <https://doi.org/10.1007/s10853-019-03368-0>
39. Panzer MA, Zhang G, Mann D, et al (2008) Thermal properties of metal-coated vertically aligned single-wall nanotube arrays. *J Heat Transfer* 130. <https://doi.org/10.1115/1.2885159>
40. Shamsa M, Liu WL, Balandin AA et al (2006) Thermal conductivity of diamond-like carbon films. *Appl Phys Lett* 89:1–3. <https://doi.org/10.1063/1.2362601>

Design and Analysis of High Sensitivity MEMS Microphone



Jins Abraham, Harsha Sanjeev, and K. Nisarga

1 Introduction

The condenser microphones based on MEMS technology have been used widely as compared to the piezoelectric and piezoresistive microphones in many applications such as mobile phones, wireless sensor networks because of their good performance in audio data quality, space efficiency, flat frequency response and minimal noise level.

The sensitivity of microphone decreases as the area of the microphone decreases. The challenge here is to increase the sensitivity by retaining the miniature size. Hence, there is scope for increasing the sensitivity and thus the performance of the microphone by choosing a suitable material and a relevant design with limited area [1].

It is reported that for capacitive-type MEMS microphones perforated back plate is used in most of the condenser microphones. Fabrication process of capacitive microphone is long, complex and costly. Creating holes on back chamber from the backside of a wafer by KOH etching is difficult process [2].

In spite of its advantages as listed in [2], there are problems of high voltage consumption and reduction in sensitivity due to stiff diaphragm. Different varieties of diaphragm designs, such as perforated diaphragm, corrugated diaphragms, coupled and slotted diaphragms have been investigated to have better sensitivity [3–5]. In this

J. Abraham
Karunya University, Coimbatore, Tamil Nadu, India

H. Sanjeev · K. Nisarga (✉)
Centre for Sensors, Vision Technology and Controls, Central Manufacturing Technology Institute,
Bengaluru, Karnataka, India
e-mail: nisargakrishna12@gmail.com

H. Sanjeev
e-mail: harsha@cmti.res.in

paper, much attribute is given to the design aspect in order to increase the sensing ability of the microphone.

The stiffness of the diaphragm can be decreased by incorporating the slots around the diaphragm. It promotes increased diaphragm deflection compared to the ones without slot, which results in the increase of mechanical sensitivity of membrane.

Various models of condenser microphones are fabricated by processing two separate wafers and then bonding them with each other. However, Silicon on Insulator (SoI) wafers would offer the ability to create the microphone on one wafer and solves positioning problems.

In this work, literature survey has been conducted with respect to capacitive-type microphones, and the various parameters are identified which contribute to the sensitivity of the microphone. The main parameters identified are materials, design and construction process. The focal materials used for the diaphragm construction are silicon, polysilicon, aluminum and gold-plated silicon diaphragms. On considering the three important factors such as density, Young's modulus and tensile strength of the material, Silicon is chosen as the most suitable material for expected performance and fabrication methods.

From the literature review for the required performance and sensitivity, silicon of density (ρ) of 2330 kg/m³, Young's Modulus (E) 129-187GPa and tensile strength (σ_p) of 4000MPa are considered as the most suitable material for the fabrication [6]. Silicon wafer is most suitable material for fabrication of MEMS components. It is the primary material for monolithic integration of integrated circuits and applications such as sensors [7, 8]. Single crystal silicon is widely used as semiconductor material in MEMS technology as substrate because of its excellent mechanical stability and its efficiency to associate sensing elements and electronics on same substrate [9].

Many researchers used different construction techniques and design considerations for designing the diaphragm which will contribute to their own specific needs, For our work, sensitivity is the most important parameter, and so the diaphragms with slots are being used. The sensitivity of a microphone is the electrical response at its output to a given standard acoustic input. This is expressed as the ratio of the input pressure to the electrical output. A microphone with a higher sensitivity value has a higher level output for a fixed acoustic input than a microphone with a lower sensitivity value. A microphone's sensitivity tolerance indicates the range of sensitivity for any given individual microphone. Therefore, for near field applications such as in stethoscope, high sensitivity returns good quality output. So, sensitivity is considered as the important parameter in this work.

The sensitivity factor is given much importance in comparison with other factors in this study due to the fact that in spite of keeping the other factors constant with reference to the existing microphones, the output efficiency of the microphone majorly depends on the sensitivity. The primary application that is targeted for this development is to incorporate this microphone in a stethoscope. As the sensitivity increases, the output efficiency increases. This helps detecting feeble signals which are important in medical diagnosis.

Rigidity in diaphragm is caused by residual stress in the material. So, the membrane of the diaphragm cannot deflect easily in low sound pressure. The residual stress in single crystalline silicon is zero [10].

According to the specifications of the proposed microphone that is, thickness of the diaphragm as $0.75 \mu\text{m}$, a diameter of $800 \mu\text{m}$ and c-type slots of $0.5 \mu\text{m}$. The minimum sensitivity of the microphone should approximately be 1.8 mV/Pa , in order to use it in the stethoscope application and to sense internal body sounds. The stethoscope should be capable of sensing the frequency of 30 kHz [11]. The objective of the present work is to overcome the disadvantages of the existing designs such as low sensitivity, interference and high voltage consumption, complex fabrication techniques and to develop condenser microphone that utilizes slotted diaphragm to increase the sensitivity.

By incorporating slots in the diaphragm, microphone's performance could be uplifted. The costly fabrication process can be made comparatively inexpensive by making holes in the back plate. Fabrication can be made easier by using silicon as wafer.

2 Design

The miniature size of MEMS microphones are affected by reduced sensitivity as a result of decrease in area [as indicated in Reference 2]. The diaphragm sensitivity can be optimized by the choice of proper structure variants in terms of dimensions [11, 12].

The deflection of diaphragm is given by,

$$(x, y) \propto \frac{A_{\text{eff}}}{\sigma h} \quad (1)$$

In the above equation, A_{eff} , σ , h are effective area, thickness and stress of the diaphragm. The above relation shows that, sensitivity of microphone is proportional to large area, thin and stress-free diaphragm. The miniaturization of the device will cause the reduction in effective area. But increasing the area of diaphragm limits the fabrication process. The response of the diaphragm, as thickness is reduced will be controlled by the diaphragm stress. The design of the microphone components and its operation principle is described along with the theoretical performance. In addition, analytical models to estimate the stiffness, deflection and first resonant frequency of the circular diaphragm are developed. Finally, the capacitance shift, output voltage and noise of the MEMS microphone are obtained.

The MEMS microphone is formed by a circular polysilicon diaphragm that is located between two polysilicon plates with a hexagonal array of holes. The substrate below the polysilicon diaphragm of the microphone must be etched to allow the application of the sound pressure to the diaphragm [13]. This pressure will cause diaphragm deflections that will be converted into electrical signals (i.e. capacitance

variations between diaphragm and dual back plates). The diaphragm and dual back plates are the capacitor electrodes, and using a bias voltage, the capacitance shifts can be measured [14].

Based on the above described principle, the substrate material is chosen as Silicon with 6 inch diameter which is available off the shelf, and the thickness of this substrate is approximately 525 μm . For the design considerations, since the microphone is to be embedded into a stethoscope, the overall dimension is restricted below 1 mm. The thickness of the diaphragm is considered so that maximum deflection can be obtained for the applied pressure. The slots are designated fixed positions and orientation depending on the stress-free output required.

The chosen single crystal silicon has induced internal stress [15].

Stress is given by,

$$S_m = \frac{A_{\text{eff}}}{K_{\text{eq}}} \quad (2)$$

where A_{eff} and K_{eq} are the diaphragm's effective area and the equivalent spring constant. From the Eq. 2 we can infer that, mechanical sensitivity of microphone depends on spring constant. In order to decrease the spring constant, diaphragm's stiffness should be decreased. To bring down the stiffness of the diaphragm, C-type single slots are incorporated on the diaphragm design initially. Further, the design is analyzed which resulted in insufficient sensitivity for the stethoscope application.

Various experiments have been conducted to arrive at the appropriate sensitivity for the proposed microphone.

The slots incorporated and the diameter of the diaphragm are mentioned. The diaphragm is designed using MEMS technology by decreasing the area and not compromising on the sensitivity.

The pull-in voltage of the condenser microphone is given by the equation.

$$V_{\text{pi}} = \sqrt{\frac{8K_{\text{eq}}d_o^3}{27\varepsilon A_{\text{eff}}}} \quad (3)$$

Where ε is the permittivity of air and d_o is the distance between the back plates and diaphragm and back plate initially.

It is clear from the equation that, by decreasing the equivalent spring constant of the diaphragm, the pull-in voltage will be reduced.

The frequency of resonance for the condenser microphone is defined as:

$$f_{\text{res}} = \frac{1}{2\pi} \sqrt{\frac{K_{\text{eq}}}{m}} \quad (4)$$

Where m is the diaphragm mass and K_{eq} is spring constant.

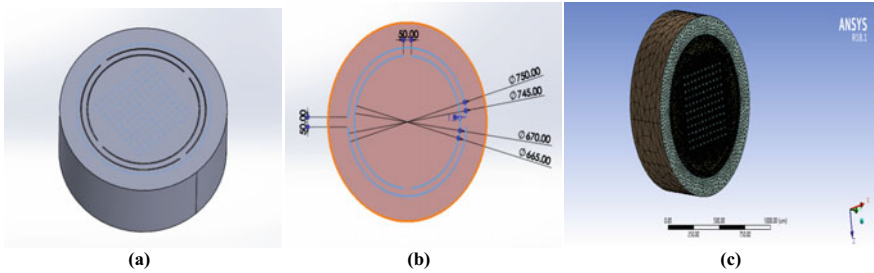


Fig. 1 Design and dimensions of diaphragm with meshed model **a** Schematic of the proposed diaphragm, **b** measures of slots and diameter of diaphragm and **c** meshed model of microphone

From these equations, it can be said that there is a relation between pull-in voltage and resonance frequency. For designing a microphone, the resonant frequency should be in the range of heart auscultations [16-60] SPL.

The efficiency of this microphone depends on the slotted diaphragm to reduce rigidity of the diaphragm [15]. In comparison with existing condenser microphones, the complex and costly manufacturing process can be avoided, and the sensitivity of microphone is increased. Isometric view of proposed slotted microphone is shown in Fig. 1a.

The sacrificial and diaphragm layers additional deposition is avoided by use of Silicon wafer to make the fabrication easier. Usage of one mask is sufficient to pattern the diaphragm. The performance of the microphone depends on the size of the diaphragm, slots, air gap thickness and area of acoustic holes.

3 Methodology

Static structural analysis is done on microphone using ANSYS workbench, and the force is applied on the diaphragm of the microphone for different steps of pressure.

It is identified that the deflection for simple clamped circular diaphragm is 13.33 pm for pressure of 2 Pa, whereas for the same pressure, using slotted diaphragm, the deflection is 2.3561 μm , which is very much greater than the simple clamped circular diaphragm. Hence, the introduction of slots in the diaphragm resulted in desired outcome of higher deflection.

4 Analysis

The required specifications of the microphone are generated using ANSYS workbench 18.1 with static structural module.

The parameters to be identified are diaphragm deflection, stress distribution, capacitance and resonant frequency. For proper analysis of a device using finite element analysis (FEA), much care should be taken while meshing. In this analysis, microphone diaphragm is meshed in tetrahedral meshing, face meshing and edge sizing is used.

The different steps used in FEA, such as assigning the material to the geometry, verifying the coordinates and boundary conditions are applied. The connections are given as bonded contacts from diaphragm to Silicon oxide layer and from Silicon oxide layer to back plate of the microphone. The meshed body is shown in Fig. 1c.

A. Diaphragm deflection

Substrate and the back plate are fixed, and free moving condition is given to the diaphragm. Tabular data of pressure from 0.2 Pa to maximum pressure of 2 Pa is given. The deflection of diaphragm to sound pressure is calculated with use of finite element method (FEM). Figures 2 and 3 show the diaphragm deflection versus applied pressure (2 Pa) for the clamped diaphragm, and the maximum central deflection is 13.33 pm.

In Table 1, the deflections found across the diaphragm with and without slots are shown. No deflection is observed when no pressure is applied. The reference data is taken keeping the input pressure 0 F. The pressure is applied non-periodically to check the variations in deformation in short range and in long range. It is inferred that, deflection is more in presence of slots, and it is comparatively low in case of non-corrugated diaphragm.

Figure 4 shows the directional deformation along the y-axis. The deformation varies depending upon the input pressure. For the maximum force applied of 2 Pa, the maximum deformation is 2.3561 μm .

The diaphragm deflection is maximized by the usage of slots on the diaphragm. It can be seen from Fig. 5, that the deflection of diaphragm without slot is not distributed

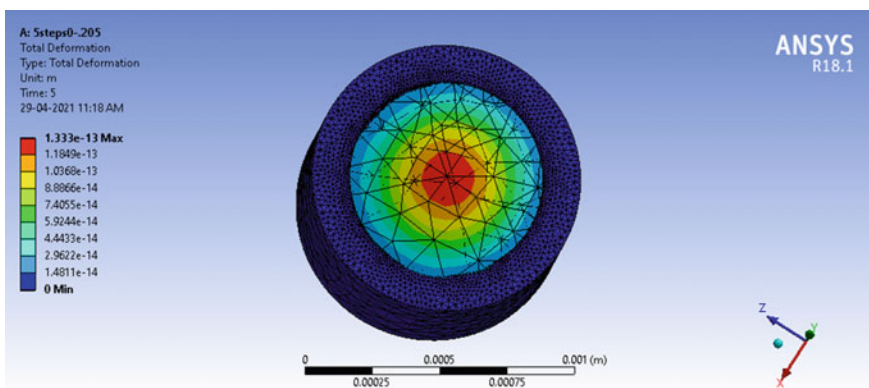


Fig. 2 Deflection of clamped simple diaphragm

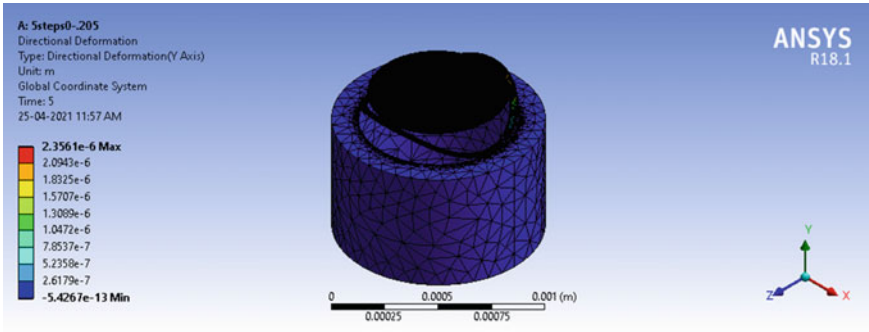


Fig. 3 Diaphragm deflected view (up-scaled)

Table 1 Comparison of deflection with and without slots

Pressure steps (Pa)	Deformation (calculated) (μm)	Deformation (μm)	Deformation (without slots) (μm)
0	0	0	0
2.0e-004	2.3e-4	2.365e-4	2.3e-21
6.3e-003	2.24e-3	7.4508e-3	7.45e-20
6.3e-002	7.24e-2	7.4508e-2	7.45e-19
0.199	0.229	0.23535	2.3e-14
1.9922	2.29	2.3561	2.35e-13

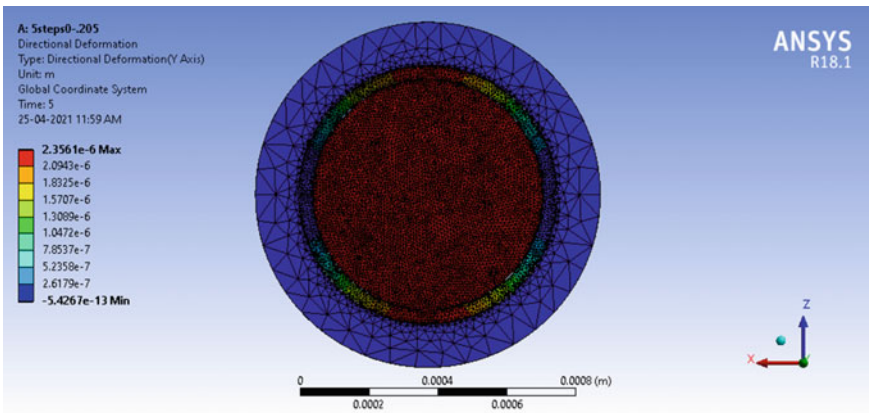


Fig. 4 Diaphragm deflection top view

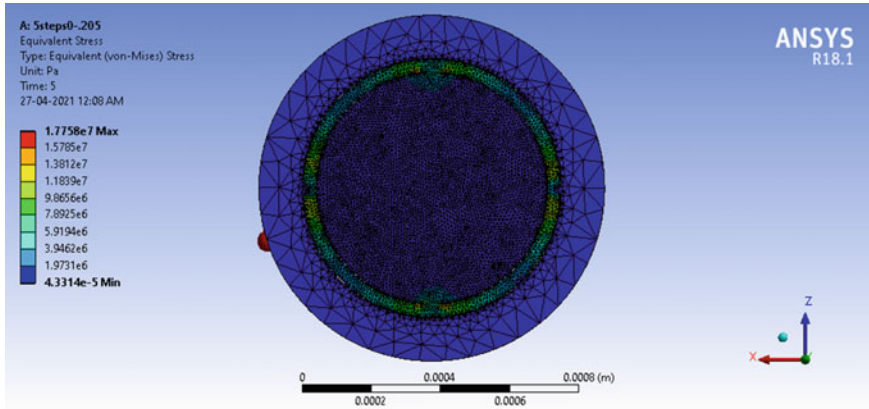


Fig. 5 Stress distribution in the diaphragm

equally and just a small part of the center is deflected. Diaphragm with slots causes it to deflect uniformly.

The mechanical sensitivity of a clamped microphone is 0.017 mV/Pa as reported in [16]. However, the mechanical sensitivity of the proposed microphone is 1.16 mV/Pa. The maximum sound pressure levels are 20 dB or 2.25 Pa. Therefore, the proposed structure meets the specification requirement for the stethoscope application.

B. Stress distribution

Figure 5 shows the distribution of stress for applied pressure of 2 Pa for simple clamped and proposed diaphragm. The stress is distributed uniformly on the proposed diaphragm. It shows that proposed diaphragm has uniform deflection too. The maximum stress induced in the diaphragm of the proposed microphone is 17.758 MPa.

C. Capacitance

Capacitance is the main output parameter of a capacitive-based MEMS microphone.

Stray capacitance is given by,

$$c = \frac{0.00885\epsilon\epsilon_0}{d} pF \tag{5}$$

The stray capacitance is found to be 1.17e-12 farads from Eq. (5). This value does not contribute to output reading. The capacitance and the deflection are proportional as per the governing Eq. 5, and the obtained values of deflection are used to find the output capacitance.

The values obtained from the capacitance analysis are in Pico farads and are tabulated in the Table 2. It can be seen that, with the increase in pressure, there is an increase in deformation and hence the capacitance.

Table 2 Capacitance with respect to deflection

Pressure (Pa)	Deformation (μm)	Output capacitance (pF)
0.080	0.55495	1.51
0.105	0.72834	1.66
0.130	0.91076	1.85
0.155	1.07520	2.06
0.180	1.24860	2.35
0.205	1.42200	2.72

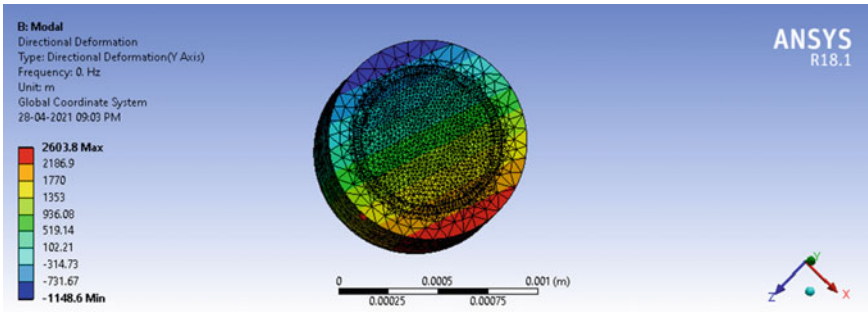


Fig. 6 Modal analysis of diaphragm

D. Resonant frequency

Substrate and the back plate are fixed, modal analysis is done without applying any pressure, and the maximum resonance frequency of the sensor is found.

Resonant frequency is the frequency at which the diaphragm tends to deflects at higher amplitude. These values are attained from nodal analysis in ANSYS workbench.

From the analysis, the maximum frequency is found to be 2.6 kHz, while the theoretical calculations made by substituting the mass of diaphragm is 2.9682×10^{-7} kg in Eq. 4, shows that the resonant frequency is 6.8 kHz. From this comparison, we understand that the working frequency is less than the resonant frequency, and the design is suitable for using in stethoscope applications.

5 Results and Discussion

The deflection analysis of simple clamped circular diaphragm microphone and slotted diaphragm microphone are done using ANSYS workbench.

Sensitivity is 1.16 mV/Pa, obtained by calculating the slope of the pressure v/s deflection plot. For each steps of pressure, the deflection of the microphone is

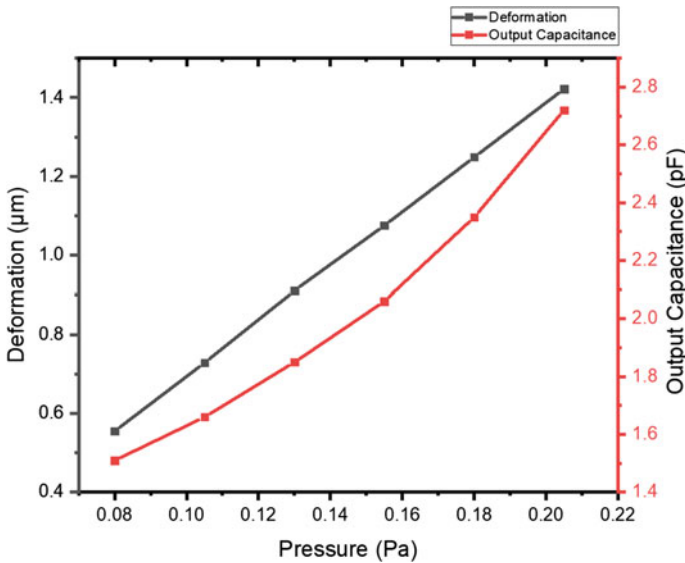


Fig. 7 Plot of deformation and capacitance for applied pressure

following a linear path which suggests the reliability of the preferred design over conventional designs.

Stress analysis is conducted on the proposed diaphragm and the maximum stress induced at the joints is found to be 17.758 MPa. The induced stress does not make any damage to the structure since the stress induced is much less than the maximum tensile stress of the silicon.

The capacitance and the deflection are proportional as per the governing equation, and the obtained value of deflection is used to find the output capacitance. The output capacitance is proportional to the applied pressure, and the variation is plotted in the pressure vs. deformation plot.

The resonant frequency for slotted diaphragm is 6.8 kHz. From the nodal analysis, the maximum frequency range is 2.6 kHz. This is because the smaller diaphragm microphones are able to produce high frequency than the one with large diaphragms. For the proper working of the microphone, the resonant frequency (6.8 kHz) should be more than the working range of the microphone (2.6 kHz). This is confirmed by the nodal analysis and hence the design works for the high sensitivity microphone.

6 Conclusion

In this work, a MEMS capacitive-based microphone is successfully designed, and analysis is done using ANSYS workbench.

The slots in the diaphragm reduce the rigidity of diaphragm. It also makes the diaphragm to deflect uniformly. Silicon is selected for the diaphragm material because of its property of low stress. Miniature size, low power consumption and high sensitivity can be achieved by introducing slots on diaphragm. The deflection is found to be $2.35e^{-13}$ in case of non-slotted diaphragm and $2.3561 \mu\text{m}$ in case of slotted diaphragm. The structure has a diaphragm thickness of $0.75 \mu\text{m}$ and diaphragm diameter of $800 \mu\text{m}$. The material used in the back plate of diaphragm is Silicon nitride (Si_3N_4) and Silicon dioxide (SiO_2) acts as an isolation layer.

The designed slotted diaphragm-based condenser microphone has sensitivity of 1.16 mV/Pa . Capacitance is 2.72 pF , for maximum applied pressure of 2 Pa . The output is amplified for read out. On analysis, it is found that working frequency (6.8 kHz) is much less than the theoretical resonant frequency (2.6 kHz). Hence, the device is capable of working for the desired specifications.

The microphone proposed has advantages such as high sensitivity and has better performance. From the literature [17] and from the analysis results, for a fixed pressure of 2 Pa , the output is $6.22e^{-15} \text{ F}$. The performance of the proposed MEMS microphone with deflection of 2.3561 and the output capacitance is 2.72 pF , which conveys the MEMS microphone is 26% better than the conventional microphones in terms of acoustic signal applied to the electric signal incurred.

Acknowledgements The authors would like to thank SVTC department of Central Manufacturing Technology Institute (CMTI), Bengaluru, for providing the facilities for accomplishment of the project.

References

1. A treatise on electricity and magnetism, 3rd edn, vol 2. Oxford, Clarendon, 1892, pp 68–73
2. AzizollahGanji B, YeopMajlis B (2009) Design and fabrication of a new MEMS capacitive microphone using a perforated aluminum diaphragm. *Sens Actuators A* 149:29–37
3. Jerman JH (1990) The fabrication and use of micro machined corrugated silicon diaphragms. In: Proceedings of the 5th international conference on solid state sensors and actuators and euro sensors, vol 23, pp 988–992
4. Gharaei H, Koohsorkhi J, Saniei F, Abbasi A (2013) Design and characterization of a high sensitive MEMS capacitive microphone using coupled membrane structure. In: First RSI/ISM international conference robotics and mechatronics (ICRoM), pp 374–377
5. Yang C (2010) The sensitivity analysis of a MEMS microphone with different membrane diameters. *J Mar Sci Technol* 18:790–796
6. Scheeper PR, Nordstrand B, Gullov JO, Liu B, Clausen T, Midjord L (2003) A new measurement microphone based on MEMS technology. *J Micro Electro Mech Syst* 6:880–891
7. Tajima T, Nishiguchi T, Chiba S, Morita A, Abe M (2003) High performance ultra-small single crystalline silicon microphone of an integrated structure. *MicroelectronEng* 67:508–519
8. Iguchi Y, Goto M, Iwaki M, Ando A, Tanioka K et al (2007) Silicon microphone with wide frequency range and high linearity. *Sens Actuators A* 135:420–425
9. Young M (1989) The technical writer's handbook. University Science, Mill Valley, CA
10. Weigold JW, Brosnihan TJ, Bergeron J, Zhang X (2006) A MEMS condenser microphone for consumer applications. In: 19th IEEE international conference on istanbul, micro electro mechanical systems, pp 86–89

11. Kimori N, Kumai Y, Hishinuma S, Ikehara T (2013) Ten-micrometerthick silicon diaphragm used in condenser microphone. *Key Eng Mater Trans Tech Publ* 538:277–280
12. Kiihama“ki J, Dekker J, Pekko P, Kattelus H, Sillanpa“a“ T, Mattila T (2004) A new concept for fabricating SOI MEMS devices. *MicrosystTechnol* 10:346–350
13. Kim BH, Lee HS (2015) Acoustical-thermal noise in a capacitive MEMS microphone. *IEEE Sens J* 15:6853–6860
14. Ganji BA, Sedaghat SB, Roncaglia A, Belsito L, Ansari R (2018) Design, modeling, and fabrication of crab-shape capacitive microphone using silicon-on-isolator wafer. *J Micro Nanolithogr MEMS MOEMS* 17:015002
15. Fuldner M, Dehe A, Lerch R (2005) Analytical analysis and finite element simulation of advanced membranes for silicon microphones. *IEEE Sens J* 5:857–863
16. Sedaghat SB, Ganji BA, Ansari R (2018) Design and modeling of a frog-shape MEMS capacitive microphone using SOI technology. *MicrosystTechnol* 24:1061–1070
17. Walser S, Siegel, Winter M, Feiertag G, Loibl M, Leidl A (2016) MEMS microphones with narrow sensitivity distribution. *Sens Actuators A Phys* 247:663–670. <https://www.cuidevices.com/blog/comparing-mems-and-electret-condenser-microphones>

Dependency of Machining Forces on Process Parameters During Sustainable MQL-Based Micro-milling of D2 Steel



Suman Saha, Shaubik Sikdar, A. Sravan Kumar, Sankha Deb, and P. P. Bandyopadhyay

1 Introduction

Machining is one type of subtractive manufacturing process, where material is gradually sheared-off from the workpiece in the form of chips using a well-defined cutting tool in order to impart pre-defined shape, size, and finish. End milling is one type of machining process, where the workpiece is fed in a pre-defined trajectory against a rotating cylindrical cutter. Based on the diameter of the cutter, end milling can be categorized as macro-scale, meso-scale, and micro-scale operation. Micro-end milling cutters typically have diameter 1.0 mm or below, with a minimum of 0.03 mm diameter cutter fabricated till now [1]. Although various researchers attempted to fabricate three and four flute cutters [2], commercial micro-mills usually come in the diameter range of 100–1000 μm , mostly two-flutes and coated. Mechanical micro-milling process can productively fabricate micro-features like slots, pockets, pillars, fins, webs, dimples, etc., on a large variety of base material requiring minimum effort.

In micro-milling, the uncut chip thickness remains very low, typically in the order of 0.5–6.0 μm (maximum values, theoretically same with the feed per flute). The curvature radius at the principal cutting edge (called edge radius, r_e) also remains in the similar range, typically within 1.0–4.0 μm . Thus, the material removal is essentially accomplished by the rounded cutting edge, rather than a perfectly sharp

S. Saha (✉) · A. S. Kumar · S. Deb · P. P. Bandyopadhyay
Department of Mechanical Engineering, IIT Kharagpur, Kharagpur, West Bengal, India
e-mail: ss.me.kgp@iitkgp.ac.in

S. Deb
e-mail: sankha.deb@mech.iitkgp.ac.in

P. P. Bandyopadhyay
e-mail: ppb@mech.iitkgp.ac.in

S. Sikdar
Department of Mechanical Engineering, Techno India University, Kolkatta, West Bengal, India

edge. As a conventional machining process, material removal in micro-milling is accomplished by deforming the workpiece material by expending mechanical energy. Cutting forces thus arise across all possible directions owing to the existence of relative velocities under solid-to-solid tool-workpiece contact. Force magnitude in different directions depends on the workpiece material, cutter geometry, process parameters, lubrication, cutting zone temperature, tribological condition, etc.

AISI D2 steel offers high abrasion and wear resistant owing to the presence of high chromium and carbon, and thus, it is used for making micro-die, micro-punch, etc. [3]. However, high chromium and carbon content reduce the machinability of this particular steel. In macro-scale cutting, Sharma and Sidhu [4] highlighted that application of small quantity lubricant (near-dry machining) can reasonably overcome difficulty in machining of the D2 steel. Sharma et al. [5] also highlighted that application of nanofluids in minimum quantity lubrication (MQL) helps improving machinability by controlling cutting temperature.

Micro-milling performances of D2 steel, particularly cutting force related aspects, are not been explored in details. During micro-milling of AISI D2 steel using two-flute 200 μm diameter helical cutters, Jin et al. [6] observed an increasing tendency of forces with the increase in feed per flute. Babu et al. [7] highlighted that dead metal zone formation ahead of the cutting edge can significantly increase the cutting forces, and a higher feed of the order of 5 $\mu\text{m}/\text{flute}$ was suggested during micro-milling of D2 steel.

Objective of this article is to analyze the measured cutting forces to understand their dependency on the process parameters during minimum quantity lubrication (MQL)-based sustainable micro-milling of AISI D2 steel using 0.5 mm diameter micro-end milling cutters.

2 Experimental Details

As-procured AISI D2 steel samples of size $20 \times 20 \times 10 \text{ mm}^3$ are first made flat by end milling using a 6.0 mm diameter end milling cutter. Flatness of the top surface is essential in order to achieve a constant depth of cut for further micro-scale operation on this sample. An island of 5.0 mm wide, 2 mm height, and 20 mm long is also made by removing material from sides using the same end milling operation (Fig. 1). Without altering the gripping, full-immersion straight slots are micro-milled on this island in transverse direction. Thus, each micro-slot is of 5.0 mm long with width equals to micro-mill diameter (0.5 mm). Entire micro-milling operation is carried out on a high-precision CNC micro-machining centre (Kern-Evo, KERN microtechnik, Germany).

Commercial micro-end milling cutters (AXIS-Microtools, India) of 500 μm diameter with flat-end are employed for cutting micro-slots. Such micro-mills consist of two helical flutes located at 180° apart with a helix angle of 30° . The tools are made of tungsten carbide with TiAlN coating. As shown in Fig. 1, average edge radius of the tool is 1.3 μm . As summarized in Table 1, cutting speed is varied in four levels,

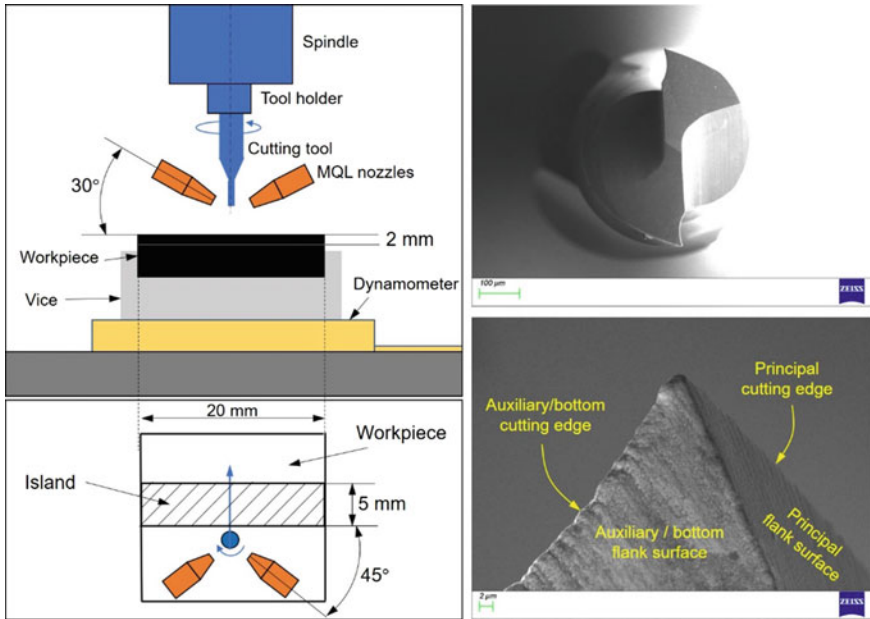


Fig. 1 Experimental setup and SEM images of the micro-milling tool employed for experimentation

from 15,000 rpm to 45,000 rpm with 10,000 rpm interval. The corresponding cutting velocity lies in the range of 24–71 m/min. Feed per flute is also varied from 0.5 to 1.5 $\mu\text{m}/\text{flute}$. Depth of cut is, however, kept constant at 50 μm . An eco-friendly (biodegradable) cutting fluid UNILUBE 2032 is also supplied at the cutting zone at a very low-flow rate (6 mL/h) using two nozzles following a sustainable cutting fluid delivery technique called minimum quantity lubrication (MQL) [8].

During the micro-milling operation, instantaneous cutting forces in three mutually perpendicular directions are measured using a piezoelectric dynamometer (Kistler

Table 1 Micro-milling operating summary

Workpiece material	D2 stainless steel
Micro-milling tool material	TiAlN-coated tungsten carbide
Micro-milled feature	Full-immersion straight slot
Tool features	500 μm diameter two-flutes flat-end
Edge radius	1.3 μm
Spindle speed	15 k, 25 k, 35 k, and 45 k rpm
Feed per flute	0.5, 1.0, 1.5 $\mu\text{m}/\text{flute}$
Axial depth of cut	50 μm
Lubrication	Sustainable MQL at 6 mL/h

9254) set under the work holding device. Force data are gathered through three separate charge amplifiers and one oscilloscope, and the same are further processed through MATLAB software to retrieve average maximum and RMS force values. Generated micro-chips are also collected using carbon tapes, and the same are observed a scanning electron microscope (SEM) (EVO 18, ZEISS, Germany).

3 Results and Discussion

Micro-milling is characteristically an intermittent type cutting process where a particular edge repeatedly engages and disengages with the workpiece in every tool rotation. In full-immersion straight slot micro-milling, each edge remains in physical contact with workpiece for only half of the rotation. During this 180° contact duration, uncut chip thickness gradually increases from zero (at the beginning of engagement) to maximum (after 90° rotation) leading to the generation of the up-milling (conventional milling) phase. Down-milling (climb milling) begins with the maximum uncut chip thickness; however, the same gradually reduces to zero within a quarter-cycle. The maximum uncut chip thickness is, however, same with the set feed per flute in absence of tool deflection or run-out.

As the chip load changes with the engagement angle, the cutting forces also vary. It is thus pertinent to consider both root means square (RMS) and maximum values of the developed forces. The maximum value of the force components determines the cutting power requirement. The cutting power, in turn, controls the limiting values of the process parameters based on machine capability. On the other hand, the RMS value of the cutting force components is useful in designing the cutter, or selecting an appropriate cutter in a defined condition. However, in micro-milling, forces usually remain very low (typically below 1.0 N) owing to very low-uncut chip thickness and depth of cut [9]. In this study, three different force components, namely the longitudinal force (P_X) that acts along the feed direction, the radial thrust force (P_Y) that acts perpendicular to the feed direction, and the vertical thrust force (P_Z) that acts along the tool axis, are considered separately. Average maximum and RMS values are retrieved and used for further analysis. When speed is varied, feed per flute is kept constant to 1.5 $\mu\text{m}/\text{flute}$. When feed per flute is varied, speed is kept unchanged to 25,000 rpm to ensure adequate lubricant supply [8].

3.1 Dependency of Cutting Forces on the Spindle Speed

As shown in Fig. 2, all three measured components of the cutting force reduce with the increase in spindle speed. Although considerable reduction can be noticed for P_X and P_Y components, P_Z force reduces marginally. Reduction of cutting forces with the increase in tool rotation speed can be attributed to two distinct factors—(i) increased plastic nature of the chip and (ii) reduced minimum uncut chip thickness.

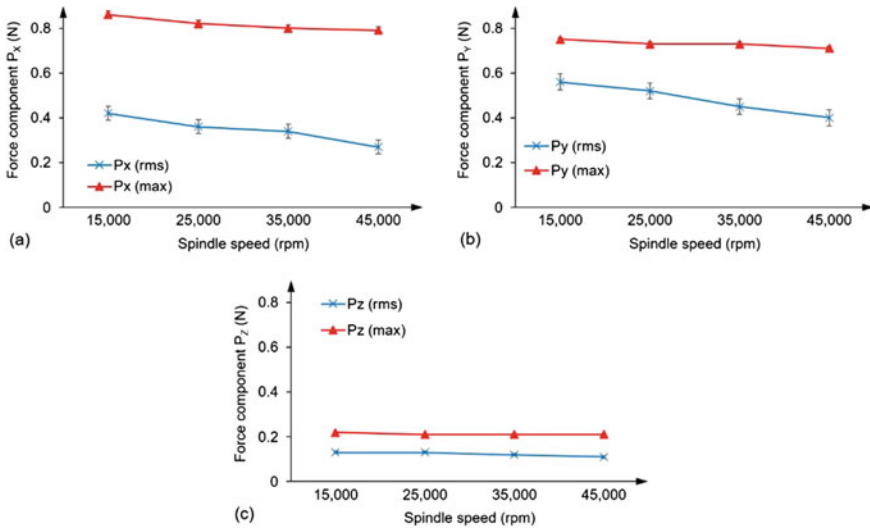


Fig. 2 Variation of RMS and maximum force components with the spindle speed

As the rotation speed of the tool increases, the tribological contact duration between the workpiece and edge for a particular engagement reduces [8]. Thus, each layer of uncut material is removed in a relatively shorter duration. In other words, the relative velocity between the tool and chip increases as spindle speed is increased. At higher velocity, the flow of the chip becomes more plastic [10], and thus, the contact friction drops. As shown in Fig. 3, the shining surface (underside) of the chips indicates such changes in frictional characteristic [11]. Chips obtained through low-speed micro-milling are characterized by the presence of scratch marks and adherence deposits. These are the indications of higher friction at the chip-tool interface. On the other hand, chips obtained at the highest speed are almost free from scratch marks and adhered deposits. Accordingly, relatively lesser energy is required to remove the same amount of material at higher speed that ultimately leads to the generation of lower forces.

Apart from lower friction, reduced minimum uncut chip thickness also contributes towards the reduction of cutting forces with speed. In micro-milling, the uncut chip thickness remains close to the edge radius owing to very small feed per feed. Accordingly, workpiece material experiences highly negative rake angle when the edge tends to compress it. Unless the uncut chip thickness exceeds a minimum uncut chip thickness (h_{min}) value, chip formation does not initiate. Rather, the material undergoes elastic-plastic deformation or ploughing (plowing) leading to lateral flow of the material mostly in the form of burr that can also be removed through separate post-milling deburring operation [12]. Even when the uncut chip thickness is higher than h_{min} , a thin layer of material having thickness h_{min} undergoes ploughing, and rest of the part undergoes shearing to produce chip. For a tool with given edge radius, the h_{min} value depends on the apparent coefficient of friction at the chip-tool interface.

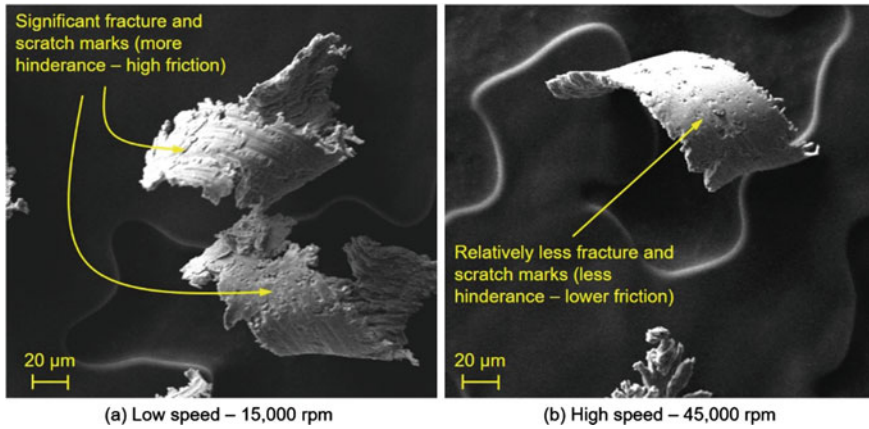


Fig. 3 Underside of the chips showing the frictional characteristics during micro-milling at the lowest and highest speed investigated here

As established by Malekian et al. [13], the h_{\min} can be expressed as a function of apparent coefficient of friction (η) and edge radius (r_e) in the form of Eq. (1).

$$h_{\min} = r_e \{1 - \cos \eta\} \quad (1)$$

Thus, the h_{\min} is proportional to the apparent coefficient of friction between the chip and rake face. As explained through Fig. 3, contact friction drops with the increase in speed. Accordingly, a lower h_{\min} is expected at higher spindle speed. As h_{\min} reduces, volume fraction of the material undergoing ploughing reduces (Fig. 4). In other words, majority fraction of the uncut chip experiences shear deformation to produce chips (instead of ploughing). It is well known that the ploughing requires significantly larger specific energy as compared to shearing [14]. As a result, relatively lower forces develop at higher spindle speeds. Whilst force components P_X and P_Y strongly depend on the frictional characteristics and minimum uncut chip thickness [11], the P_Z component is less dependent on such factors. For micro-milling with a constant depth of cut, the P_Z force mainly changes with nose radius, chip clogging, and tool wear. Accordingly, P_Z force does not change significantly with speed even though P_X and P_Y components decrease considerably.

3.2 Dependency of Cutting Forces on the Feed Per Flute

The frictional properties do not change considerably with the change in feed per flute. Therefore, the minimum uncut chip thickness remains more-or-less constant when feed per flute is increased. However, for a given edge radius, the fraction of

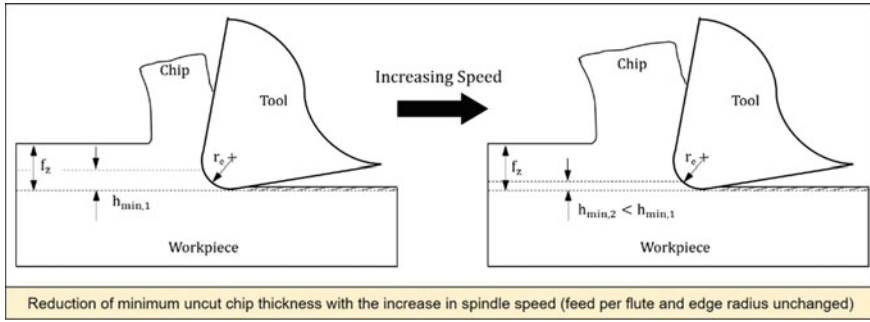


Fig. 4 Schematic representation on the changes in shear-able and plough-able material when h_{min} reduces owing to the increase in speed

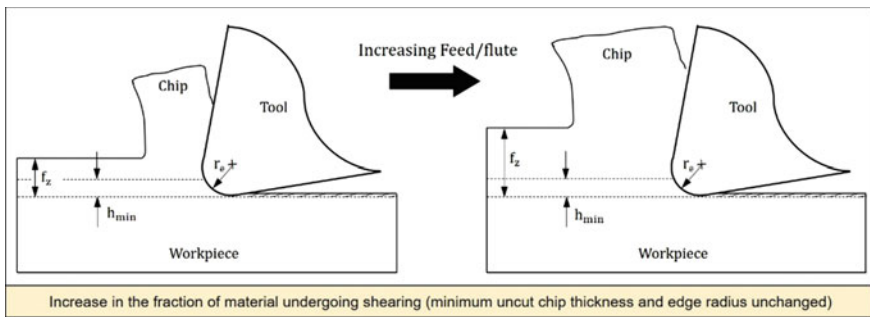


Fig. 5 Schematic representation on the increase in shear-able material when feed per flute is increased (plough-able material remains unchanged)

workpiece material undergoing shearing increases when feed per flute is increased. This scenario is schematically shown in Fig. 5.

As the chip load per cutting edge increases, more energy is required for removing the material, and hence, high-cutting forces are expected at higher feed per flute. As shown in Fig. 6, an increasing tendency amongst force components P_X and P_Y can be observed with the increase in feed per flute. P_Z component also increases, however, only marginally. For all of the feeds per flute investigated here, the maximum value of the P_X component is somewhat higher than that of the P_Y component. However, an opposite scenario can be observed for the RMS values of the force components. An increasing nature of the micro-milling forces with the increase in feed per flute was also observed by Yadav et al. [15].

To identify the parameter (amongst speed and feed) that has relatively more influence on cutting forces, percentage change can be calculated. In this regard, three-fold increase in response valuable is considered only. When speed is increased three-fold (from 15,000 rpm to 45,000 rpm), RMS value of the P_X component changes (actually reduces, but only magnitude is considered) as much as 36% (Fig. 7a). On the other hand, for three-fold increase in feed per flute (from 0.5 $\mu\text{m}/\text{flute}$ to 1.5 $\mu\text{m}/\text{flute}$),

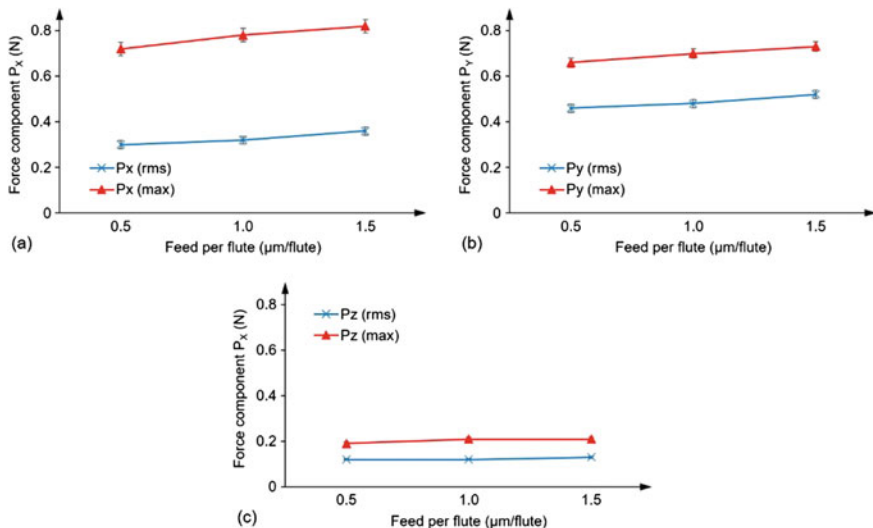


Fig. 6 Variation of RMS and maximum force components with the feed per flute

the RMS value of the P_x component changes (increases) only 20%. Similar pattern of variation can be observed for RMS values of all other force components. Thus, RMS values of the force components are more sensitive towards cutting forces as compared to feed per flute. However, a reverse situation occurs when maximum values of the force components are considered. As shown in Fig. 7b, relatively less change in the force components occur as speed is increased three-fold as compared to the same when for three-fold increase in per flute.

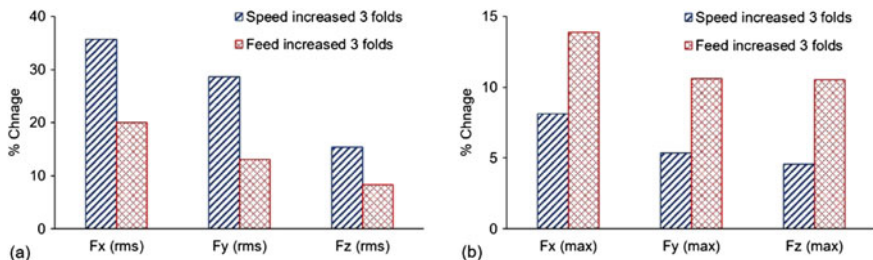


Fig. 7 Sensitivity of speed and feed per flute on the a RMS values and b maximum values of the cutting force components

4 Conclusions

This article analyzed the variation of cutting forces with spindle speed and feed per flute during sustainable minimum quantity lubrication (MQL)-based micro-milling of full-immersion straight slots on AISI D2 steel samples using 500 μm diameter two-flute micro-mills. Based on the analysis of the results, the following conclusions can be drawn.

- At higher cutting speed, the chips flow over the rake surface with lesser tribological hindrances. Volume fraction of the plough-able material also drops with the increase in speed. These two factors, together, lead to the reduction in cutting forces with the increase in spindle speed.
- The higher the feed per flute, the more is the chip load for each cutting edge in every rotation of the tool. The volume of plough-able material remains unchanged with the increase in feed per flute; however, the volume of the shear-able material increases leading to the growth of cutting forces. Accordingly, cutting forces increase with the increase in feed per flute.
- The RMS values of the cutting force components are more sensitive towards the spindle speed (as compared to the feed per flute). On the contrary, the maximum values of the cutting force components are more sensitive towards the feed per flute (as compared to the spindle speed).
- Vertical thrust force (along the tool axis) is least influenced by the variation of the spindle speed and feed per flute.

References

1. Oliaei et al (2018) Micro tool design and fabrication: A review. *J Manuf Processes* 36:496–519. <https://doi.org/10.1016/j.jmapro.2018.10.038>
2. Malayath et al (2020) Study of different Materials response in Micro milling using four edged micro end mill tools. *J Manuf Processes* 56:169–179. <https://doi.org/10.1016/j.jmapro.2020.04.079>
3. Venkata et al (2019) Power consumption optimization strategy in micro ball-end milling of D2 steel via TLBO coupled with 3D FEM simulation. *Measurement* 132:68–78. <https://doi.org/10.1016/j.measurement.2018.09.044>
4. Sharma et al (2014) Investigation of effects of dry and near dry machining on AISI D2 steel using vegetable oil. *J Cleaner Prod* 66:619–623. <https://doi.org/10.1016/j.jclepro.2013.11.042>
5. Sharma et al (2015) Investigation of effects of nanofluids on turning of AISI D2 steel using minimum quantity lubrication. *J Cleaner Prod* 108:72–79. <https://doi.org/10.1016/j.jclepro.2015.07.122>
6. Jin et al (2009) The characteristics of cutting forces in the micro-milling of AISI D2 steel. *J Mech Sci Technol* 23(10):2823–2829. <https://doi.org/10.1007/s12206-009-0804-7>
7. Babu et al (2021) Modeling and optimization of dead metal zone to Reduce cutting forces in micro-milling of hardened AISI D2 steel. *J Braz Soc Mech Sci Eng* 43(3). <https://doi.org/10.1007/s40430-021-02861-5>

8. Saha et al (2020) An analytical approach to assess the variation of lubricant supply to the cutting tool during MQL assisted high speed micromilling. *J Mater Process Technol* 285:116783. <https://doi.org/10.1016/j.jmatprotec.2020.116783>
9. Kumar et al (2020) Tribological characteristics and micromilling performance of nanoparticle enhanced water based cutting fluids in minimum quantity lubrication. *J Manuf Processes* 56:766–776. <https://doi.org/10.1016/j.jmapro.2020.05.032>
10. Hamdan et al (2011) An optimization method of the machining parameters in high-speed machining of stainless steel using coated carbide tool for best surface finish. *Int J Adv Manuf Technol* 58(1–4):81–91. <https://doi.org/10.1007/s00170-011-3392-5>
11. Saha et al (2021) Progressive wear based tool failure analysis during dry and MQL assisted sustainable micro-milling. *Int J Mech Sci* 212:106844. <https://doi.org/10.1016/j.ijmecsci.2021.106844>
12. Kumar et al (2021) Ultrasonic-assisted abrasive micro-deburring of micromachined metallic alloys. *J Manuf Processes* 66:595–607. <https://doi.org/10.1016/j.jmapro.2021.04.019>
13. Malekian et al (2012) Modeling of minimum uncut chip thickness in micro machining of aluminum. *J Mater Process Technol* 212(3):553–559. <https://doi.org/10.1016/j.jmatprotec.2011.05.022>
14. Wu et al (2015) Experimental investigation of specific cutting energy and surface quality based on negative effective rake angle in micro turning. *Int J Adv Manuf Technol* 82:1941–1947. <https://doi.org/10.1007/s00170-015-7548-6>
15. Yadav et al (2021) Methodology for prediction of sub-surface residual stress in micro end milling of Ti-6Al-4V alloy. *J Manuf Processes* 62:600–612. <https://doi.org/10.1016/j.jmapro.2020.12.031>

Two-Dimensional Finite Element Simulation of Micro-Electric Discharge Machining of Ti-6Al-4 V



B. C. Karthik , P. K. Pradeesh Karun , P. Sanal , Ch. Surendra ,
and Basil Kuriachen 

1 Introduction

Machining process is one among the most prominent processes spreads widely in the whole domain of mechanical and manufacturing engineering. Technological advancements emerging day by day enhance the efficiency of processes being conducted and make processes further simpler. Miniaturization is a significant trend coming into the present technological level of manufacturing. Manufacturing micro-sized machine parts and components have got a great application in the various industries which includes the fabrication of micro-holes and other micro-level features in turbine blades, fuel injection nozzles, optical products, hydro-pneumatic valves, etc., that require higher amount of precision and accuracy.

Micro-electrical discharge machining is an important non-traditional machining process which exerts negligible residual stress due to its non-contact nature. It also enables to produce a lot of geometrically complex micro-features in electrically conductive solid materials with high accuracy irrespective of their hardness. So EDM

B. C. Karthik (✉) · P. K. P. Karun · P. Sanal · Ch. Surendra · B. Kuriachen
Department of Mechanical Engineering, National Institute of Technology Calicut, Calicut,
Kerala 673601, India
e-mail: karthik_b180814pe@nitc.ac.in

P. K. P. Karun
e-mail: pradeesh_b180367pe@nitc.ac.in

P. Sanal
e-mail: sanal_b180803pe@nitc.ac.in

Ch. Surendra
e-mail: surendra_b180818pe@nitc.ac.in

B. Kuriachen
e-mail: bk@nitc.ac.in

is one of the main techniques used for manufacturing complex-shaped dies, components for surgical, aerospace and other precision engineering industries [1]. It utilizes electrical discharges (sparks) for obtaining required machined surface. Removal of workpiece material takes place by a series of discharge pulses between two electrodes separated by dielectric fluid on applying a voltage.

From a source, the sparks are made to discharge at high frequency in which a suitable spark gap is maintained between tool and workpiece that can be adjusted with the help of a servo motor. The main advantage of EDM is that a uniform MRR is obtained as the closest distance at each spot changes after each spark. When suitable voltage is built up, emission of electrons from cathode to anode takes place which collides with the atoms of dielectric molecules to split up and produce more ions and electrons. A conductivity channel is established as these electrons and positive ions move towards anode and cathode, respectively. This causes high temperature, melting and vaporizing of both the tool electrode as well as workpiece. But due to the impact produced by positive ions on cathode is much smaller than caused by electrodes on anode, tool wear is comparatively less as that of workpiece wear. In addition, a thin carbon film produced from pyrolysis of dielectric fluid creates a protective layer on tool.

It is very difficult to study and experimentally observe the exact theory of mechanism behind the EDM process which can exactly predict the amount of material removal during EDM machining because of its complexity [2]. So modelling of EDM process can help to understand the comprehensive view of the process which includes the temperature distribution in the workpiece material due to the effect of discharge pulses. Finite element model is accurate and powerful technique to model any complex shapes by applying necessary boundary conditions, and in this work, the finite element analysis is coded in MATLAB software. FEM can help in providing a good approximation of the material removed in the machining process. This can help in suitably choose parameters for process in the machining. It will also aid in predicting the rate of material removal as well as tool wear ratio.

This paper studies a model based on the electro-thermal theory to find out the geometry of crater formed from single discharge pulse. The developed model is able to anticipate the temperature distribution using the average voltage and current values obtained from voltage and current probes during the material removal process. By solving this thermal problem, the temperature distribution inside the workpiece from which the shape as well as the radius and depth of the generated craters can be estimated by comparing the temperature value at each node with the melting temperature of the material. The material removal rate can be found by means of both radius and depth of the crater. Further, an algorithm for tool wear compensation can be developed by real-time monitoring of the material removal rate and comparison with target volume to be removed. So online monitoring of EDM process can help get optimum machining conditions thereby achieving higher machining efficiency and performance [3]. Temperature distribution is one of the main factors affecting the material removal in electric discharge machining. Hence, it is given importance in this particular study of EDM. Various parameters of thermal process were considered while developing the model. It comprises various heat transfer modes that includes

conduction and convection, latent heat associated with the material melting and evaporating, the efficiency of heat transfer to the workpiece material, the radius of spark and electrode and thermal properties of workpiece material. In addition, Gaussian heat flux was considered for applying the heat flux boundary condition on to the developed model. Moreover in case of implementing online tool monitoring system for tool wear compensation, the developed FEM model can be used to predict the material removed based upon the voltage and current values obtained so that the machining need not be stopped in between for getting the measured value of crater dimensions. This helps in obtained the crater volume which can be compared with target volume to get the required tool compensation length.

Yeo et al. developed an analytical model to estimate the dimensions of the crater which showed that the theoretical and experimental results are found to be very close [4]. Nadda et al. proposed that the finite element simulation can be used to determine the crater dimensions created by a spark discharge [5]. The value of crater depth and crater radius varies according to the voltage and current of the machining. Here they found that the crater size obtained by finite element simulation is very close to the experimentally obtained values. Kuriachen et al. showed that thermal analysis of single spark model gives the results that are very close to experimental results [6]. This utilized the Gaussian distribution of heat flux for performing the transient thermal analysis and predicted the crater geometry for different voltage and capacitance. Xie et al. proposed a model to predict the crater geometry of EDM by considering that the energy dissipated to the workpiece will be only a part of the total energy of the spark discharge [7]. Rajeev Kumar and Vinod Yadava presented a thermal model to analyse the temperature distribution in the zone of influence of micro-EDM spark discharges and determined the crater radius and crater depth by using the melting isotherm curve at various energy levels [8]. It predicted how the energy partition influencing the crater dimension. Nadda et al. proposed that the energy of each discharge pulse and the corresponding volume of material removed is a variable that depending up on the electrical parameters [9]. Marafona and Chousal proposed an electro-thermal model by using Joule heating factor, and it assumes the discharge channel as a heat dissipating electrical conductor where the conductor radius is a function of intensity of current and pulse duration. Zhang et al. inferred that expansion of the plasma diameter must be taken into consideration in order to be more consistent with the actual EDM process. Also, the power density was an important factor that affects the material removal and energy efficiency. With short pulse duration, the material removal and energy efficiency were much higher due to the higher power density [10]. Jamwal et al. concluded that in EDM, electrical parameters like voltage peak current, pulse on time, pulse off time, etc., affect the quality of surface produced. In addition, non-electrical parameters like dielectric flushing, rotation of tool and workpiece, proper addition of additive in dielectric, etc., also have a role in obtaining optimum performance of EDM [11]. Jithin et al. observed that with rising values of discharge current and pulse on time, crater depth and radius increases. It was because of increased duration of input heat flux and input pulse energy. In addition to it, the aspect ratio has a high value at low values of current and pulse on time due to less penetration of heat into workpiece at lower parameter

values [12]. Zhang et al. developed a parameterized Gaussian heat flux model to obtain the optimal Gaussian heat flux distribution. The results were validated by comparing with the experimental single discharge results to find the optimal heat flux distribution [13]. Zhang et al. concluded that volume wear increases with the increase of current, voltage and pulse width. Moreover, the simulation can tell about the material removal rate with less error rate [14]. Jain mentions that unlike in EDM, the damage due to heat-affected zone in micro-EDM is very much less because of the low energy sparks in micro-EDM [15].

2 Electro-thermal Modelling of a Single Discharge Pulse

The single discharge pulse can be modelled by defining a suitable computational domain, providing necessary governing equation and applying appropriate initial and boundary conditions.

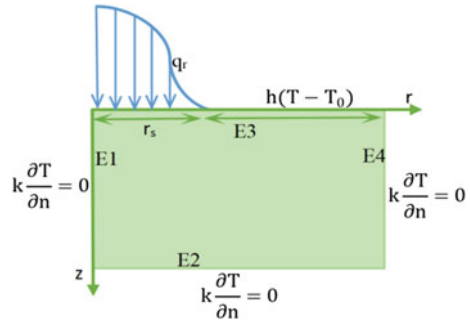
2.1 Assumptions

1. The heat flux distribution over the top edge of the domain is a Gaussian distribution.
2. Flushing efficiency is 100%, i.e. flushed workpiece particles will not deposit on the workpiece again.
3. The radiative heat transfer from the workpiece is neglected.
4. Electro-thermal model of a single spark is considered to study.
5. Negligible heat transfer on the left, right and bottom edges.
6. Transient analysis is to be conducted.
7. Eight percentage of the total heat flux is used up for the material removal from workpiece.
8. The material is homogenous and isotropic in nature.

2.2 Computational Domain

The computational domain taken for the simulation of a single discharge pulse crater involves a cross-sectional rectangular plane with one of the top corners at centre of the plasma channel centre, as shown in Fig. 1.

Fig. 1 Schematic diagram of the axisymmetric domain with boundary conditions



2.3 Governing Equation

With regards to all assumptions for the single discharge model, the partial differential equation taken as the governing equation is:

$$\frac{\partial^2 T}{\partial r^2} + \frac{\partial^2 T}{\partial z^2} + \frac{1}{r} \frac{\partial T}{\partial r} = \frac{1}{\alpha} \frac{\partial T}{\partial t} \tag{1}$$

where $T(x, y)$ is the temperature distribution across the domain and α is thermal diffusivity.

The thermal diffusivity can be calculated as:

$$\alpha = \frac{k}{\rho c_p} \tag{2}$$

where ρ is the density of workpiece material.

Here the thermal conductivity, k , and specific heat, c_p , are both considered as temperature dependent functions.

2.4 Initial Condition

Before the application of the heat source, we assume the temperature of the domain (workpiece) to be constant and equal to the room temperature T_a , i.e.

$$T(r, z, t = 0) = T_a \tag{3}$$

2.5 Boundary Conditions

We assume that the convective heat transfer between edges $E1$, $E2$ and $E4$ is negligible, making the heat flux equal to zero, i.e.

$$\frac{\partial T}{\partial n} = 0 \quad (4)$$

where n is a unit vector normal to the surface of the domain.

For edge $E3$, the heat flux due to the spark, q_r , acts within the spark radius r_s . Beyond r_s , convective heat transfer takes place due to the application of dielectric fluid, with heat transfer coefficient taken as $1000 \text{ W/m}^2\text{K}$.

$$-k(T) \frac{\partial T}{\partial y} = \begin{cases} q_r & \text{if } r < r_s \\ h(T - T_a) & \text{if } r > r_s \end{cases} \quad (5)$$

where T_a is the ambient temperature, taken as 298 K .

2.6 Formulation of Heat Flux

By assuming Gaussian heat distribution, the heat flux can be written as:

$$q_r = q_0 e^{-3\left(\frac{r}{r_s}\right)^2} \quad (6)$$

where the maximum heat flux, $q_0 = 3.157q$, and q is the uniform heat flux density rate [16].

The spatial distribution of heat flux density rate is given by:

$$q = \frac{Q_a}{\pi r_s^2} \quad (7)$$

where Q_a is the available heat flux.

The ratio of available heat flux to total heat flux, η , can be taken as 8% [17]. Therefore,

$$\eta = \frac{Q_a}{Q} = 0.08 \quad (8)$$

The total heat flux can be calculated as:

$$Q = \frac{E_d}{T_{On}} \quad (9)$$

where E_d is the energy dissipated by the capacitor and T_{on} is the pulse on time of the voltage pulse [18].

The energy stored in the capacitor is formulated as:

$$E_d = \frac{1}{2} C_d V_d^2 \quad (10)$$

where C_d and V_d are respective capacitance and voltage of the RC relaxation circuit that produces the pulse for the micro-EDM.

Using power regression, the equation for spark radius, r_s , is found to be [19]:

$$\begin{aligned} r_s = & 21.47 + (0.0026 * C) - (0.046 * V) \\ & + (1.47 * 10^{-4} * C * V) - (1.27 * 10^{-5} * C^2) \end{aligned} \quad (11)$$

2.7 Consideration of Latent Heat of Fusion

During the micro-electric discharge machining, a part of the heat is utilized for the phase change of the workpiece material from solid to liquid state. An apparent specific heat can be used for incorporating the effect of latent heat with the specific heat value. Therefore, apparent heat capacity can be defined as,

$$c'_p = c_p + \frac{L_f}{\Delta T_M} \quad (12)$$

where c_p is the specific heat capacity.

L_f is the latent heat of fusion.

ΔT_M is the difference between solidus and liquidus temperature.

3 Finite Element Analysis

For conducting, the transient axisymmetric thermal analysis for a single pulse discharge in micro-electric discharge machining, Partial Differential Equation Toolbox available in MATLAB is used for modelling and solving the problem. The steps in thermal analysis of single pulse discharge on MATLAB are as follows:

Table 1 Process parameters for the micro-EDM

Process parameter	Type/Value
Type of analysis	Two-dimensional transient thermal analysis
Convective heat transfer coefficient (h)	1000 W/m ² K
Work material	Ti-6Al-4 V
Initial temperature	25 °C
Spark on time (T_{on})	3 μ s
Voltages	80 V, 115 V, 150 V
Capacitances	1.1 μ F, 2.2 μ F

3.1 Pre-processing

- i. Define a thermal model as an axisymmetric steady state analytical model.
- ii. Open the PDE Modeler app in MATLAB to create a geometry and name the geometry description, set formula and name space matrices.
- iii. Add the geometry with the thermal model defined, using the `geometryFromEdges()` function in the PDE Toolbox.
- iv. Add the thermal properties of the workpiece such as heat transfer coefficient and specific heat capacity as given in Table 1 with the model.
- v. Generate a mesh grid in the domain with appropriate element size.

Use the `thermalBC()` function to define the boundary conditions for edges E1, E2 and E4 as zero heat flux. Then define the boundary conditions in edge E3 as given in Eq. 1.

- vi. Use the `thermalIC()` function to define the initial condition as $T(t = 0) = 0$.

3.2 Solution

Using `solve()` function, the thermal model can be solved and the result is stored.

3.3 Post Processing

- i. Plot the temperature in the result to get the temperature distribution contour.
- ii. Find the value of z for which the temperature on the domain becomes equal to melting point of the workpiece, in order to find the crater radius and crater depth, respectively.

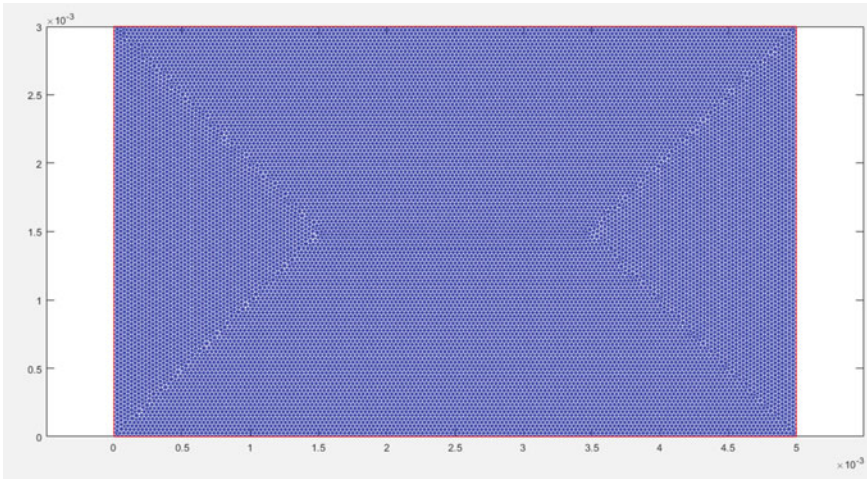


Fig. 2 2D meshed grid

4 Results

The temperature distributions are shown in Figs. 3, 4, 5 and 6. The temperature is maximum at the left top corner, and it decreases along the r and z axes. Since, the input parameters that are in our control are voltage and capacitance, it is important to analyse the variation of temperature with these parameters. In order to find the relation between capacitance and temperature of the workpiece, maximum temperature in the resultant temperature distribution is found for various values of capacitance (1.1 and $2.2\mu\text{F}$), while keeping the voltage constant at 80 V (Figs. 3 and 4). It was found that the maximum temperature increases with increase in capacitance of the RC relaxation circuit. This can be reasoned that, with increase in capacitance, the energy stored in the capacitor increases according to Eq. 9. The discharge of the capacitor causes the increase in the available heat flux, which causes an increase in the temperature.

For checking the changes in temperature with change in voltage, three values of voltage are considered (80, 115 and 150 V), at a constant capacitance of $1.1\mu\text{F}$. It also shows an increase in temperature with increase in voltage, due to the increase in the energy stored in the $1\mu\text{F}$ capacitor (Figs. 4, 5 and 6).

Possible error that can raise in the solution is that flushing efficiency is assumed to be 100%, which means that deposition of the removed particles will not occur. In reality, the efficiency is less than 100%, which can cause a decrease in the crater size and radius than expected.

It can be seen from the graphs for temperature along R and Z axes that temperature reduces through the axis more quickly for Z axis than along R axis. This is because of the presence of direct heat source acting along the radial axis which increases the temperature along r axis (Figs. 7 and 8).

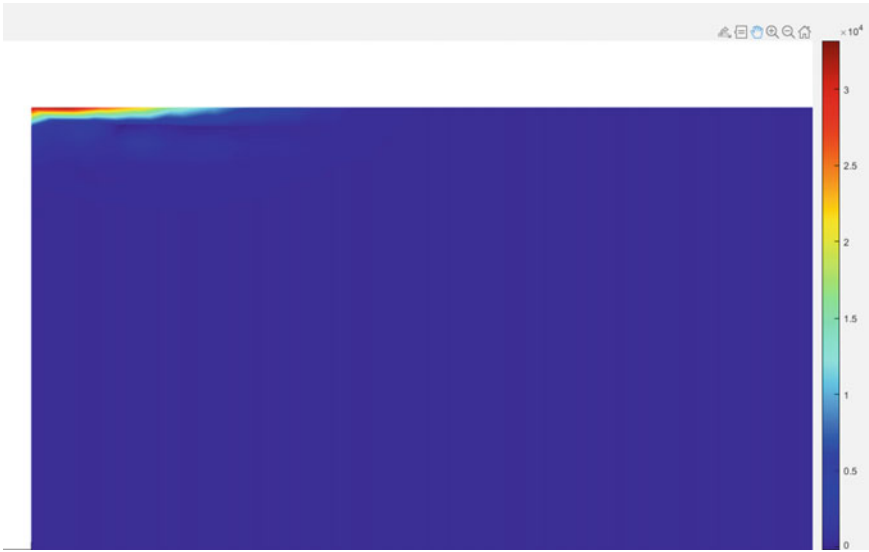


Fig. 3 Zoomed view of temperature distribution for $V = 80$ V and $C = 2.2\mu\text{F}$



Fig. 4 Zoomed view of temperature distribution for $V = 80$ V and $C = 1.1\mu\text{F}$

5 Conclusion

On completion of the transient thermal analysis of the electro-thermal model of the single discharge pulse in micro-electric discharge machining, it can be inferred that:

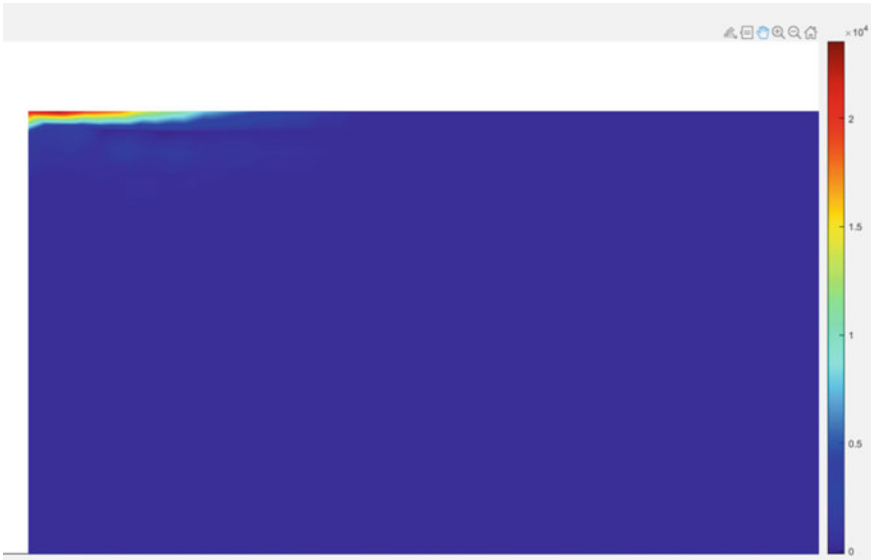


Fig. 5 Zoomed view of temperature distribution for $V = 115$ V and $C = 1.1\mu\text{F}$

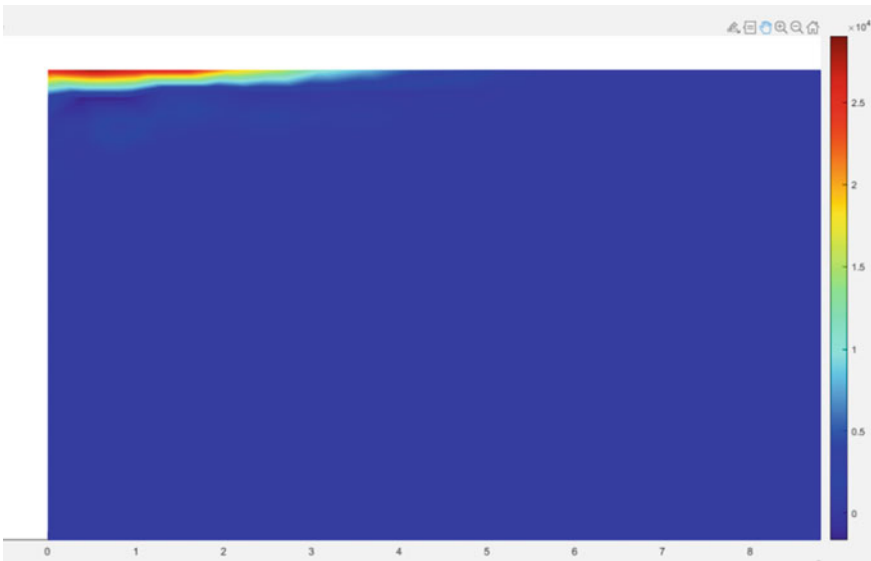


Fig. 6 Zoomed view of temperature distribution for $V = 150$ V and $C = 1.1\mu\text{F}$

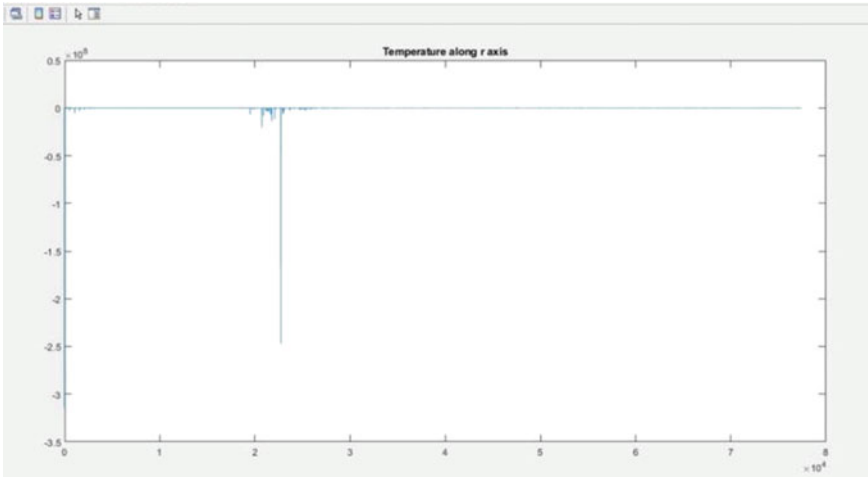


Fig. 7 Temperature variation along radial axis for $V = 80$ V and $C = 0.01\mu\text{F}$

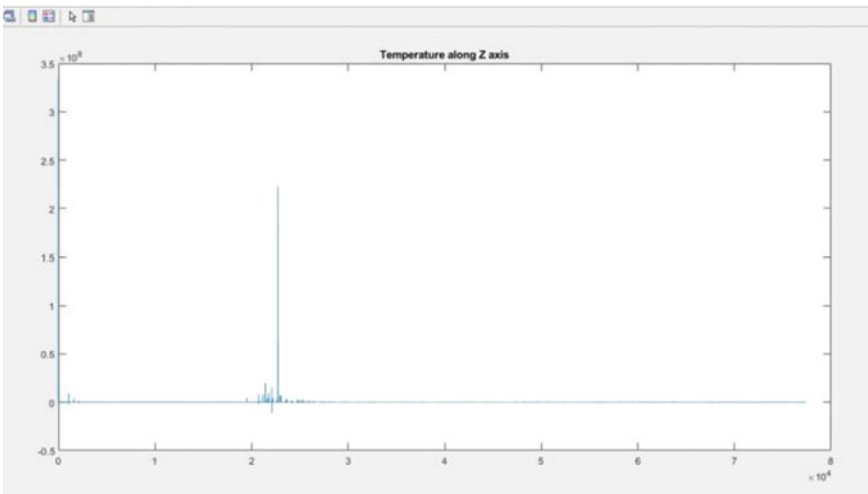


Fig. 8 Temperature variation along Z axis for $V = 80$ V and $C = 0.01\mu\text{F}$

- i. The result obtained after solving the finite element problem closely check with the existing numerical simulations and studies regarding micro-EDM.
- ii. Increase in capacitance and voltage can increase the maximum temperature in the resultant temperature distribution.
- iii. In continuation with this analysis, an algorithm to compensate the real-time tool wear in micro-EDM is under development, along with the help of a suitable pulse discrimination strategy.

- iv. Due to the presence of heat flux on the radial axis, the temperature varies quickly along the z axis than that along radial axis.


References

1. Rajurkar KP, Levy G, Malshe A, Sundaram MM, McGeough J, Hu X, Resnick R, DeSilva A (2006) Micro and nano machining by electro-physical and chemical processes. *CIRP Ann Manuf Technol* 55(2):643–666
2. Descoedres A (2006) Characterization of electrical discharge machining plasmas. Ph.D. Thesis. EPFL Lausanne
3. Nahak B, Gupta A (2019) A review on optimization of machining performances and recent developments in electro discharge machining. *Manuf Rev* 6(2)
4. Yeo SH, Kurnia W, Tan PC (2007) Electro-thermal modeling of anode and cathode in micro EDM. *J Phys D Appl Phys* 40(8):2513. <https://doi.org/10.1088/0022-3727/40/8/015>
5. Nadda R, Nirala CK (2020) Thermal modeling of single discharge in prospect of tool wear compensation in μ EDM. *Int J Adv Manuf Tech* 107:4573–4595. <https://doi.org/10.1007/s00170-020-05238-5>
6. Kuriachen B, Varghese A, Somashekhar KP, Panda S, Mathew J (2015) Three-dimensional numerical simulation of microelectric discharge machining of Ti-6Al-4V. *Int J Adv Manuf Tech* 79(1–4):147–160. <https://doi.org/10.1007/s00170-015-6794-y>
7. Xie BC, Wang YK, Wang ZL, Zhao WS (2011) Numerical simulation of titanium alloy machining in electric discharge machining process. *Trans Nonferrous Metals Soc China* 21:434–439. [https://doi.org/10.1016/s10036326\(11\)61620-8](https://doi.org/10.1016/s10036326(11)61620-8)
8. Kumar R, Yadava V (2008) Finite element thermal analysis of micro-EDM. *Int J Nanoparticles* 1(3):224. <https://doi.org/10.1504/ijnp.2008.022898>
9. Nadda R, Nirala CK, Saha P (2019) Tool wear compensation in micro-EDM. In: Kibria G, Jahan M, Bhattacharyya B (eds) *Micro-electrical discharge machining processes. Materials forming, machining and tribology*. Springer, Singapore, pp 185–208. https://doi.org/10.1007/978-981-13-3074-2_9
10. Zhang Y, Liu Y, Shen Y, Li Z, Ji R, Cai B (2014) A novel method of determining energy distribution and plasma diameter of EDM. *Int J Heat Mass Transf* 75:425–432. <https://doi.org/10.1016/j.ijheatmasstransfer>
11. Jamwal A, Aggarwal A, Gautam N, Devarapalli A (2018) Electro-discharge machining: Recent developments and trends. *Int Res J Eng Tech (IRJET)* 05(02):433–448
12. Jithin S, Rauta A, Bhandarkara UV, Joshia SS (2018) FE modeling for single spark in EDM considering plasma flushing efficiency. In: 46th SME North American Manufacturing Research Conference, NAMRC 46, TX, USA
13. Zhang F, Gu L, Zhao W (2015) Study of the Gaussian distribution of heat flux for micro-EDM. In: ASME 2015 International Manufacturing Science and Engineering Conference MSEC2015-9276. <https://doi.org/10.1115/MSEC2015-9276>
14. Zhang S, Zhang W, Wang P, Liu Y, Ma F, Yang D, Sha Z (2019) Simulation of material removal process in EDM with composite tools. *Adv Materials Science Eng*, 1–11
15. Jain VK (2010) *Introduction to micromachining*, 2nd edn. Narosa Publications
16. Murali MS, Yeo SH (2005) Process simulation and residual stress estimation of micro electric discharge machining using finite element method. *J Appl Phys* 44(7):5254–5263. <https://doi.org/10.1143/JJAP.44.5254>
17. Somashekhar KP (2010) *Theoretical and experimental investigations on micro electric discharge machining processes*. PhD Thesis, National Institute of Technology, Kerala, India

18. Ghosh A, Mallik AK (1986) Manufacturing science. Ellis Horwood
19. Kuriachen B, Mathew J (2015) Spark radius modeling of resistance-capacitance pulse discharge in micro-electric discharge machining of Ti-6Al-4V: an experimental study. *Int J Adv Manuf Tech* 85(9–12):1983–1993

Corrosion Studies on AA7075-T7352 Alloys Under Adverse Environments



N. R. Karthik Varma, Neeraj K. Namboodiri, Sandeep Justin, S. Sreegovind, and K. Manoj Kumar 

1 Introduction

AA7075 aluminum alloys find extensive application in aircraft industries owing to its high specific strength and excellent mechanical properties [1]. Elements like Zn, Cu, Mg, Cr, etc., are commonly added during the alloying process to enhance its mechanical properties. However, the fatigue resistance of this alloy often found to be adversely affected by the presence of intermetallic phases comprising Fe, Cu and Si [2]. The effect of micro-galvanic corrosion caused by these intermetallic phases often resulted in pitting at the matrix–particle interface, which acts a source of fatigue cracking and subsequent failure of these alloys [3]. Corrosion generally appears as pitting, stress corrosion cracking, exfoliation corrosion, crevice corrosion and intergranular cracking. Such localized corrosion phenomena will be accelerated as the potential difference between different intermetallic phases increases and is severe for compounds containing copper [4]. Thus, it is inevitable to achieve a proper balance between corrosion resistance and strength for aluminum alloys particularly when used for high strength applications.

The size, distribution and microchemistry of precipitates at the grain boundary and the structure of precipitate free zone adjacent to grain boundaries are usually ensured by following a suitable heat treatment procedure, which includes steps like solution treatment, quenching and aging [5]. Out of these, quenching rate is having a significant role on controlling microstructure of grain boundary precipitates. A slow quenching rate adversely affects mechanical characteristics of AA7075 alloys along with its corrosion resistance owing to precipitation of $MgZn_2$ along grain boundaries and lowered presence of Cu at grain and sub-grain boundaries [6]. On the contrary, a quick quenching from solution treatment temperature results in high

N. R. K. Varma · N. K. Namboodiri · S. Justin · S. Sreegovind · K. Manoj Kumar (✉)
Muthoot Institute of Technology and Science, Varikoli, Cochin, India
e-mail: manojkumark@mgits.ac.in

thermal residual stress, particularly in larger components. Thus, a step quenching and aging are usually followed so as to ensure a homogeneous precipitation of grain boundary precipitates at the grain boundaries [6].

Age hardening also can influence mechanical properties and corrosion behavior of aluminum alloys used for high strength application. Highest mechanical strength is usually achieved in T6 heat treatments or peak-aging condition. However, these materials usually lack corrosion resistance and are prone to stress corrosion cracking under external loading. Thus, over aging treatments, T7 treatments, are usually followed, at the expense of 10–15% of mechanical strength, which ensures larger and dispersed precipitates at the grain boundary thereby improving corrosion resistance [7]. The above said heat treatments and subsequent broadened grain boundary precipitates are associated with precipitation of stable equilibrium phase, $MgZn_2$.

Even though AA7075-T7352 alloys are expected to bring out excellent resistance against stress corrosion cracking, these materials were identified to be prone to corrosion cracking in certain applications especially in adverse environments [8]. These alloys are extensively used in aircraft industries as critical components which are commonly produced by methods like hot rolling, forging, etc. A deviation from the standard billet processing can influence the microstructure and corrosion behavior of the resultant material. This work aims at analyzing the effect of thermomechanical working on microstructure of an aluminum alloy forging and its subsequent impact on strength and corrosion behavior of the material.

2 Experimental Details

2.1 Material and Its Microconstituents

AA7075-T7352 alloy was selected for investigation. The samples were cut into 10 mm × 10 mm × 10 mm size for experiments. Samples for microstructure study were ground using different grade SiC emery papers followed by cloth polishing in 1-micron alumina suspension, and final polishing using diamond polishing paste is cleaned thoroughly in water. The prepared specimens were then etched in Keller's reagent (5 ml-HNO₃, 3 ml-HCL, 2 ml-HF and 190 ml-water) to divulge the grain structures. The microconstituents of the AA7075 are given in Table 1.

Table 1 Composition of AA7075 (wt. %)

Material	Si	Fe	Cu	Mn	Mg	Cr	Zn	Ti	Al
Al-7075	0.40	0.50	1.3	0.30	2.4	0.22	5.4	0.20	Balance

2.2 Potentiodynamic Polarization Test

A potentiodynamic polarization test was carried out to evaluate corrosion resistance of AA7075-T7352, and the experiment was conducted using Zahner IM6ex electrochemical work station (Pforzheim, Germany). Samples were taken from the forged bars to make specimens and were covered with epoxy resin exposing an area of 1cm^2 . This surface was subsequently ground using SiC emery paper (1000 grit) and alumina followed by thorough cleaning with acetone. NaCl solution (3.5 wt.%) was used for conducting experiments and was prepared by using reagent grade NaCl salt and distilled water. A typical three electrode setup was used for conducting the polarization tests in which platinum and saturated calomel (SCE) were used as counter and reference electrodes. The scans were started from 350 mV, well below the corrosion potential (E_{corr}), followed by a scan rate of 0.5 mV/sec. The measurements were done in duplicate for each sample. The corrosion rate in mm/yr for all the samples was calculated using the relation

$$\text{C.R} = 0.00327 * I_{\text{corr}} * W/\rho \quad (1)$$

where I_{corr} = corrosion current density in $\mu\text{A}/\text{cm}^2$.

W = the equivalent weight of AA7075.

ρ = density of AA7075.

2.3 Slow Strain Rate Test (SSRT)

SSRT was conducted on a CORTEST make tensile testing machine at a strain rate of $1 \times 10^{-6}/\text{s}$ in 3.5% NaCl solution. The specimen was held in an acrylic container to generate the working environment, and all sides of the sample were polished using an 800 grit SiC emery paper. A pair of linear variable displacement transducers (LVDT) placed on either side of the specimen was used to measure average elongation of the work specimen. The interface between grip portions and the specimen was coated with the help of silicon rubber sealant to avoid galvanic corrosion of both the materials. The susceptibility of the material to SCC was assessed by evaluating the SCC index which is inevitably the ratio of elongation of the material at failure in NaCl and in air environments.

3 Results and Discussion

3.1 Microstructure

The microstructure of AA7075-T7352 alloy examined in three different grain orientations, namely long transverse (LT), short transverse (ST) and longitudinal (L) is shown in Fig. 1. The microstructure of the alloy shown in figures displays severe dendritic coring in all the orientations. The remnant cast structure indicates that the alloy forging was not properly worked out. Second phase particles like Al_7Cu_2Fe , $(Al,Cu)_6(Fe,Cu)$ were observed to be randomly distributed in the Al matrix and is appeared as black in color [9]. These microstructural inhomogeneities would affect the general as well as localized corrosion phenomena like pitting and stress corrosion cracking which in turn influence mechanical behavior of this material.

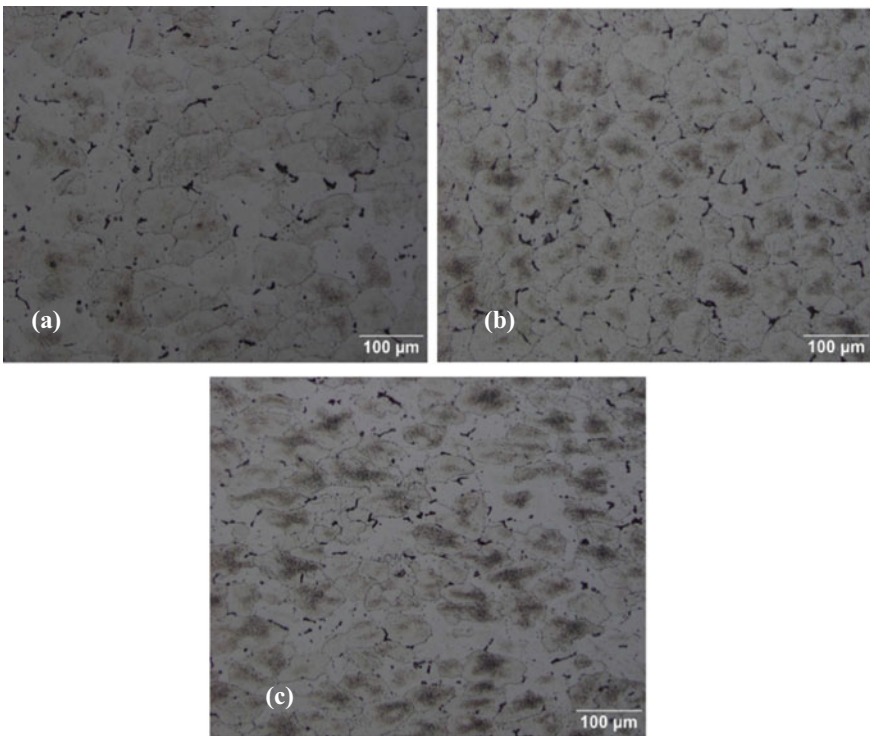


Fig. 1 Microstructure of the forging observed in the **a** long transverse **b** short transverse and **c** longitudinal directions

Fig. 2 Potentiodynamic polarization curve measured for AA7075-T7352 in NaCl (3.5wt.%) solution

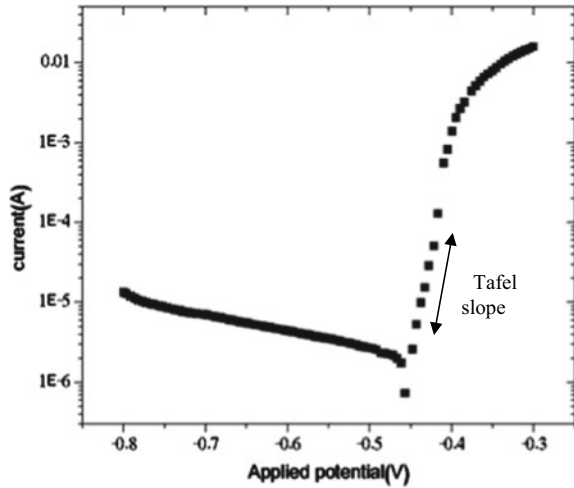


Table 2 Electrochemical parameters measured from polarization curves

S. no	Sample	E_{corr} (mV/SCE)	I_{corr} ($\mu\text{A}/\text{cm}^2$)
1	AA7075-T7352	-455	6.188

3.2 Polarization Test Results

The potentiodynamic polarization curve obtained for aluminum alloy AA7075-T7325 is presented in Fig. 2, and the parameters obtained from the polarization graphs are summarized in Table 2.

From the polarization plots, corrosion potential and corrosion current density of the tested sample were obtained as -455 mV/SCE and $6.188 \mu\text{A}/\text{cm}^2$, respectively. The corrosion morphology of the AA7075-T7325 alloy sample obtained after potentiodynamic polarization test is shown in Fig. 3. Localized corrosion in the form of pitting throughout the surface is observed from the corrosion morphology of the sample. The corrosion rate (CR) of the sample was calculated to be 0.06898 mm/yr.

3.3 Slow Strain Rate Test (SSRT) Results

The stress vs. strain curves obtained in air and 3.5% NaCl solution for AA7075-T7325 alloy samples are displayed in Fig. 4. The data from SSRT such as ultimate tensile strength (UTS), SCC index (SI) and % elongation measured from the plots are summarized in Table 3. On analyzing the stress vs. strain behavior and the mechanical properties summarized in Table 3, it is evident that, there is a significant reduction in deformation for the material under NaCl environment when compared to that in air. This indicates a chance for the material to undergo SCC.

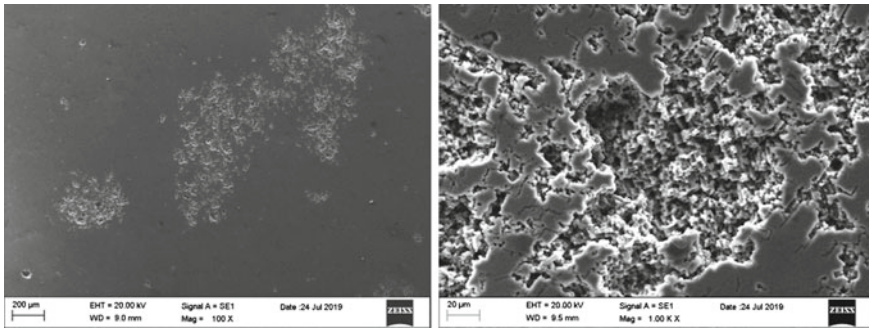


Fig. 3 Corrosion morphology of AA7075-T7352 sample after potentiodynamic polarization test at lower and higher magnifications

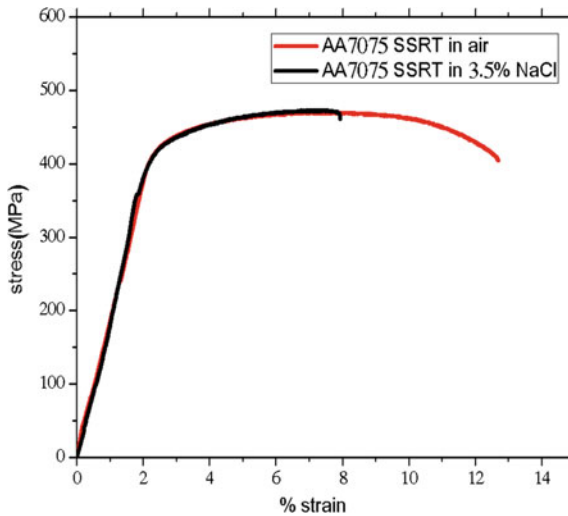


Fig. 4 Stress versus strain plots obtained for AA7075-T7352 alloy in air and in NaCl (3.5wt.%) medium

Table 3 Mechanical properties of the material after SCC test

Material	Environment	UTS (Mpa)	Percentage elongation	SCC index
AA7075-7352	Air	469.65	12.51	0.69
	NaCl	472.15	7.714	

The fracture morphology of the alloy was further examined under SEM to have a clear picture on the vulnerability of the material toward SCC. The fracture morphology of the samples obtained after SSRT is presented in Figs. 5 and 6. The fracture morphology of the samples tested in air and NaCl both exhibited typical

ductile cracking morphology. Several localized corrosion points were observed at the periphery of the workpiece samples, when tested in NaCl environment. This was not visible for samples tested in air. Hence, the drastic reduction in elongation and a low SCC index of 0.69 for sample tested in NaCl environment can be because of the pitting effect occurred as a result of localized corrosion. Pitting corrosion generally occurs in Al matrix near intermetallic phases containing Cu or Fe because of the galvanic interaction of these particles with Al matrix. It can also be noted that the sample subjected to electrochemical polarization also showed severe pitting due to the heterogenous microstructure. The presence of significant coring resulted in severe pitting corrosion leading to increase in stress intensity and a typical mechanical failure. The extent of coring in the alloy forging even though affected the mechanical properties, the SCC resistance of the alloy forging was not much affected.

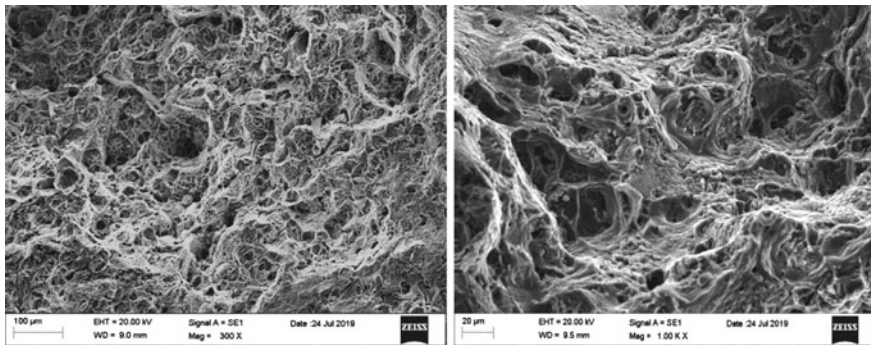


Fig. 5 Fracture morphology of AA7075-7352 alloy in air, observed after SSRT at lower and higher magnifications

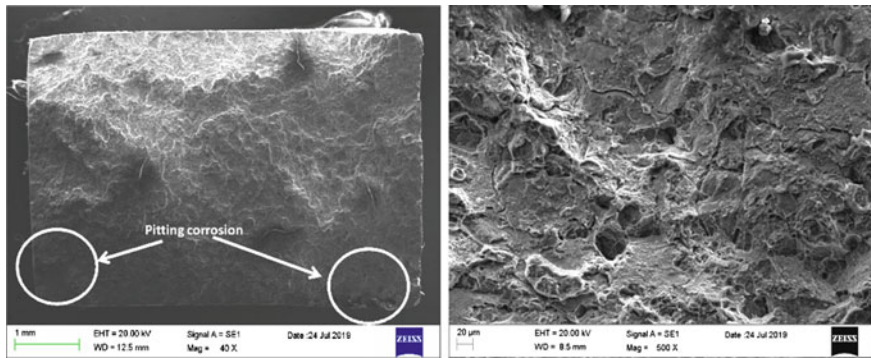


Fig. 6 Fracture morphology of AA7075-7352 alloy in NaCl solution observed after SSRT at lower and higher magnifications

4 Conclusions

The following observations are made based on the previous results.

- AA7075-T7352 with coring exhibited a corrosion rate of 0.06898 mm/yr. The corrosion morphology of the alloy examined using SEM revealed severe pitting corrosion due the presence of dendritic cast structure. This is attributed by the galvanic nature of corrosion existing between alloy matrix and the segregated phases.
- The SCC index ratio was found to be very less (0.69). The poor SCC index ratio can be attributed due to the severe pitting corrosion of the alloy during environmental exposure. As a result, the stress intensity was increased significantly resulting in sudden mechanical failure. The elongation also was suggestively reduced due to this. However, the alloy did not show any intergranular cracking.

Acknowledgements The authors would like to acknowledge the wholehearted support from Material Characterization Center, Vikram Sarabhai Space Center, Thiruvananthapuram, during the course of this study.

References

1. Andreatta F, Terryn H, de Wit J (2004) Corrosion behaviour of different tempers of AA7075 aluminium alloy. *Electrochim Acta* 49:2851–2862
2. Reboul MC, Barouxv B (2011) Metallurgical aspects of corrosion resistance of aluminium alloys. *Mat Corros* 62(3):215–233
3. Pao PS, Feng CR, Gill SJ (2000) Corrosion fatigue crack initiation in aluminum alloys 7075 and 7050. *Corros* 56:1022–1031
4. Bertonecello JCB, Manhabosco SM, Dick LFP (2015) Corrosion study of the friction stir lap joint of AA7050-T76511 on AA2024-T3 using the scanning vibrating electrode technique. *Corros Sci* 94:359–367
5. Song F, Zhang X, Liu S, Tan Q, Li D (2014) The effect of quench rate and over ageing temper on the corrosion behaviour of AA7050. *Corros Sci* 78:276–286
6. Tian W, Li S, Chen X, Liu J, Yu M (2016) Intergranular corrosion of spark plasma sintering assembled bimodal grain sized AA7075 aluminum alloys. *Corros Sci* 107:211–224
7. Gupta RK, Fabijanic D, Zhang R, Birbilis N (2015) Corrosion behaviour and hardness of in situ consolidated nanostructured Al and Al–Cr alloys produced via high-energy ball milling. *Corros Sci* 98:643–650
8. Venugopal A, Panda R, Manwatkar SK, Sreekumar L, Krishna R, Sundararajan G (2012) Effect of micro arc oxidation treatment on localized corrosion behavior of AA7075 aluminum alloy in 3.5% NaCl solution. *Trans Nonferrous Metals Society China* 22(3):700–710
9. Ma C, Lin C, Bindi L, Steinhardt PJ (2017) Hollisterite (Al₃Fe), kryachkoite (Al,Cu)₆(Fe,Cu), and stolperite (AlCu): three new minerals from the Khatyrka CV3 carbonaceous chondrite. *Am Mineral* 102(3):690–693. <https://doi.org/10.2138/am-2017-5991>

Surface Modification of Al-7075 Alloy by Electro-Discharge Coating Process Using SiC/Cu Green Compact Electrode



Lokesh Kumar Ranjan, Sujoy Chakraborty, Uttam Kumar Mandal, Vidyut Dey, and Kanishka Jha

1 Introduction

Nowadays, most engineering-based industries require high-strength but low-weight materials for various applications. Aluminum alloy is broadly used in many industrial applications owing to its various properties. Aluminum alloy fits well in this perspective [1]. Due to the good strength to mass ratio of aluminum-7075, it has been broadly used in areas like aerospace, automotive, etc. Aluminum blends have also good machinability but a limited surface finish and lack of wear behavior, but pure aluminum is not in demand for the industrial requirements [2]. To improve these properties still, various researches are going on. To increase the existing assets of the material, surface treatment is to be done. Nowadays, large number of surface treatment methodologies are being developed and also still in the development phase [3].

EDM is a novel machining mode for cutting hard material and comes under non-conventional techniques [4]. It requires a dielectric medium to operate under the machining zone, and another basic requirement of this process is the workpiece which should be in favor of the electrical side [5]. A surface development through a machining practice has emerged as a new methodology for researchers [6]. Nowadays, coating of required material is widely done by the orthodox EDM process recognized equally coating via electro-discharge machine (EDC) besides it remains under research and development phase [7].

EDC process has advantages to depositing a thin and thick layer of the required kind on the surface of the work [8]. EDC takes the potential benefits toward the overall cost of production as compared to other well-known coating techniques [9]. There are many surface coating techniques available nowadays, but these methods

L. K. Ranjan (✉) · S. Chakraborty · U. K. Mandal · V. Dey · K. Jha
Department of Production Engineering, NIT Agartala, Agartala, India
e-mail: ranjaniped@gmail.com

require much time and cost concerning too. Hence, a technique is required which can overcome these issues. EDC method has the facility to regulate the features of deposition by changing its process parameters [10].

Many pieces of research have been done using powder metallurgical tools, but the use of the SiC-Cu tool on the material Al-7075 is not yet reported. Hence, an effort has been made to deposit SiC-Cu on aluminum-7075 alloy using an electro-discharge coating process. The TWR and MDR calculated and Taguchi method have been used to get a better result under different process parameters. SEM, EDS, and XRD analysis is also carried out for the confirmation of the occurrence of the matter of tool at the exterior of the substrate.

2 Experimental Methodology

The required deposition has been carried out on a die sink electro-discharge machine. In this experiment, Sparkonix F25 die sink has been used. This EDM contains a servo head, dielectric tank, pump, control unit, etc. To maintain the required gap between workpiece and tool; a servo head is used which maintains the constant gap throughout the operation. The main process parameters in this process are compaction load, peak current, and electrode composition (Fig. 1).

2.1 Tool Electrode Preparation

For making the tool for the study, a mixture of SiC and Cu powder at different compositions were taken. In this work, the material composition for the tool was taken as 30:70, 40:60, and 50:50 ratios. In this mixture, copper serves like as a material to hold which enhances the conductance of the electrode. To make a uniform mixture, the mixture is mixed for one hour in a set of pestles plus mortar. After this, each powder stayed pressed in a pellet press of a maximum load capacity of 25 tons to prepare the electrodes. Having a thickness of 2.5 and a diameter of 13 mm.

After pellet preparation, the next step was to attach the pellet with a copper tool (extension). A silver paste (conductive) was used to join the compacted pellet part and tool extension. This complete electrode has been used for the whole experiments from which material erosion took place and get deposited over the surface of the workpiece.

2.2 Machining Procedure

For an experiment, an orthogonal arrangement under the design of experiment (DOE) has been used. The input parameters selected for the work are compaction load, peak



Fig. 1 Experimental setup of spark EDM

current, and composition. Based on the number of the trial experiment; compaction load, current, and composition these factors have been considered as the input parameter as these are the most influencing parameters for the responses. For making make the process economical, and hence Taguchi-based design of the experiment has been considered for getting an optimal result. An L-9 orthogonal array is used for the experimentation having their factor at three levels. For deposition to occur, the tool electrode is connected with positive polarity. The observed MDR was calculated by a gain in weight method. The duty cycle has been kept constant at 0.5 and test timing has been static and aimed at 4 min, and pulse duration has also been kept constant throughout the experiments. For the supply of voltage, the knob sense was adjusted at 55–60 V during the test. ANOVA has also been used by statistical software named Minitab-17. The influence of parameters has been observed using graphs and response mean value (Fig. 2; Tables 1, 2, 3, and 4).

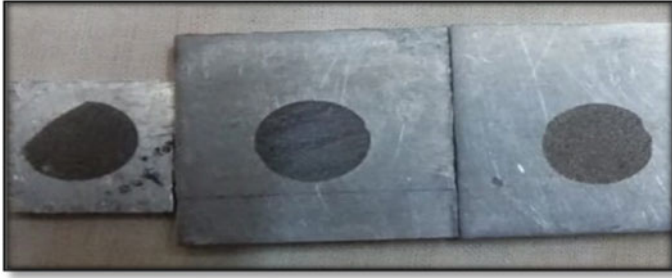


Fig. 2 Photograph of specimens after experiment

Table 1 The alloy composition of the Al-7075

Mn	Cr	Fe	Cu	Si	Zn	Ti	Mg	Al
0.3%	0.2%	0.5%	2%	0.4%	6.1%	0.2%	2.9%	balance

Table 2 L9 orthogonal array for levels and factors

Parameters	Unit	Level 1	Level 2	Level 3
Compaction Load	ton	5	10	15
Current	ampere	2	4	6
Composition	percentage	30:70	40:60	50:50

Table 3 Taguchi L9 orthogonal array

Exp. no	Input parameters		
	Compaction load (ton)	Current (Ampere)	Composition (SiC:Cu)
1	1	1	1
2	1	2	2
3	1	3	3
4	2	1	2
5	2	2	3
6	2	3	1
7	3	1	3
8	3	2	1
9	3	3	2

3 Result and Discussion

A total of nine experiments have been carried out in this study. For evaluation of MDR and TWR, the weight of the workpiece after the experiment and before the

Table 4 Experimental result of responses

Exp. no	MDR (mg/min)	TWR (mg/min)
1	0.124	4.3793
2	0.150	4.6620
3	0.385	13.6509
4	0.210	7.5015
5	0.177	5.7102
6	0.171	5.2240
7	0.107	4.9988
8	0.166	7.4317
9	0.215	5.7759

experiment was measured by a precision balance device. MDR has been intended via this Eq. 1.

$$\text{MDR} = \frac{\text{Wt of } w/p \text{ after experiment} - \text{Wt of } w/p \text{ before the experiment}}{\text{Time of experiment}} \text{mg/min} \quad (1)$$

And, TWR has been calculated by the following Eq. 2:

$$\text{TWR} = \frac{\text{Wt of the tool before experiment} - \text{Wt of the tool after experiment}}{\text{Time of experiment}} \text{mg/min} \quad (2)$$

The influence of parameter on MDR (material deposition rate) is intrigued in Fig. 3. The individual effect of process parameters, viz., compaction load, current, and composition on MDR is discussed.

Compaction Load: It is vibrant from Fig. 3 Rate of deposition is relatively more at less load of compaction, i.e., five tons, and it decreases with increase in compaction load which is due to higher bonding strength incorporated by higher compaction load.

Peak Current: It is vibrant due to increment in peak current material deposition rate is more, and highest material deposition rate is seen at highest peak current, i.e., 6A. An increase in current increases the energy content in the discharge gap resulting in higher material deposition.

Composition: It is vibrant from the figure that deposition of material rate is lower in the case of tools with a higher amount of copper. Due to the good nature of copper toward the binding affection, the transfer of material on the work surface gets reduced and hence at a higher composition ratio (70%) the less material transfer takes place.

Thus, for getting the best process parameter, we have a combination of 1-3-3. This means that for optimum material deposition rate the compaction load is five tons, current at 6 amp, and composition is 50:50.

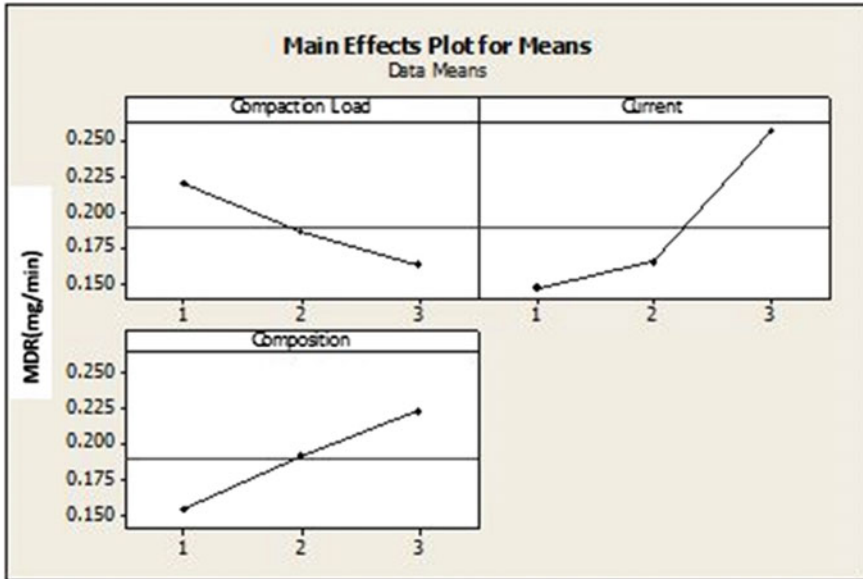


Fig. 3 Influence of i/n parameters on MDR

Similarly, the effect of process parameters on tool wear rate is plotted in Fig. 4. The individual effect of process parameters, viz., current, composition, and compaction load on TWR is discussed.

Compaction Load: It is vibrant from Fig. 4 that the wear of the tool is uppermost when the current electrode is used at less compaction load and it gradually drops with the rise in a load of compaction which is due to higher binding strength incorporated by a higher load of compaction [5].

Peak Current: It is seen that the wear of the tool rises with rising in the current (peak). The rise in the value of current rises the energy content in the discharge area that leads to the high wear of tool during the test.

Composition: From the graph plotted, it is seen that TWR is higher in the case of tools with a lower amount of copper and it increases with a decrease in the content of copper. Copper increases the binding strength of the compact. So, at a higher composition ratio (70%) the less tool wear takes place.

For the best process parameter, we have a combination of 3-1-1. This means that for optimum tool wear rate the compaction load is 15 tons, current at 2 amp, and composition is 30:70.

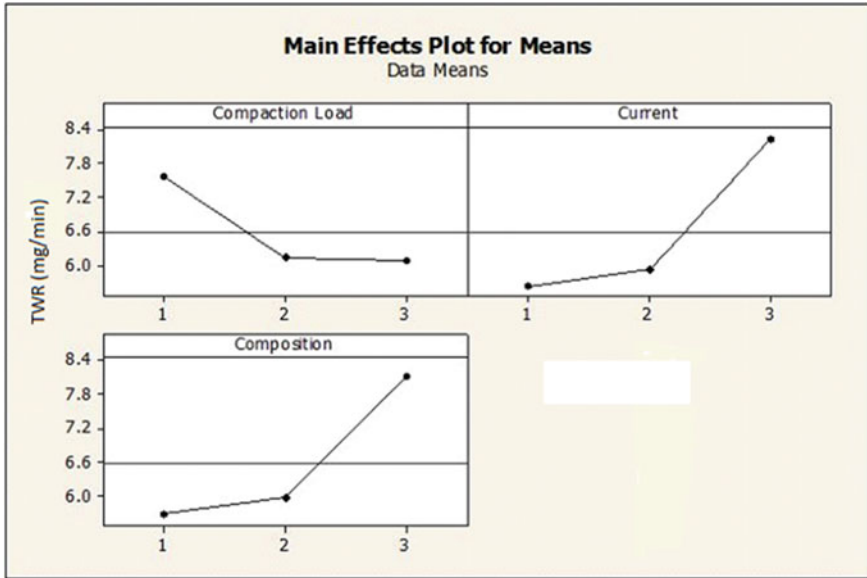


Fig. 4 Influence of *i/n* parameters on TWR

3.1 ANOVA of Response Parameters

For analysis of response, ANOVA is done at a common level supported by the p-value of responses. Report of significance level for responses is with p-value is shown in Figs. 5 and 6, respectively. The percentage number depicts the significant effects of compaction pressure, peak current, pulse duration, and tool composition on the responses.

3.1.1 ANOVA of Material Deposition Rate

Table 5 shows the results of ANOVA for MDR. Compaction load is an utmost important factor that upsetting the MDR by 50.03%, followed by tool composition and peak current as they contribute 32.24% and 14.41%, respectively, on the MDR obtained.

3.1.2 ANOVA of Tool Wear Rate

Table 6 shows the result of ANOVA for TWR. Compaction load is an utmost important factor that upsetting that. This affects the TWR via 46.33%, followed by tool composition and peak current as they contribute 39.63% and 10.67%, respectively, on the TWR obtained.

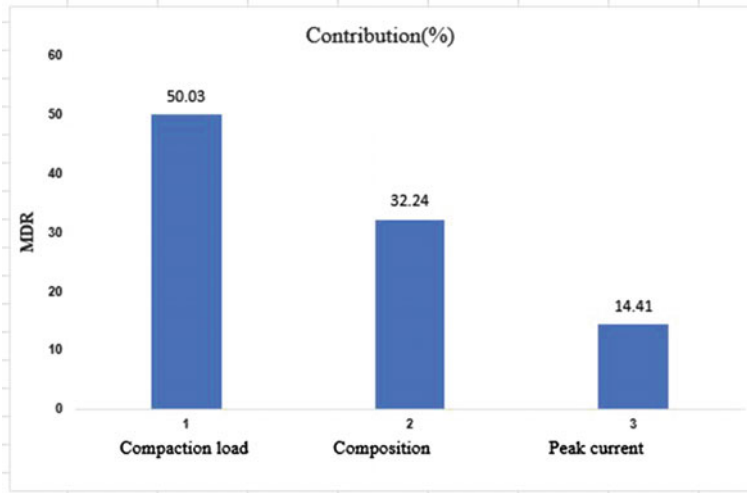


Fig. 5 Result of ANOVA for material deposition rate

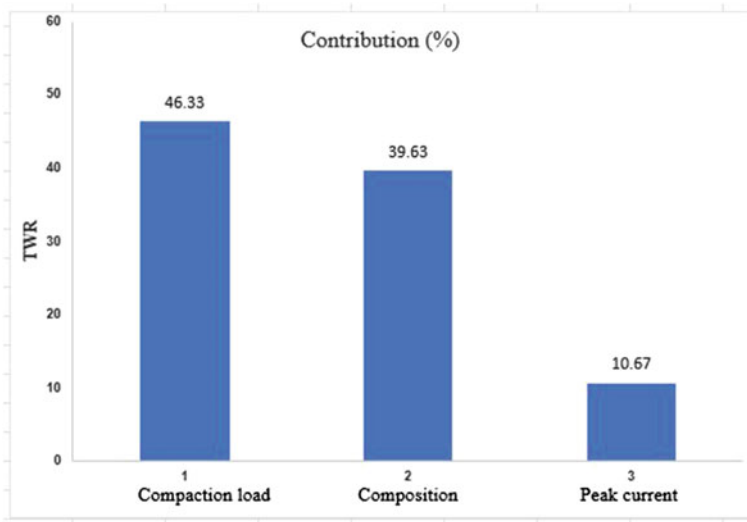


Fig. 6 Result of ANOVA for tool wear rate

3.2 Surface Characterization

Material deposition over the exterior of work was captured under SEM analysis has been shown in Fig. 7. The SEM pictures authorize the migration tool content which gets deposited on the surface of the workpiece and exists in form of a cluster. The

Table 5 ANOVA for MDR

Source	DF	SS	MS	F	p
C LOAD	2	0.004927	0.002463	0.25	0.801
Current	2	0.020988	0.010494	1.06	0.486
Compo	2	0.007233	0.003616	0.36	0.733
Error	2	0.019851	0.009925		
Total	8	0.052998			

Table 6 ANOVA for TWR

Source	DF	SS	MS	F	p
C LOAD	2	4.25	2.127	0.11	0.901
Current	2	12.014	6.007	0.31	0.764
Compo	2	10.633	5.316	0.27	0.785
Error	2	38.933	19.467		
Total	8	65.835			

image indicates the transfer of material tools and carbon particles (SiC) on the Al-7075 alloy work surface. In the figure, the specimen is treated at a compaction load of five tons, peak current 2 amp, and composition is at 40:60.

Along with the deposition, crater formation is also observed on the surface at which is clearly shown in Fig. 8. This deposition is at the compaction capacity of 10 tons, the peak current of 4 amp, and the composition is at 30:70.

An XRD analysis is also carried out to analyze surface constituents and the presence of the phases present in the deposited layer (Fig. 9). It is evident from the figure

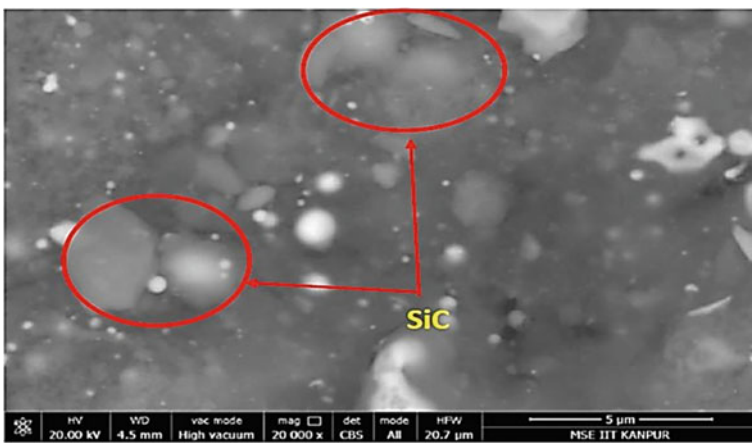


Fig.7 SEM image of the substrate at P: 5 IP: 2 Ct:40:60

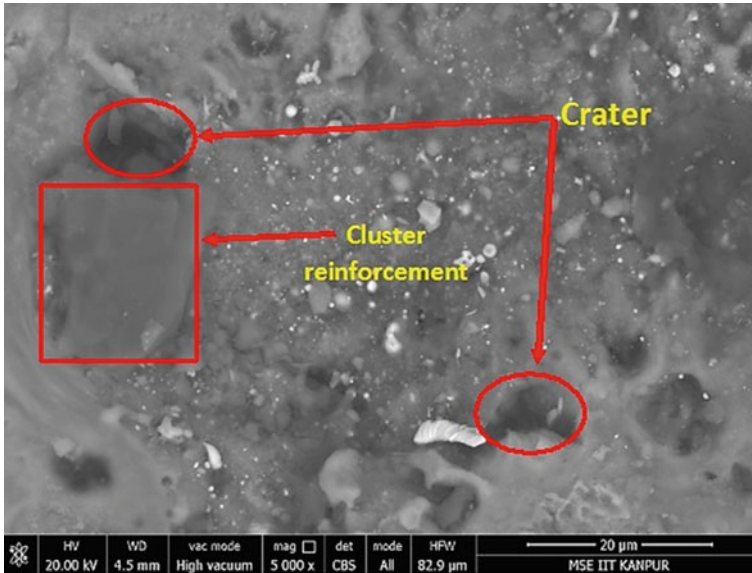


Fig. 8 SEM image of the substrate at P: 10 IP: 4 Ct: 30:70

that the different peaks of Si, SiC, Cu, and Al are present on the sample surface along with intermetallic phases of Al_2Cu . This analysis assure the transfer of tool content on the surface of the workpiece. Energy dispersive spectroscopy (EDS) analysis is also been done for the sample and shown in Fig. 10.

After deposition, all sample's cross sections were cut using EDM (wire) for measurement of the thickness of the layer. The cross-section area was polished with different grades of emery paper and the cross-section was refined with diamond paste. After that, surface of the polished cross-section was etched in Keller solution for 1 min to disclose the deposited layer over the substrate. After measurement, the average thickness layer of the samples was found $25.01 \mu m$ (Fig. 11).

4 Conclusion

In the present study, the surface modification of Al-7075 has been done with SiC-Cu powder compacted green electrode. The statistical experiment plan L-9 orthogonal array is devised and implemented. The main conclusion is listed here:

- (a) Higher MDR is achieved at increase peak current followed by a lower compact load. Moreover, less TWR is at a higher compact load and low peak current. The range of MDR is found 0.107 to 0.385 mg/min while 4.3793 to 13.6509 mg/min for TWR.

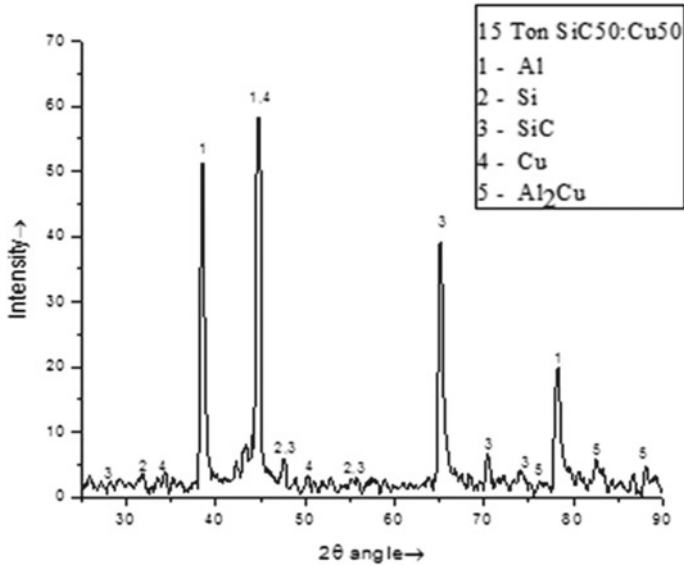


Fig. 9 XRD image of the substrate at 15 Ton and 50:50 composition

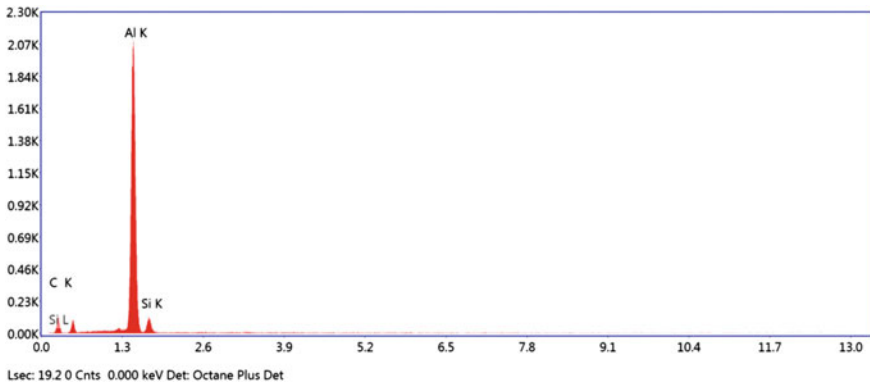


Fig. 10 EDS image of the substrate at 15 Ton and 50:50 composition

- (b) SEM, EDS, and XRD image reveal the progress of the hard film on the work surface that confirms the surface change done by the use of powder compacted electrode tool under Electro-discharge coating process.
- (c) The coating of very fine quality with fewer pores and voids was also found on the works sample. The thickness of the average coating layer is observed as 25.01 μm . ANOVA analysis is also done in this present study which shows the process parameters consequence toward responses target.

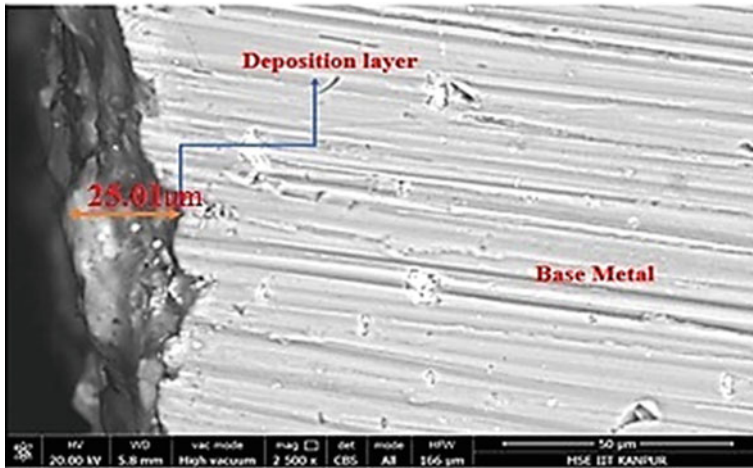


Fig. 11 SEM images of the coated layer

References

1. Tijo D, Masanta M (2014) Surface modification of aluminum by electrical discharge coating with tungsten and copper mixed powder green compact electrodes. In 5th International and 26th All India Manufacturing Technology, Design and Research Conference, Guwahati, Assam, p 190
2. Chakraborty S, Kar S, Dey V, Ghosh SK (2017) Optimization and surface modification of al-6351 alloy using SiC–Cu green compact electrode by electro discharge coating process. *Surf Rev Lett* 24(01):1750007
3. Krishna ME, Patowari PK (2014) Parametric study of electric discharge coating using powder metallurgical green compact electrodes. *Mater Manuf Processes* 29(9):1131–1138
4. Beri N, Pungotra H, Kumar A (2012) To study the effect of polarity and current during electric discharge machining of Inconel 718 with CuW powder metallurgy electrode. In: Proceedings of the National Conference on Trends and Advances in Mechanical Engineering, Faridabad, Haryana, pp 476–481, October
5. Chakraborty S, Kar S, Ghosh SK, Dey V (2017) Parametric optimization of electric discharge coating on Aluminium-6351 alloy with green compact silicon carbide and copper tool: a Taguchi coupled utility concept approach. *Surf Interfaces* 7:47–57
6. Gill AS, Kumar S (2016) Surface roughness and microhardness evaluation for EDM with Cu–Mn powder metallurgy tool. *Mater Manuf Processes* 31(4):514–521
7. Hwang YL, Kuo CL, Hwang SF (2010) The coating of TiC layer on the surface of nickel by electric discharge coating (EDC) with a multi-layer electrode. *J Mater Process Technol* 210(4):642–652
8. Janmanee P, Muttamara A (2012) Surface modification of tungsten carbide by electrical discharge coating (EDC) using a titanium powder suspension. *Appl Surf Sci* 258(19):7255–7265
9. Patowari PK, Saha P, Mishra PK (2015) An experimental investigation of surface modification of C-40 steel using W-Cu powder metallurgy sintered compact tools in EDM. *Int J Adv Manuf Tech* 80(1):343–360
10. Chakraborty S, Kar S, Dey V, Ghosh SK (2018) Multi attribute decision making for determining optimum process parameter in EDC with Si and Cu mixed powder green compact electrodes

Effect of Heat Input on Corrosion Resistance of 316 Austenitic Stainless Steel Cladding on Low-Carbon Steel Plate



Soumak Bose  and Santanu Das 

1 Introduction

Cladding concerns with thick deposition of a wear-resistive material on a base material [1, 2]. To reduce production cost, every manufacturing industry uses cheap material like low alloy structural steel to produce all products [3, 4]. But to increase their durability, hardness and for achieving desire properties, surface treatment is required [5, 6]. Corrosion and erosion are a vital problem for these cheap corrosion-prone materials. Corrosion is a danger thing which cannot be totally eliminated but it can be prevent little more. There are many process available to fight against corrosion like anodizing, physical vapor deposition, electroplating, weld cladding, etc., from these, weld cladding is much dependable process [7, 8]. Among different weld cladding techniques, gas metal arc welding (GMAW) is much reliable and economically suitable process for commercial purpose [9, 10].

As GMAW has wide application on various materials, specially, stainless steel, and it has relatively high productivity maintaining quality of welding supported by servo-controlled wire feeding mechanism, and thus can be easily automated or robotized, GMAW is chosen as the cladding technique [11, 12]. In this experiment, ESAB India made Auto K 400 GMAW machine is used to deposit 316 austenitic stainless steel (with 1.2 mm diameter wire electrode) upon low-carbon steel plate. In this particular model of GMAW machine, welding current and welding voltage can be controlled. Three variables (weld current, open-circuit voltage and travel speed of weld torch) are chosen for experimentation to explore the nature of variation of bead geometry.

S. Bose · S. Das (✉)

Department of Mechanical Engineering, Kalyani Government Engineering College, Kalyani, Nadia, West Bengal 741235, India
e-mail: santanu.das@kgec.edu.in

Table 1 Constituents of the substrate in %

C	Si	Mn	P	S	Cr	Mo
0.313	0.161	0.62	0.08	0.041	0.029	0.016
Ni	Al	Co	Cu	Nb	Ti	V
0.03	0.005	0.01	0.081	0.014	<0.001	0.002
W	Sn	Ce	B	N	Mg	Fe
0.007	0.012	0.007	0.001	0.012	0.008	98.4

Table 2 Constituents of the filler (316) in %

C	Si	Mn	P	S	Cr	Mo
0.077	0.182	1.102	0.029	0.008	15.046	2.091
Ni	Al	Co	Cu	Nb	Ti	V
9.937	0.01	0.074	0.342	0.002	0.032	0.047
W	Sn	Ce	B	Fe		
0.026	0.01	0.01	0.001	<70.952		

2 Experimental Setup

2.1 Base Plate for GMAW Cladding

Corrosion-prone low-carbon steel plates having dimension 60 mm × 75 mm × 25 mm are chosen as the substrate. Table 1 shows chemical composition of these plates.

2.2 Filler Wire for GMAW Cladding

316 austenitic stainless steel wire having diameter 1.2 mm is used as solid filler wire electrode. Table 2 depicts the constituent elements of this filler wire.

2.3 Experimental Set Up for Cladding Operation

Auto K 400 model of GMAW machine of ESAB is employed in this experimental investigation (Figs. 1 and 2). Welding torch is mounted on a motor-driven small vehicle. Speed of the vehicle can be regulated and it is driven along a straight way. Maintained a constant torch angle of 75° between welding gun and work table with the help of a fixture. Only CO₂ gas is supplied as the gas shield with 15 lit/min flow

rate. So, it is a MAG welding. For measuring bead geometry, GIPPON advanced stereo microscope (Japan made) is used.



Fig. 1 ESAB, India made auto K 400 GMAW machine



Fig. 2 Welding gun mounted on motor-driven vehicle

2.4 *Experimental Setup for Macro Hardness Testing*

Macro hardness of test samples is measured by Rockwell hardness testing machine (Make: Fine Testing Machine, India, Model No.: TSM/FTM, Sl. No. 97/068). Hardness of the test samples is measured on three different zones in C scale by applying 150 kg load with diamond indenter, and then, these values are averaged. For hardness testing, surfaces of test samples are made rust free and smooth.

3 Experimental Procedure

3.1 *Trial Runs*

As suitable parametric combination is required to get an optimal cladding outcome, so before going to actual cladding experiment, there are numbers of trial runs done to make weld bead on low-carbon steel plate. It helps to set the range of welding process parameters to carry out this experiment. More than a few trial runs were made for selecting the appropriate range. Each weld bead is cut crosswise and polishes up to mirror finish, then measured to find bead geometry like width, reinforcement and penetration by using GIPPON advanced stereo microscope (Japan made). Different beads on plate were made which are shown in Fig. 3. By using one variable at a time approach, weld current, open-circuit voltage and travel speed are selected in the range of 175–210A, 25.5–30 V and 360–420 mm/min, respectively, and the corresponding heat input is calculated. Average height of reinforcement of all weld beads was between the ranges of 2.519 to 3.808 mm.



Fig. 3 Bead on plate during trial runs

Table 3 Experimental details

Sl. no	Sample no	Welding current (A)	Open-circuit voltage (V)	Torch travel speed (mm/min)	Heat input (kJ/mm)
1	MC ₁	175	30	420	0.6
2	MC ₂	210	25.5	360	0.714
3	MC ₃	210	30	390	0.775

3.2 Cladding Operation

For cladding operation, austenitic stainless steel electrode is used upon MS base plate using the process variables obtained from trial runs as detailed in [13]. For cladding operation, after cleaning the base plate, 50% overlaps of the bead are taken similar to that reported in [14] [15]. The same cladding procedure is replicated twice, taking the total number of clad workpiece to 6. Table 3 shows experimental details.

3.3 Corrosion Test Setup

Clad base plates are cut down in specific dimension, i.e., (10×10) mm² for corrosion test. After cutting and polishing, weights of samples are taken in a weighing machine (Model: PGB200, WENSAR) with a readability up to 0.001gm. Then coated test specimens are covered by Teflon tapes except clad area. Then all samples are deep in a corrosive medium for 24 h [16] that is made with 30gm ferric chloride, 27 ml HCl and 73 ml distilled water [17]. After 24 h, all samples are removed from corrosive medium and cleaned by plane water. Then dried it and weighed again. Difference between initial and final weight gives the result of weight loss by corrosive medium. Corrosion rate is found by using Eq. (2). Pits present are counted under the stereo microscope.

4 Results and Discussion

4.1 Results Obtained from Macro Hardness Test

Macro hardness values are obtained by Rockwell hardness testing machine on three different zones of the test samples in C scale by applying 150 kg load with diamond indenter. As austenitic stainless steel filler wire electrode contains large quantity of chromium, molybdenum, nickel, etc., which are hardening materials, hardness value is much more on the clad zone than on the low-carbon steel base metal. Table 4 shows the hardness value of base plate, Table 5 shows the hardness value of austenitic

Table 4 Hardness measurements of base plate

Hardness value (HRC)					
1st	2nd	3rd	4th	5th	Average
40	37	34	36	33	36

Table 5 Hardness measurements of austenitic stainless steel wire electrode

Hardness value (HRC)					
1st	2nd	3rd	4th	5th	Average
43	44	39	38	42	41.2

Table 6 Hardness on clad samples

Replications	Sl. no	Heat input (kJ/mm)	Hardness value on the clad zone (HRC)			
			1st value	2nd value	3rd value	Average value
First replication	MC ₁	0.6	59	60	56	58
	MC ₂	0.714	58	56	55	56
	MC ₃	0.775	55	55	53	54
Second replication	M'C ₁	0.6	56	57	59	57
	M'C ₂	0.714	54	57	56	56
	M'C ₃	0.775	51	55	54	53

stainless steel wire electrode and Table 6 shows the hardness values of austenitic stainless steel clad test specimens of both replications by GMAW process.

The hardness results show that hardness values of austenitic stainless steel clad test specimens in the clad zone are in the range of 53.33 HRC to 58.33 HRC, whereas the average hardness value of austenitic stainless steel wire electrode is found to be 41.2 HRC and the average hardness value of low-carbon base plate is found to be 36 HRC.

Figure 4 shows decreasing hardness values of the clad specimens made with increasing heat input from 0.6 kJ/mm to 0.775 kJ.mm. This may be due to lower nitrogen absorption at high heat input. Nitrogen absorption plays an important role on hardness that can be affected by higher heat input and shielding gas.

4.2 Results Obtained from Corrosion Test

Corrosion test results of the MS substrate are given in Table 7. Rate of pitting corrosion and counted number of pits/cm² of clad samples is given in Table 8. Pitting corrosion rate of austenitic stainless steel clad test specimen decreases remarkably than the low-carbon steel base plate. Pitting corrosion rate as well as number of pits

Fig. 4 Variation of hardness (HRC) with heat input

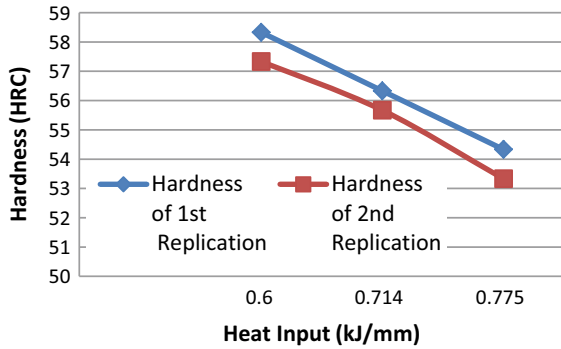


Table 7 Results of corrosion test of MS substrate

Substrate	Area (mm ²)	Weight loss (gm)	Corrosion rate (gm/m ² hr)
Low-carbon steel (MS)	10 × 10	1.003	417.917

count per unit area (count/cm²) increases with increasing heat input. Presence of large amount of chromium, molybdenum, nickel, etc., in austenitic stainless steel is the main cause behind the corrosion resistive property.

Both Figs. 5 and 6 show remarkable increase in pitting corrosion rate on the clad specimens with increasing heat input.

Elmer et al. [3] demonstrated that high ratio of Cr and Ni solidifies with α -phase primarily. Because of short timing of solid-state transformation from ferrite (α) to austenite (γ), the ferrite content of these alloys increases with increasing cooling rate. With decreasing cooling rate, the final microstructure would be single-phase ferrite with second-phase austenite. On the other hand, low Cr-Ni ratio alloys solidify with austenite as primary phase. Because of high cooling rate, solute redistribution during solidification is reduced, ferrite content also decreases. With decreasing cooling rate, ferrite precipitates from austenite and form primary γ -phase with secondary α -phase.

Austenitic stainless steel electrode contains approx. 15% Cr, 2% Mo, and 10% Ni. For austenitic stainless steel electrode, Cr and Ni equivalent are 17.43 and 12.76. High heat input causes low cooling rate and so, with increasing heat input, more time availability for solid-state transformation may cause more ferrite precipitation from austenite.

Table 8 Results of pitting corrosion test of clad specimens of two replications

Replications	Sample no	Heat input (kJ/mm)	Welding voltage (V)	Welding current (A)	Torch travel speed (mm/min)	Weight loss (gm)	Pitting corrosion rate (gm/m ² hr)	Average pitting corrosion rate (gm/m ² hr)	No. of pits (count/cm ²)	
1st	MC ₁	A	30	175	420	0.270	112.58	114.17	701	
		B				0.278	115.76			
	MC ₂	A	25.5	210	360	0.326	135.7	137.29	814	
		B				0.333	138.88			
	MC ₃	A	0.775	30	210	390	0.377	157.16	158.75	916
		B					0.385	160.34		
2nd	M'C ₁	A	30	175	420	0.253	105.5	107.09	586	
		B				0.261	108.68			
	M'C ₂	A	0.714	25.5	210	360	0.354	147.37	148.96	1016
		B					0.361	150.55		
	M'C ₃	A	0.775	30	210	390	0.497	206.96	208.55	1391
		B					0.504	210.14		

Fig. 5 Variation of pitting corrosion rate with heat input for first replication

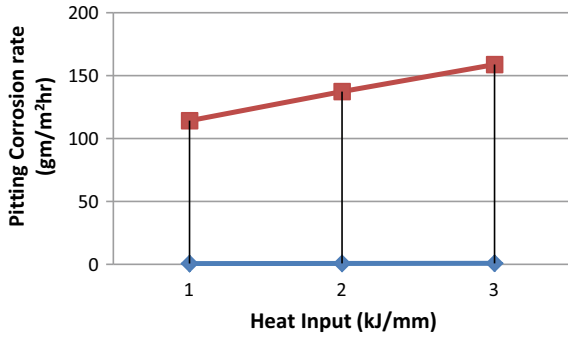
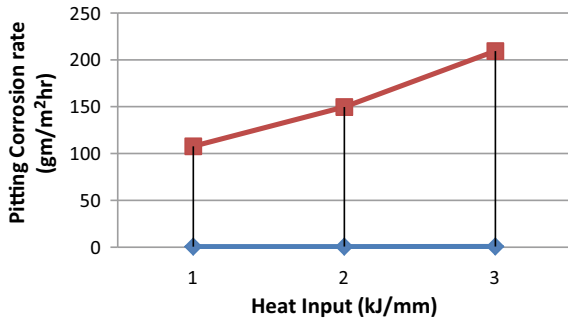


Fig. 6 Variation of pitting corrosion rate with heat input for second replication



4.3 Results of Number of Pits Count from Pitting Corrosion Test Samples of Both Replications by GMAW Cladding

Using a microscope, number of pits on corroded surface of test samples is counted. Microscopic views of all corroded surfaces of those samples are depicted in Fig. 7, 8, 9, 10, 11, and 12 and counted number of pits/cm² is given in Table 8.

Pitting corrosion is a minor hole or pit that is exerted on the corroded surface of corrosion-prone material. It penetrates and attacks the surface swiftly [4] and is difficult to identify. From Fig. 7, 8, 9, 10, 11 and 12, number of counted pits/cm² clearly indicates that number of pits/cm² is affected by heat input, hardness and pitting corrosion rate. Number of pits/cm² increases with increasing pitting corrosion rate and heat input, and decreasing hardness. Results show that number of pits per unit area is minimum with a heat input of 0.6 kJ/mm.

5 Conclusion

After the experimental investigation on cladding on MS substrate, it can be concluded that:

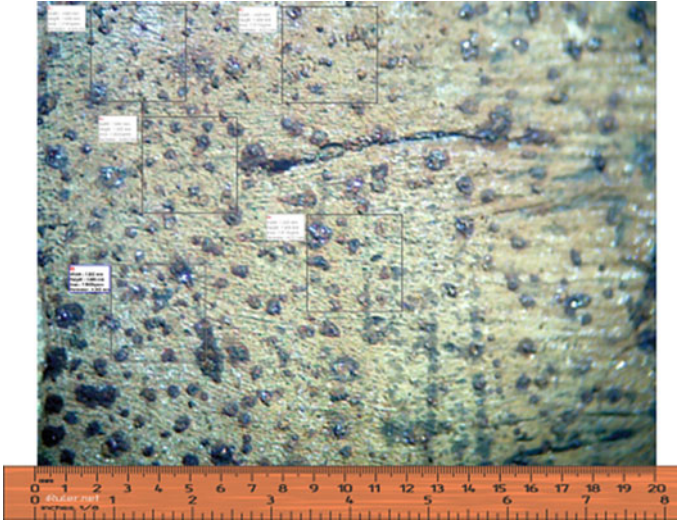


Fig. 7 Microscopic view of corroded test sample (MC₁) [Area of clad portion: $6.54 \times 4.84\text{mm}^2$, No. of pits counted = $701/\text{cm}^2$, heat input = 0.6 kJ/mm]

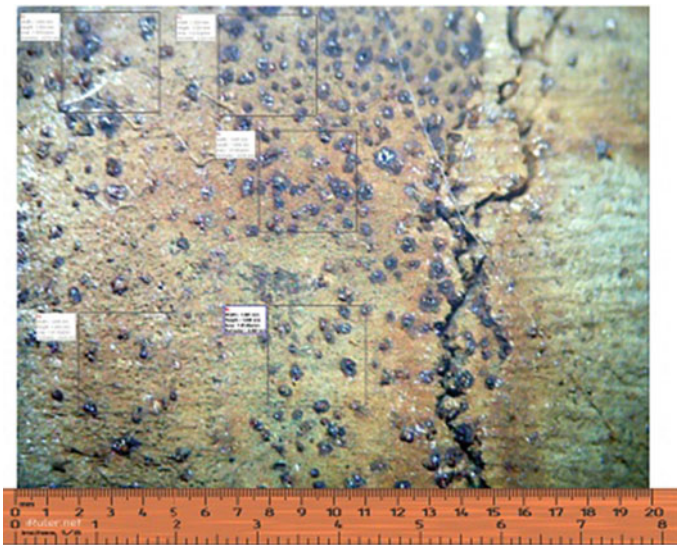


Fig. 8 Microscopic view of corroded test sample (MC₂) [Area of clad portion: $6.54 \times 4.84\text{mm}^2$, No. of pits counted = $814/\text{cm}^2$, heat input = 0.714 kJ/mm]

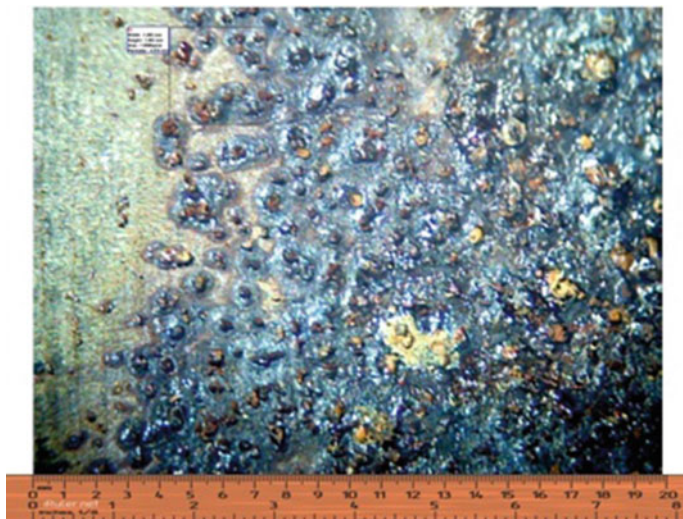


Fig. 9 Microscopic view of corroded test sample (MC₃) [Area of clad portion: $6.54 \times 4.84\text{mm}^2$, No. of pits counted = $916/\text{cm}^2$, heat input = 0.775 kJ/mm]

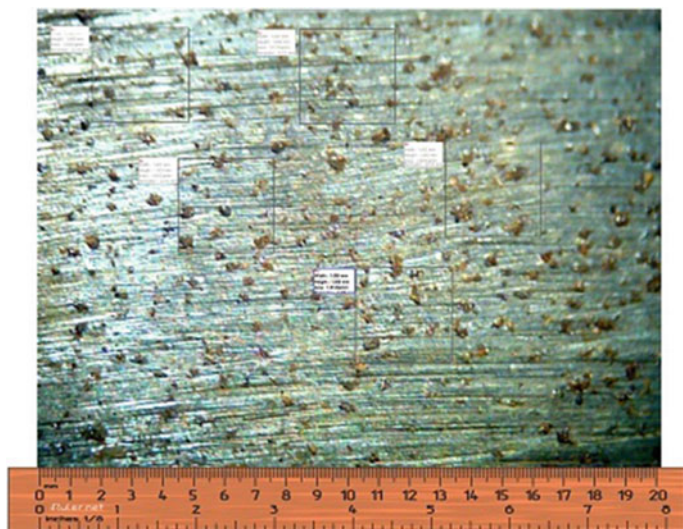


Fig. 10 Microscopic view of corroded test sample (M¹C₁) [Area of clad portion: $6.54 \times 4.84\text{mm}^2$, No. of pits counted = $586/\text{cm}^2$, heat input = 0.6 kJ/mm]

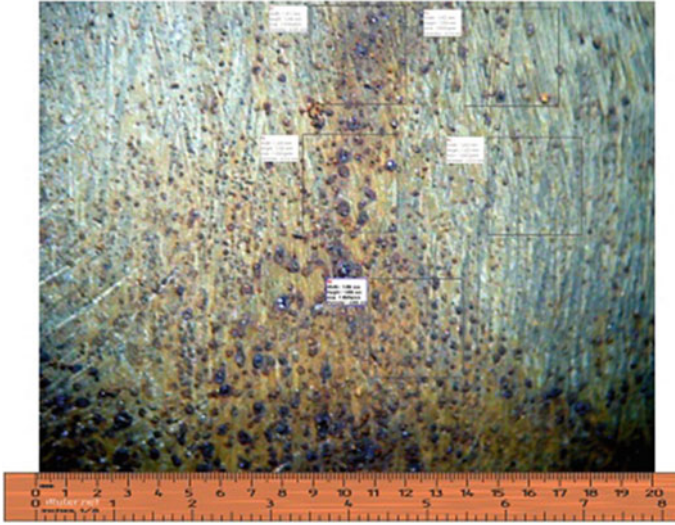


Fig. 11 Microscopic view of corroded test sample (M^1C_2) [Area of clad portion: $6.54 \times 4.84\text{mm}^2$, No. of pits counted = $1016/\text{cm}^2$, heat input = 0.714 kJ/mm]

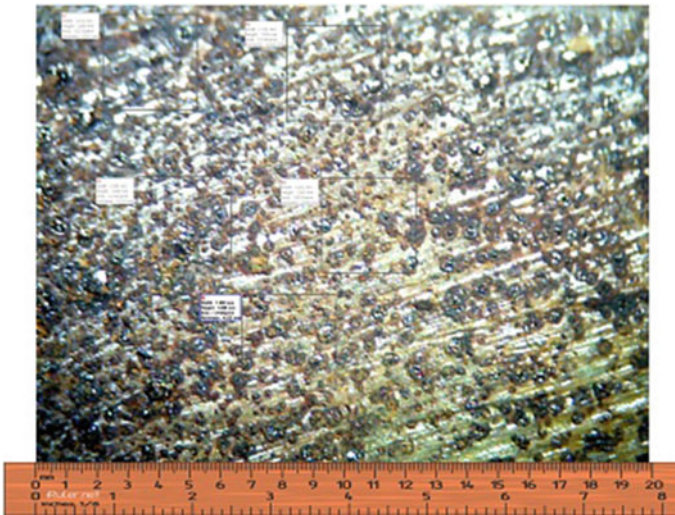


Fig. 12 Microscopic view of corroded test sample (M^1C_3) [Area of clad portion: $6.54 \times 4.84\text{mm}^2$, No. of pits counted = $1391/\text{cm}^2$, heat input = 0.775 kJ/mm]

- Hardness of the clad portion is much higher than the low-carbon base plate for gas metal arc welding cladding practices.
- Macro hardness test results point to hardness decreases with the increase of heat input in GMAW (MAG) clad portion. This may be due to lower nitrogen absorption at high heat input.
- By studying the results of corrosion test, it can be pointed out that corrosion rate of cladding with austenitic stainless steel wire electrode in MAG cladding process increases with increasing heat input.
- With increasing pitting corrosion rate and heat input, numbers of pits on corroded surface are found to be increased.
- For GMAW cladding, least pitting corrosion rate is found at the lowest heat input of 0.6 kJ/mm with 30 V open-circuit voltage, 175A welding current and 420 mm/min torch travel speed. So, this parametric combination may be recommended for industrial practice.

References

1. Smith WF, Hashemi J, Prakash R (2012) *Material science & engineering*, 4th edn. Tata-McGraw Hill
2. Elmer JW, Allen SM, Eager TW (1989) Microstructural development during solidification of stainless steel alloy. *Metall Trans A* 20A(10):2117–2131
3. Ahmad Z (2006) *Principles of corrosion engineering and corrosion control*. Elsevier Ltd., pp 120–270
4. Karadeniz E, Ozsarac U, Yildiz C (2007) The effect of process parameters on penetration in gas metal arc welding processes. *Mater Des* 28:649–656
5. Sabiruddin K, Das S, Bhattacharya A (2009) Application of analytical hierarchy process for optimization of process parameters in GMAW. *Indian Welding J* 42(1):38–46
6. Chakraborty B, Das H, Das S, Pal TK (2013) Effect of process parameters on clad quality of duplex stainless steel using GMAW process. *Trans Indian Institute Metals* 66(3):221–230
7. Verma AK, Biswas BC, Roy P, De S, Saren S, Das S (2013) Exploring quality of austenitic stainless steel clad layer obtained by metal active gas welding. *Indian Sci Cruiser* 27(4):24–29
8. Senthilkumar B, Birundha P, Kannan T (2014) Modelling and simulation of austenitic stainless steel claddings deposited by GMAW. *Int J Sci Eng Res* 5(5):363–370
9. Saha MK, Sadhu S, Ghosh P, Mondal A, Hazra R, Das S (2020) Dependency of bead geometry formation during weld deposition of 316 stainless steel over constructional steel plate. *Adv Eng Optimization Through Intelligent Tech* 949(5):417–429
10. Verma AK, Biswas BC, Roy P, De S, Saren S, Das S (2014) On the effectiveness of duplex stainless steel cladding deposited by gas metal arc welding. In: *Proceeding of the 6th IIW Annual Assembly and International Conference*, Seoul, Korea
11. Verma AK, Biswas BC, Roy P, De S, Saren S, Das S (2017) An investigation on the anti-corrosion characteristics of stainless steel cladding. *Indian Welding J* 50(3):52–63
12. Giriya S, Mudali K, Andreev C, Raj B (2012) Corrosion behavior of nitrogen-containing stainless steel in nitric acid and chloride environments. *Corrosion* 68(10):922–931
13. Paulraj P, Garg R (2016) Effect of welding parameters on pitting behavior of GTAW of DSS and super DSS weldments. *Eng Sci Tech* 19(2):1076–1083
14. Zunaka L, Kalyankar VD (2021) On the performance of weld overlay characteristics of Ni-Cr-Si-B deposition on 304 ASS using synergetic pulse-GMAW process. *Sci Technol Weld Joining* 26(2):106–115

15. Caley F et al (2009) Probability distribution of pitting corrosion depth and rate in underground pipelines. *Corros Sci* 51:1925–1934
16. Saha MK, Hazra R, Mondal A, Das S (2019) Effect of heat input on geometry of austenitic stainless steel weld bead on low carbon steel. *J Institution Engineers (India): Series C* 100(4):607–615
17. Mondal J, Saha MK, Das S (2021) Investigation on corrosion resistance of 316 γ stainless steel clad constructional steel. *Manuf Tech Today* 20(3–4):8–16

Surface Characterization of Miniature Structures for Electronic Device Manufacturing



Swarup Paul

1 Introduction

Research works on fabrication and characterization of electronic devices at the micro level are advancing rapidly. During fabrication of the structures, material consideration plays an important role to increase the efficiency and reduce the size of the devices [1–3]. Characterization of the fabricated devices is important with a view to their classification based on which application of the devices can be meaningfully explored in different situations [4, 5]. In 2001, Simonetti et al. developed a quantum model of metal oxide semiconductor. The model is used in accumulation to extract the oxide thickness of N^+ polycrystalline silicon– SiO_2 –P silicon capacitors in the range of 2–5 nm. They also discussed the influence of tunneling current [6]. In the same year, Soliman et al. [7] determined the intermediate layer thickness of miniature structures. They applied electrical capacitance and voltage (C–V) for the measurement purpose. Authors compared the results for two such devices with the same intermediate thickness but different surface areas. It was observed that the device of large area is capable of giving accurate results by classical method, but it is not suitable for the smaller one. They suggested a new method for precise calculating the intermediate layer thickness of smaller devices [8]. In 2003, S. Kaschieva studied surface characteristics of miniature devices by the application of current generated during the process of irradiation through thermal stimulation. They explained that concentration of interface traps of those miniature structures mainly depends on the ion implantation during radiation inducing process [9]. In 2001, S. Neimchoroen et al. investigated the bias effects of the current on miniature structures through optical illumination of both dc and ac conditions. They calculated their dc and low-frequency photoresponse properties together with optoelectronic conversion function. These

S. Paul (✉)

Production Engineering Department, National Institute of Technology, Agartala, Tripura, India
e-mail: pswarup2008@gmail.com

miniature structures gave response to an appreciable voltage controllability of the photo current on the device [10]. In the year of 2004, Jian-Baixia et al. reviewed some work in the field of semiconductor nanostructures including semiconductor clusters, self-assembled quantum dots, and diluted magnetic semiconductor quantum dots [11]. In 2005, S. E. Tyaginor et al. investigated simulation study miniature structures using current–voltage characteristics. They focused investigations considering the effect of spatial non-uniformity of the oxide layer. The variation of the averaged current density is simulated dependent on the ratio between the gate dimensions and the characteristic length of thickness variations. They also shared some experimental observations related to the oxide thickness statistics [12]. In 2004 N. Conofaos investigated MOS devices replacing SiO_2 layer by silicon oxy-nitride film grown on Si substrates by CVD. Electrical measurements were done by I–V and C–V characteristics. The analysis of the data also took into account the presence of traps at the Si/SiON interface calculated by a fast conductance technique [13]. Ranuacraz et al. [14] in the year of 2006, studied MOS devices, caused by carriers tunneling through a classically forbidden energy barrier. They reviewed the physical mechanism tunneling in an MOS structure. The modeling approach to gate current used in several compact MOS models is presented and compared [15].

However, in this present work, three types of metal-insulator-semiconductor devices have been fabricated by E-beam technique using physical deposition method, and I–V characteristics of each device have been measured by means of KEITHLEY, 238 high current source measure unit set up which instantaneously provides current–voltage characteristics of the devices. Two types of studies with each device have been investigated, viz., metal grounded and silicon grounded to compare their performances. Now using current–voltage characteristics, graphs of $1/A$ versus $\ln I_0$ are developed with a view to clarify the devices for their particular application.

2 Experimental Methods and Materials

The experimental work comprises mainly of the following stages:

1. Fabrication of the device.
2. The study of current–voltage characteristics of the MIS structure, with and without illumination.

A metal mask has been first prepared satisfying the required dimensions and using it, the device is fabricated. The fabrication of the device consists of the following steps, viz., mask preparation, wafer cleaning, oxidation, and metallization. These steps are described in detail later. The study of current- voltage characteristics of the device has been carried out using “KEITHLEY 238 HIGH SOURCE MEASURE UNIT”. The complete arrangement is shown in Fig. 1.



Fig. 1 Arrangement for experiment with MIS device (under illumination for studying volt-ampere characteristics, using Keithley, 238 high source measure units)

3 Fabrication of the Device

An *n*-type silicon substrate is taken as the wafer. Their specifications are:

Diameter = 2 inches.

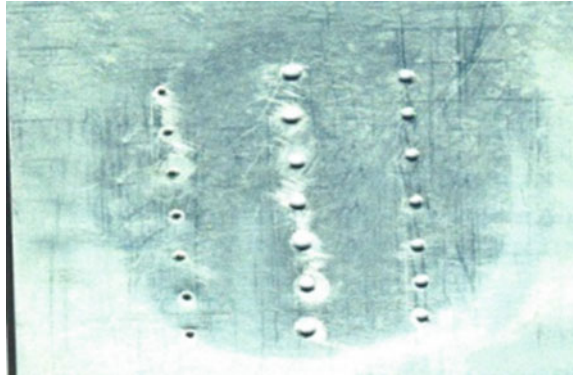
Thickness = 500 micron.

Orientation = $\langle 111 \rangle$.

Here, $\langle 111 \rangle$ is the Miller indices of the crystal and is used to specify directions and planes of the lattice or crystal. The fabrication of the device has been carried out in the following steps.

3.1 Mask Preparation

An aluminum sheet of thickness 0.035 inches is taken and a circle of radius 1-inch is drawn using a compass. Inside the circle, large number of dots are punched using a center punch. The mask is then cleaned by sand paper and acetone. The mask, thus prepared, is shown in Fig. 2.

Fig. 2 Aluminum mask

3.2 Wafer Cleaning Steps

There are standard procedures for the wafer cleaning. The sequential steps which are followed for the present study are mentioned below.

1. Cleaned in deionized water.
2. Rinsed in warm (50C) trichloroethylene (TCE) ultrasonically for few minutes.
3. Rinsed in warm acetone for two minutes.
4. Ultrasonic cleaning in hot deionized water for five minutes is done.
5. Dipped in dilute warm HCL/HNO₃ for few minutes.
6. Dipped in methanol for five minutes.
7. Alternately dipped in HF and deionized water till the wafer is hydrophobic.

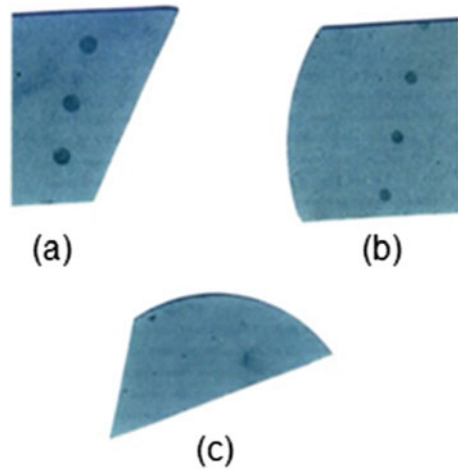
3.3 Oxidation

The hydrophobic wafer is dipped in HNO₃ for 1 min, and then it is exposed to open air/atmosphere for few seconds. Here, HNO₃ acts as an oxidizing agent and oxides Si–SiO₂. Thus, we have approximately 70–100 angstrom oxide (SiO₂) layer is formed on top of the *n*-type substrate.

3.4 Metallization

The metal mask is cleaned with acetone and then dried in open air. The oxidized sample is then placed on a substrate holder and metal mask is placed over it. The whole thing is tied with the help of printed circuit board (PCB) masking tape such that there is no movement of mask and the oxidized sample. The metallization of the device is done with the help of a “Vacuum Coating Unit” shown in Fig. 3.

Fig. 3 Fabricated devices of different diameters **a** 1.98 mm **b** 1.5 mm **c** 0.9 mm



4 Results and Discussion

The current-voltage characteristics of the fabricated device have been measured by using a H.P semiconductor measurement system (KEITHLEY, 238 high current source measure unit). The measurements were done by proper biasing of the metal with respect to semi conductor or vice-versa. Semiconductor is biased positively with respect to metal first, and then the semiconductor is biased negatively with respect to the metal and measurements are repeated. The results are plotted through Figs. 4, 5, and 6. The I–V characteristics of the diodes with metal ground and silicon ground have been attained for three diameters (0.9, 1.5, and 1.9 mm) of the metal dot. When diameter increases the amount of space charge increases and there by current increases. For larger diameters, variation of increase of current is small. It is also observed from Figs. 4 to 5 that in case of metal grounded, low applied voltage is required than that of silicon grounded to generate same current, and this is not the exactly same for Fig. 6, i.e., for the largest diameter of 1.9 mm. Silicon grounded device is required low voltage than that of metal grounded device to produce same current.

The volt-ampere characteristics are called static characteristics and can be described by the d.c behavior of the diode. These characteristics can be described by the analytical equation called Boltzmann diode equation. Now for checking the Schottky barrier formation, the following graphs (Figs. 7, 8 and 9) of $1/A$ versus $\ln I_0$ are developed. From Figs. 7 and 8, it is seen that $1/A$ versus $\ln I_0$ characteristics are linear and passing through the origin. It appears that the behavior of the curve is similar to a Schottky barrier junction. This is due to the fact that the insulating layer is very thin. For the device of 1.9 mm, the characteristics of $1/A$ versus $\ln I_0$ (Fig. 9) are linear but not passing through the origin. Here, tunnel current component is existing and the device behaves like a tunnel diode.

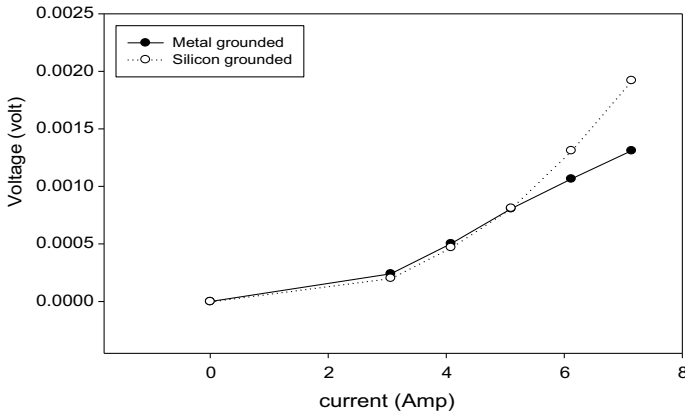


Fig. 4 I-V characteristics of M-I-S diode (dia 0.9 mm)

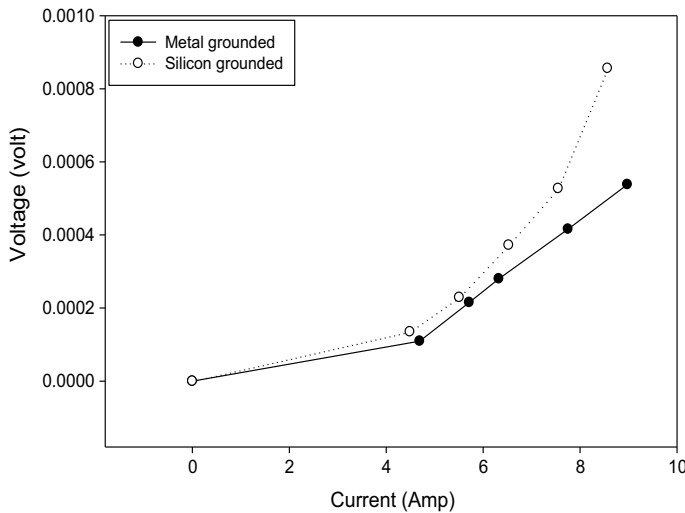


Fig. 5 I-V Characteristics of M-I-S diode (dia 1.5 mm)

5 Conclusion

In MIS structure, a very thin insulating layer is present between metal and semiconductor layer. Since the thickness of insulating layer is very narrow always there is some probability of tunneling of electron through this narrow insulating layer. For that reason, small tunnel current must exist through this MIS structure. The results can be further explained by considering tunneling component of current. But for a metal-insulator-semiconductor diode, the current voltage characteristics critically depend on the insulator thickness. If the insulator layer is sufficient thick

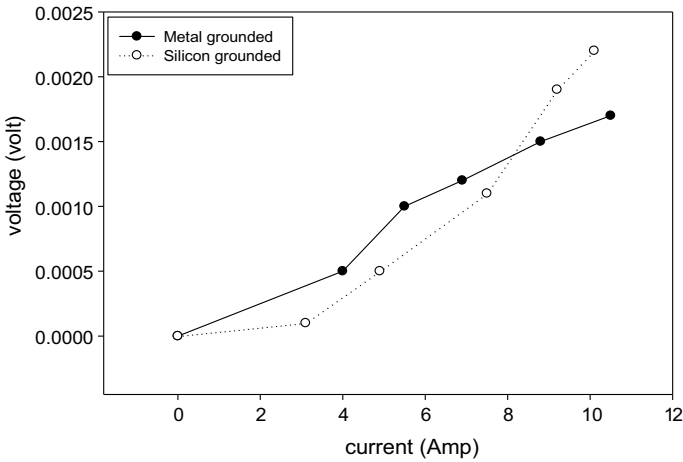


Fig. 6 I-V characteristics of M-I-S diode (dia 1.9 mm)

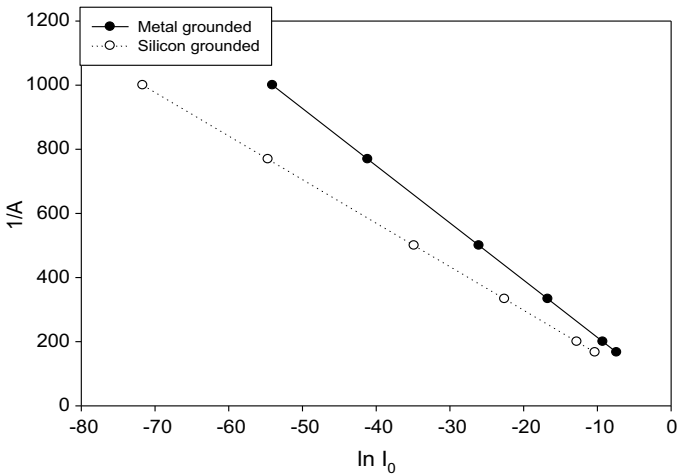


Fig. 7 Variation of 1/A versus Ln I₀ (MIS diode of dia 0.9 mm)

(>50 angstrom for the silicon di oxide system), carrier transport through the insulator layer is negligible and the MIS diode represents a conventional MIS capacitor. Alternatively, if the insulating layer is very thin (<10 angstrom), little impediment is provided to carrier transport between metal and semiconductor, and the structure represents a Schottky barrier diode. The third class of device with an intermediate layer thickness (10 angstrom < d < 50 angstrom) is the MIS tunnel diode. From our experimental results and discussion, we can classify the fabricated MIS devices of diameters 0.9 and 1.5 mm as Schottky barrier diode and when MIS device diameter has been increased to 1.9 mm, the device behaves like a tunnel diode.

Fig. 8 Variation of $1/A$ versus $\ln I_0$ (MIS diode of dia 1.5 mm)

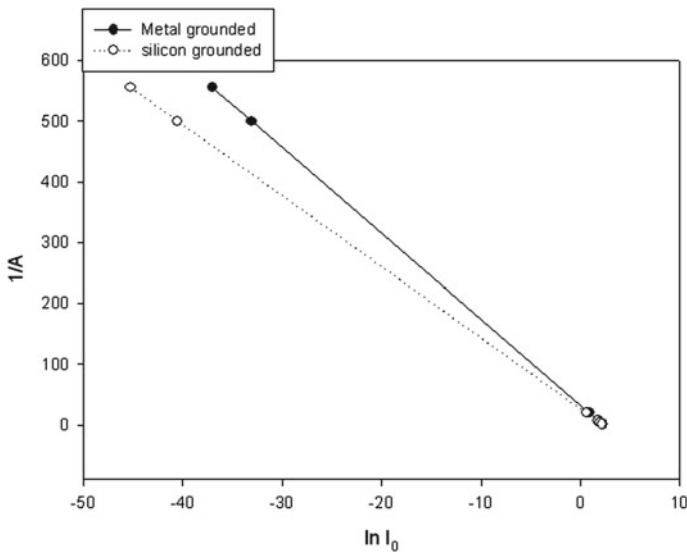
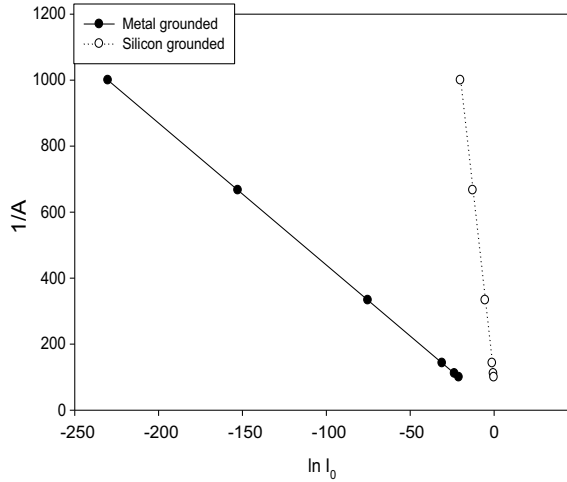


Fig. 9 Variation $1/A$ versus $\ln I_0$ (MIS diode of dia 1.9 mm)

References

1. Sarikhani F, Soleymani AR, Naseri M, Zabardasti A (2022) Synthesis of p–n heterojunction SrFeO₃2x/TiO₂ via thermal treatment/hydrolysis precipitation method with enhanced visible-light activity. <https://doi.org/10.1007/s10854-022-07763-3>
2. Abd El-Rahman AM, Mohamed SH, Khan MT, Awad MA (2021) Plasmonic performance, electrical and optical properties of titanium nitride nanostructured thin films for optoelectronic applications. *J Mater Sci: Mater Electron* 24:28204–28213

3. Sasikumar K, Bharathikannan R, Raja M, Mohanbabu B (2020) Fabrication and characterization of rare earth (Ce, Gd, and Y) doped ZrO₂ based metal-insulator-semiconductor (MIS) type Schottky barrier diodes. *Superlattices Microstruct* 139:106424
4. Kaur R, Arora A, Tripathi SK (2020) Fabrication and characterization of metal insulator semiconductor Ag/PVA/GO/PVA/n-Si/Ag device. *Microelectron Eng* 233:111419
5. Kuhlmann B, Aberle AG, Hezel R, Heiser G (2000) Simulation and optimization of metal-insulator-semiconductor inversion-layer silicon solar cells. *IEEE Trans Electron Devices* 11:2167–2178
6. Simonetti O, Maurel T, Jourdain M (2001) Extraction of the oxide thickness using a MOS structure quantum model for SiO₂ <5 nm thickness. *J Non-crystalline Solids* 280: 110–115
7. Soliman L, Duval E, Benzohra M, Lheurette E, Ketata K (2001) Improvement of oxide thickness determination on MOS structures using capacitance-voltage measurements at high frequencies. *Mater Sci Semicond Process* 4:163–166
8. Kaschieva S (2003) An advantage of MOS structures with ultra thin oxide during irradiation. *Mater Sci Eng* 3100:23–36
9. Niemcharoen S, Kabyashi K, Kimura M, Sato K (2001) Voltage dependence of photo current in metal-semiconductor-metal structures under front-illuminated conditions. *Solid State Electron* 45:1815–1819
10. Xia JB, Chang K, Li SS (2004) Electronic structure and optical property of semiconductor nanocrystallites. *Comput Mater Sci* 30:274–277
11. Tyaginor SE, Vexeler MI, Shulekin AF, Grekhov IV (2005) Statistical analysis of tunnel currents in scaled MOS structures with a non-uniform oxide thickness distribution. *Solid-State Electron* 49:1192–1197
12. Konofaos N (2004) Electrical characterisation of SiON/n-Si structures for MOS VLSI electronics. *Microelectron J* 35:421–425
13. Ranuarez JC, Deen MJ, Chen CH (2006) A review of gate tunneling current in MOS devices. *Microelectron Reliab* 46:1939–1956
14. Ghandhi SK (2008) *VLSI fabrication principles*, 2nd edn. Wiley India Edition
15. Tyagi MS (2008) *Introduction to semiconductor materials and devices*. Wiley India Edition

An Empirical-Statistical and Experimental Analysis of Direct Laser Metal Deposition of WC-12Co Mixed Powder on SS 304 Substrate



Anitesh Kumar Singh , Kalinga Simant Bal , Dilip Kumar Pratihar , and Asimava Roy Choudhury 

1 Introduction

Direct laser metal deposition is one of the additive manufacturing techniques and is also known as the laser cladding process. This process is widely used by industries (automobiles, aerospace, etc.) as a surface modification technique to improve the functional properties of a given material [1, 2]. The substrate is clad with the desired quality clad material to increase the surface quality without altering the bulk qualities of the substrate [1]. With minimal dilution, the laser deposition technique forms a strong metallurgical link between the substrate and the formed clad material [3]. Due to these qualities, the laser deposition technique is unique from other thermal processes, which are used for surface modification. The clad material along with the carrier gas flows coaxially with the laser beam, which melts and gets deposited on the substrate surface. To protect the cladding zone from air contamination, shielding is used. Dilution ratio (D) plays a crucial role to decide the quality of the deposited clad [4]. Excessive dilution causes loss of the clad material property, whereas too little dilution may lead to weak bonding strength between the substrate and clad material.

A. K. Singh · D. K. Pratihar · A. Roy Choudhury (✉)
Department of Mechanical Engineering, Indian Institute of Technology Kharagpur, Kharagpur,
West Bengal 721302, India
e-mail: archie@mech.iitkgp.ac.in

A. K. Singh
e-mail: aniteshsingh08@gmail.com

D. K. Pratihar
e-mail: dkpra@mech.iitkgp.ac.in

K. S. Bal
Department of Mechanical Engineering, National Institute of Technology Raipur, Raipur,
Chhattisgarh 492010, India
e-mail: kalingamech@yahoo.co.in

Aspect ratio (AR) is also one of the key parameters in laser cladding that affect the quality of deposited clad tracks [5]. Very low aspect ratio value causes excessive build-up, which may lead to lower adhesion of deposited clad with the substrate material along with the low-quality clad layer in overlapping laser deposition. On the other hand, excessive AR decreases the deposition height (for a fixed laser spot diameter), which may cause more dilution and lead to loss of the property of clad material. Therefore, the study of dilution ratio and aspect ratio is important to achieve a sound quality clad track.

The family of stainless steel (SS) has a variety of industrial applications such as gas turbines rotor blades, aircraft components, naval vessels, automotive, and pipelines [6]. Among them, SS 304 is used in pipelines for slurry transportation [7] which require a wear-resistant surface to sustain the erosion caused by slurry and have a longer service life. WC is one of high hardness and excellent wear resistance carbide which is used as a wear-resistant coating [8]. Due to the very brittle nature of WC, Co is commonly used as a binder with WC to obtain a clad track with less crack and porosity [9]. A study by Paul et al. [9] disclosed that the minimum required laser energy for successful deposition of WC-12Co powder on steel was 30 J/mm². Singh et al. [2] carried out the optimization of dilution during deposition of WC and Co powder mixture (WC-12wt.%Co) and studied the effect of dilution on microstructure and hardness of deposited clad track. Erfanmanesh et al. [10] obtained a processing range to deposit a sound quality clad track with WC-12wt.%Co powder.

In the present study, WC and Co powder mixture (WC-12wt.%Co) was deposited on SS304 substrate by considering laser power, laser scan speed and powder feed rate as input parameters. An empirical analysis was performed to see the impact of input parameters on outputs (aspect ratio, dilution ratio, and deposited clad cross-section area). The micro-hardness of a selected clad track was analyzed along with the study of melting and diffusion behavior of small and relatively large size WC particles in the clad matrix. The selection of clad track was based on an acceptable range of aspect ratio and dilution ratio.

2 Experimental Detail

2.1 Experimental Setup

A 5-axis computer numerical control (CNC) controlled Yb-Fiber laser (IPG Photonics, Model no. YLR2000), which operates at a wavelength of 1.07 μm and has a maximum output power of 2 kW, was used for the experiment. The spot diameter of 1 mm was used for the deposition process. The powder was supplied to the deposition zone coaxially using a powder feeder. Argon gas was used at the flow rate of 10 L/min and 20 L/min as the carrier and shrouding gas, respectively. Figure 1 depicts the setup for the direct laser metal deposition process.



Fig. 1 Setup for direct laser metal layer deposition

2.2 Material

In the present study, SS 304 of dimension $100 \times 100 \times 10$ mm was chosen as substrate. WC particle of size range $45\text{--}150 \mu\text{m}$ and Co powder having size range $50\text{--}150 \mu\text{m}$ were selected as clad materials. WC and Co powders were uniformly mixed in the ratio of 88:12 (wt.%) in a low-energy planetary ball mill for 4 h. SEM of the ball-milled powder mixture has been shown in Fig. 2. The elemental composition of the substrate and powders has been given in Table 1.

For the laser deposition experiment, three major input parameters, laser power, laser scan speed and powder feed rate were chosen. A full-factorial design was implemented to determine the experimental run. A single track was deposited corresponding to each run for further analysis. The levels of input parameters have been shown in Table 2.

The present study deposited a total of 27 tracks using a full-factorial design. Three replicates were cut using wire-EDM and polished with abrasive paper before

Fig. 2 SEM of ball-milled WC and Co powder mixture

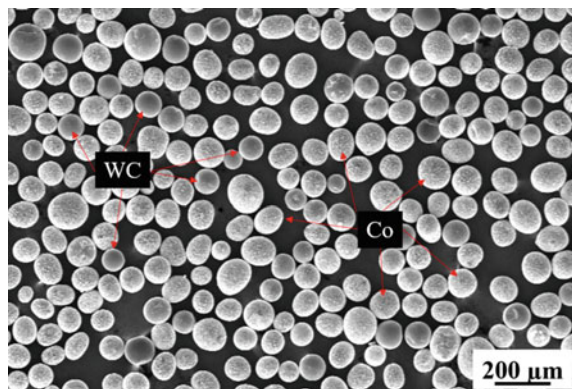


Table 1 Composition of substrate and powders [2]

Material	Element composition (wt. %)											Other
	W	Ni	Cr	Mo	Co	Fe	Si	Mn	C	P	S	
SS 304	–	8.55	18.9	0.22	–	Bal	0.75	1.73	0.07	0.05	0.03	–
WC	Bal	–	–	–	–	–	–	–	3.8	–	–	0.7
Co	–	–	–	–	99.8	–	–	–	–	–	–	–

Table 2 Input parameters for deposition [2]

Factor (SI unit)	Symbol	Experimental value		
		Level 1	Level 2	Level 3
Laser power (W)	P	500	600	700
Laser scan speed (mm/min)	S	400	550	700
Powder feed rate (mg/s)	F	400	480	560

polishing with a 1 μm diamond [11]. Scanning electron microscope (SEM) images of the cross sections were acquired, and then the clad geometry was determined using ImageJ image processing software.

Figure 3 displays a typical cross-section of deposited clad leveling with cladding geometric elements. In this Figure, ‘w’, ‘h’, ‘d’, and ‘A’ represent clad width, clad height, clad depth, and deposited clad cross-section area, respectively.

For further analysis, AR, D and A were selected as the outputs of interest. The ratio of clad width to clad height is termed as aspect ratio, which is given in Eq. (1). The dilution ratio was defined in Eq. (2).

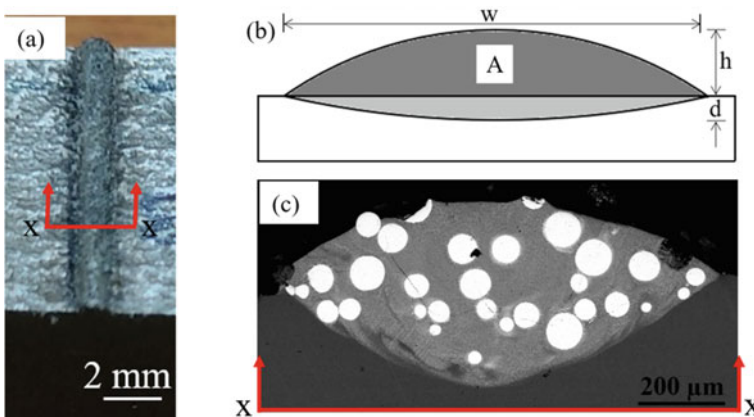


Fig. 3 a As-deposited clad track b schematic of deposited cross section c actual cross section of deposited clad track

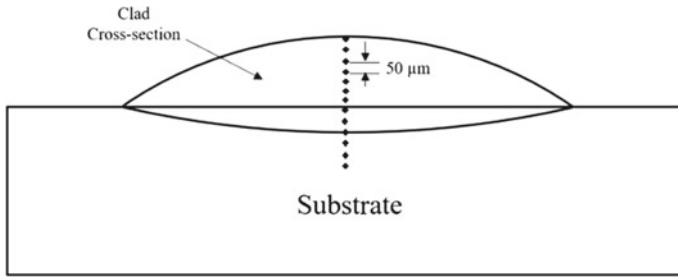


Fig. 4 The schematic of pattern for hardness test

$$\text{Aspect ratio (AR)} = \frac{\text{clad width}}{\text{clad height}} = \frac{w}{h} \tag{1}$$

$$\text{Dilution ratio (D)} = \frac{\text{clad depth}}{\text{clad height} + \text{clad depth}} = \frac{d}{(h + d)} \tag{2}$$

An empirical analysis between selected output responses and input parameters was done to study the impact of a combination of input parameters on the AR, D, and A. One deposited track had been selected based on minimum dilution criteria along with the optimum aspect ratio to obtain a sound quality track. Microstructural analysis of selected good-quality deposited clad track had been done to show the correlation with their hardness behavior.

Hardness is indicative of a material’s ability to resist penetration, indentation, and scratching. In the present work, hardness was measured on the polished cross-section of the clad track along with the depth, by taking a 50 μm gap, as shown in Fig. 4. Vickers micro-hardness tester (OMNI TECH—S. Auto) [12] was used with a 300 g load and dwell time of 10 s to measure the hardness. The average of the measured hardness on the deposited clad cross section (from top of the cladding to the substrate surface) was measured and this was termed as the hardness of the clad track. Microstructural analysis was carried out using a SEM on the clad cross section.

3 Results and Discussion

Table 3 displays the value of the outputs corresponding to input parameters, calculated from the deposited track cross sectional for each run.

Table 3 Input and output values

Input parameter			Output		
Laser power (W)	Laser deposition speed (mm/min)	Powder feed rate (mg/s)	AR	D (%)	A (μm^2)
500	400	400	3.001	30.981	394,094.58
500	400	480	2.421	23.277	467,204.92
500	400	560	1.797	15.419	625,092.75
500	550	400	3.148	41.052	261,878.60
500	550	480	3.010	28.060	329,644.37
500	550	560	2.649	23.759	408,756.25
500	700	400	5.088	54.027	140,443.96
500	700	480	3.320	28.048	327,007.88
500	700	560	2.841	26.986	349,865.14
600	400	400	2.955	35.687	497,111.21
600	400	480	2.285	24.273	712,054.67
600	400	560	2.044	20.092	841,724.82
600	550	400	3.614	44.629	286,103.33
600	550	480	2.610	28.660	494,971.17
600	550	560	2.234	20.268	668,114.67
600	700	400	5.061	64.612	169,638.14
600	700	480	3.077	32.539	363,890.33
600	700	560	2.633	29.092	440,819.49
700	400	400	3.016	38.178	664,301.81
700	400	480	2.116	24.208	955,779.03
700	400	560	1.861	19.804	1,055,002.80
700	550	400	3.770	50.703	329,657.14
700	550	480	2.288	24.318	737,805.94
700	550	560	2.266	23.402	728,197.96
700	700	400	4.153	57.510	243,223.88
700	700	480	3.135	35.748	408,598.33
700	700	560	2.314	23.731	604,170.39

3.1 Empirical Analysis

To analyze the physical phenomena occurring during laser direct metal deposition, an empirical analysis was implemented to reduce the complexity of the problem. Empirical factor, by taking significant input parameters, were formulated for each output response. The relationship between input and output terms can be easily observed from this factor. The steps for obtaining the empirical factor have been given below [2, 13].

Step 1: Converting input and output value (Table 3) into corresponding natural log value.

Step 2: Generating linear regression expression in terms of logarithmic input and output. The obtained expression for the aspect ratio has been given below.

$$\ln(\text{AR}) = 5.839 + (0.6538 \times \ln S) - (1.446 \times \ln F) \tag{3}$$

Here, $R^2 = \text{Goodness of fit}$ [14]

Step 3: Extract empirical relation from the obtained logarithmic regression expression.

$$\text{AR} = e^{5.839} \times S^{0.6538} \times F^{-1.446} \tag{4}$$

The proportionality relationship was established after putting the unit of each input parameter in the above empirical formula. The method of obtaining proportionality relationship for aspect ratio has been shown below.

$$\begin{aligned} \text{AR} &\propto f\left(\frac{\frac{\text{mm}}{\text{s}}}{\frac{\text{mg}}{\text{s}}}\right) \\ &\Leftarrow \text{AR} \propto f\left(\frac{1}{\text{mg/mm}}\right) \\ &\Leftarrow \text{AR} \propto f\left(\frac{1}{\text{Powder delivered per unit clad length}}\right) \end{aligned}$$

The empirical expression and proportionality relation of dilution ratio and deposited clad cross-section area were also established following the above method, and the same is presented in Table 4. Figure 5 shows the variation of output with the obtained empirical factor.

The proportionality relationship (in Table 4) indicates that the aspect ratio and dilution ratio were inversely dependent on powder delivered per unit clad length. An increase in powder delivered per unit clad length (F/S) increased the incoming powder in the cladding zone, which increased the amount of melting powder reaching the substrate surface. The higher amount of melted powder increased the height of the deposited track, which resulted in a decrease in the aspect ratio. Also, the increased amount of incoming powder in the deposition zone consumed a higher amount of

Table 4 Empirical expression and proportionality relationship

Output	Empirical expression	Proportionality relationship
AR	$e^{5.839} \times S^{0.6538} \times F^{-1.446}$	$f\left(\frac{1}{\text{Powder delivered per unit clad length}}\right)$
D	$e^{12.20} \times S^{0.698} \times F^{-2.137}$	$f\left(\frac{1}{\text{Powder delivered per unit clad length}}\right)$
A	$e^{-1.44} \times P^{1.548} \times S^{-1.341} \times F^{2.107}$	$f(\text{linear heat input, powder feed rate})$

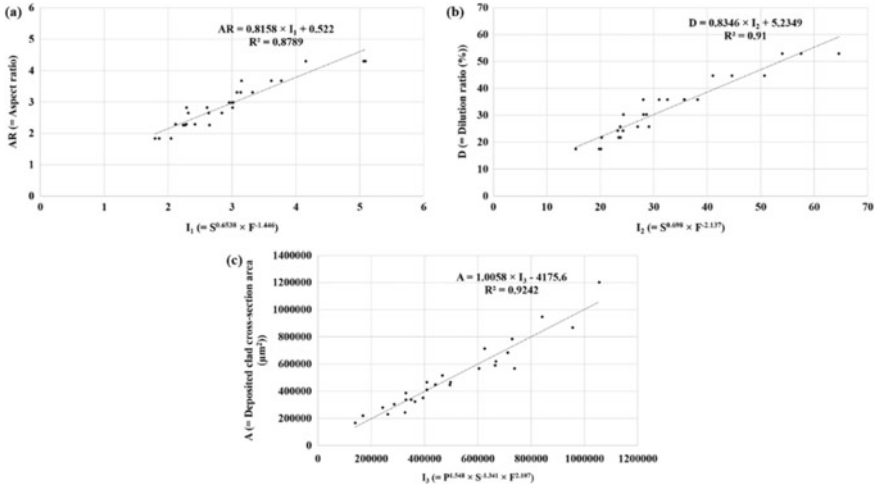


Fig. 5 Variation of output with the empirical factor

available energy, which caused less heat to be transferred toward the substrate. This led to lower dilution during the deposition.

The deposited clad cross-section area was seen to be proportional to the powder feed rate and linear heat input. This means that at a constant powder feed rate, an increase in linear heat input increased the deposited clad cross-section area. Also, at constant linear heat input, an increase in powder feed rate caused an increase in deposited clad cross-section area. Higher linear heat input increased the deposition of powder on the substrate, which led to an increase in the deposited clad cross-section area. On the other hand, increasing the powder feed rate while maintaining a constant feed rate increased the amount of powder in the deposition zone, increasing the amount of melt powder and resulting in enhanced deposition on the substrate surface.

3.2 Clad Track Characterization

In the laser deposition process, it is important to obtain sound quality clad track. The quality of the track strongly depends on the aspect ratio and dilution ratio of the deposited clad track [2, 15]. An advisable range of aspect ratio is 3–5 for a better-quality clad layer [16]. Less value of AR causes excessive build-up, which may lead to less adhesion of deposited clad with the substrate material along with the low-quality clad layer in overlapping laser deposition. Very high AR is also not desirable, as it decreases the deposition height (for a fixed laser spot diameter), which may cause more dilution and lead to loss of the property of clad material. Therefore, the aspect ratio should be in between the optimum range. Dilution is one of the

Table 5 Input and output value selected for deposited track characterization

Input parameter			Output value		
Laser power (W)	Laser deposition speed (mm/min)	Flow rate (mg/s)	AR	D (%)	A (μm^2)
500	700	480	3.320	28.048	327,007.88

key factors to decide the quality of the deposited track. A high value of dilution degrades the quality of clad material by higher mixing of substrate material in the clad track, whereas a very low value of dilution causes weak bonding between the substrate and deposited material. So, the value should be optimum (a minimum value should be 10% [10]) to make strong bonding between clad material and substrate. The dilution has a direct effect on the clad quality, as it shows the amount of mixing of clad material to the substrate. Therefore, considering low dilution as the main criterion, the parameters were selected that had fulfilled the aspect ratio criterion. After considering aspect ratio and dilution criteria, the input parameters along with their output values were selected from the experimental input combination (shown in Table 5) for further microstructure and hardness analysis.

Microstructure analysis of the clad track

The SEM image in Fig. 6 corresponds to the microstructure surrounding the WC particle in the deposited clad track. Figure 6a displays the backscatter diffraction (BSD) image of clad bead cross section around the larger size WC particle. The BSD image for smaller size WC particle is displayed in Fig. 6b. It can be observed from the figure that there were many white patches in the matrix for both cases [2]. The energy-dispersive X-ray spectroscopy (EDS) result confirmed the presence of tungsten in these patches, which can be seen in Fig. 6. As the temperature increased, WC particle surface started melting, which caused diffusion between the WC particle and the matrix. The molten pool lifetime was sufficient to melt the smaller size WC particles, which led to complete diffusion of the small WC particle in the metal matrix and a partial (surface) diffusion of relatively large size WC. The phenomena toward complete diffusion of smaller size WC particles have been shown in Fig. 6b.

Micro-hardness analysis of the clad track

The average micro-hardness of the deposited track was measured and it was found to be 1047.21 ± 39.08 HV, which was almost 5.3 times the substrate hardness. The partial diffusion of larger size WC and complete diffusion of small size WC particle in the matrix might be the main reason for the high hardness of the deposited clad track, which was explained in the earlier paragraph. The hardness at the clad cross section from the top surface along the depth is shown in Fig. 7. It was found that the hardness was almost constant along the depth of the clad track up to WC-Co deposited clad, and decreased at the clad-substrate interface followed by substrate hardness, as the indenter reached the substrate.

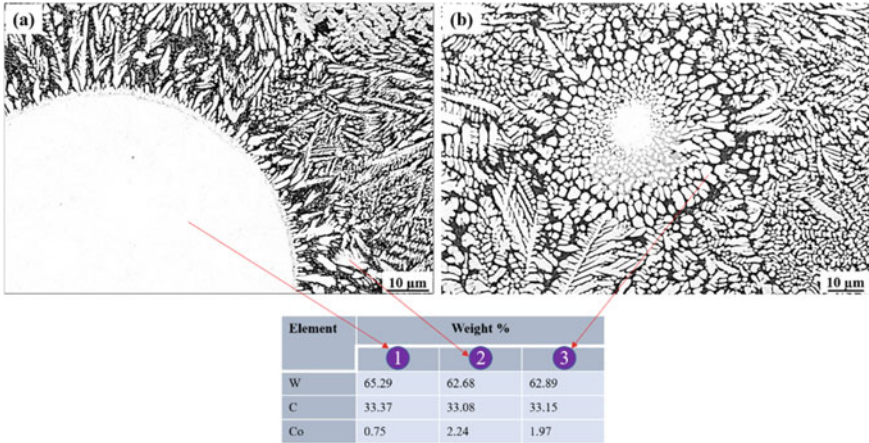


Fig. 6 SEM image of the clad track cross section along with EDS data for **a** larger size WC, **b** smaller size WC

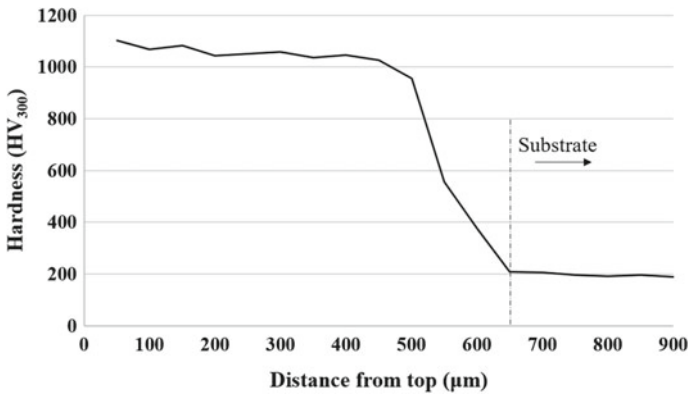


Fig. 7 Hardness variation along the depth of the clad track

4 Conclusions

1. Powder delivered per unit clad length was found to be the determining factor in controlling the aspect ratio and dilution ratio.
2. For the same molten pool lifetime, smaller WC particles underwent complete diffusion in the clad matrix as compared to partial diffusion of larger size WC particles.
3. Average hardness of clad track was found out to be five times the substrate hardness due to the diffusion of WC in the metal matrix.

Acknowledgements We are very grateful to all the faculty members, technical staffs and research scholars of Mechanical Engineering Department, IIT Kharagpur for extending their support in carrying out various experiments. The authors are grateful to the financial support from the Department of Science and Technology, Ministry of Science and Technology, Government of India, under the FIST Program-2007 (SR/FIST/ETII-031/2007) and Ministry of Human Resource Development and Department of Heavy Industries, Government of India, under the IMPRINT Program-2017 for Project-6917.

References

1. Dey D, Bal KS, Singh AK, Roy Choudhury A (2020) Hardness and wear behaviour of multiple component coating on Ti-6Al-4V substrate by laser application. *Optik—Int J Light Electron Optics* 202:163555
2. Singh AK, Bal KS, Dey D, Das AK, Pal AR, Pratihari DK, Roy Choudhury A (2020) Experimental investigation and parametric optimization for minimization of dilution during direct laser metal deposition of tungsten carbide and cobalt powder mixture on SS304 substrate. *Powder Technol* 390:339–353
3. Yuan C, Zhang Q, Chen Z, Wang L, Yao J, Kovalenko V (2019) Study on the element segregation and Laves phase formation in the carbon nanotubes reinforced IN718 superalloy by laser cladding. *Powder Technol* 355:163–171
4. Lupoi R, Sparkes M, Cockburn A, O'Neill W (2011) High speed titanium coatings by supersonic laser deposition. *Mater Lett* 65(21–22):3205–3207
5. Tiwari GK, Dubey AK, Siddiqui AA (2020) A hybrid approach for modelling and optimization of laser cladding process. *Int J Adv Prod Indus Eng* 5(1):17–24
6. Dinu M, Mouele ESM, Parau AC, Vladescu A, Petrik LF, Braic M (2018) Enhancement of the corrosion resistance of 304 stainless steel by Cr–N and Cr (N, O) coatings. *Coatings* 8(4):132
7. Kumar K, Kumar S, Gupta M, Garg HC (2018) Tribological behaviour of WC-10Co4Cr coated slurry pipe materials. *Indus Lubric Tribology*
8. Upadhyaya GS (2001) Materials science of cemented carbides—an overview. *Mater Des* 22(6):483–489
9. Paul CP, Alemohammad H, Toyserkani E, Khajepour A, Corbin S (2007) Cladding of WC–12 Co on low carbon steel using a pulsed Nd: YAG laser. *Mater Sci Eng, A* 464(1–2):170–176
10. Erfanmanesh M, Abdollah-Pour H, Mohammadian-Semnani H, Shojai-Razavi R (2017) An empirical-statistical model for laser cladding of WC-12Co powder on AISI 321 stainless steel. *Opt Laser Technol* 97:180–186
11. Singh AK, Bal KS, Sharma S, Harbajanka A, Prasad M, Dey D, Roy Choudhury A (2020) Effect of beam offset on dissimilar laser beam welding of Ti6Al4V and Inconel 718 superalloy. In: Shunmugam M, Kanthababu M (eds) *Advances in additive manufacturing and joining*, 7th international and 28th All India manufacturing technology, design and research conference 2018, LNMUINEN, vol 1, pp 533–544. Springer, Singapore
12. Gupta SK, Jaypuria S, Pratihari DK, Saha P (2020) Study on mechanical and metallurgical properties of fiber laser welded Nb-1% Zr-0.1% C alloy. *Optics Laser Technol* 127:106153
13. Singh AK, Bal KS, Pal AR, Dey D, Roy Choudhury A (2021) A novel method to reduce dross in laser beam cutting of Ti-6Al-4 V alloy sheet. *J Manuf Process* 64:95–112
14. Bal KS, Dutta Majumdar J, Roy Choudhury A (2019) Optimization of melt zone area for electron beam welded Hastelloy C-276 sheet and study of corrosion resistance of the optimized melt zone in 3.5 wt% NaCl Aqueous Solution. *Arabian J Sci Eng* 44:1617–1630
15. Mohammed S, Zhang Z, Kovacevic R (2020) Optimization of processing parameters in fiber laser cladding. *Int J Adv Manuf Technol* 111:2553–2568
16. Steen WM (2003) *Laser materials processing*, 3rd edn. Springer Verlag, London

Experimental Investigation on AFF of FDM Printed Pattern for Extrusion Die Insert



Harlal Singh Mali, Abdul Wahab Hashmi, Manish Kumar Jangid, and Anoj Meena

1 Introduction

Extruded product dimensions are influenced by various factors, including die design, die manufacturing process, extrusion process parameters, and polymer/metal qualities. The die's flow control devices are incorporated to maximize flow distribution inside the die. Most of the dies have to streamline flow passage shapes to prevent flow stagnation in the die [1]. The investment casting process has greater flexibility to produce any complex shape of products. The integration of the 3D printing process and investment casting process may give a better solution for manufacturing freeform shapes of products [2]. Singh et al. [3] have used the fused deposition modeling (FDM) based 3D printed pattern for investment casting applications. The authors fabricated the customized human implants using the FDM pattern in the investment casting method. The FDM pattern benefits resilience, dimensional correctness, clean burnout, and the ability to be handled without harm. Holker et al. [4] experimentally investigated the effect of conformal cooling channels in hot extrusion die manufactured by additive manufacturing (AM) process. The selective laser melting (SLM) process manufactures hot aluminum extrusion dies. The authors compared the performance of the die without cooling and with cooling by conformal channel.

H. S. Mali (✉) · A. W. Hashmi · M. K. Jangid · A. Meena
Advanced Manufacturing and Mechatronics Lab, Department of Mechanical Engineering,
Malaviya National Institute of Technology, Jaipur 302017, India
e-mail: harlal.singh@mnit.ac.in

A. W. Hashmi
e-mail: 2018rme9108@mnit.ac.in

M. K. Jangid
e-mail: 2019ppe5486@mnit.ac.in

A. Meena
e-mail: ameena.mech@mnit.ac.in

The extrusion force significantly increases in the case without die cooling. The AM components are affected by various surface defects, i.e., stair casing/stair-stepping effect, powder adhesions, and bailing effects. The stair-stepping effect has commonly occurred in surface defects in metal and polymer-based AM processes. Jain et al. [5] investigated the AFM process to show how different process parameters affect the outcome, such as the number of finishing cycles, abrasive concentration, abrasive mesh size, and media flow rate. The authors discovered that the better the surface finish, the greater the abrasive concentration and the larger the abrasive mesh size. can show how different process parameters affect the outcome, such as the number of finishing cycles, abrasive concentration, abrasive mesh size, and media flow rate. Sambharia et al. [6] have reviewed the recent trends of AFM processes. The authors discussed the advantages and limitations of AFM processes. The authors discussed the various low cost and environment-friendly AFM media to finish the hard materials like metal matrix composite, nickel alloys, and titanium alloys. Jain et al. [7] have mathematically modeled the AFM process using the FEM method to see how AFM process settings affect the outcome. The results showed that increasing the piston pressure boosted material removal while decreasing the abrasive mesh size decreased it. The surface roughness reduced with increasing the piston velocity and abrasive concentration. Mali et al. [8] experimentally investigated the finishing of FDM printed ABS parts using sustainable AFM media by one-way AFF method. The results showed that maximum surface finish improvement was found ΔR_a 21.37 μmm on the outer and ΔR_a 6.27 μmm on the inner of ABS finished parts. Bouland et al. [9] have used the AFM process to finish 3D printed Ti-6Al-4 V alloy parts by laser powder bed fusion (L-PBF) process. The authors have implemented the CFD simulation of the AFM process. Experimental results corroborated the simulated findings. Duval-Chaneac et al. [10] used the AFM process to finish non-heat-treated and heat-treated selective laser melting (SLM) parts. The results showed that the surface roughness was improved in the range of from 12 to 14 μm . Wang et al. [11] employed the AFM to polish metal AM (SLM) parts. The findings revealed that AFM can effectively remove surface defects such as bailing, powder adhesion, and stair stepping. Tan et al. [12] investigated the hybrid finishing process, namely, ultrasonic cavitation abrasive flow machining (UCAFM), to enhance the surface finish of additively manufactured Inconel 625 parts. After 30 min, the surface roughness had improved by 45%. Kumar et al. [13] investigated the AFM process to finish the aluminum and EN8 materials using the natural rubber-based media. The AFM media was prepared by mixing the following constituents: butyl rubber as base material, silicon carbide (SiC) as an abrasive, and naphthenic oil in an appropriate concentration. These natural rubber-based media may increase the abrasive loading capacity by 47%. Mali et al. [14] investigated the AFM process to finish the Al/SiC metal matrix composites using Taguchi process L_{18} ($6^1 \times 3^7$) mixed orthogonal array-based design experiments (DOE). The authors reported that the surface roughness R_a and R_t was improved by 79.39% at 6 MPa extrusion pressure, 67% abrasive concentration, 30 finishing cycles, and “L” grade media viscosity. Walia et al. [15] studied the active abrasive grains in the polishing media of the centrifugal assisted AFM (CFAAFM) process. To generate the centrifugal force, the authors incorporated a

rotating centrifugal force-generating (CFG) rod inside the cavity of the workpiece. The results were confirmed using both analytical and experimental methods. Ahmed et al. [16] proposed a hybrid additive and subtractive process to a manufactured spur gear. The FDM process was integrated with a CNC milling machine to manufacture the finished spur gear. Sambharia et al. [17] investigated the finishing of HSS trim die by newly developed polymer abrasive gel (PAG) based media using a one-way AFM process. The authors reported that maximum surface roughness improvement was found at 13.57% finishing time and 20.99% extrusion pressure. Yadav et al. [18] have developed a low-cost media for the AFM process. The authors prepared a media using a styrene-butadiene rubber (SBR) as base material, and the proportion of the media's composition is 78% abrasive, 14% SBR, and 8% oil. The surface roughness was improved by 87%. Fu et al. [19] have done the rheological characterization of SBR-based AFM media. The authors reported by comparing the pressures in the restricted passage under different conditions, media can withstand extrusion pressures of 2.5, 3.0, and 3.5 MPa. By combining locust bean gum and fumed silica, Dixit et al. [20] studied the finishing of copper workpieces using newly created media, namely XG-based abrasive media. Locust bean gum was used as a crosslinker, while fumed silica was used as a thickening agent, according to the authors. By combining locust bean gum and fumed silica, Dixit et al. [20] studied the finishing of copper workpieces using newly created media, namely, XG-based abrasive media. Locust bean gum was used as a crosslinker, while fumed silica was used as a thickening agent, according to the authors. The surface roughness of XG-based media improved by 31.08%, while polymer-based abrasive media improved by 24.17%. Ravi Shankar et al. [21] proposed finishing of Al alloy/Sic MMCs by AFM process. The authors reported that the surface roughness was improved from the initial value of $0.6 \pm 0.1 \mu\text{m}$ to the final value of $0.25 \pm 0.05 \mu\text{m}$. Peng et al. [22] investigated the AFM process to finish additively manufactured AlSi10Mg aluminum alloy parts. According to the authors, surface roughness improved significantly from Sa 13 to 1.8 m, and surface defects were eradicated due to the natural balling action or powder adherence. Williams et al. [23] investigated the finishing of the stereolithography parts by the AFM process. Before and after AFM, the effects of various processing factors were investigated using statistical analysis data-based systems (DDS).

This paper describes the results of an experimental study using a one-way AFM method to polish the surface of an FDM-produced extrusion “die insert” pattern. Natural resources such as corn starch as a material for the base and waste vegetable oil as a carrier medium are used to create the new environmentally friendly media. For optimum enhancement of surface roughness, the media viscosity and abrasive flow finishing process parameters have been examined.

2 Materials and Methods

The following flow is followed for exploration through experimentation of abrasive flow finishing of FDM-based 3D printed extrusion “die insert” pattern, as shown in Fig. 1.

2.1 Design and Fabrication of an Extrusion “Die Insert” Pattern

Using Autodesk Fusion360 software, a circular in-line extrusion “die insert” pattern with 50 mm length, 10 mm inlet diameter, and 5 mm outlet diameter is CAD designed. It is produced with acrylonitrile butadiene styrene (ABS) material by a fused deposition modeling (FDM) machine after modeling the circular in-line “die insert” pattern. A concept design and cross-sectional view of a circular in-line “die insert” pattern design are shown in Fig. 2.

The following steps are used in the fabrication of an extrusion circular in-line “die insert” pattern, as shown in Fig. 3.

Nine samples of circular in-line extrusion “die insert” patterns fabricated using the FDM process are shown in Fig. 4.

2.2 CAD Modeling and Manufacturing of AFM Tooling

Using Autodesk® fusion360, a one-way AFM tooling/fixture has been created to support and retain the circular in-line extrusion “die insert” pattern. The fixture is intended in such a way that the fixture cavity allows the medium to flow inside the internal passage of circular in-line extrusion “die insert” pattern under pressure and finish the passage inside the fixture, as shown in Fig. 5.

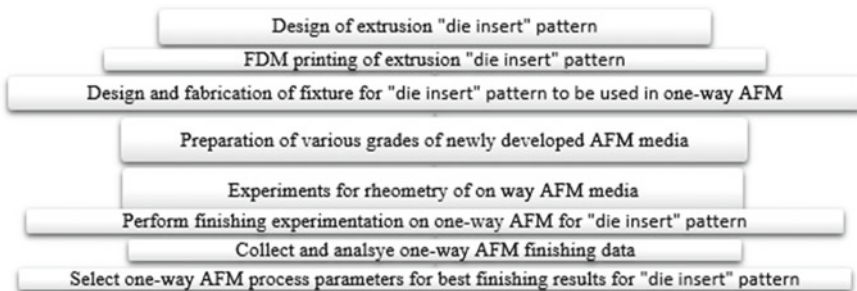


Fig. 1 The flow of experimental investigation

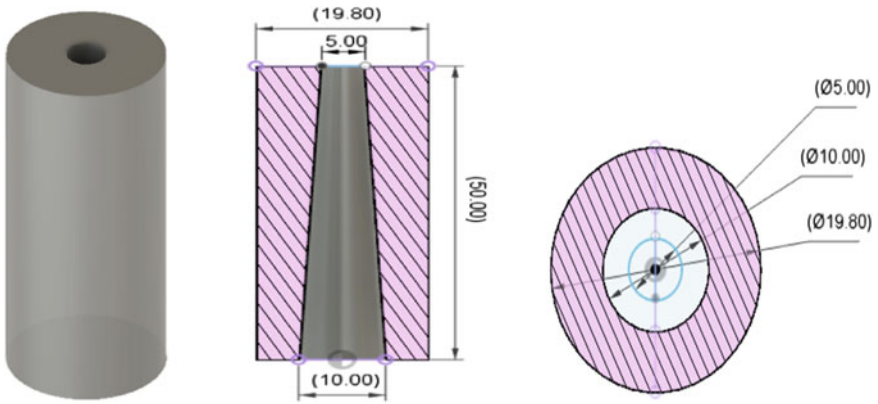


Fig. 2 Designed model of the circular in-line extrusion die insert patterns and C/S views

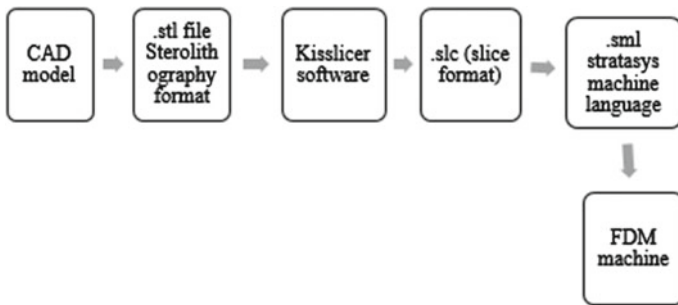


Fig. 3 Processing sequences of the FDM process

Fig. 4 3D printed circular in-line extrusion “die insert” patterns samples



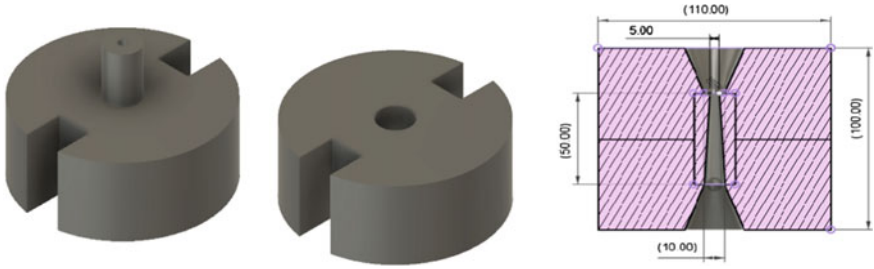


Fig. 5 Fixture/tooling for circular in-line extrusion “die insert” pattern

Fig. 6 Top view of a fixture for circular in-line extrusion “die insert” pattern



One-way AFM fixture for circular in-line extrusion “die insert” pattern is fabricated by FDM process using ABS material after designing, as shown in Fig. 6.

3 Experimentation on the Rheology of AFM Media

3.1 Development of AFM Media

As indicated in Fig. 7, AFM Media is formed by blending cornstarch powder as a foundation, waste vegetable oil (groundnut oil) as a carrier medium, aloe barbadensis miller (aloe vera gel), and glycerine as additives.

3.2 Experimentation for Media Rheology

Nine samples of cornstarch-based media to identify the viscosity of AFM media were prepared. Three parameters, namely, abrasive mesh size, percent abrasive concentration, and percent liquid synthesizer with respect to three levels, were evaluated when producing the AFM medium. As indicated in Fig. 7, the abrasive mesh size is



Fig. 7 Cornstarch-based media samples

120, 220, 320, and the percentage of abrasive concentration is 33, 50, 66, and the percentage of the liquid synthesizer is 40, 60, and 80.

Table 1 shows the process parameters with respective levels for the experimental design of AFM media viscosity.

Table 2 shows the viscosity results of cornstarch-based AFM media.

According to the results of the investigation, the most relevant media parameter is the abrasive particles mesh size. It has an impact on the viscosity of the medium, followed by the percentage of abrasive concentration. The media concentration was 220 mesh number, 33% abrasive particles concentration, and 60% liquid synthesizer within the considered range (Fig. 8).

Table 1 Process levels and parameters of experimentation of AFM media viscosity (media—cornstarch-based AFM media)

Factor and symbols	Level 1 (-1)	Level 2 (0)	Level 3 (1)
Abrasive mesh size (A)	120	220	320
% Abrasive con. (B)	33	50	66
% Liquid synthesizer (C)	40	60	80

Table 2 Plan of experimental results for the AFM media viscosity

S. No.	Abrasive mesh size	% Abrasive concentration	% Liquid synthesizer	Viscosity (pa-sec)
1	120	33	40	0.88
2	120	50	60	0.82
3	120	66	80	0.58
4	220	33	60	1.00
5	220	50	80	0.97
6	220	66	40	0.66
7	320	33	80	0.57
8	320	50	40	0.40
9	320	66	60	1.20

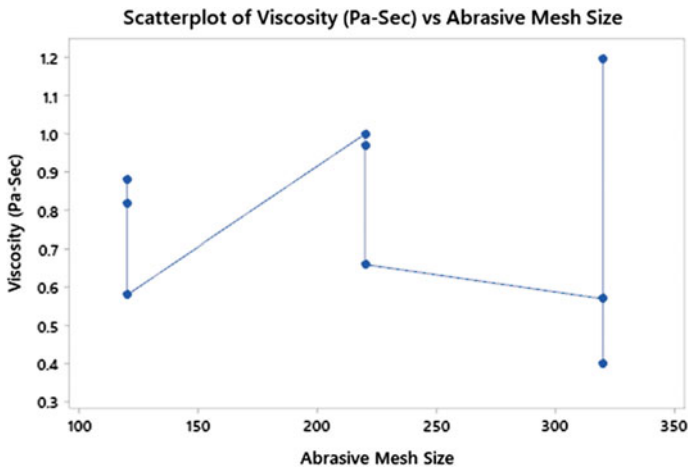


Fig. 8 Scatterplot of viscosity (pa-sec) versus abrasive mesh size

3.3 Effect of Abrasive Particles Concentration

Figure 9 shows how the concentration of abrasive particles affects the viscosity of cornstarch-based AFM media. The viscosity of the AFM media increases as the abrasive content rises. Abrasive particle mobility is reduced when the fraction of abrasive particles in the media is higher. The volumetric flow rate decreases as a result, and the media viscosity increases.

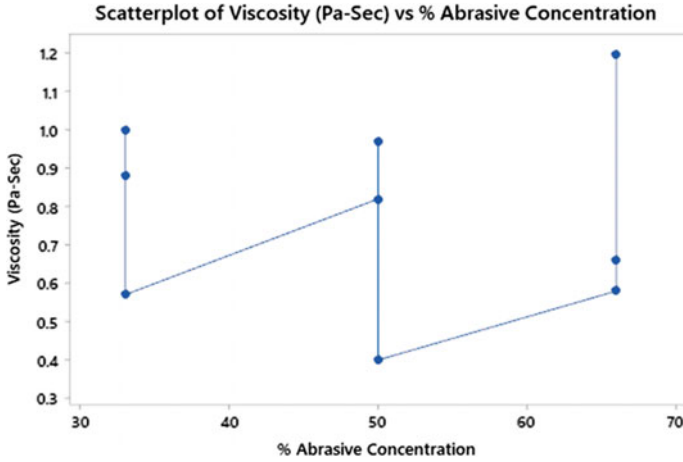


Fig. 9 Scatterplot of viscosity (pa-sec) versus % abrasive concentration

3.4 Effect of Liquid Synthesizer

Figure 10 depicts the influence of the percentage liquid synthesizer on the viscosity of cornstarch-based media. The scatter figure shows that the viscosity decreases as the percentage of liquid synthesizer increases. It's because the fluidity of the media has improved, and the stiffness of the media has decreased.

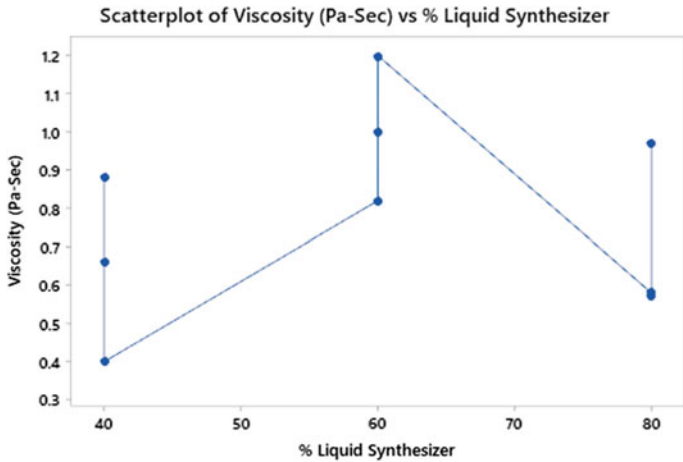


Fig. 10 Scatterplot of viscosity (pa-sec) versus % liquid synthesizer

4 Experimental Design for Finishing

Nine samples of patterns for extrusion “die insert” are printed by the FDM process. Taylor Hobson’s Talysurf® PRO surface roughness tester is used to determine the initial surface roughness. One-way AFM was used to finish the samples of the extrusion die insert pattern. The surface roughness of the final samples was measured using a surface roughness tester. The effects of AFM process parameters were investigated in this study. A total of nine experiments were created. Table 3 displays four process parameters that were used as control factors in the experimentation: abrasive particles concentration, layer thickness, finishing time, and abrasive particles mesh size. Low, medium, and high levels are assigned to each parameter. These process settings and their values were chosen based on the existing literature on AFM.

Table 4 shows the response parameter, which is the percent improvement in surface quality, i.e., the reduction in R_a .

Table 3 Experimental design of the AFM process parameters and their respective levels (finishing of FDM printed “die insert” pattern)

Parameters	Level 1	Level 2	Level 3
Abrasive mesh size	120	220	320
% Abrasive concentration	33	50	66
Layer thickness	0.1	0.2	0.3
Finishing time (min.)	30	45	60

Table 4 Design for a surface enhancement experiment on an FDM-based 3D printed “die insert” pattern

S. No.	Abrasive mesh size	% of abrasive	Layer thickness (mm)	Finishing time (min.)	Initial surface roughness (R_a in μm)	Post finishing surface roughness (R_a in μm)	% improvement in (ΔR_a)
1	120	33	0.1	30	13.40	10.66	20.44
2	120	50	0.2	45	22.73	03.70	83.72
3	120	66	0.3	60	28.20	14.33	49.18
4	220	33	0.2	60	22.50	12.93	42.53
5	220	50	0.3	30	28.63	15.23	46.80
6	220	66	0.1	45	16.50	03.53	78.58
7	320	33	0.3	45	29.60	16.26	45.06
8	320	50	0.1	60	13.60	03.26	76.02
9	320	66	0.2	30	22.93	02.20	90.40

Table 5 Analysis of variance for % improvement in (ΔR_a), using adjusted SS for tests

Source	DF	Seq. SS	Adj. SS	Adj. MS	F	P
Abrasive mesh size	2	2358.8	2358.8	1179.2	2.58	0.001
% of abrasive	2	1894.3	1894.3	947.2	3.74	0.211
Layer thickness (mm)	2	446.9	446.9	223.4	0.88	0.531
Finishing time (min.)	2	2130.9	2130.9	1065.5	4.21	0.004
Error	2	506.6	506.6	253.3		
Total	8	7337.6				

4.1 Variance Analysis for Percentage Improvement in R_a

The analysis of variance (ANOVA) is used to examine the selected process factors and see which ones have a considerable impact on surface quality improvement. This analysis aids in determining the relative impact of the finishing parameter on the AFF process’ reaction. Table 5 displays the results of the ANOVA and “F” tests and the “P percent” value, which indicates the efficiency of the various abrasive flow finishing parameters on the percentage improvement response, i.e., percent R_a .

Table 5 indicates the effectiveness of each AFF process parameter in affecting the output response of % ΔR_a within the specified range using the “P percent” value. The analysis of variance is carried out with Minitab statistical software at a 95% confidence level. Table 5 shows that the abrasive mesh size is the most important element for achieving the greatest % improvement in R_a . The next important process parameter affecting ΔR_a is finishing time. Analysis of the results shows that with 320 abrasive mesh size, 66% of abrasive concentration, 0.2 layer thickness, and finishing time of 45 min showed the best improvement in surface roughness (ΔR_a).

5 Conclusions and Scope of Work

The experimentation study on abrasive flow finishing of FDM based 3D printed extrusion die insert pattern yielded the following conclusions:

- The use of FDM has been shown for developing customized AFM fixture/tooling for the product to be finished.
- An environmentally friendly media has been developed using corn-starch powder as a base material and waste vegetable oil (groundnut oil) as a carrier liquid for completing FDM-produced patterns.
- The viscosity of AFM media was influenced by abrasive mesh size, abrasive %, and synthesizer percentage.
- In rheological research of cornstarch-based media viscosity, the optimal parameters were 66% abrasive concentration and 220 abrasive mesh size.
- The method improved the surface finish (R_a) to 2.2 m with a 90.40% improvement.

- As the abrasive mesh size and finishing time were increased, the surface quality improved.

Based on the experimentations, the following scope is envisioned on abrasive flow finishing of FDM based 3D printed extrusion die insert pattern:

- Fused deposition modeling is a common manufacturing method among the material extrusion family of additively created technologies because of its low cost and flexibility.
- Due to layer addition, the surface of these FDM printed components has poor surface quality.
- FDM process could be used to fabricate the pattern of any product for investment casting application.
- If needed, a pattern for casting the FDM printed parts needs to be finished.
- The abrasive flow finishing process could be an excellent option for finishing these FDM printed parts before using them as patterns for developing extrusion die inserts.
- These die inserts provide a modular and customized option for the development of extruded parts out of polymers as well as metals.

References

1. Kostic MM, Reifschneider LG (2006) Design of extrusion dies. *Encyclop Chem Process* 10:633–649
2. Turazza A, Davoudinejad A, Calaon M, Pedersen DB, Tosello G (2020) Towards the integration of additively manufactured photopolymer dies in the polymer profile extrusion process chain. *Proc CIRP* 93:3–8
3. Singh S, Singh R (2016) Fused deposition modelling based rapid patterns for investment casting applications: a review. *Rapid Protot J*
4. Hölker R, Haase M, Khalifa NB, Tekkaya AE (2015) Hot extrusion dies with conformal cooling channels produced by additive manufacturing. *Mater Today Proc* 2(10):4838–4846
5. Jain VK, Adsul SG (2000) Experimental investigations into abrasive flow machining (AFM). *Int J Mach Tools Manuf* 40(7):1003–1021
6. Sambharia J, Mali HS (2019) Recent developments in abrasive flow finishing process: a review of current research and future prospects. *Proc Inst Mech Eng Part B: J Eng Manuf* 233(2):388–399
7. Jain RK, Jain VK, Dixit PM (1999) Modeling of material removal and surface roughness in abrasive flow machining process. *Int J Mach Tools Manuf* 39(12):1903–1923
8. Mali HS, Prajwal B, Gupta D, Kishan J (2018) Abrasive flow finishing of FDM printed parts using a sustainable media. *Rapid Prototyping J*
9. Bouland C, Urlea V, Beaubier K, Samoilenko M, Brailovski V (2019) Abrasive flow machining of laser powder bed-fused parts: numerical modeling and experimental validation. *J Mater Process Technol* 273:116262
10. Duval-Chaneac MS, Han S, Claudin C, Salvatore F, Bajolet J, Rech J (2018) Experimental study on finishing of internal laser melting (SLM) surface with abrasive flow machining (AFM). *Precis Eng* 54:1–6
11. Wang X, Li S, Fu Y, Gao H (2016) Finishing of additively manufactured metal parts by abrasive flow machining. In: *Proceedings of the 27th annual international solid freeform fabrication symposium, Austin, TX, pp 2470–2472*

12. Tan KL, Yeo SH (2017) Surface modification of additive manufactured components by ultrasonic cavitation abrasive finishing. *Wear* 378:90–95
13. Kar KK, Ravi Kumar NL, Tailor PB, Ram Kumar J, Sathiya Moorthy D (2009) Performance evaluation and rheological characterization of newly developed butyl rubber based media for abrasive flow machining process. *J Mater Process Technol* 209(4):2212–2221
14. Mali HS, Manna A (2010) Optimum selection of abrasive flow machining conditions during fine finishing of Al/15 wt % Sic-MMC using Taguchi method. *Int J Adv Manuf Technol* 50(9–12):1013–1024
15. Walia RS, Shan HS, Kumar P (2008) Determining dynamically active abrasive particles in the media used in centrifugal force assisted abrasive flow machining process. *Int J Adv Manuf Technol* 38(11–12):1157–1164
16. Ahmed M, Chowdhury R, Srishti NR, Rahman MA, Comparative analysis of additive and subtractive manufacturing processes through the fabrication of a Spur gear.
17. Sambharia JK, Mali HS, Garg V (2018) Experimental investigation on unidirectional abrasive flow machining of trim die workpiece. *Mater Manuf Process* 33(6):651–660
18. Yadav P, Jayswal SC (2019) Study of media in abrasive flow machining and its hybrid processes. *Mater Today Proc* 18:3017–3026
19. Fu Y, Gao H, Yan Q, Wang X, Wang X (2020) Rheological characterization of abrasive media and finishing behaviours in abrasive flow machining. *Int J Adv Manuf Technol* 107(7):3569–3580
20. Dixit N, Sharma V, Kumar P (2021) Development and characterization of xanthan gum-based abrasive media and performance analysis using abrasive flow machining. *J Manuf Process* 67:101–115
21. Sankar MR, Ram Kumar J, Jain VK (2009) Experimental investigation and mechanism of material removal in nano finishing of MMCs using abrasive flow finishing (AFF) process. *Wear* 266(7–8):688–698
22. Peng C, Fu Y, Wei H, Li S, Wang X, Gao H (2018) Study on improvement of surface roughness and induced residual stress for additively manufactured metal parts by abrasive flow machining. *Procedia CIRP* 71:386–389
23. Williams RE, Melton VL (1998) Abrasive flow finishing of stereo lithography prototypes. Singh S, Shan HS, Kumar P (2008) Rapid Protot

Experimental Study on Cylindrical Grinding of Bearing Bush to Improve Surface Finish



M. S. Karthik, V. R. Raju, K. N. Reddy, N. Balashanmugam,
and M. R. Shankar

1 Introduction

Grinding processes are needed for a wide range of needs for surface generation with every new or emerging technology which provides value addition to them. These grinding surfaces are required to meet specific functional needs in various engineering applications needs such as to support guide and motion, transmit force, reduce friction, reduce wear, to increase efficiency and service life. Various grinding conditions like wheel speed, work speed, feed, depth of cut, dressing of wheel, etc., play a major role in achieving functional requirements of engineering components. Jagtap [1] conducted grinding experiments on AISI 5120 steel to obtain parameters to improve the surface finish and maximize the material removal rate. Results showed that work speed was the most dominating factor for reducing surface roughness and for material removal rate number of passes is the most dominant factor. Melwin Jagadeesh Sridhar [2] performed grinding experiments on OHNS steel in order to increase the material removal rate and found that number of pass is the most

M. S. Karthik (✉) · V. R. Raju · K. N. Reddy · N. Balashanmugam
Central Manufacturing Technology Institute, Tumkur Road, Bengaluru 560022, India
e-mail: karthik@cmti.res.in

V. R. Raju
e-mail: rajuvr@cmti.res.in

K. N. Reddy
e-mail: niranjan@cmti.res.in

N. Balashanmugam
e-mail: balashanmugam@cmti.res.in

M. S. Karthik · M. R. Shankar
Department of Mechanical Engineering, Indian Institute of Technology Tirupati, Chindapalle,
Andhra Pradesh 517506, India
e-mail: evmrs@iittp.ac.in

influencing factor to improve the material removal rate. Stephenson [3] used CBN cup wheel to grind very high hardness material M50 and evaluated the influence of wheel speed, work speed feed, and electrolytic in process dressing to increase the high material removal rate and surface finish. Results showed that by using the CBN grit wheel and electrolytic in process grinding, optical surface quality can be achieved. Hecker [4] presented an analytical model for prediction of surface roughness for the ground parts and obtained experimental surface roughness value was in agreement with predicted value. This model also predicted that at the higher wheel velocity the number of grains involved in removing the material from the work piece is more and due to this depth of penetration is less on work piece which leads to smooth surface surfaces. Deshmukh [5] applied response surface methodology to study the influence of grinding parameters on surface roughness value and MRR and also stated that due to increase in the depth of cut and spindle speed, the wheel grit becomes dulls which leads to high grinding force and affect the surface geometry of the work piece. Daneshi [6] studied the effect of dressing on CBN internal grinding wheels and explained that soon after the dressing, the CBN wheel pores were closed which increases the cutting force, and after removal of material of some volume from the work piece force reduces due to opening of the pores. Grzesik [7] has done comparison studies between hard turned and ground surface textures and reported that ground hard surface have better bearing properties and fluid retention ability than the hard turned parts. Singh [8] conducted cylindrical grinding experiments on AISI 4140 steel and studied the effect of grinding parameters on surface roughness and depth of cut which is the dominant factor to improve surface finish value. Sadeghi [9] conducted an investigation on using minimum quantity lubrication for surface grinding of AISI 4140 steel and compared with different cutting fluids with respect to grinding forces and surface quality of work pieces. Results explained that material removal in MQL takes place due to shearing and breaking and also cutting forces and specific energy are reduced. Deresse [10] investigated the effect of external cylindrical parameters on material removal rate on EN45 steel using Taguchi analysis. It was found that from the ANOVA, depth of cut was the most influencing factor for material removal rate before heat treatment and after treatment feed rate was the dominant factor in material removal rate. Mekala [11] performed cylindrical grinding experiments on austenitic stainless steel rods to investigate the parameters which influences the material removal rate and surface roughness. The depth of cut plays vital role in improving material removal rate and cutting speed parameter influences the surface roughness during cylindrical grinding austenitic stainless steel. Raju [12] conducted experiments on axial feed rollers having hardness more than 45 HRC using CBN inserts in hard turning machine to obtain best cutting parameters and study the tool wear of the CBN inserts. Results showed that feed rate is an important factor in influencing the surface roughness and for tool flank wear cutting speed is the significant parameter. In this present work, optimization of grinding process parameters to improve the surface roughness during cylindrical grinding of inner diameter (ID) and outer diameter (OD) was studied using aluminum oxide wheels and the optimum grinding parameters for achieving minimum surface roughness was obtained using Taguchi method.

Table 1 Input OD grinding parameters

OD grinding parameters	L1	L2	L3
Work speed (RPM)	100	150	200
Feed (<i>F</i>) (m/min)	0.5	1	1.5
Depth of cut (<i>D</i>) (μm)	10	20	30

Table 2 Input ID grinding parameters

ID grinding parameters	L1	L2	L3
Work speed (RPM)	200	250	300
Feed (<i>F</i>) (m/min)	0.25	0.5	0.75
Depth of cut (<i>D</i>) (μm)	10	20	30

2 Experimental Plan

2.1 Input Parameters for OD and ID Grinding

Work speed, feed, and depth of cut are the input grinding parameters at three levels are used in the experiments. These input parameters are selected from the manufacturer’s recommendation of the grinding machine. Tables 1 and 2 provide the OD and ID grinding parameters at three different levels.

2.2 Design of Experiments

Taguchi method is the popular method for optimization of cutting parameters and to obtain the most significant parameter which influences the output results. Taguchi L9 orthogonal array is selected for design of experiments to using three input grinding parameters to achieve minimum surface roughness for both OD and ID. Design of experiments for OD and ID grinding parameters are shown in Tables 3 and 4, respectively.

2.3 Experimentation

Kellenberger universal cylindrical grinding machine was used for carrying out the cylindrical grinding experiments for OD and ID as per the design of experiments. The work piece round bar of diameter 50 mm EN 31 steel diameter was rough turned to 43 mm at the OD and 35 mm at the ID by keeping the grinding stock using Lathe and were heat treated to 60 HRC. Rough bearing bush components were prepared for OD and ID grinding as per the design of experiment. Aluminum oxide (Al₂O₃)

Table 3 Design of experiments for OD grinding

S. No.	<i>A</i>	<i>B</i>	<i>C</i>	<i>S</i> (RPM)	<i>F</i> (m/min)	<i>D</i> (μm)
1	1	1	1	100	0.5	10
2	1	2	2	100	1	20
3	1	3	3	100	1.5	30
4	2	1	2	150	0.5	20
5	2	2	3	150	1	30
6	2	3	1	150	1.5	10
7	3	1	3	200	0.5	30
8	3	2	1	200	1	10
9	3	3	2	200	1.5	20

Table 4 Design of experiments for ID grinding

S. No.	<i>A</i>	<i>B</i>	<i>C</i>	<i>S</i> (RPM)	<i>F</i> (m/min)	<i>D</i> (μm)
1	1	1	1	200	0.25	10
2	1	2	2	200	0.50	20
3	1	3	3	200	0.75	30
4	2	1	2	250	0.25	20
5	2	2	3	250	0.50	30
6	2	3	1	250	0.75	10
7	3	1	3	300	0.25	30
8	3	2	1	300	0.50	10
9	3	3	2	300	0.75	20

wheel of 400 mm diameter was used for OD grinding and diameter of 20 mm for ID grinding experiments. OD grinding was done by holding the bearing bush in a fixture in work head and grinding wheel speed running at 2000 RPM. Bearing bush was held in a special fixture for ID grinding and the grinding wheel was mounted on the precision spindle rotating at 15,000 RPM. The universal cylindrical grinding machine is shown in Figs. 1 and 2a, b shows OD and ID grinding set up. Figure 3a shows the feed rollers used in bearing industries in super finishing applications, and Fig. 3b shows the bearing bush component.



Fig. 1 Kellenberger cylindrical grinding machine



Fig. 2 a OD grinding set up. b ID grinding set up

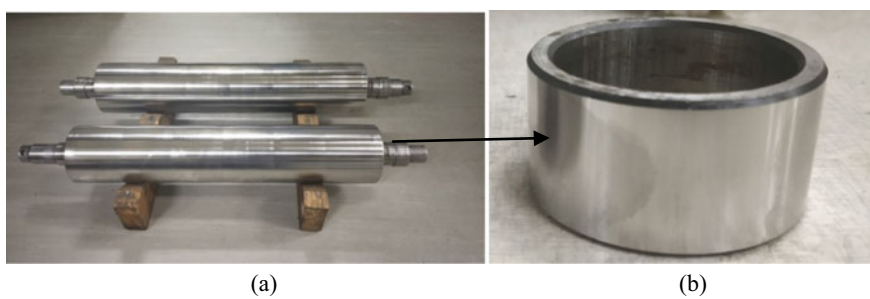


Fig. 3 a Feed rollers. b Bearing bush

3 Results and Discussions

3.1 Experimental Results

The surface roughness for all the components was measured using form Talysurf surface roughness tester for both the OD and ID. Tables 5 and 6 give details of measured surface roughness values and S/N ratios values for all the components for OD grinding and ID grinding, respectively.

For OD grinding of bearing bush and the input grinding parameter of work speed $S = 200$ RPM, feed $F = 0.5$ m/min, and depth of cut $D = 30$ μm , the minimum surface roughness value of 0.2245 μm was achieved with S/N ratio value 12.9757.

The minimum surface roughness value of 0.2259 μm was obtained for the input grinding parameters of work speed $S = 200$ RPM, feed $F = 0.75$ m/min, and depth of cut $D = 30$ μm with S/N Ratio value 12.9217.

Table 5 Output responses for OD grinding

S. No.	S (RPM)	F (m/min)	D (μm)	R_a (μm)	S/N ratios
1	100	0.5	10	0.2781	11.1160
2	100	1	20	0.3233	9.8079
3	100	1.5	30	0.4037	7.8788
4	150	0.5	20	0.2709	11.3438
5	150	1	30	0.2831	10.9612
6	150	1.5	10	0.3170	9.9788
7	200	0.5	30	0.2245	12.9757
8	200	1	10	0.2331	12.6492
9	200	1.5	20	0.2703	11.3631

Table 6 Output responses for ID grinding

S. No.	S (RPM)	F (m/min)	D (μm)	R_a (μm)	S/N ratios
1	200	0.25	10	0.2581	11.7642
2	200	0.50	20	0.2567	11.8115
3	200	0.75	30	0.2259	12.9217
4	250	0.25	20	0.3723	8.5821
5	250	0.50	30	0.3346	9.5095
6	250	0.75	10	0.3129	10.0919
7	300	0.25	30	0.4208	7.5185
8	300	0.50	10	0.4231	7.4711
9	300	0.75	20	0.4057	7.8359

3.2 Response Table and Main Effect Plots for OD and ID Grinding

3.2.1 Outer Diameter (OD)

To obtain optimum grinding parameters for the minimum surface roughness value, the smaller is better condition was selected. The average of *S/N* ratios of individual parameter and the maximum and minimum *S/N* ratios average value difference of individual parameters are shown by response Table 8. Response table shows that the difference between the maximum and minimum average value of *S/N* ratio is maximum for the work speed (2.728), followed by the feed (2.072), depth of cut (0.643), and the work speed plays significant role in obtaining the minimum surface roughness.

Response table for *S/N* ratios and the main effect plots for OD grinding are shown in Table 7 and Fig. 4, respectively.

Each parameter which has higher *S/N* ratio values of provides the optimum grinding parameter. The optimum grinding parameters obtained from the response table and main effect plot are shown in Table 7 and Fig. 4, respectively. Optimum conditions obtained are work speed, *S* = 200 RPM; feed, *F* = 0.5 m/min; and depth of cut, *D* = 10 μm.

Table 8 shows the ANOVA results for OD grinding, it shows that work speed (59.18%) contributes more in achieving desired surface roughness than the other parameters like feed rate (35.27%) and depth of cut (3.34%).

Table 7 Response table for *S/N* ratios for OD grinding

Level	<i>S</i>	<i>F</i>	<i>D</i>
1	9.601	11.812	11.248
2	10.761	11.139	10.838
3	12.329	9.740	10.605
Delta	2.728	2.072	0.643
Rank	1	2	3

Table 8 ANOVA results for OD grinding

Source	DF	SS	MS	<i>F</i>	<i>P</i>	%C
S	2	11.2424	5.6247	27.27	0.035	59.18
F	2	6.7013	3.3506	16.24	0.058	35.27
D	2	0.6353	0.3177	1.54	0.394	3.34
Error	2	0.4125	0.2063			2.17
Total	8	18.9985				100

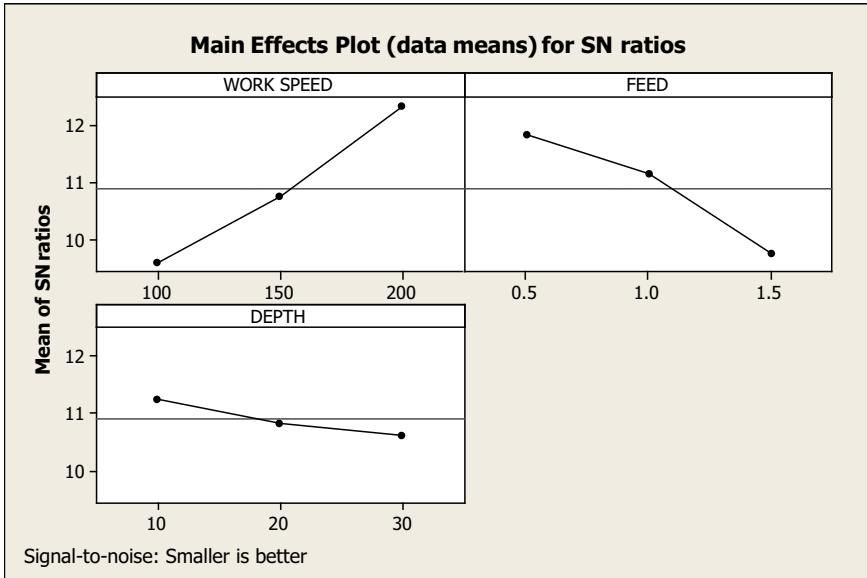


Fig. 4 Main effect plots for OD grinding

3.2.2 Inner Diameter (ID)

Response table for *S/N* ratios and main effect plots for ID grinding are shown in Table 9 and Fig. 5, respectively.

Response table shows that the maximum and minimum average value difference of *S/N* ratios is maximum for the work speed (4.557) followed by the feed (0.995) and depth of cut (0.573), and the work speed plays significant role in obtaining the minimum surface roughness.

Response table and main effect plot which are shown in Table 10 and Fig. 5, the optimum grinding parameters were obtained to reduce the surface roughness. Optimum conditions obtained are work speed, $S = 200$ RPM; Feed, $F = 0.75$ m/min; and depth of cut, $D = 30 \mu\text{m}$.

Table 9 Response table for *S/N* ratios of surface roughness on ID grinding

Level	<i>S</i>	<i>F</i>	<i>D</i>
1	12.166	9.288	9.776
2	9.395	9.597	9.410
3	7.609	10.283	9.983
Delta	4.557	0.995	0.573
Rank	1	2	3

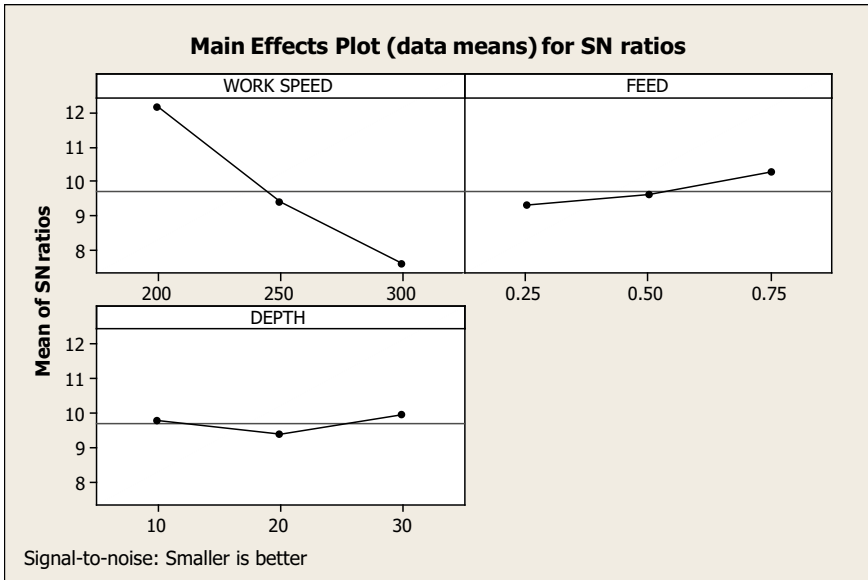


Fig. 5 Main effect plots for ID grinding

Table 10 ANOVA results for ID grinding

Source	DF	SS	MS	F	P	%C
V	2	31.6388	15.8194	902.97	0.001	93.79
F	2	1.5556	0.7778	44.40	0.022	4.61
D	2	0.5057	0.2528	14.43	0.065	1.50
Error	2	0.0350	0.0175			0.1
Total	8	33.7351				100

Table 10 shows the ANOVA results for ID grinding, it shows that work speed (93.79%) contributes more in achieving desired surface roughness than the other parameters like feed rate (4.61%) and depth of cut (1.50%).

3.3 Interaction Plots

Interaction plots show the input parameters interaction between work speed, feed rate, and depth of cut on obtained surface roughness for OD and ID are shown in Figs. 6 and 7, respectively. Interaction plot for OD grinding also suggests and proves that work speed is the dominating factor in deciding the surface roughness values for the selected input parameters.

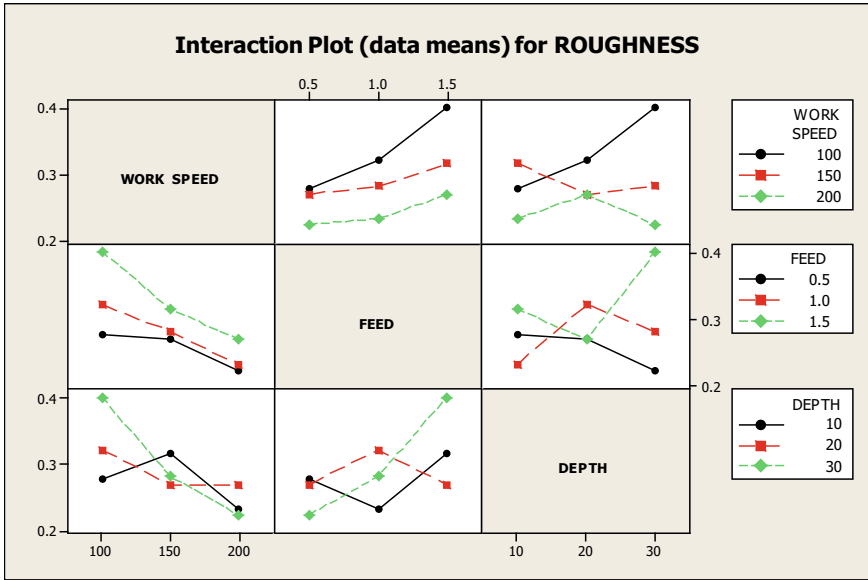


Fig. 6 Input parameters interaction plots for OD grinding

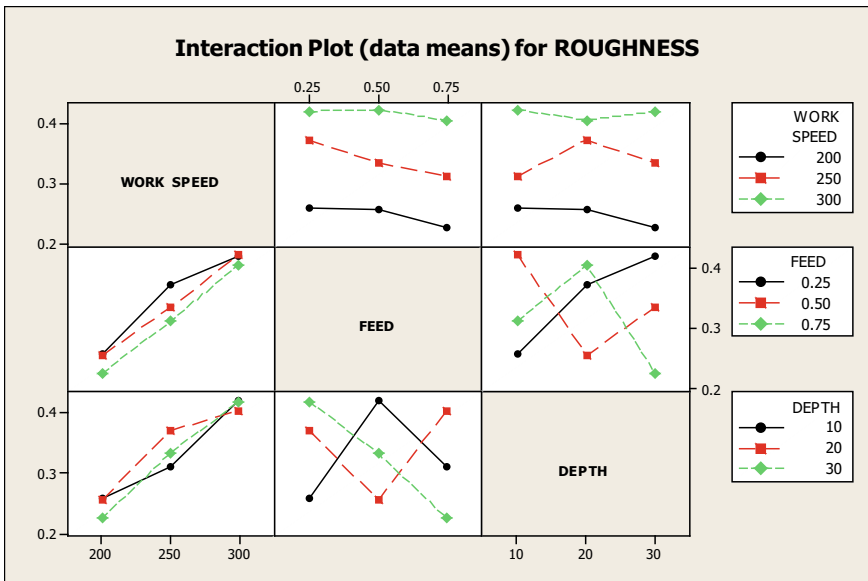


Fig. 7 Input parameters interaction plots for ID grinding

Table 11 Minimum surface roughness for OD grinding

Optimum OD grinding parameters	Predicted surface roughness (μm)	Experimental surface roughness (μm)
200, 0.5, 10	0.197867	0.201

Interaction plot for ID grinding clearly suggests that surface roughness value increases for ID with the increase in work speed with the feed rate and depth of cut combination. This proves that work speed is the dominating factor in deciding the surface roughness values for the selected input parameters.

4 Confirmation Test Results

The surface roughness value predicted from the Taguchi analysis for optimum grinding parameters were $S = 200$ RPM, $F = 0.5$ m/min and $D = 10 \mu\text{m}$ is $0.197 \mu\text{m}$ for OD grinding. Confirmation test was performed for the optimum grinding parameters values, i.e., for work speed $S = 200$ rpm, $F = 0.5$ m/min, and $D = 10 \mu\text{m}$ using Al_2O_3 wheel, obtained from the response tables. The surface roughness value obtained from the confirmation test is $0.201 \mu\text{m}$ and it was compared with predicted R_a $0.197 \mu\text{m}$. The result was found to be in agreement with the predicted surface roughness value which is better than experiment number 7 value is $0.2245 \mu\text{m}$. For ID grinding, the optimum grinding parameters are $S = 200$ RPM, $F = 0.75$ m/min, and $D = 30 \mu\text{m}$ which is same as experiment number 3.

Table 11 provides the details about the minimum surface roughness for optimum grinding parameters.

5 Conclusions

Cylindrical grinding experiments were conducted to study the effect of grinding parameters to reduce the surface roughness and obtained the optimum grinding parameters to achieve minimum surface roughness value for both the OD and ID grinding of bearing bush. The conclusion is shown below,

- (a) The work speed is the most important influencing factor to control the surface roughness for both the OD and ID grinding.
- (b) Optimum grinding parameters for achieving minimum surface roughness for OD grinding are work speed = 200 RPM, feed = 0.5 m/min and depth of cut = $10 \mu\text{m}$.
- (c) Optimum grinding parameters for achieving the minimum surface roughness for ID grinding are work speed = 200 RPM, feed = 0.75 m/min and depth of cut = $30 \mu\text{m}$.

- (d) Confirmation test was performed for the optimum grinding parameters and the results obtained are in agreement with the predicted surface roughness value. Minimum surface roughness value of 0.201 μm was achieved for optimum grinding conditions for OD grinding.
- (e) These optimized parameters can be used during finish grinding of bearing bush on feed rollers.

References

1. Jagtap KR, Ubale SB, Kadam MS (2011) Optimization of cylindrical grinding process parameters for AISI 5120 steel using taguchi method. *Int J Design Manuf Technol* 2:47–56
2. Melwin Jagadeesh Sridhar M, Manickam M, Kalaiyarasa V, Abdul Ghani Khan M, Kanna T (2014) Optimization of cylindrical grinding process parameters of OHNS steel (AISI 0–1) round using design of experiments concept. *Int J Eng Trends Technol* 17:109–114
3. Stephenson DJ, Veselovac D, Manley S, Corbett J (2001) Ultra-precision grinding of hard steels. *J Int Soc Precis Eng Nanotechnol* 25:336–345
4. Hecker RL, Liang SY, Majumder P (2003) Predictive modelling of surface roughness in grinding. *Int J Mach Tools Manuf* 43:755–761
5. Deshmukh SM, Shelke RD, Bhusare CV (2015) Optimization of cylindrical grinding process parameters of hardened material using response surface methodology. *Int J Innov Sci Eng Technol* 3:216–219
6. Daneshi A, Jandaghi N, Tawakoli T (2014) Effect of dressing on internal cylindrical grinding. *Procedia CIRP* 14:37–41
7. Grzesika W, Żaka K (2014) PiotrKiszka: comparison of surface textures generated in hard turning and grinding operations. *Procedia CIRP* 13:84–89
8. Singh K, Kumar P, Goyal K (2014) To study the effect of input parameters on surface roughness of cylindrical grinding of heat treated AISI 4140 steel. *Am J Mech Eng* 2(3):58–64
9. Sadeghi MH, Hadad MJ, Tawakoli T, Vesali A, Emami M (2010) An investigation on surface grinding of AISI 4140 hardened steel using minimum quantity lubrication-MQL technique. *Int J Mater Form* 3:241–251
10. Deresse NC, Deshpande V, Taifa IWR (2020) Experimental investigation of the effects of process parameters on material removal rate using Taguchi method in external cylindrical grinding operation. *Eng Sci Technol Int J* 23:405–420
11. Mekala K, Chandradas J, Chandrasekaran K, Kannan TTM, Ramesh E, Narsingh Babu R (2014) optimization of cylindrical grinding parameters of austenitic steel rods (AISI 316) by Taguchi method. *Int J Mech Eng Robot Res* 3(2)
12. Raju VR, Chellamalai M, Shashikumar PV (2012) Study on surface quality and accuracy of hardened axial feed rollers of honing machine. *Int J Precis Technol* 3(1):82–90

Study of Correlation Between Areal Surface Parameters and CoF of Ti6Al4V



M. Venkata Krishna Reddy , Jino Joshy , Basil Kuriachen ,
and M. L. Joy 

1 Introduction

The Titanium (Ti) and its alloys are in demand and has acquired popularity. They exhibit inherent properties such as high strength to density ratio, corrosion resistance, biocompatibility, good workability, and mechanical behavior [1]. Among titanium alloys, Ti6Al4V (Ti64, grade V, and α - β alloy) emerges 50% (approx.) of the production all over the world. Ti64 alloy is extensively used in aerospace, biomedical implants, automotive, chemical industry, propulsion systems [2], etc. However, the alloy exhibits poor tribological properties and low thermal conductivity [3]. Post finishing methodologies, namely, laser peening [4] and thermal oxidation, are difficult to perform as they require advanced equipment and special surface to observe the wear and friction behavior of Ti64. Jibin et al. [5] concluded that electric discharge machined Ti64 (ETi64) surface produces better tribological properties than the bare Ti64 surface. They reported that the surface of ETi64 contains a hard and recast layer at the top of the surface. In recent days, laser surface texturing (LST) [6], electrical discharge texturing (EDT), and laser beam texturing are available to modify the surfaces which can reduce wear rate and friction force during tribo interaction. The applications of electrical discharge texturing (EDT) are mill roll texturing [7], solar cell texturing [8], orthopedic implant texturing [9], and texturing on the rake face of the tool.

M. V. K. Reddy (✉) · J. Joshy · B. Kuriachen · M. L. Joy
Department of Mechanical Engineering, National Institute of Technology Calicut,
Calicut 673601, India
e-mail: mvkr464@gmail.com

M. L. Joy
e-mail: mlj@nitc.ac.in

The surface topography formed during the manufacturing process is of random texture composed of microscopic peaks and valleys. Modifying surface topographies have been a new technique to control friction and wear during tribological interactions [10]. Nowadays, to characterize the surface, researchers use areal (3D) surface parameters because it is a closer representation of the real surface compared to equivalent profile (2D) surface parameters. Lundberg [11] found that R_{max} and R_t are the most important surface parameters in the case of lubrication. Shi et al. [12] studied the influence of areal surface parameters on the tribological behavior of the random rough surface. They considered four ISO 25178 areal surface parameters, namely, S_a , S_{ku} , V_{vv} , and V_{vc} . The results have shown that with the increase of areal surface parameters, the CoF decreased first and then increased. They observed that surface wear is small when void volume is higher. Menezes et al. studied the correlation coefficient between surface roughness parameters and CoF [13]. They found maximum correlation coefficient was 0.72 between CoF and kurtosis (S_{ku}) under dry conditions. Prajapathi and Tiwari [14] studied the correlation between CoF and areal topography parameters. They observed a positive correlation between CoF and S_q , S_{sc} , and S_{dq} , whereas a negative correlation between CoF and S_{al} , S_k . Surface roughness parameters S_{ku} , S_{sk} , and S_{vk} show a good correlation to the tribological properties. Surfaces which has more S_{ku} value and negative S_{sk} value tend to reduce friction [15]. Dzierwa [16] concluded that volumetric wear was strongly correlated with S_{pd} and S_{sk} parameters. Higher values of S_{td} and S_{ku} and smaller values of S_{sk} had shown less volumetric wear in the surface.

From the literature review, it is understood that research work on the effect of random textured surface through EDM on tribological behavior is limited to date. Evaluation of areal (3D) surface parameters on textured surfaces are few. Hence, in this paper, the influence of areal surface parameters on the tribological behavior has been evaluated.

2 Experimental Methodology

2.1 Materials

Ti64 is selected as workpiece material for the present work, procured as thin rods (length = 30 mm, and diameter = 6 mm). For random texturing through electric discharge machine (EDM), copper was chosen as a tool material and EDM 3 oil as a dielectric. Copper was selected as a tool because of its high electrical conductivity, whereas EDM 3 oil does not favor high carbon deposition. To perform tribo test, random textured Ti64 through EDM at constant process parameters was chosen as the pin, and EN 31 (60 HRC) steel disk (165 mm diameter and 8 mm thickness) was chosen as the counter body surface. In many tribological applications, steel is used as a counter body and also steel-titanium pair is used in antifriction bearings [5].

Table 1 Process parameters of EDM

Sl. No.	Factor	Description/value
1	Tool electrode	Copper
2	Workpiece	Ti6Al4V
3	Dielectric fluid	EDM 3 oil
4	Current (I, Amp)	18
5	Pulse on time (T_{on} , μ s)	100
6	Duty cycle (%)	25
7	Voltage (V)	60

2.2 Development of Random Textured Surface

The experimentations to develop random textured surface on Ti64 were achieved through a die sinker EDM machine. The specimens were accurately positioned on the vice and fastened; a magnetic chuck is used to fix the vice to the bottom of the machining tank. The specimens are textured at the similar process parameters and specimens are designated as TiS1, TiS2, and TiS3, for easy identification. Table 1 shows the process parameters of EDM [17] related to the ED texturing of Ti64.

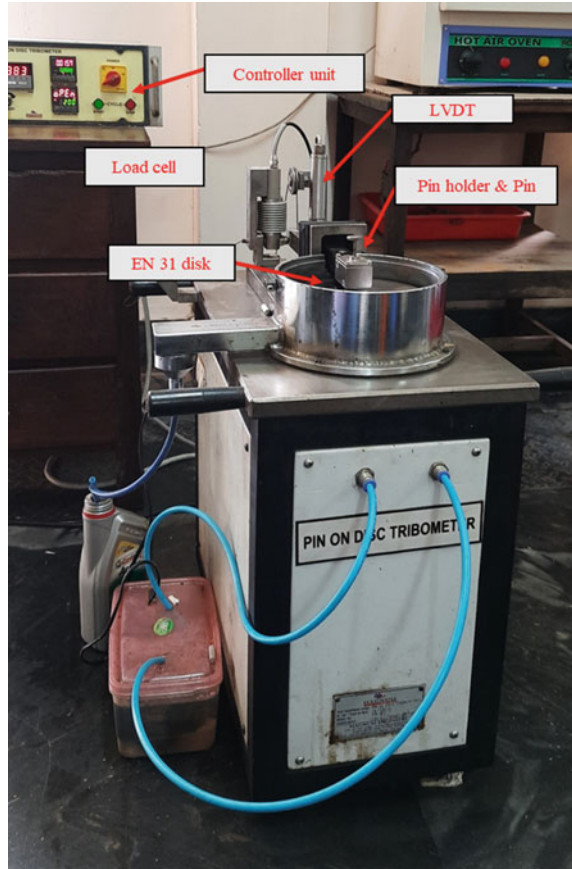
2.3 Tribo-Test

The tribological characteristics of the random textured surfaces of the specimens were carried out on computerized PoD by following ASTM G99-05 at ambient and dry conditions. The test setup was shown in Fig. 1. The tests were performed at constant parameters of 50 N normal load, 0.838 m/s sliding velocity, and a sliding distance of 1000 m [13] for all specimens. The pin and the disc were cleaned and dried using acetone before each experiment. Frictional force was measured using load cell which is arranged on PoD. To calculate weight loss and specific wear rate, weight of each specimen was measured before and after the tribo test (Table 2).

3 Results and Discussion

The random textured surfaces developed on Ti64 through EDM at constant process parameters are characterized quantitatively with the help of 3D profilometer (Alicona InfiniteFocus G5) at 10 X magnification. Before characterization, the surface was cleaned and dried using acetone. Then specimens are tested under PoD to calculate CoF. Figure 2 shows the variation of CoF with sliding distance for all the specimens. The CoF is in the range 0.56–0.59; earlier work [18] also had reported almost the same values.

Fig. 1 Pin-on-disk tribometer setup



From the literature [19], there are 25 areal surface parameters available to characterize the surface texture. Even if two surfaces have the same surface parameters, their frictional behavior could be different. It is observed that areal surface parameters are different, though random texturing was done at constant process parameters of EDM. Therefore, it is necessary to evaluate the effect of areal surface parameters with CoF. An endeavor was made to study the dependence between CoF and areal surface parameters. To study the dependency between two parameters, a linear correlation coefficient is used, which ranges from -1 to $+1$. The higher the absolute value of a correlation coefficient, the stronger the relationship between two parameters. For the present study, 14 surface parameters are considered, and calculated correlation coefficient between surface parameters and CoF. Figure 3 shows the analysis of correlation with CoF under dry conditions. From Fig. 3 observed that absolute maximum and minimum correlation coefficient values are 0.946 and 0.347, respectively.

The correlation coefficient between CoF and areal surface parameters was calculated to be 0.946, the absolute maximum value and it was obtained between CoF and

Table 2 Nomenclature of areal surface parameters

Areal surface parameter	Description
Sa (μm)	Arithmetic mean height
Sq (μm)	Root mean square height
Sp (μm)	Maximum peak height
Sv (μm)	Maximum valley height
Sz (μm)	Maximum height
Ssk	Skewness
Sku	Kurtosis
Sdq	Root mean square gradient
Sk (μm)	Core roughness depth
Spk (μm)	Reduced peak height
Svk (μm)	Reduced valley height
Vvc (ml/m^2)	Core void volume
Vvv (ml/m^2)	Valley void volume
Sal (μm)	Auto correlation length

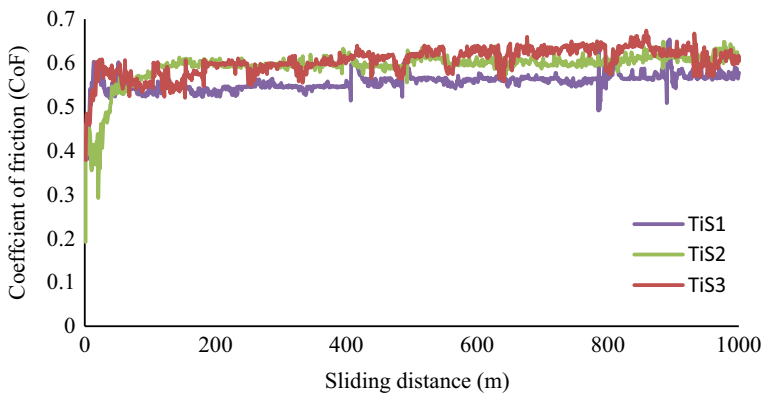


Fig. 2 Variation of CoF with sliding distance

Sk (core roughness depth). The immediate absolute maximum correlation coefficient was obtained between CoF and Sp (maximum peak height); the calculated value was 0.933. The areal surface parameters root mean square gradient (Sdq) and reduced peak height (Spk) are negatively correlated with CoF (see Fig. 3); the values obtained were -0.862 and -0.552 , respectively.

Figure 4a–f shows the variation between the CoF and areal surface parameters, which are positively correlated. core roughness depth Sk has a strong correlation with CoF and lower the (Core roughness depth (Sk) value, the minimum is the CoF (see Fig. 4a). When the maximum peak height (Sp) value is $518 \mu\text{m}$ (approx.), the

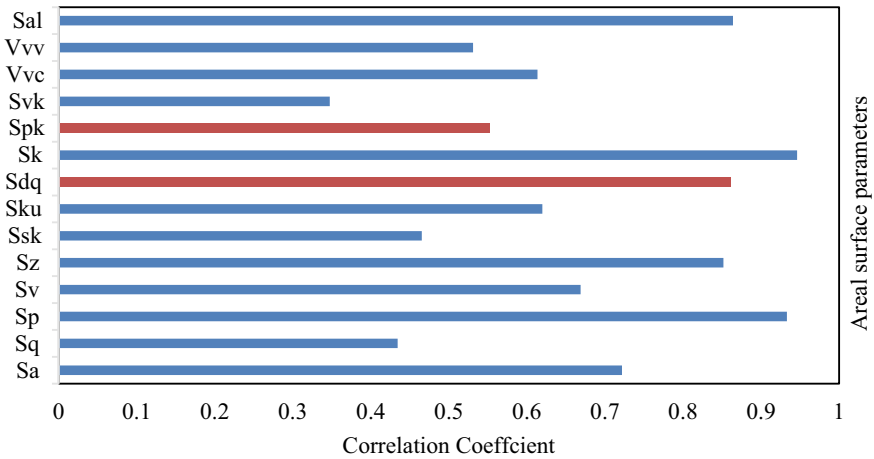


Fig. 3 Correlation coefficient between CoF and areal surface parameters: blue and orange bar indicates positive and negative correlation, respectively

CoF was 0.56, which is the lowest among all the specimens (refer Fig. 4b). Figure 4c shows as auto correlation length (Sal) value increases, CoF increases. maximum height (Sz) is the maximum height of the surface, which means higher the maximum height (Sz) value, the more asperities will contact the counter body during the tribotest. As anticipated, higher maximum height (Sz) value has shown higher CoF (refer Fig. 4d). Figure 4e–f shows a similar trend of CoF with skewness (Ssk) and kurtosis (Sku), respectively. The lowest skewness (Ssk) value exhibits low CoF.

Figure 5a–b shows the variation of CoF with negatively correlated areal surface parameters. Root mean square gradient (Sdq) parameter has a maximum correlation coefficient with CoF, and the obtained value was -0.862 . The correlation coefficient between CoF and reduced peak height (Spk) was -0.552 .

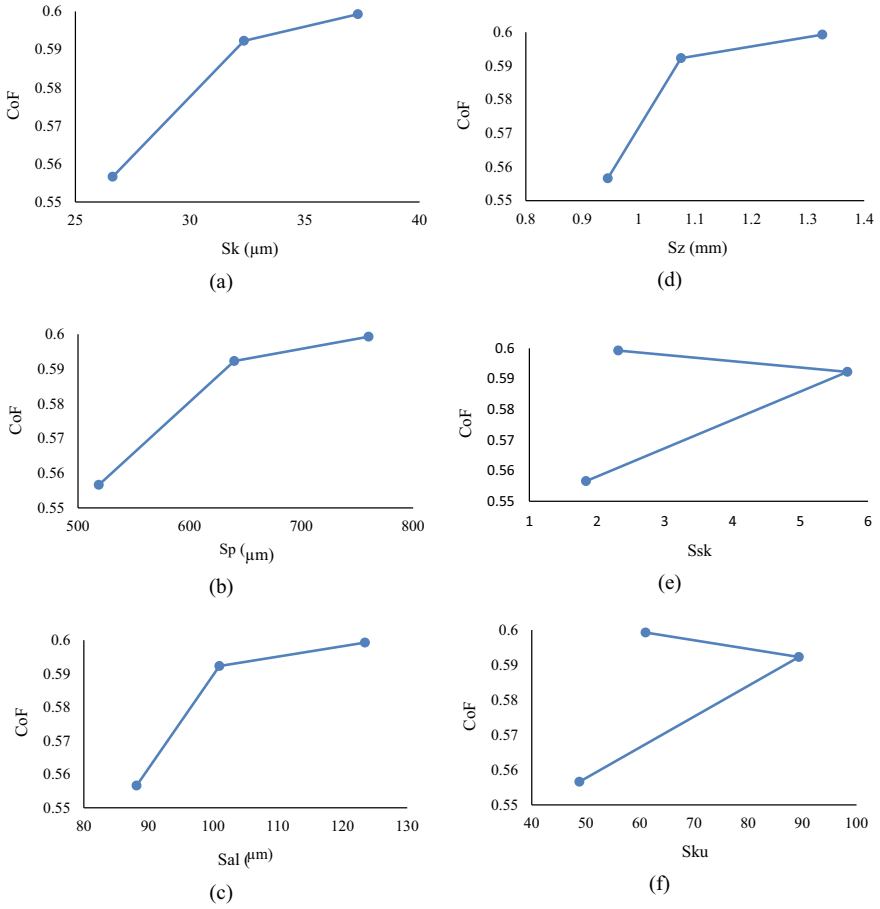
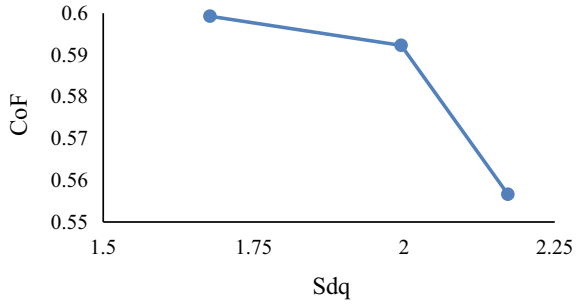
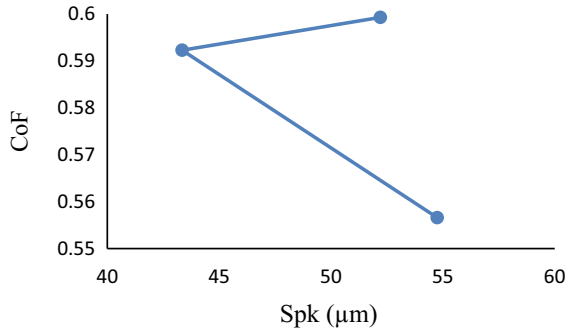


Fig. 4 a-f Variation of CoF with positively correlated areal surface parameters

Fig. 5 a-b Variation of CoF with negatively correlated areal surface parameters



(a)



(b)

4 Conclusions

In the present work, PoD was used to study the influence of areal surface parameters on the CoF. The following inferences were obtained:

- Random texturing developed through EDM at constant process parameters on Ti64 surfaces exhibits different areal surface parameters.
- PoD test was conducted, and the CoF of all specimens was in the range 0.56–0.59.
- Areal surface parameters core roughness depth (Sk), maximum peak height (Sp), auto correlation length (Sal), root mean square gradient (Sdq), were observed to show a good correlation with CoF.
- Higher the core roughness depth (Sk), maximum peak height (Sp), auto correlation length (Sal), lesser root mean square gradient (Sdq), and reduced peak height (Spk) parameters had shown more CoF.

Acknowledgements Authors would like to thank Department of Science and Technology, Govt. of India for supporting this work under the scheme FIST (No. SR/ FST/ETI-388/2015).

References

1. Jibin Philip et al (2021) Tribological investigations of wear resistant layers developed through EDA and WEDA techniques on Ti6Al4V surfaces: part II—high temperature. *Wear*, pp 466–467
2. Geetha M et al (2009) Ti based biomaterials, the ultimate choice for orthopaedic implants—a review. *Prog Mater Sci* 54:397–425
3. Budinski KG et al (1991) Tribological properties of titanium alloys. *Wear* 151:203–217
4. Kumar D et al (2015) Tribological performance of laser peened Ti-6Al-4V. *Wear* 322–323:203–217
5. Philip J et al (2019) Wear characteristic evaluation of electrical discharge machined Ti6Al4V surfaces at dry sliding conditions. *Trans Indian Inst Met* 72:2839–2849
6. Kovalchenko et al (2005) The effect of laser surface texturing on transitions in lubrication regimes during unidirectional sliding contact. *Tribol Int* 38:219–225
7. Aspinwall et al (1992) Electrical discharge texturing. *Int J Mach Tools Manuf* 32:183–193
8. Qian et al (2002) EDM texturing of multicrystalline silicon wafer and EFG ribbon for solar cell application. *Int J Mach Tools Manuf* 42:1657–1664
9. Harcuba et al (2012) Surface treatment by electric discharge machining of Ti-6Al-4V alloy for potential application in orthopaedics. *J Mech Behav Biomed Mater* 7:96–105
10. Edachery et al (2022) The role of surface topography and normal load in the initiation of ratchetting-peak friction, seizure, scuffing, and elastic shakedown. *J Tribol* 144:1–7
11. Lundberg (1995) Influence of surface roughness on normal-sliding lubrication. *Tribol Int* 28:317–322
12. Shi et al (2019) Effect of surface topography parameters on friction and wear of random rough surface. *Materials* 12:7
13. Menezes et al (2009) Influence of surface texture and roughness parameters on friction and transfer layer formation during sliding of aluminium pin on steel plate. *Wear* 267:1534–1549
14. Prajapati, Tiwari (2021) The correlation between friction coefficient and areal topography parameters for AISI 304 steel sliding against AISI 52100 steel. *Friction* vol 9, pp 41–60
15. Sedlaček et al (2012) Correlation between standard roughness parameters skewness and kurtosis and tribological behaviour of contact surfaces. *Tribol Int* 48:102–112
16. Dzierwa (2017) Influence of surface preparation on surface topography and tribological behaviours. *Arch Civil Mech Eng* 17:502–510
17. Kumar R et al (2018) Analysis of MRR and surface roughness in machining Ti-6Al-4V ELI titanium alloy using EDM process. *Procedia Manuf* 20:358–364
18. Philip J et al (2020) Monitoring of EDM parameters to develop tribo-adaptive Ti6Al4V surfaces through accretion of alloyed matrix. *Ind Lubr Tribol* 72:291–297
19. Leach R (2013) Characterisation of areal surface texture. 1st edn. Springer, UK

Wear and Hardness Behavior of Duplex-Treated AISI 1045 and AISI 4142 Steels



B. Vaishnavi, A. Adhiyamaan, D. J. Hiran Gabriel,
and Vinoth Kanna Chandrasekar

1 Introduction

The steel can be defined as a crystalline alloy of iron, carbon, and several other elements, which hardens above its critical temperature. It is multi-functional and most adaptable material with low production cost. The AISI 1045 and AISI 4142 steels which finds various applications, especially in the axles, crankshafts, gears, and hydraulic shafts are subjected to different kinds of wear that limits the extent of its application. The various uses of steel which in turn is a measure of its adaptability come from its remarkable characteristics [1]. This can be achieved by various surface modification technologies that improves its surface properties in various applications thus furthering its utility value. Surface hardening is a broad phrase that refers to a variety of procedures that improve the wear resistance of ferrous parts while preserving the softer and tough interior. Furthermore, surface hardening of steel has an edge over through hardening in which low- and medium-carbon steels could be surface hardened without distortion or cracking difficulties. [2].

Duplex surface engineering entails the use of two (or even more) established surface technologies in a sequential manner to create a surface composite with combined features that are not possible with any single surface technology. Although the number of conceivable surface technology combinations is virtually limitless, the list of duplex surface technologies might go on forever. Only a handful duplex procedures have been created to date, and only a few have found real-world applications.

B. Vaishnavi · A. Adhiyamaan · D. J. H. Gabriel (✉) · V. K. Chandrasekar
Department of Mechanical Engineering, PSG College of Technology, Coimbatore 641 004, India
e-mail: victorrajn1996@gmail.com

B. Vaishnavi
e-mail: bvi.mech@psgtech.ac.in

A. Adhiyamaan
e-mail: aam.mech@psgtech.ac.in

The primary benefit of the duplex treatment is that it first modifies the substrate's surface and subsurface to form a deep hardened case that can be a few micrometers thick. The coating is then effectively supported by such a subsurface. The final efficiency of the duplex treatment is determined not only by the best substrate material and coating, but also by substrate roughness, subsurface microstructure homogeneity, and microhardness characteristics. [3].

Boronizing is a surface hardening technique in which boron atoms infiltrate into a base metal (steel) and form a hard metallic boride layer on the surface using a thermochemical approach. By heating the substrates to temperatures between 700 and 1000 °C for many hours, the boronizing process can be used to both ferrous and nonferrous materials. The technique produces a 20–300 μm thick metallic boride layer with remarkable features such as high hardness, strong wear and corrosion resistance, and mild oxidation resistance at high temperatures. As a result of the narrow atomic radius of the boron atom (0.46 Å), an interstitial boron compound is generated using either a single-phase boride or a poly-phase boride layer [4].

Physical vapor deposition is an atomistic deposition technique in which material is evaporated from a solid source as atoms or molecules, then transferred to the substrate in a vacuum or low pressure gaseous (or plasma) environment, in which it condenses to form a coating. PVD processes are frequently used to deposit thin films ranging in thickness from a few nanometers to several microns. As a result, the film's physical, structural, and tribological properties are tuned to a strong bond between the coating and the tooling substrate. [3]. PVD hard coatings on steel were known to provide surfaces with improved tribological qualities, such as lower friction and increased wear resistance. However, other steel surface treatments, such as boronizing and nitriding, gave similar effects to PVD coatings. As a result, research was conducted on duplex treatments, which comprise dual coating on substrates or single coating on the pre-hardened surface, resulting in a duplex structure, in order to expand the use of steels in diverse applications. [3, 5, 6].

The mechanical properties of borides produced on AISI H13 hot work tool steel and AISI 304 stainless steels were examined by Taktak [7]. Boriding treatment was carried out for 3, 5, and 7 h in a slurry salt bath containing borax (60 wt%), boric acid (20 wt%), and ferrosilicon (20 wt%) at temperatures ranging from 800 to 950 °C. Due to the high concentration of Cr and Ni borides in stainless steel, the hardness of the boride layer on boride 304 stain-free steel was found to be greater than that of the borides on H13 tool steel. The rise in boride layer hardness ensued in a decrease in fracture toughness. Additionally, as the boriding temperature and time increased, the surface roughness of borided H13 and 304 steels increased [7].

Kul et al. [8] investigated the impact of boronizing composition on hardness of boronized AISI 1045 steel. Various chemical agents were employed to boronize in liquid and solid media. This study examined the hardness and thickness of the layers formed by the boronizing composition. The most satisfactory boronizing compositions in the liquid media was found to be 70% borax ($\text{Na}_2\text{B}_4\text{O}_7$) + 30% B_4C for obtaining the hardest and thickest borid layer on AISI-1045 steel samples. About 5% B_4C + 90% SiC + 5% KBF_4 was shown to be the best combination for boronizing solid media [8].

Leyva et al. [9] compared single-layered TiAlN and TiN to the micro-abrasive wear of duplex coatings consisting of plasma nitriding followed by PVD coating of TiAlN and TiN. It was shown that the duplex treatment significantly improves the micro-abrasive wear resistance of its single-layered equivalent, which had a lower wear coefficient than the duplex TiN, implying that the PVD coating choice is critical in lowering micro-abrasive wear resistance [9].

By surface hardening method called boronizing, the mechanical properties of the tool steels were much improved, but there occurred damage on the borided layer due to the increasing expansion coefficient under the thermal fatigue testing, resulting in drastic wear. Similarly, the plastic deformation of the substrate hindered PVD single layer hard coatings, which were well recognized for producing surfaces with superior tribological qualities in terms of low friction and high wear resistance. This eventually caused coating failure. [6, 9, 10].

As a result, combining any two procedures in which substrates are treated before coating constituted a novel approach in terms of increasing subsurface properties, resulting in a harder and wear resistant surface. Nowadays, duplex treatments are used to enhance the surface characteristics of mechanical components. A duplex treatment is a combination of two treatments that improves surface qualities by combining their benefits [11]. The goal of this study is to examine the microhardness, wear performance, and micro-chemical analysis of PVD TiN coatings coated on boronized AISI 1045 and AISI 4142 steels. Energy-dispersive X-ray spectroscopy (EDS) was used to detect the distribution of alloying elements from the surface to the inside, and scanning electron microscopy was used to examine the thickness of the deposited layer (SEM). A comparative measurement of microhardness and wear was performed to determine the performance of the treated samples.

2 Materials and Methods

The AISI 1045 and AISI 4142 steels were identified as a substrate material. The chemical composition of the steels is illustrated in Table 1. AISI 1045 and AISI 4142 steel samples with dimensions 23 mm diameter and 13 mm length were used for micro abrasion wear testing. Each rod was cut into five pieces by wire cut EDM followed by grinding process. These specimens were cut perpendicular to the coating using wire cut EDM process.

The samples were covered with boron paste (B4C with 76 wt% boron) to the desired thickness and subjected in a standard furnace at 1153 K for 1 h. The boronizing paste was removed after the treatment by brushing or washing. In the same furnace, the samples were heated to 1128 K once again.

The samples were quenched in oil at the end of the process. One of the most essential characteristics of a boronized layer is that it retains its hardness during further heat treatments. The boronized layer maintains its hardness up to 1173 K, allowing heat treatment to be given to the matrix material over a wide range of temperatures. TiN material was deposited as a thin and high adherent coating onto

Table 1 Chemical composition of AISI 1045 steel and AISI 4142 steel

Element	AISI 1045 steel composition	AISI 4142 steel composition
C	0.423	0.437
Mn	0.715	0.615
Si	0.177	0.214
S	0.022	0.019
P	0.017	0.020
Cr	–	1.182
Cu	–	0.055
Mo	–	0.275
Ni	–	0.064
Fe	Balance	Balance

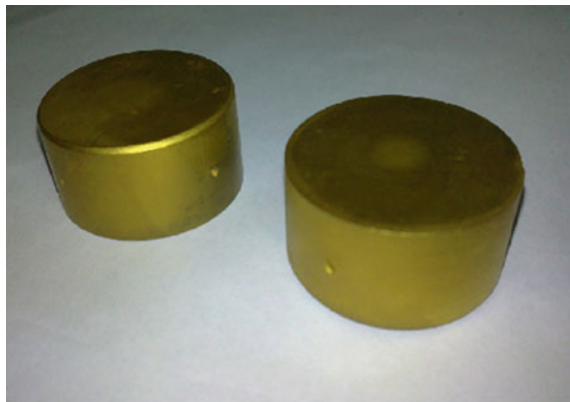
the boronized surfaces at a temperature of 350°C by PVD coating process, so that the layer is not destabilized. Figure 1 shows the photograph of the coated samples.

X-ray diffraction (XRD) was done to study the material deposited on the samples. The diffraction angle 2θ was kept between 15 and 65.

Micro Vickers Hardness Tester-Wolpert Group was used to measure microhardness on the cross section of the samples. The objects' surfaces were polished, and measurements were taken in a Vickers hardness tester with a 0.1 kgf load. This load was kept constant during all measurements so that the results could be compared by altering the depth from the base surface. However, in order to avoid inaccuracies that may arise when indenting on these scratches, the test surface should be properly polished and free of fine scratches.

Micro abrasion testing was used to assess the wear performance of the duplex-treated and bare substrates. The samples were tested using the block-on-ring method, with diamond slurry used as an abrasive medium to increase the abrasion's intensity.

Fig. 1 Duplex-treated samples (boronized + PVD TiN coated)



The Plint-TE-66 micro abrasion tester is available from M/s Phoenix tribology Ltd. in the UK. The coated samples were pressed against a directly driven steel ball rotating at 150 rpm, in line with ASTM G 77. Furthermore, the duplex-treated samples were subjected to abrasion with two different loads, viz, 1 and 2 N for a duration of 3 and 5 min in each of these loads. Diamond particles which are less than a sub-micrometer range are mixed with turpentine to form diamond slurry. Throughout the test, this diamond slurry was continually fed on the ball-to-sample interface. For the coefficient of friction versus time, an instantaneous plot was obtained. These plots were used to calculate the wear coefficient, which was then compared.

3 Results and Discussion

The microhardness values of the uncoated and duplex treated samples were measured using Vickers Hardness Tester. The samples were measured at a load of 0.1kgf. The microhardness values of AISI 1045 and AISI 4142 steels are illustrated in Table 2. The microhardness values of the boronized specimens were about 1500–1700 Hv0.1, respectively. The increase in hardness values was attained through the formation of borides during the boronizing process that had enhanced the surface hardness of metal surfaces. When the microhardness values were examined for the TiN layer which is coated over the boronized surface, it was observed that the hardness values reached a maximum of 3806 HV in case of AISI 4142 steel and 3529 HV in AISI 1045 steel. Finally, the results pointed out that the boronized layer improved the mechanical support for the single-layered TiN coating, which is responsible for higher hardness values in the duplex-treated system. The microhardness value along the cross section of the duplex-treated samples with respect to distance in μm is given in Fig. 2a and b. From the graph plotted it is evident that the microhardness of the AISI 4142 steel is higher than the AISI 1045 steel. The increase in the microhardness results of the AISI 4142 steel could be due to the presence of the alloying elements and increased carbon content in it.

Table 2 Microhardness values for AISI 1045 and AISI 4142 steels

Indentation regions	Hardness (Hv _{0.1})	
	AISI 1045	AISI 4142
Base material	287	443
Base material	291.6	465
Interface	487.2	510.6
Interface	546.5	525.3
25 μm from interface	1599.3	1695.5
35 μm from interface	1680.4	1738.8
PVD region	3503.6	3795.1
PVD region	3529	3806

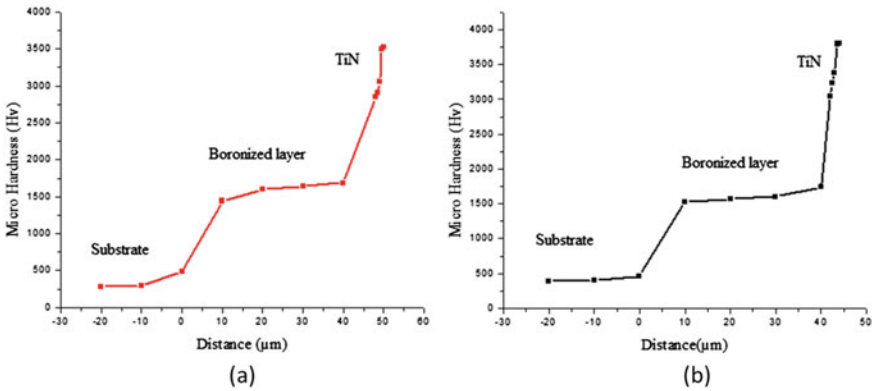


Fig. 2 Microhardness profile of duplex treated **a** AISI 1045 steel **b** AISI 4142 steel

The thickness of the compound layer was determined using SEM examination of polished cross sections of duplex-treated samples. It can be seen that the thickest boride layer was obtained in AISI 1045 steel, which is a low carbon steel that contains no alloy components. With the increasing of carbon and the alloying content, the boride layer thickness decreased. This decrease is attributed to the low solubility of carbon in the boride layer. As a result, it was demonstrated that this investigation was consistent with prior studies stating that boron diffusion is often higher in low alloy steels than in alloyed and high carbon steels. Table 3 shows the layer thickness of the samples. Figure 3 shows micrographs of the deposited layer in AISI 1045 and AISI 4142 steels (a and b).

The boride layer had a serrated morphology, which was uniformly distributed across the surface, according to the micrographs of the samples. Boron diffusion into the surface resulted in the formation of the boride layer. The foundation material was located beneath the diffusion zone. Above the diffused zone, the TiN layer was found to have a denser and finer microstructure with a variable thickness of 2–3 μm.

According to the micrographs of the samples, the boride layer showed a serrated morphology that was uniformly distributed across the surface. The development of the boride layer was caused by boron diffusion into the surface. The diffusion zone was beneath the foundation material. The TiN layer, which lies above the diffused zone, has a denser and finer microstructure with a variable thickness of 2–3 μm. At 1 N applied load, the duplex layer outperforms the substrate significantly, whereas at 2 N applied load, the coating outperforms the substrate only by about 20% and 15%, respectively.

Table 3 Thickness of the deposited layer

Samples	Boride layer thickness (μm)	TiN coating thickness (μm)
AISI 1045	47.8	2.98
AISI 4142	42.6	2.18

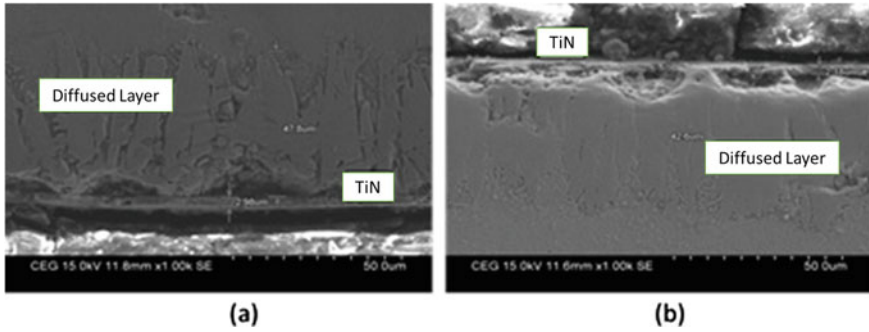


Fig. 3 Micrograph of the duplex layer in **a** AISI 1045 steel and **b** AISI 4142 steel

This hypothesis states that because the diamond abrasive has a significant effect on the wear mechanism, regardless of the applied load, the coating consistently performs with less wear resistance. It can be observed from Table 4 that the AISI 4142 steel showed decreased wear volume with respect to time when compared with AISI 1045 steel. The higher wear resistance of AISI 4142 steel is attributed to the higher hardness in it.

The friction coefficient of the treated and untreated samples of both AISI 1045 and 4142 steel as a function of time is shown in Fig. 4a and b. It was observed that all the samples had little fluctuations in friction coefficient during wear test. The coefficient of friction was found to decrease with time in the duplex-treated samples when compared to the untreated samples. However duplex treated AISI 4142 steel sample showed low coefficient of friction values than duplex-treated AISI 1045 sample, thus confirming that the sample with higher hardness shows higher wear resistance and thereby friction is reduced.

The XRD pattern of the duplex treated surfaces shows the presence of TiN and CBN phases. With reference to the results from the Match software, the peaks formed confirmed to the corresponding phases [12]. Fig. 5 illustrates the diffraction pattern calculated by Match software. The monolayer TiN coating and the cubic boron nitride phase demonstrates the occurrence of the preferential (111) crystallographic

Table 4 Wear volume analysis of AISI 4142 steel and AISI 1045 steel

Load	Time (min)	AISI 4142 steel		AISI 1045 steel	
		Wear volume of untreated samples (mm ³)	Wear volume of duplex-treated samples (mm ³)	Wear volume of untreated samples (mm ³)	Wear volume of duplex treated samples (mm ³)
2 N	5	0.3180	0.3132	0.3329	0.3257
2 N	3	0.2991	0.2889	0.3019	0.2995
1 N	5	0.2628	0.2602	0.2696	0.2638
1 N	3	0.2459	0.2401	0.2486	0.2418

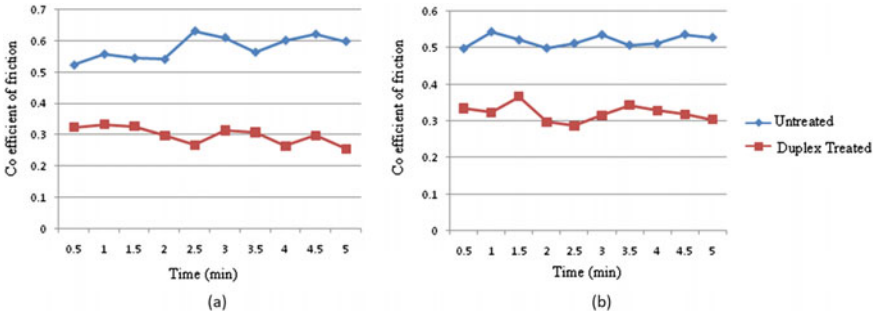


Fig. 4 Coefficient of friction of untreated and duplex-treated samples of a AISI 1045 steel and b AISI 4142 steel at 2 N load

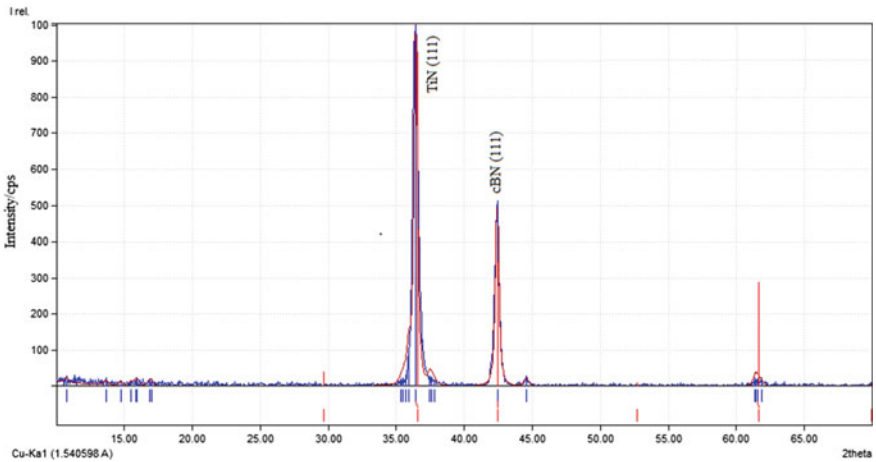


Fig. 5 XRD pattern of AISI 4142 steel

orientation. The formation of cubic boron nitride is responsible for the improved hardness and wear resistance in the samples. The TiN peak corresponds to the coating material over the boronized surfaces of the samples. This result suggests that the nitrogen in the coated region reacted with boron which is present in the diffusion zone to form the cubic boron nitride phases.

4 Conclusions

The AISI 1045 and the AISI 4142 steels were found to exhibit improved properties after the duplex surface treatment. This method which involves boronizing process followed by a PVD TiN coating is a new approach in the field of duplex surface

engineering. Hence, in this work, the new method of duplex treatment was established to improve the subsurface properties of the steels which extend its utility in various applications.

- The microhardness measurements pointed out that the hardness values of the AISI 4142 steel were comparatively greater than that of the AISI 1045 steels which is because of the alloying elements that is present in AISI 4142 steel.
- The borided layer not only provides mechanical support for the single-layered TiN coating, but it also modifies the coating hardness behavior throughout the coating system, resulting in a considerable increase in the microhardness of the treated samples as compared to the substrate surface.
- The results observed for wear performance analysis revealed that the AISI 4142 steel showed low wear volume and low co-efficient of friction thus giving improved wear resistance than the AISI 1045 steel. The higher microhardness value is responsible for higher wear resistance in AISI 4142 steel.
- The friction coefficient decreases with time in case of duplex-treated samples when compared to that of the untreated samples.
- The layer thickness of the samples as measured by the SEM showed that the boride layer of AISI 1045 steel was more than that of AISI 4142 steel, thus stating that the boron diffusion in low alloy steels is generally higher than that in alloyed and high carbon steels.
- The XRD pattern of AISI 4142 sample resulted in the formation of mainly two peaks, namely, TiN and cBN. The cubic boron nitride phase is responsible for the higher hardness and wear resistance in the treated samples.

References

1. Davim JP, Maranhão C (2009) A study of plastic strain and plastic strain rate in machining of steel AISI 1045 using FEM analysis. *Mater Des* 30(1):160–165
2. Şahin S (2009) Effects of boronizing process on the surface roughness and dimensions of AISI 1020, AISI 1040 and AISI 2714. *J Mater Process Technol* 209(4):1736–1741
3. Batista JC, Joseph M, Godoy C, Matthews A (2001) Micro-abrasion wear testing of PVD TiN coatings on untreated and plasma nitrided AISI H13 steel. *Wear* 249(10–11):971–979
4. Lee SY, Kim GS, Kim B-S (2004) Mechanical properties of duplex layer formed on AISI 403 stainless steel by chromizing and boronizing treatment. *Surf Coat Technol* 177–178:178–184
5. Bektes M, Calik A, Ucar N, Keddami M (2010) Pack-boriding of Fe-Mn binary alloys: characterization and kinetics of the boride layers. *Mater Charact* 61(2):233–239
6. Fenker M, Balzer M, Kappell H (2014) Surface & coatings technology corrosion protection with hard coatings on steel: past approaches and current research efforts. *Surf Coat Technol* 257:182–205
7. Taktak S (2007) Some mechanical properties of borided AISI H13 and 304 steels. *Mater Des* 28(6):1836–1843
8. Kul M, Danacı I, Karaca B (2020) Effect of boronizing composition on hardness of boronized AISI 1045 steel. *Mater Lett* 279:128510
9. Leyva CAL, Godoy C, Bozzi AC, Wilson JCA (2011) Ultra-low carbon (ULC) steel modified by triode plasma nitriding and PVD coating: effects on micro-abrasive wear behavior. *Surf Coat Technol* 206(7):1796–1808

10. Campos I, Ramírez G, VillaVelázquez C, Figueroa U, Rodríguez G (2008) Study of microcracks morphology produced by Vickers indentation on AISI 1045 borided steels. *Mater Sci Eng A* 475(1–2):285–292
11. Nistor AM, Becheru A, Foltut D, Buzdugan RM, Buzdugan D, Radu B (2020) Mechanical properties of duplex treated steels obtained by instrumented indentation. *Adv Mater Res* 1157:130–135
12. Zheng M, Liu Y, Wang P, Xiao Y (2013) Synthesis and formation mechanism of cubic boron nitride nanorods in lithium bromide molten salt. *Mater Lett* 91:206–208

Prediction of Mechanical Behaviour of AA 3003-O with Varying Volume Fractions of White Fly Ash and SiC



P. Ilanthirayan, M. Kalayarasan, and S. Mohanraj

1 Introduction

Metal matrix composites (MMC) possess high strength-to-weight ratio, which makes them attractive for use in various industries. The aluminium matrix composites (AMCs) are a category under MMCs that also possess low density, high stiffness and strength and better stability at elevated temperatures. Fly ash is one of the by-products from thermal power plants during of combustion of coals. Fly ash has been used in cement and concrete applications, bricks, fillers and road bases. Fly ash is underutilized or disposed of like garbage in most nations. The possible responsible materials for the grey-black colour of fly ash are due to unburnt coal, carbon black and iron in form of magnetite.

Udaya Prakash et al. [1] found that the material density of AMCs decreases with an increase in fly ash. David Raja Selvam et al. [2] studied the AA6061 composite reinforced with fly ash prepared by compocasting method. The microhardness and ultimate tensile strength (UTS) of the AMCs were improved when fly ash particles were incorporated.

Omyma El-Kady et al. [3] investigated the effect of the size of silicon carbide particle on Al matrix composite.

It is observed that hardness and compressive strength increase as the size of the silicon carbide particle decreases, whereas heat conductivity decreases. Dhar et al. [4] found that with an increase in fly ash amount, the mechanical properties such as

P. Ilanthirayan (✉) · M. Kalayarasan · S. Mohanraj
Department of Mechanical Engineering, PSG College of Technology, Coimbatore 641 004, India
e-mail: sithirayan2196@gmail.com

M. Kalayarasan
e-mail: mkn.mech@psgtech.ac.in

S. Mohanraj
e-mail: smr.mech@psgtech.ac.in

tensile strength and hardness increase. Umanath et al. [5] analysed the wear behaviour of Al6061-T6 discontinuously reinforced with SiC and Al₂O₃. They found a relation to find estimate wear using analysis of variance (ANOVA). Orthogonal arrays for required parameters were formed using the Taguchi method.

Kiran et al. [6] studied the dry sliding wear behaviour ZA-27 alloy reinforced with SiC and Gr fabricated using the stir casting method. Taguchi and ANOVA methods were employed to determine the influencing wear parameters. Renukappa [7] studied the dry wear behaviour of epoxy filled with organo-modified montmorillonite. L9 orthogonal array was used to study the wear parameters. Ravi Kumar et al. [8] studied the wear behaviour of Al reinforced with fly ash. Akhmad [9] studied the colour of fly ash using chemical analysis and found that the iron content in fly ash is important as it is increasing the whiteness. Sri Bandyopadhyay [10] found that the composite with whiteness as close to polypropylene matrix can be produced using fly ash.

The paper focuses on optimizing both white fly ash and SiC in the preparation of aluminium hybrid composite. White fly ash is used in composites nowadays mainly due to its aesthetic appeal. This experimental study is being done for the first time with AA 3003-O and white fly ash.

2 Experimental Details

2.1 Composite Preparation

Untreated fly ash is procured from industries, and 100 g was taken and heated in a furnace to oxidize them. They were heated to 200 °C, 600 °C and 1000 °C with increasing temperature of 5 °C/min under air, then held for one hour and finally annealed down to room temperature. Due to this, the fly ash powder was changed from grey colour to whitish colour and is used in the preparation of composite. The chemical composition and mechanical properties of aluminium alloy (AA 3003-O) are indicated in Tables 1 and 2. The aluminium alloy (AA 3003-O) in the form of ingots is cut into small pieces to facilitate easy melting of the metal and to produce a uniform distribution of fly ash. The white fly ash and SiC powders are weighed according to their wt %. The micrograph of white fly ash and the different sizes of the SiC powder was analysed using scanning electron microscopy (SEM). The powders were mixed in an indigenous mixing chamber using a turbine stirrer and a vortex was created to obtain a homogenous mixture of fly ash and silicon carbide. The AA 3003-O pieces were placed into the graphite crucible and heated by an electric furnace to a temperature of about 1195 °C till semi-solid state for better dispersion of particles. The mixed composition of fly ash and silicon carbide powders based on the composite design is initially preheated separately at a temperature of 1195 °C for 90 min to remove moisture and to improve the wettability with the molten AA 3003-O. The dispersion of fine particles in the melt happens by centrifugal action. Simultaneous stirring is carried by a mechanical stirrer which rotates at 600 rpm to

Table 1 Chemical composition of aluminium alloy (AA 3003-O) used in this experiment

Si	Fe	Cu	Zn	Mn	Others	Al
0.6	0.7	0.1	0.1	1.25	0.15	Balance

Table 2 Mechanical properties of aluminium alloy (AA 3003-O) used in this experiment

Tensile strength (MPa)	Yield strength (MPa)	Elongation (%)	Hardness (BHN)
101.12	42.4	30	49

Table 3 Control parameters and their levels

Parameters	Unit	Level 1	Level 2	Level 3
Volume fraction of fly ash	wt%	5	7.5	10
Volume fraction of SiC	wt%	5	7.5	10
Size of SiC	μm	15	30	45

form a fine vortex. The stirrer is placed such that the liquid below is 35% and liquid above is 65% to reduce porosity in the composite. Stirring is continued until all the powders are added to the semi-solid alloy. Then, the furnace temperature was raised to about 2035 °C to facilitate the pouring of molten composite into the mould.

2.2 Experimental Design

Due to its robust nature when compared to a full factorial method, the Taguchi technique is implemented for designing the experimental trails. To perform the experimental design, the levels of control parameters are given in Table 3.

L9 orthogonal array was chosen and the general form of Taguchi's L9 orthogonal array is given in Table 4.

2.3 Tensile Test

The fabricated composites were machined to the dimension required for the tensile test. Figures 1 and 2 show a schematic representation of the tensile specimen and the specimens prepared according to the ASTM E8 M-04, respectively. The tensile test was conducted using a universal testing machine with a capacity of 100 kN and at a strain rate of 0.001 s^{-1} at room temperature. The specimens were held on a universal testing machine and tensile load is applied until it underwent fracture. The strength of parent alloy AA 3003-O was found to be 101.12 MPa. Three trials were carried out and average tensile strength values were taken.

Table 4 Taguchi's L9 orthogonal array

Composite No.	Volume fraction of fly ash (wt%)	Volume fraction of SiC (wt%)	Size of SiC (μm)
1	5	5	15
2	5	7.5	30
3	5	10	45
4	7.5	5	30
5	7.5	7.5	45
6	7.5	10	15
7	10	5	45
8	10	7.5	15
9	10	10	30

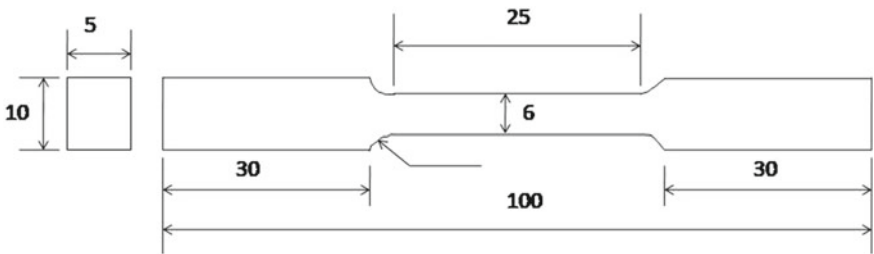


Fig. 1 Schematic representation of tensile sample—ASTM E8 M-04 standard



Fig. 2 Tensile specimens

3 Results and Discussion

3.1 Single Response Parameter Optimization

To analyse the individual effect of wt % of fly ash and silicon carbide and size of silicon carbide on the mechanical properties of hybrid composite such as tensile strength, the signal-to-noise (S/N) ratio analysis is performed by utilizing the loss function. Using this as a parameter, we can find the performance characteristic. Generally, the performance characteristics are classified into three types as follows,

1. Lower the better
2. Higher the better
3. Nominal the better.

Depending upon the intent for particular parametric optimization, the appropriate type should be followed for exact results. The S/N ratios corresponding to the experimentally predicted values are computed for each parameter to study its significant influence. Then, the mean S/N ratios are calculated at each level of process parameters by averaging at respective levels. These results were tabulated along with their corresponding main effect plots. The statistical analysis methodology known as analysis of variance (ANOVA) has been implemented by utilizing data of S/N ratio to study the significance of individual process parameters on responses based on P-value and F-value at 95% confidence level. Finally, experimental runs were conducted to confirm the optimal process parameters. The main effect plots and ANOVA analysis were performed using Minitab 18 software.

3.1.1 Tensile Strength

For better performance in quality, it is always preferred to have higher tensile strength. Therefore, the same procedure mentioned above was carried out to study the individual effect of parameters on tensile strength. The following formula (Higher the better) has been used to compute the S/N ratio of tensile strength.

$$S/N = -10 * \log(\Sigma(1/Y^2)/n) \quad (1)$$

It is found that the tensile strength of the hybrid composite is high for the composite 7 which is a combination of 10 wt% of fly ash, 5 wt% of silicon carbide and 45 microns of silicon carbide. The clear behaviour of each parameter on the tensile strength is known only after the S/N ratio analysis. From the above below, the tensile strength increases as the wt% of the reinforcement increase up to 15%. The reduction in tensile strength in composites 8 and 9 is due to the size of the silicon carbide used. It is also found that the increase in tensile strength compromises the ductility behaviour of the hybrid composite. The elongation of the hybrid composite reduces with the increase in tensile strength. The increase in tensile strength is mainly due to the load

transfer from the matrix to reinforcement and also due to the difference in their elastic constants (Table 5).

It is evident from the S/N ratio analysis as given in Table 6, the wt% of fly ash plays an important role in affecting the tensile strength of the hybrid composite which is followed by the wt% of silicon carbide and the size of silicon carbide. This effect in turn proved to be in relation with the ANOVA analysis as observed in Table 7. The individual effect of each parameter on the tensile strength of the hybrid composite is shown in Fig. 3.

It is observed from Fig. 3 that the tensile strength of the composite increases with an increase in wt% of fly ash and silicon carbide. It may be attributed to strengthening due to load transfer of the reinforcement. The inclusion of particles as reinforcement

Table 5 Experimental results with predicted values and S/N ratio of tensile strength

Exp No.	Volume fraction of fly ash	Volume fraction of SiC	Size of SiC	Tensile strength (MPa)	S/N ratio
1	1	1	1	102	40.14
2	1	2	2	104	40.33
3	1	3	3	105	40.42
4	2	1	2	119	41.48
5	2	2	3	120	41.58
6	2	3	1	120	41.58
7	3	1	3	137	42.70
8	3	2	1	136	42.68
9	3	3	2	136	42.74

Table 6 Mean S/N ratio response table for tensile strength

Parameters	Level 1	Level 2	Level 3	Max–Min	Rank
Volume fraction of fly ash	40.30	41.55	42.70	2.40	1
Volume fraction of SiC	41.44	41.53	41.58	0.14	2
Size of SiC	41.46	41.52	41.57	0.05	3

Table 7 ANOVA for tensile strength

Source	DF	Adj SS	Adj MS	F-value	P-value	% Contribution	Rank
Volume fraction of fly ash	2	1635.47	817.74	3310.63	0	99.52	1
Volume fraction of SiC	2	5	2.50	10.12	0.09	0.30	2
Size of SiC	2	2.37	1.15	4.8	0.17	0.14	3
Error	2	0.49	0.247			0.03	
Total	8	1643.33					

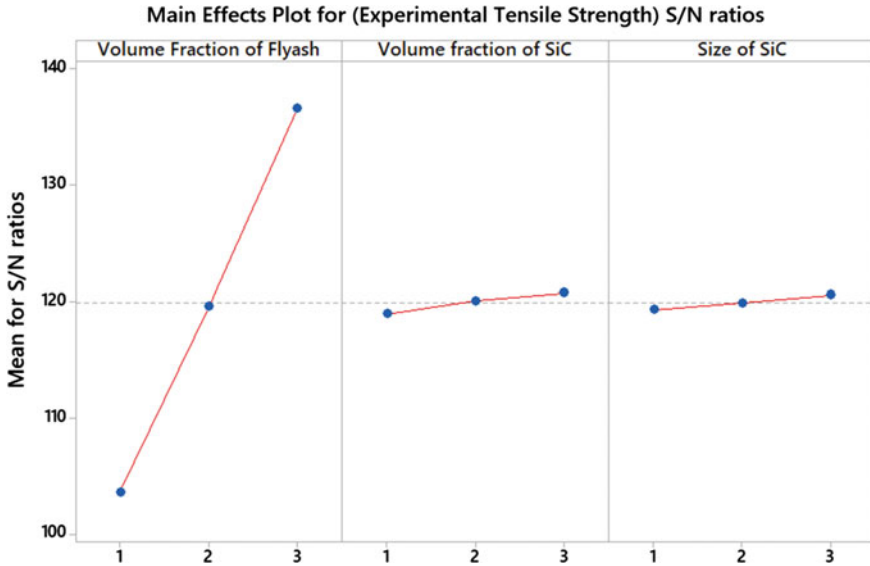


Fig. 3 Main effect plot ultimate tensile strength (UTS) for S/N ratios

increases the strength by taking the load and offers high resistance to tensile stresses. The size of silicon carbide shows a different behaviour on tensile strength. The tensile strength of the hybrid composite first reduces and then increases with the increase in the size of silicon carbide.

3.2 Confirmation Test

The optimal parametric combination obtained from the S/N ratio, ANOVA analysis and main effect plot was used for confirmation test runs. For tensile strength, the optimal parametric combination is given as follows in Table 8.

The confirmation test was computed experimentally for each factor and given as follows in Table 9. The predicted S/N ratio value was calculated using the optimal level of the process parameters with the formula (2) as given below,

Table 8 Optimal control factors and their levels for tensile strength

Parameters	Level	Value
Volume fraction of fly ash	3	10 (wt%)
Volume fraction of SiC	3	10 (wt%)
Size of SiC	3	45 (µm)

Table 9 Results of confirmation experiment for tensile strength

	Initial process parameter	Optimal process parameter	
		Predicted value	Experimental value
Level	1–2–1	3–3–3	3–3–3
Tensile strength	113.62		147.23
S/N ratio (dB)	41.11	42.82	43.36
Improvement in S/N ratio = 2.25			

Table 10 Experimental value versus predicted value for tensile strength

Composite No.	Experimental tensile strength	Predicted values	Residual
1	101.65	101.3	0.35
2	103.98	103.39	0.59
3	105.02	105.48	-0.45
4	118.59	118.76	-0.16
5	120.07	120.85	-0.78
6	120.05	120.39	-0.34
7	136.5	136.22	0.28
8	136.12	135.76	0.36
9	136.09	136.85	0.76

$$\hat{Y} = Y_m + \sum_{i=0}^n (Y_m - Y_i) \tag{2}$$

where Y_m is the total mean of the S/N ratio, Y_i is the mean S/N ratio at the optimal level, and n is the number of the main design parameters that significantly affect the performance characteristics.

The actual experimental value and the predicted values were found to be in good agreement as observed in Table 5 with negligible percentage loss. After optimization, the improvement in the S/N ratio has been observed as 2.2509 for tensile strength. In addition, the predicted values were also found to be close to experimental values for optimal process parameters as given in Table 10.

3.3 Mathematical Model

Tensile strength was dependent variables which can be represented as a linear combination of independent variables, namely volume fraction of fly ash, volume fraction

of silicon carbide and size of silicon carbide particles. To implement regression analysis on experimental data, the least square method is utilized to obtain the required response. The coefficients for the regression equation can be obtained by solving the following equation:

$$Y = \{\beta_0 + [\beta_1^* (\text{Volume Fraction of Flyash})] + [\beta_2 * (\text{Volume Fraction of SiC})] + [\beta_3 * (\text{Size of SiC})]\} \quad (3)$$

where Y is the required response, β_0 is constant called the intercept of the plane and β_1 , β_2 and β_3 are regression coefficient. This is a multiple linear regression model with three independent variables. The term coefficient of determination denoted as R^2 is generally used to know the precision of regression models that are developed. Furthermore, a normal probability plot is carried out to the effect of the regression model developed.

The following is the regression equation obtained by the least square method for the experimental data as specified in Table 4.

$$\begin{aligned} \text{Tensile strength} = & 83.822 + (16.508 * \text{Volume Fraction of Flyash}) \\ & + (0.903 * \text{Volume fraction of SiC}) \\ & + (0.628 * \text{Size of SiC}); R^2 = 99\% \end{aligned} \quad (4)$$

The obtained determination coefficients (R^2) represent the variability in tensile strength. The value of R approaching the unity shows the better prediction of responses and fitting of the model with the data. A normal probability plot versus residuals of tensile strength is plotted to check whether the residuals lie approximately along a straight line or not. Figure 4 shows the residuals reasonably lie close to the straight line and it shows that the errors are normally distributed. The less residual value as represented in Table 10 for the developed models claims its significance.

4 Conclusions

The present work focuses on the experimental investigation of mechanical and wear properties on stir cast AA 3003-O with white fly ash and SiC (Al/SiC hybrid composite). To improve the tensile strength, the individual effects of parameters were optimized by utilizing Taguchi L9 orthogonal array. Mathematical models were developed with linear regression analysis and their significance has been analysed. The following is the major findings:

- The optimal parametric combination for ultimate tensile strength is found to be 3–3–3 from the main effect plot, ANOVA and S/N ratio analysis, meaning, the better performance in tensile strength is observed when the volume fraction of

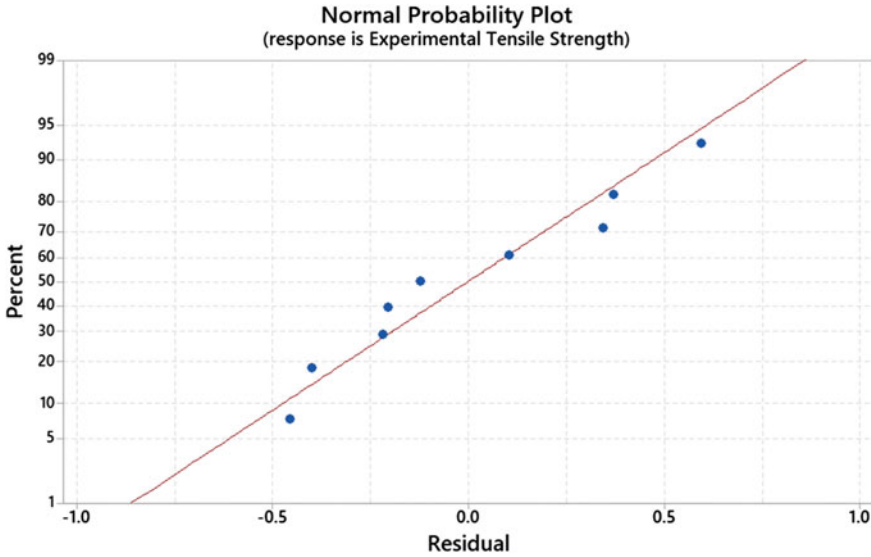


Fig. 4 Normal probability plot of the residuals for tensile strength

white fly ash is 10 (wt%), the volume fraction of SiC is 10 (wt%) and size of SiC is 45 (μm).

- The improvement in S/N ratios was found to be 2.2509 dB for tensile strength.
- Mathematical models with determination coefficients (R^2) approaching unity show the solid significance of the models developed.

References

1. Udaya Prakash J, Divya SA, Ananth S, Arun Pillai KV (2021) Optimization of wear parameters of aluminium matrix composites (LM6/Fly Ash) using Taguchi technique. *Mater Today: Proc* 39(4):1543–1548
2. Robinson Smart DS, David Raja Selvam J, Dinaharan I (2013) *Mater Des* 49:28
3. El-Kady O, Fathy A (2014) Effect of SiC particle size on the physical and mechanical properties of extruded Al matrix nanocomposites. *Mater Des (1980–2015)* 54:348–353
4. Dhar AK, Sutradhar G (2021) Experimental analysis of microstructure and mechanical characteristics of LM6 & fly ash composite through stir casting method. *J Phys: Conf Ser* 2070
5. Umanath KPSSK, Palanikumar K, Selvamani ST (2013) Analysis of dry sliding wear behaviour of Al6061/SiC/Al₂O₃ hybrid metal matrix composites. *Compos B Eng* 53:159–168
6. Kiran TS, Kumar MP, Basavarajappa S, Viswanatha BM (2014) Dry sliding wear behavior of heat treated hybrid metal matrix composite using Taguchi techniques. *Mater Des* 63:294–304
7. Renukappa NM, Suresha B, Devarajaiah RM, Shivakumar KN (2011) Dry sliding wear behaviour of organo-modified montmorillonite filled epoxy nanocomposites using Taguchi's techniques. *Mater Des* 32(8–9):4528–4536

8. Kumar KR, Mohanasundaram KM, Arumaikkannu G, Subramanian R (2012) Analysis of parameters influencing wear and frictional behavior of aluminum-fly ash composites. *Tribol Trans* 55(6):723–729
9. Zaeni A, Bandyopadhyay S, Yu A, Rider J, Sorrell CS, Dain S, Blackburn D, White C (2010) Colour control in fly ash as a combined function of particle size and chemical composition. *Fuel* 89(2):399–404
10. Bandyopadhyay S, Zaeni A, Nath D, Yu A, Zeng Q, Blackburn D, White C (2010) Advanced utilization of as received and near whitened fly ash in polypropylene polymer to improve mechanical, notched impact and whiteness colour properties. *Int J Plast Technol* 14(1):51–56

Development of Novel Low-Cost Sintered Magnetic Abrasive for Surface Finishing



Yogendra Kumar  and Harpreet Singh 

1 Introduction

The manufacturing industry, particularly in the fields of medical parts, optical instruments, electronic components, dies and molds, and mechanical components, requires a much superior polished surface for its critical applications [1–4]. For example, an ultra-smooth finish of Ra 0.5 nm is required on the bearing surfaces of medical implants (e.g., hip and knee joints) to ensure performance and longevity under dynamic loading [5, 6]. The required polished surface necessitates a premium price tag as well as advanced manufacturing methods. As a result, progress in various surface finishing methods are being developed at a rapid pace in order to meet market demands. [7–10].

Magnetic abrasive particles used in magnetic-aided finishing procedures serve as a micro-cutting tool as well as a carrier of removed material [11]. As a result, high permeability, high magnetic susceptibility, strong bonding between carbonyl iron matrix phases, and high hot hardness of magnetic abrasive grains are all critical parameters [8]. It necessitates the use of magnetic abrasives that are simple to manufacture, inexpensive, and evenly formed. Weakly bonded or unbonded magnetic abrasives, on the other hand, can be considered due to their ease of preparation, but they are always less effective when compared to bonded abrasives [12]. Bonded magnetic abrasive is a powdered composite consisting of ferromagnetic material and ceramic hard abrasive grains. Several methods for making magnetic abrasives have been reported, including gel-based, mechanically alloyed, adhesive-based, and plasma

Y. Kumar (✉) · H. Singh
Department of Mechanical Engineering, PDPM IITDM, Jabalpur, Madhya Pradesh 482005, India
e-mail: ykd.gni@gmail.com

H. Singh
e-mail: hps.dme@iiitdmj.ac.in

spraying [13, 14]. These preparation procedures are frequently time-consuming, difficult, costly, or inefficient.

The cost of magnetic material is primarily responsible for the higher price of MR fluid. Carbonyl iron, which is produced by the thermal decomposition of iron penta carbonyl, is the most commonly used magnetic material [15]. This material is more than 80% the price of MR fluid. As a result, alternative economical magnetic materials are required for these fluids' commercial viability [16].

Kim [17] used sintered magnetic abrasive powder to perform surface finishing operations and revealed that large-sized MAPs are suitable for rough machining to improve surface roughness. Lin et al. [18] found that a sintered magnetic abrasive with a size of 75 microns can yield surface roughness of the order of 100 nm. Ahmed et al. [12] research demonstrated that bonded sintered abrasive has excellent finishing results on titanium alloys.

To the best of the author's knowledge, no work on the production of low-cost sintered magnetic abrasives has been reported. As a result, an attempt was made in this study to manufacture a low-cost composite magnetic abrasive using a sintering process that combines high-pressure compression, crushing, and sieving to obtain appropriate particle size using electrolytic iron powder (EIP) and alumina as abrasive. Characterization of SMA abrasives includes particle size and distribution, morphology, and magnetic properties.

2 Materials and Method

2.1 Abrasive and EIP Particles

Magnetic particles used in MR fluids should have a high value of saturation magnetization and a minor coercivity [11]. These requirements are met by carbonyl iron powder, nickel zinc ferrite, iron oxide-coated polymer composite particles, and iron cobalt alloy [16]. All of the magnetic materials mentioned above are expensive, and thus do not fit the current low-cost synthesis objective. As a result, for the current synthesis, a low-cost (US\$8 per kg) magnetic particle with high purity was chosen. The electrolytic iron powder of EC-10 grade is used, which has fine particles with a particle size of less than 10 micron. The concentration of α -iron is greater than 98%. Alumina is mixed with EIPs particles during the fabrication of SMA abrasive alumina. Figure 1 depicts the element morphology of the electrolytic iron particle and alumina abrasive, and Table 1 gives the element purpose, composition, and particle size.

While mixing, a small amount of pure ethanol is added to act as a process controlling agent. In order to achieve a higher degree of purity in SMA abrasive, no bonding element is added during mixing.

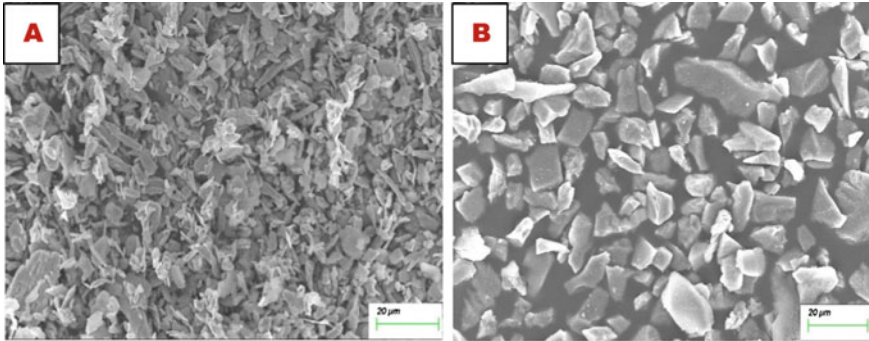


Fig. 1 Element morphology of the **a** electrolytic iron particle (EIP) and **b** alumina

Table 1 SMA abrasive element composition

S. No.	Element	Purpose	Composition (% weight)	Particle size (μm)
1	EIPs	Ferromagnetic particle	70%	10
2	Alumina	Abrasive	30%	4
3	Ethanol	Controlling agent	1 ml	–

2.2 Experiment Detail

The process of manufacturing sintered magnetic abrasive (SMA) involves basic steps as shown in Fig. 2. In the first step of the process, EIP and alumina were mixed in a planetary ball mill at a weight ratio of 30% alumina and 70% EIP powder. Table 2 gives the detailed mixing prerequisites for the preliminary stage.

The mixture was then compacted in a cylindrical die of 14 mm diameter made of tungsten carbide, which was subjected to 10-ton pressure. The prepared green compact pellets were kept at 950 °C in a tubular furnace for 3 h before being set to

Fig. 2 Process flowchart of SMA abrasive preparation

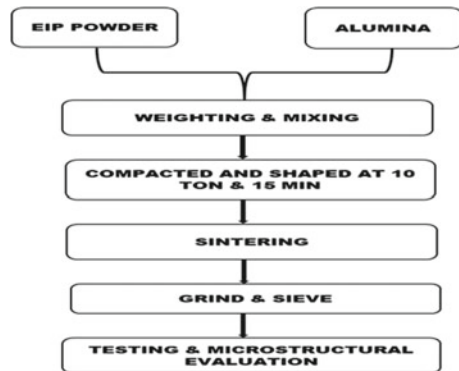


Table 2 Detailed mixing condition used for SMA

S. No.	Mixing element	Description
1	Mill type	Planetary ball mill
2	Milling media	Stainless steel ball of 5 mm diameter
3	Ball to powder ratio	8:1
4	Milling speed	200 rpm
5	Milling time	6 h
6	Milling condition	At room temperature

Table 3 Conventional sintering parametric conditions

S. No.	Condition	Description
1	Furnace type	Tubular furnace
2	Heating rate	3 °C/min
3	Sintering temperature	950 °C
4	Holding time	3 h
5	Cooling condition	At room temperature

cool to ambient temperature in the same furnace. Table 3 lists the various sintering conditions. Figure 3 depicts the steps involved in the preparation of SMA abrasive. After sintering, the pellets were ground into a powder in a ball mill. To create powder of the desired size, a 45-micron test sieve is used.

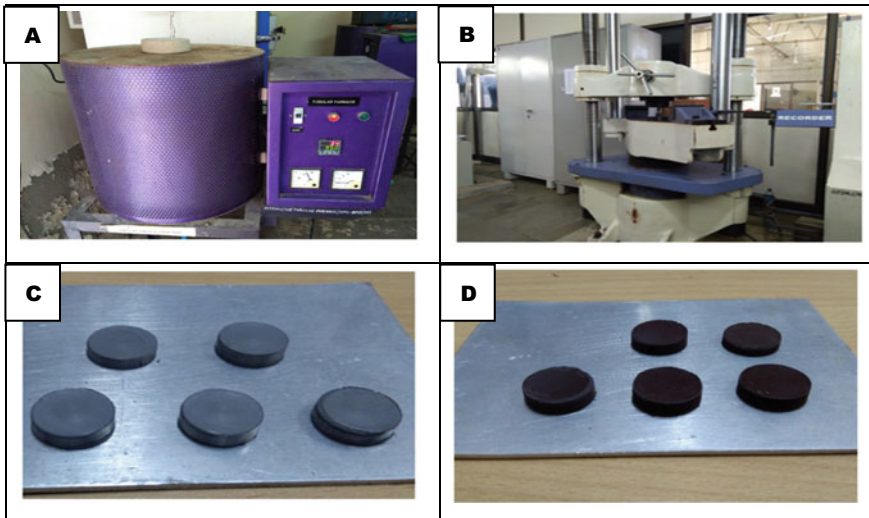


Fig. 3 Preparation stages of sintered magnetic abrasive **a** tubular furnace, **b** compacting process, **c** green compacts of the mixture, and **d** sintered compacts

3 Results and Discussion

3.1 SMA Morphology

The SMA abrasive has been successfully produced as shown in Fig. 4c due to appropriate compaction pressure control and controlled sintering temperature. The larger size of the EIPs permits a greater percentage of the abrasives particle to cover it from all sides, and the complete matrix is created in the same way. Individual magnetic abrasive particles have a shape that is determined by the form of the ferromagnetic particle used thus, changing the shape from random to ideal is simple. Appropriate proportions of alumina abrasive can have a considerable impact on the magnetic abrasive’s hardness. Active alumina oxides, which modify the machining action during the abrasive finishing process, can determine the wedge angle of the cutting tool tips of the SMA acting as a cutting tool. As a result of the described controlling criteria, sintered magnetic abrasive (SMA) with optimal strength and hardness, good magnetic properties, and high processing capacity was obtained.

Figure 4a shows high magnification SEM images of the developed SMA abrasive. The prepared SMA has a good shape, and the alumina particles are evenly distributed on the electrolytic particle core. Figure 4b depicts the SMA’s energy-dispersive spectrum, which clearly shows the peaks of Fe, Al, and O, indicating that the SMA is primarily composed of ferromagnetic particles and alumina.

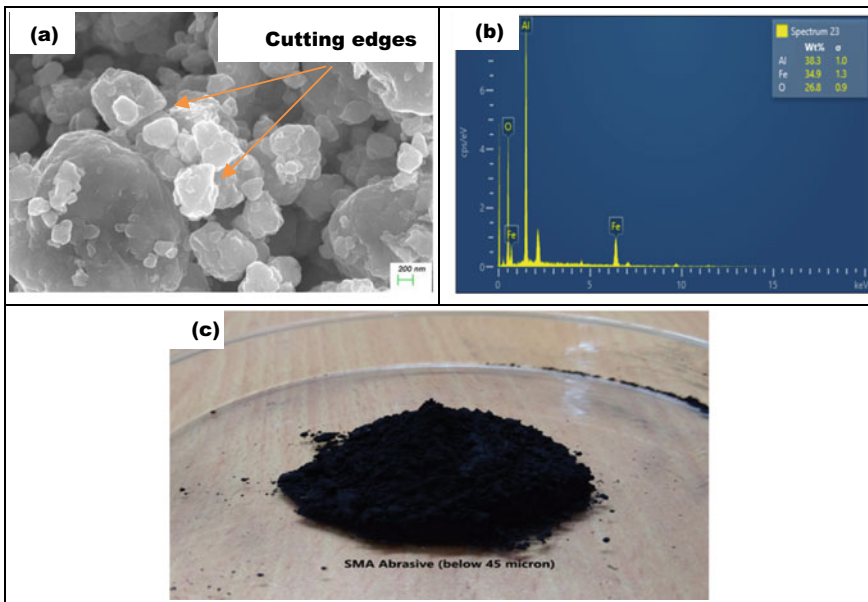
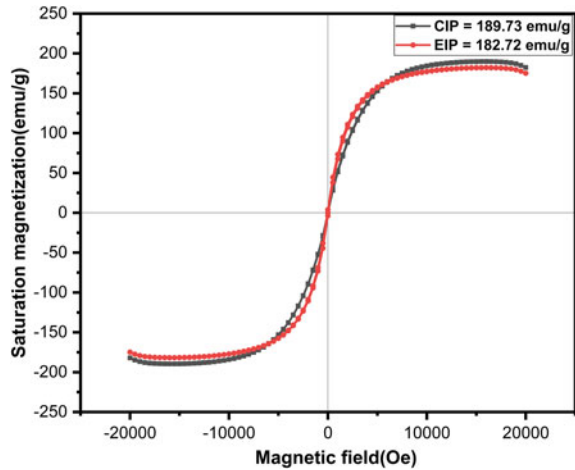


Fig. 4 Developed sintered magnetic abrasive **a** SEM (high magnification image), **b** energy-dispersive test result, and **c** fine grained SMA powder

Fig. 5 Comparative magnetization value of CIP and EIP



3.2 SMA Magnetic Properties

The magnetic properties of ferromagnetic particle used in this study were determined using vibrating sample magnetometer (VSM). VSM study is also done to compare the magnetic properties of expensive carbonyl iron (CI) powder and inexpensive electrolytic iron (EI) powder. Figure 5 depicts the M-H plots of EI and CI powder accessed at room temperature. The saturation magnetization value of electrolytic iron powder is 182.72 emu/g, which is approximately with same order as the saturation magnetization value of high-cost carbonyl iron powder that is 189.73 emu/g, according to the VSM results. As a result, the difference in magnetic properties between electrolytic iron powder and magnetic iron powder is negligible due to differences in impurities.

Figure 6 depicts the M-H curve for the newly developed sintered magnetic abrasive. The highest magnetization value obtained is 100.86 emu/g. When heated to high temperatures, the magnetization property of EIPs changes from ferromagnetic to paramagnetic and transforms into ferrite and coarse pearlite after furnace cooling, resulting in a decrease in magnetization. The achieved magnetization value is greater than that reported in previous work, as given in Table 4. As a result, the developed SMA abrasive has a significant high magnetization value, demonstrating its process capability.

4 Conclusions

The cost-effective sintered magnetic abrasive is successfully developed in this study. The following is the major findings based on the outcome and discussion:

Fig. 6 Magnetization value of SMA through conventional sintering

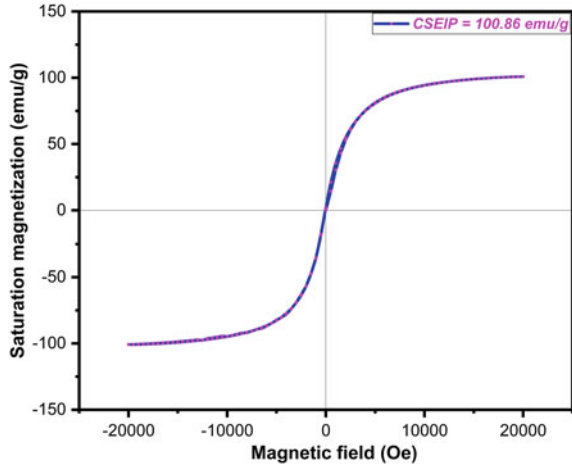


Table 4 Comparative study of magnetization value required with respect to SMA abrasive

S. No.	Authors	Ferromagnetic particle used	Magnetization value (emu/g)
1	Nagdeve et al. [19]	CIP	88.6
2	Niranjan et al. [20]	CIP	78.67
3	Sidpara et al. [21]	CIP	80
4	Niranjan et al. [22]	SMA	50
5	Current research	SMA	100.86

1. The magnetic properties of cost-efficient electrolytic iron powder are nearly as good as those of expensive carbonyl iron powder.
2. SMA abrasive formed by sintering has a fine structure, with abrasive particles distributed uniformly and densely on the EIP powder grain.
3. The maximum saturation magnetization of SMA abrasive achieved is 100.86 emu/g.
4. This method is relatively simple and cost-effective, making it suitable for large-scale commercial production.

References

- Jain VK, Ranjan P, Suri VK, Komanduri R (2010) Chemo-mechanical magneto-rheological finishing (CMMRF) of silicon for microelectronics applications. *CIRP Ann Manuf Technol* 59:323–328. <https://doi.org/10.1016/j.cirp.2010.03.106>
- Singh H, Jain PK (2016) Remanufacturing of functional surfaces using developed ECH machine. *J Remanufacturing*. 6:0–8. <https://doi.org/10.1186/s13243-016-0024-0>
- Jain VK (2008) Abrasive-based nano-finishing techniques: an overview. *Mach Sci Technol* 12:257–294. <https://doi.org/10.1080/10910340802278133>
- Kumar Y, Singh H (2021) Chemomechanical magnetorheological finishing: process mechanism, research trends, challenges and opportunities in surface finishing. *J Micromanufacturing*. 2516598421103888. <https://doi.org/10.1177/25165984211038878>
- Petare AC, Jain NK (2018) A critical review of past research and advances in abrasive flow finishing process. *Int J Adv Manuf Technol* 97:741–782. <https://doi.org/10.1007/s00170-018-1928-7>
- Barman A, Das M (2018) Magnetic field assisted finishing process for super-finished Ti alloy implant and its 3D surface characterization. *J Micromanufacturing* 1:154–169. <https://doi.org/10.1177/2516598418785506>
- Singh H, Jain PK (2016) Developments in electro-chemical honing (ECH): a review on experimental investigation of precision finishing of mechanical parts. *Int J Precis Technol* 6:17. <https://doi.org/10.1504/ijptech.2016.074177>
- Bedi TS, Singh AK (2016) Magnetorheological methods for nanofinishing—a review. *Part Sci Technol* 34:412–422. <https://doi.org/10.1080/02726351.2015.1081657>
- Jain VK, Sidpara A, Sankar MR, Das M (2012) Nano-finishing techniques: a review. *Proc Inst Mech Eng C J Mech Eng Sci* 226:327–346. <https://doi.org/10.1177/0954406211426948>
- Kumar Y, Singh H (2021) Optimum design of magnetic field assisted finishing tool: a finite element study. In: *Advances in systems engineering*. Springer, pp 245–250. https://doi.org/10.1007/978-981-15-8025-3_24
- Nagdeve L, Sidpara A, Jain VK, Ramkumar J (2018) On the effect of relative size of magnetic particles and abrasive particles in MR fluid-based finishing process. *Mach Sci Technol* 22:493–506. <https://doi.org/10.1080/10910344.2017.1365899>
- Ahmad S, Singari RM, Mishra RS (2021) Development of Al₂O₃-SiO₂ based magnetic abrasive by sintering method and its performance on Ti-6Al-4V during magnetic abrasive finishing. *Trans Inst Met Finish* 99:94–101. <https://doi.org/10.1080/00202967.2021.1865644>
- Shukla VC, Pandey PM (2017) Experimental investigations into sintering of magnetic abrasive powder for ultrasonic assisted magnetic abrasive finishing process. *Mater Manuf Process* 32:108–114. <https://doi.org/10.1080/10426914.2016.1176199>
- Zhao Z, Huang Y, Zhao Y (2010) Preparation of magnetic abrasive by sintering method. *Adv Mater Res* 135:382–387. <https://doi.org/10.4028/www.scientific.net/AMR.135.382>
- Kordonski W, Golini D (2002) Multiple application of magnetorheological effect in high precision finishing. *J Intell Mater Syst Struct* 13:401–404. <https://doi.org/10.1106/104538902026104>
- Sukhwani VK, Hirani H (2007) Synthesis and characterization of low cost magnetorheological (MR) fluids. *Behavior and mechanics of multifunctional and composite materials 2007*, p 6526, 65262R. <https://doi.org/10.1117/12.720870>
- Kim JD (2003) Polishing of ultra-clean inner surfaces using magnetic force. *Int J Adv Manuf Technol* 21:91–97. <https://doi.org/10.1007/s001700300011>
- Lin CT, Yang LD, Chow HM (2007) Study of magnetic abrasive finishing in free-form surface operations using the Taguchi method. *Int J Adv Manuf Technol* 34:122–130. <https://doi.org/10.1007/s00170-006-0573-8>
- Nagdeve L (2018) Differential finishing of freeform/sculptured surfaces using inverse replica in rotational-magnetorheological abrasive flow finishing (R-MRAFF) process

20. Niranjan MS, Jha S (2015) Experimental investigation into tool aging effect in ball end magnetorheological finishing. *Int J Adv Manuf Technol* 80:1895–1902. <https://doi.org/10.1007/s00170-015-6996-3>
21. Sidpara A, Das M, Jain VK (2009) Rheological characterization of magnetorheological finishing fluid. *Mater Manuf Process* 24:1467–1478. <https://doi.org/10.1080/10426910903367410>
22. Niranjan MS, Jha S (2014) Performance analysis of ball end magnetorheological finishing using sintered magnetic abrasive based magnetorheological polishing fluid. All India manufacturing technology, design and research conference, pp 1–6

Characterization and Optimization of Pistachio Shell Filler-Based Epoxy Composites Using TOPSIS



Sandeep Gairola, Hitesh Sharma, and Inderdeep Singh

1 Introduction

The demand of the natural fiber-based composite materials is continuously increasing due to their excellent environment and ecological benefits, i.e., lesser pollution discharge, reduced reliance on conventional materials/energy sources, improved energy recapture, and lesser greenhouse gas discharges. Plant fibers are the lignocellulosic fibers and are known the most renewable and copious bio-based material available in nature [1–4]. Lignocellulosic fillers have also been used for the development of the polymer composites, as they are helpful in achieving desired properties with reduced cost. Stiffness and hardness are two properties mostly affected by addition of these natural fillers in polymer matrix. Natural fillers are also incorporated into the polymer matrix to enhance scratch resistivity and dimensional stability of the end product. These fillers are also obtained by processing various wastes like fruit waste, agricultural waste, etc. Researchers throughout the globe have been using these waste materials, i.e., groundnut shell, wood flour, peanut shell, bagasse, citrus limetta peel,

S. Gairola (✉) · I. Singh

Centre of Excellence in Disaster Mitigation and Management, Indian Institute of Technology Roorkee, Roorkee, Uttarakhand, India

e-mail: s_gairola@dm.iitr.ac.in; sandeepgairola.12345@gmail.com

I. Singh

e-mail: inderdeep.singh@me.iitr.ac.in

H. Sharma

Mechanical Engineering Department, National Institute of Technology, Srinagar, Uttarakhand, India

e-mail: hiteshsharma@nituk.ac.in

I. Singh

Mechanical and Industrial Engineering Department, Indian Institute of Technology Roorkee, Roorkee, Uttarakhand, India

© The Author(s), under exclusive license to Springer Nature Singapore Pte Ltd. 2023

B. Bhattacharyya et al. (eds.), *Advances in Micro and Nano Manufacturing*

and *Surface Engineering*, Lecture Notes in Mechanical Engineering,

https://doi.org/10.1007/978-981-19-4571-7_24

etc., in the form of fillers for development of polymeric composites [5–11]. These natural fillers have been found to play an important role in enhancing properties of composites both at nanoscale as well as macroscale. One such agricultural waste material is pistachio shell (PS) which is discarded after its fruit is extracted. Iran, USA, and Turkey are among the top producers of pistachio which suggests that these countries are also top PS waste producing countries producing tons of waste in the form of pistachio shell. As per the data provided by FAOstat (2020), these three nations contribute around 90% of the total pistachio production (1,239,007 tons/year) around the globe. Out of the total fruit, 51–69% of its weight is contributed by the shell of the fruit. The use of shells of pistachio fruit includes but is not limited to fire starter, medium for orchids, animal feed, etc. Guru et al. [5] utilized PSF along with fly ash in urea–formaldehyde matrix to develop composites with improved flame resistance. The PSF-based urea formaldehyde composites have shown an increase in hardness and flexural strength. Karaagac et al. [6] incorporated PSF in rubber matrix to develop polymer composites. It was reported that increment in filler content lower the tensile strength and improves the abrasion resistance. Among various cellulosic fillers-based composites studied, very few articles were found with pistachio shell as reinforcement in epoxy matrix. However, the use of PSF for developing polymer composites is still not explored to full potential. Although, pistachio shell with epoxy matrix showed enhanced mechanical properties [11], but its effect on wear and water absorption behavior has not been investigated extensively.

The current research work focus on the development and characterization of PSF/epoxy composites. The effect of PSF filler loading on mechanical, water absorption, and wear behavior has been investigated. In the end, TOPSIS technique under multi-criterion decision making (MCDM) or multi-criterion decision analysis (MCDA) was adopted to find out the optimum filler loading content for different properties.

2 Materials and Methods

2.1 Matrix and Reinforcement

The composites were developed by using a medium viscosity epoxy (Grade LY-556 and specific gravity 1.18) along with hardener (Grade HY-951 specific gravity 0.98) as matrix material, and pistachio shell filler (PSF) was used as reinforcement. Epoxy LY-556 and hardener HY-951 were purchased from Singhal Chemicals, Meerut, India. Pistachio shells (PSs) were collected from the local dry fruit shop and washed with the distilled water to remove the impurities present. The PS was then ground and prepared as filler form of size $< 500 \mu\text{m}$ by passing it through the $500 \mu\text{m}$ sieve.



Fig. 1 Preparation of PSF/epoxy composites

Table 1 PSF/epoxy developed composites with varying PSF loading

Sample No.	Specification	Designation
1	Neat Epoxy	S ₁
2	Epoxy + 5% PSF	S ₂
3	Epoxy + 10% PSF	S ₃
4	Epoxy + 15% PSF	S ₄

2.2 Composite Fabrication

The hand-layup process, commonly known as solution casting, was used for fabricating the composite samples using a specially designed glass mold of size $200 \times 200 \times 5 \text{ mm}^3$. Epoxy LY-556 and hardener HY-951 were mixed in the ratio of 10:1 in order to initiate the curing reaction. The mixture was stirred by hand using a glass rod for 10 min. The PSF was then added in a ratio of 5, 10, and 15 wt.%, and the stirring was continued for another 5 min. The mixture was then poured into the glass mold and was kept for curing at room temperature for 24 h. The same procedure was followed for fabricating the samples with different filler content. The steps in the fabrication of composite samples are shown in Fig. 1. Table 1 gives different samples with their specification and designation.

2.3 Characterization of Developed Composites

The physical (density and void fraction) properties investigated to explain the limitations of processing technique. The theoretical and experimental density calculated with the help of the rule of mixture and Archimedes principle, respectively. Water absorption behavior was investigated as per ASTM D570. The samples were exposed to the water environment for 5 days and were weighed at a regular interval of 24 h,

Table 2 Selected wear parameters

Run	Load (N)	Speed (rpm)	Time (min)	Track diameter (mm)
1	10	191	17	100
2	20	191	17	100
3	30	191	17	100
4	10	382	8	100
5	20	382	8	100
6	30	382	8	100

48 h, 72 h, 96 h, and 120 h. The tensile and flexural tests were performed using universal testing machine (Make: Instron, Type 5982). Test samples were prepared for tensile and flexural tests according to ASTM D638 and ASTM D790, respectively. The impact test was performed in a digital impact testing machine (AIT D300) according to ASTM D256. Shore hardness (scale D) was calculated using durometer HT-6510-D according to ASTM D2240. The wear test was performed in accordance with standard ASTM G-99-17 in which the samples were prepared with size $30 \times 6 \times 3.5 \text{ mm}^3$. Samples were cleaned and pressed against a EN 32 steel disk having a hardness of 65HRC to conduct a wear test. All the controlling parameters for wear testing are mentioned in Table 2. The sample was weighed before and after every test cycle using a weighing machine (Aczet-CY124C), having the capacity to measure from 0.0001 g to 120 g.

2.4 Multi Criterion Decision Analysis

The current research investigation has focused on development and characterization of PSF/epoxy composites by modifying the epoxy resin with different PSF loading. However, the incorporation of PSF results in improved properties, but the trend of improvement is not following the same behavior with all developed samples. Therefore, a techniques for order preference by similarity to ideal solution (TOPSIS) technique of MCDM was adopted to find the optimal solution for the experiments. The steps involved are as follows:

Step: 1 A decision matrix was developed in which rows represent the alternative and columns represent the criterion.

$$D_{ij} = \begin{bmatrix} X_{11} & X_{12} \\ X_{21} & X_{22} \end{bmatrix} = [X_{ij}],$$

where $i = 1$ to 4 and $j = 1$ to 10.

Step: 2 Normalized matrix N_{ij} is developed by dividing each element of D_{ij} by square root of summation of each column.

$$N_{ij} = \frac{[X_{ij}]}{\sqrt{\sum_{i=1}^{i=4} X_{ij}^2}},$$

where $i = 1$ to 4 and $j = 1$ to 10.

Step: 3 Weighted normalized matrix W_{ij} is calculated by multiplying each element of N_{ij} by, respectively, given weightage.

$$W_{ij} = w_j \times [N_{ij}],$$

where $j = 1$ to 10 and $i = 1$ to 4.

Step: 4 Selection of positive (V_j^+) and negative (V_j^-) ideal solution.

V_j^+ = best value for the given criterion

V_j^- = worst value for the given criterion

Step: 5 Measure of separation S_j^+ and S_j^- of each alternative was calculated from positive and negative ideal solution, respectively, by the m-dimensional Euclidian distance.

$$S_i^+ = \sqrt{\sum_{j=1}^{j=10} (W_{ij} - V_j^+)^2} \quad S_i^- = \sqrt{\sum_{j=1}^{j=10} (W_{ij} - V_j^-)^2},$$

$i = 1$ to 4 and $j = 1$ to 10.

Step: 6 Compute the performance index (PI)

$$PI = \frac{S_j^-}{S_j^+ + S_j^-}$$

Step: 7 Rank according to the PI , greater the PI best the rank.

3 Results and Discussion

3.1 Physical Properties

The actual density, theoretical density, and a void fraction (calculated using Eq. 1) are tabulated as shown in Table 3. From the estimated values, it can be observed that, as PSF content increases, the void fraction also increases and was found maximum for the S_4 composite of about 4.93%. The acceptable range of void fraction for polymer composites is reported in the range of 1.01–6.5 [8, 12]. However, the density was found to decrease with increase in PSF content. This can be attributed to the fact that PSF has lower density than epoxy resin, and thus resulting in a decrease in the

Table 3 Physical properties of the developed PSF/epoxy composites

S. N.	Composites	Actual density (g/cm ³)	Theoretical density (g/cm ³)	Void fraction (%)
1	S ₁	1.206	NA	NA
2	S ₂	1.148	1.195	3.94
3	S ₃	1.135	1.190	4.62
4	S ₄	1.127	1.185	4.93

overall density of composites.

$$\text{void content} = \frac{(\rho_t - \rho_a)}{\rho_t} \times 100 \quad (1)$$

where ρ_t = theoretical density and ρ_a = actual density.

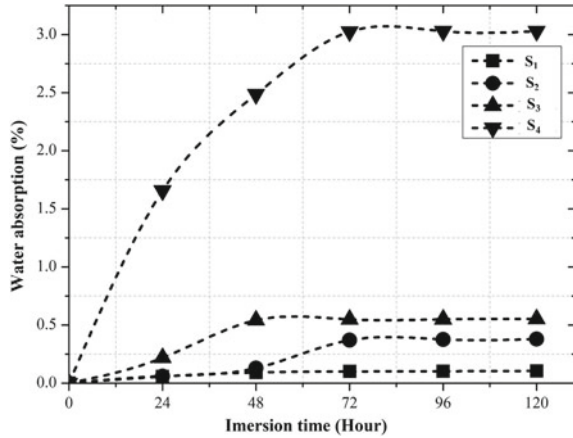
3.2 Water Absorption

Figure 2 shows the water absorption behavior of the PSF/epoxy composites. The water absorption was calculated using Eq. (2). It is revealed from the water absorption test that water absorption in the case of developed composites is solely dependent upon reinforcement content. With the incorporation of PSF, water absorption has shown an increasing trend (Fig. 2) with increased PSF loading. Composite reinforced with 15 wt. % of PSF showed maximum water absorption of about 3.029%. It can be attributed to the three-phase mechanism in the case of NFRC [13–15]. Initially, the water molecules are diffused into the micro-voids present between the polymer chains. Secondly, due to the action of capillary transport, the liquid molecules penetrate into crevices and micro-gaps present between the reinforcement and the matrix. Finally, these water molecules enter into the micro-cracks of the matrix, which occurred due to insufficient impregnation and wettability of natural reinforcement into the matrix. In addition, the lignocellulosic reinforcements contain free OH groups, which make this reinforcement to have a great affinity toward water molecules [16, 17]. As the PSF content increases, the free OH group and voids present in the composite also increases, leading to an increase in the moisture absorption. This phenomenon is in good agreement with the phenomenon that water absorption does not depend only on the PSF content but also on the void present in the material. Therefore, it can be said that sample S₄ has a higher PSF content with voids that made it absorb the maximum amount of water.

$$\text{Water absorption(\%)} = \frac{(W_f - W_i)}{W_i} \times 100 \quad (2)$$

where W_f = weight after immersion and W_i = initial weight.

Fig. 2 Water absorption behavior with immersion time



3.3 Mechanical Behavior

The mechanical behavior of the developed composites is illustrated in Fig. 3 in terms of tensile strength, tensile modulus, flexural strength, flexural modulus, and shore hardness. It is depicted from Fig. 3 that incorporation of PSF in the epoxy matrix has significantly improved tensile strength. As PSF content increases, the tensile strength shows a gradual increment. The maximum tensile strength of 48.67 MPa was observed for sample *S*₄ with an increment of about 46.57% and 39.53% compared to *S*₂ and *S*₃ samples. The failure behavior can be attributed to the mechanism that after the crack initiation in the matrix, it propagated to the whole sample and lead to the bulk failure. The reinforcement used in the epoxy matrix acts as a barrier to propagating crack further and reduces the risk of bulk failure of composite material [18]. This was confirmed by various studies [5, 6, 19]. From the flexural test plot, it was found that there is a reduction in flexural strength of the fabricated samples with the increase in loading of PSF. It may be due to the fact that as PSF loading increases, a composite’s ability to resist the deformation decreases, which further leads to a decrease in the flexural strength. The maximum flexural strength obtained in this work is 38.2 MPa for the 10% pistachio filler content, and minimum flexural strength was obtained for 15% pistachio filler content. The maximum flexural strength obtained in this work is much improved than that obtained with coir-based epoxy composite 25.65 MPa [20].

The PSF-based epoxy composite shows a significant increment in the impact strength as compared to unfilled epoxy composite specimens. The maximum amount of impact energy was absorbed by 10% filler sample (*S*₃) with an overall improvement of about 36.56%, and a minimum amount of energy was absorbed by 5% filler sample (*S*₂). As filler content increases, the impact strength shows an increment. Maximum impact strength of 22.67 kJ/m² was observed when filler content increased from 5 to 10%. This increment in impact strength can be attributed to the improved compatibility between the pistachio shell filler and the epoxy matrix. Further increase in filler

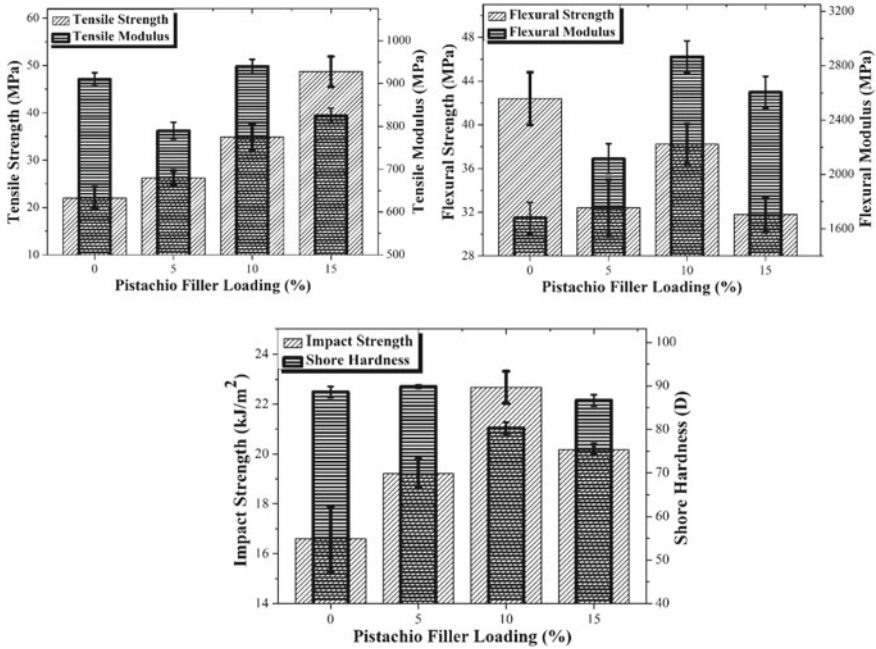


Fig. 3 Mechanical properties of the developed PSF/epoxy composites

content shows a decrement in the impact strength compared to S_2 . This reduction in impact strength is because as filler content increases more than an optimum content, the stress transfer efficiency gets reduced, leading to poor compatibility between the filler and matrix [21]. Shore hardness tester gives a maximum hardness of about 89.83 D for sample S_2 and a minimum hardness of approximately 80.30 D for sample S_3 . It is seen from the results that incorporation of pistachio filler content of 5% has slightly improved the hardness of the composite, but further addition of pistachio filler shows the reduction in hardness.

3.4 Wear Behavior

The response of wear rate with varying pistachio filler content at different loads is shown in Fig. 4. The test was performed on the pin on the disk machine with a varying load of 10–30 N (with a step of 10) and speed of 1 m/sec, 2 m/sec at a constant sliding distance of 1000 m. The reported mass loss and wear rate are tabulated in Table 4. From Fig. 4, it is observed that filler incorporation has significantly improved the wear properties of the fabricated composite. It can be seen from the Fig. 4 that at 1 m/sec, as the load increases, wear rate also increases in the S_2 (5%) sample, but as filler content increases beyond 5%, the wear rate shows a decrement with the

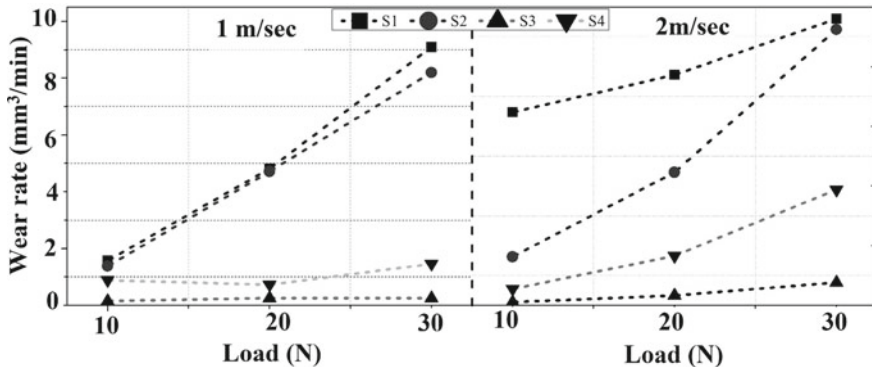


Fig. 4 Wear behavior of developed composites

Table 4 Wear properties of PSF/epoxy composites

Load (N)	Speed (rpm)/(m/sec)	Time (min)	Mass loss Σm (mg)				Wear rate v (mm ³ /min)			
			Composites				Composites			
			S ₁	S ₂	S ₃	S ₄	S ₁	S ₂	S ₃	S ₄
10	191/1	17	32	27	3	17	1.572	1.383	0.155	0.887
20	191/1	17	98	92	5	14	4.815	4.714	0.259	0.730
30	191/1	17	185	160	5	28	9.091	8.198	0.259	1.461
10	382/2	8	62	15	1	5	6.474	1.633	0.110	0.554
20	382/2	8	74	41	3	9	7.727	4.460	0.330	1.663
30	382/2	8	92	85	7	9	9.607	9.250	0.77	3.881

load. The same behavior was observed for a speed of 2 m/sec. As speed increase to 2 m/sec, the wear rate for the samples S₃ and S₄ shows a significant reduction. This can be attributed to the phenomenon that at lower load, the exposed PSF offers more resistance than epoxy alone. Further increased filler content also results in more resistance to wear [12, 22]. Thus, there should be an optimum PSF content reinforced with epoxy for good wear properties that allows the minimum amount of wear for a particular composite material.

3.5 MCDM Analysis

TOPSIS technique was applied to find the optimal material for the experimentally examined properties. The techniques have been applied to the physical (density;Dn and void fraction;V.F.), water absorption (W.A.), mechanical (tensile strength;T.S., tensile modulus;T.M., flexural strength;F.S., flexural modulus;F.M., impact strength;I.S., and shore hardness;S.H.) and wear properties (wear rate;W.R.)

Table 5 Decision matrix

Composites	Dn	V.F	W.A	T.S	T.M	F.S	F.M	I.S	S.H	W.R
S1	1.206	0	0	22	910	42.4	1680	16.6	88.6	9.607
S2	1.148	3.94	0.375	26.21	790	32.4	2115	19.21	89.83	9.25
S3	1.135	4.62	0.546	34.88	940	38.2	2865	22.67	80.3	0.77
S4	1.127	4.93	3.029	48.67	825	31.8	2605	20.17	86.7	3.881

of the developed composites. The ideal composition was intended to possess the best physical, mechanical, and wear properties in which physical, water absorption, and wear rate are non-beneficial criteria, and mechanical properties are beneficial criteria. Beneficial criteria are better to be maximum, and non-beneficial criteria are better to be minimum. The higher and equal preference (12.143%) was given to all the mechanical and wear properties, and lower and equal preference (5% each) was given to all the physical and water absorption properties. Table 5 gives the decision matrix having four alternatives and ten criteria taken into consideration. As per the mentioned steps in Sect. 2.4, the normalized decision matrix and weighted normalized matrix are calculated and given in Tables 6 and 7, respectively. After the weighted normalized matrix, the positive (V_j^+) and negative (V_j^-) ideal solutions were selected as shown in Table 8. Table 9 gives the calculated performance index according to which the alternatives were ranked. It can be seen from Table 9 that composite developed with 5% filler loading (S_2) became the optimum among the developed composites. The ranking of selection depends upon a preference to be given to criteria, and preference depends on the application for which the material is to be designed.

4 Conclusions

The following conclusions can be drawn from the current research endeavor:

1. The density of the developed composites decreases contradictorily to the increase in void fraction while water absorption capacity increases with PSF loading.
2. The presence of voids and higher PSF content (15% filler content) was the driving mechanism for the maximum water absorption of sample with 15% PSF loading.
3. The mechanical performance of the developed PSF/epoxy composites was experimentally investigated and compared with the neat epoxy. Based on the experimental results, it has been found that mechanical properties were better in the case of epoxy resin modified with the pistachio shell filler.
4. The wear behavior of developed composites was improved with an increase in pistachio shell filler as a reinforcement in the epoxy matrix until 10% of fiber loading (S_3).
5. The TOPSIS analysis suggested that the optimal PS loading comes out to be at 5%, i.e., S_2 composite material.

Table 6 Normalized decision matrix (N_{ij})

Composites	Dn	V.F	W.A	T.S	T.M	F.S	F.M	I.S	S.H	W.R
S1	0.522349272	0	0	0.318996842	0.52395638	0.581422456	0.355840574	0.419615774	0.5125212	0.690654206
S2	0.497227997	0.503752573	0.120967742	0.380041238	0.454863231	0.444294518	0.447977866	0.485591507	0.5196363	0.664989216
S3	0.491597367	0.590694642	0.176129032	0.505754993	0.541229667	0.523828722	0.606835265	0.573053589	0.4645085	0.055355859
S4	0.488132363	0.630329996	0.977096774	0.705708013	0.475015399	0.436066842	0.5517647	0.509858443	0.5015303	0.2790007908

Table 7 Weighted normalized matrix (W)

Composites	Dn	V.F	W.A	T.S	T.M	F.S	F.M	I.S	S.H	W.R
S1	0.026117464	0	0	0.045191219	0.074227154	0.082368181	0.050410748	0.059444568	0.0726072	0.083866154
S2	0.0248614	0.025187629	0.006048387	0.053839175	0.064438958	0.062941723	0.063463531	0.06879213	0.0736151	0.080748691
S3	0.024579868	0.029534732	0.008806452	0.071648624	0.076674203	0.074209069	0.085968329	0.081182592	0.0658054	0.006721783
S4	0.024406618	0.0315165	0.048854839	0.099975302	0.067293848	0.061776136	0.078166666	0.072229946	0.0710501	0.033879532

Table 8 Determination of positive (V_j^+) and negative (V_j^-) ideal solution

Ideal solution	Dn	V.F	W.A	T.S	T.M	F.S	F.M	I.S	S.H	W.R
V_j^+	0.024406618	0	0	0.099975302	0.076674203	0.082368181	0.085968329	0.081182592	0.0736151	0.006721783
V_j^-	0.026117464	0.0315165	0.048854839	0.045191219	0.064438958	0.061776136	0.050410748	0.059445568	0.0658054	0.083865154

Table 9 Separation measures by m-dimensional Euclidian distance and ranking

Composites	S_j^+	S_j^-	$S_j^+ + S_j^-$	Performance index	Ranking
S_1	0.11351128	0.060307892	0.173819172	0.346957655	4
S_2	0.080290539	0.092545831	0.172836371	0.535453452	1
S_3	0.059460686	0.051540947	0.111001634	0.464326025	2
S_4	0.082769999	0.056745567	0.139515566	0.406732872	3

References

- Jawaid M, Abdul Khalil HPS (2011) Cellulosic/synthetic fiber reinforced polymer hybrid composites: a review. *Carbohydr Polym* 86:1–18
- Kalia S, Kaith B, Kaur I (2009) Pretreatments of natural fibers and their application as reinforcing material in polymer composites—a review. *Polym Eng Sci* 49:1253–1272
- Majeed K, Jawaid M, Hassan A, Abu Bakar A, Abdul Khalil HPS, Salema AA, Inuwa I (2013) Potential materials for food packaging from nanoclay/natural fibres filled hybrid composites. *Mater Des* 46:391–410
- John M, Thomas S (2008) Biofibres and biocomposites. *Carbohydr Polym* 71:343–364
- Gürü M, Şahin M, Tekeli S, Tokgöz H (2009) Production of polymer matrix composite particleboard from pistachio shells and improvement of its fire resistance by fly ash. *High-Temp Mater Process* 28(3):191–195
- Karaağaç B (2014) Use of ground pistachio shell as alternative filler in natural rubber/styrene-butadiene rubber-based rubber compounds. *Polym Compos* 35(2):245–252
- Sutivisedsak N, Cheng HN, Burks CS, Johnson JA, Siegel JP, Civerolo EL, Biswas A (2012) Use of nutshells as fillers in polymer composites. *J Polym Environ* 20(2):305–314
- Sharma H, Singh I, Misra JP (2019) Mechanical and thermal behaviour of food waste (Citrus limetta peel) fillers-based novel epoxy composites. *Polym Polym Compos* 27(9):527–535
- Sharma H, Singh I, Misra JP (2020) Effect of particle size on physical, thermal and mechanical behaviour of epoxy composites reinforced with food waste fillers. *Proc Inst Mech Eng, Part C: J Mech Eng Sci* 0954406220958434
- Altun M, Celebi M, Ovali S (2021) Preparation of the pistachio shell reinforced PLA biocomposites: effect of filler treatment and PLA maleation. *J Thermoplast Compos Mater* 08927057211010880
- Chandrakar S, Agrawal A, Prakash P, Khan IA, Sharma A (2021) Physical and mechanical properties of epoxy reinforced with pistachio shell particulates. In: AIP conference proceedings, vol 2341, no 1. AIP Publishing LLC, p 040012
- Ranakoti L, Rakesh PK (2020) Physio-mechanical characterization of tasar silk waste/jute fiber hybrid composite. *Compos Commun* 22:100526
- Sekar S, Suresh Kumar S, Vigneshwaran S, Velmurugan G. Evaluation of mechanical and water absorption behavior of natural fiber-reinforced hybrid biocomposites. *J Nat Fibers*
- Arju SN, Afsar A, Khan MA, Das DK (2015) Effects of jute fabric structures on the performance of jute-reinforced polypropylene composites. *J Reinf Plast Compos*
- Saw SK, Akhtar K, Yadav N, Singh AK (2014) Hybrid composites made from jute/coir fibers: water absorption, thickness swelling, density, morphology, and mechanical properties. *J Nat Fibers*
- Zhang K, Liang W, Wang F, Wang Z (2021) Effect of water absorption on the mechanical properties of bamboo/glass-reinforced polybenzoxazine hybrid composite. *Polym Polym Compos*
- Dhokal H, Zhang Z, Richardson M (2007) Effect of water absorption on the mechanical properties of hemp fibre reinforced unsaturated polyester composites. *Compos Sci Technol* 67(7–8):1674–1683

18. Shakuntala O, Raghavendra G, Samir Kumar A (2014) Effect of filler loading on mechanical and tribological properties of wood apple shell reinforced epoxy composite. *Adv Mater Sci Eng*
19. Chun KS, Husseinsyah S, Osman H (2013) Properties of coconut shell powder-filled polylactic acid eco-composites: effect of maleic acid. *Polym Eng Sci* 53(5):1109–1116
20. Obele C, Ishidi E (2015) Mechanical properties of coir fiber reinforced epoxy resin composites for helmet shell. *Industrial Eng Lett* 5(7)
21. Yallew TB, Aregawi S, Kumar P, Singh I (2018) Response of natural fiber reinforced polymer composites when subjected to various environments. *Int J Plast Technol* 22(1):56–72
22. Sharma H, Misra JP, Singh I (2020) Friction and wear behaviour of epoxy composites reinforced with food waste fillers. *Compos Commun* 22:100436

Effect of Ball Milling Mechanism on the Density and Hardness of Al Matrix Consolidated Through Pressure Less Sintering



Kishor Kumar Sadhu, Nilrudra Mandal, and Rashmi R. Sahoo

1 Introduction

Aluminium (Al) and its alloys are widely used in aerospace and automotive industry due to their high strength-to-weight ratio, good ductility and fatigue, low coefficient of thermal expansion, high workability and good corrosion resistance. Due to high strength-to-weight ratio of Al, it can reduce the overall weight of the structure of vehicles or aircrafts, which reduces the fuel consumption, hence enhances the efficiency. However, pristine Al and its alloys do not possess the required level of mechanical properties, which are suitable for structural applications in automobile or aviation industries. The properties can be enhanced by reinforcing ceramic particles, altering the particle size and by changing the fabrication method. Fabrication routes of metal matrix composites are mainly of two types, namely: solid-state processing and liquid-state processing. However, liquid processing routes like stir casting, squeeze casting and compocasting have certain limitations like improper dispersion of reinforcements in Al matrix and poor wetting between reinforcements and the matrix. These limitations can be omitted by adopting solid-state processing route, i.e. powder metallurgy.

K. K. Sadhu · R. R. Sahoo (✉)

Environmental Engineering Division, CSIR—Central Mechanical Engineering Research Institute, Durgapur 713209, India

e-mail: rr_sahoo@cmeri.res.in

N. Mandal

Materials Processing & Microsystems Laboratory, CSIR-Central Mechanical Engineering Research Institute, Durgapur 713209, India

e-mail: n_mandal@cmeri.res.in

K. K. Sadhu · N. Mandal · R. R. Sahoo

Academy of Scientific and Innovative Research (AcSIR), Ghaziabad 201002, India

© The Author(s), under exclusive license to Springer Nature Singapore Pte Ltd. 2023

283

B. Bhattacharyya et al. (eds.), *Advances in Micro and Nano Manufacturing*

and *Surface Engineering*, Lecture Notes in Mechanical Engineering,

https://doi.org/10.1007/978-981-19-4571-7_25

Powder metallurgy is most useful when it comes to fabricate a complex shape. This includes cold pressing, hot pressing, spark plasma sintering followed by secondary deformation. Hot forging, hot extrusion, hot rolling and friction stir processing are used as secondary deformation processes. Primary step in powder metallurgy is mechanical alloying of constituent powders. High energy ball milling is used for mechanical alloying. It is used to repeatedly deform, fracture and cold weld the constituent powders by hard balls resulting in homogenous dispersion and particle size reduction [1, 2]. However, excessive cold welding leads to bigger size particles after alloying, which results in reduced mechanical properties. Hence, it is necessary to bring a balance between cold welding and fracturing. Generally, two methods are used for this purpose: surface modification and modification in deformation mode.

Surface modification can be done by adding process control agent (PCA) which prevents one to one contact between metal particles, whereas modification in deformation mode can lead to enhance fracturing of the powder particles at large compressive strains required for cold welding [3]. The amount of powder which gets trapped in between two balls during collision is 0.2 mg; this amount of powder contains around 1000 particles [4]. These particles get flatten due to the collision and get cold welded together due to their softness. This results in formation of layered composite powder particle consisting other reactant which were present initially [5].

A recent work [6] compares the effect of dual speed ball milling, low-speed ball milling and high-speed ball milling on mechanical alloying process. Dual speed ball milling gives an advantage of both low-speed ball milling and high-speed ball milling. This plays a vital role in improving dispersion of silicon carbide (SiC) particles in the aluminium matrix. They also suggest that dual speed ball milling is effective in improving microhardness of the composite fabricated through hot isostatic pressing. Further, the effect of milling time on mechanical, microstructural and physical properties of Al-5 wt% Al₂O₃ is shown by a literature [7]. They found increasing milling time improves dispersion of Al₂O₃ particles in aluminium matrix. This also resulted in reduction in particle size and gap between particles. The effect of rotational speed is studied by [8]. They found increasing rotational speed resulted into increase in particle size and thickness. The particles size and thickness at 200 rpm were ca. < 20 μm and 800 nm, whereas at 250 rpm, particle size increased and increased to ca. 45 μm and 1.7 μm. However, average diameter decreased from 100 μm to 85 μm.

This work is aimed to improve the physical and mechanical properties of the matrix of Al by changing milling conditions: milling time and speed and cold pressing compaction load.

2 Methods and Materials

For mechanical alloying of Al powder, planetary ball milling is used. In high energy ball milling (HEBM), the milling media has to absorb a large amount of energy. As the vial rotates in high rpm, the balls and stock strike the inner wall of the vial

Table 1 Summary of HEBM process

Process	Ball milling speed (rpm)	Ball milling time (hr)
Low-speed ball milling (LSBM)	200	8 (200)
Dual speed ball milling (DSBM)	200 + 600	8 (200) + 2 (600)

with a centrifugal force which can reach up to 20 times of the gravitational force of the vial. This centrifugal force is the reason behind cold welding and fracturing of the particles of the powder. In planetary ball milling, the supporting disc and vial rotate in opposite direction, hence, the slurry inside the vial and the milling media alternatively strikes the vial's inner wall and thrown off inside the vial with high speed.

Pristine Al powder of 99% purity and of particles 325 mesh was bought from Sisco Research Laboratories (SRL). Stearic acid and methanol act as a process control agent (PCA), were bought from Loba Chemie and Finar limited, respectively. Slurry was prepared by adding 2 vol% of stearic acid ($\text{CH}_3(\text{CH}_2)_{16}\text{COOH}$) in Al powder, and this combo was mixed properly in methanol media (40 ml) for 1 h using magnetic stirrer. Further, the slurry was transferred to a vial made of hardened stainless steel. The powder-to-ball ratio was fixed at 1:20. Steel balls were used each having 10 mm diameter. High energy ball milling (HEBM) process was used to grind the powder in a planetary ball mill Retsch 400 M. Two mechanisms low-speed ball milling (LSBM) and dual speed ball milling (DSBM) were used to grind the powder separately. Table 1 gives the ball milling speed and time used in LSBM and DSBM process. In HEBM process, 20 min operation time with direction reversal and 2 min dwell period was fixed.

After ball milling by different mechanism, the slurry was dried in a hot air oven (Testing Instruments Mfg. Co. Pvt. Ltd.) for 5 h at 70 °C. Grinding of the dry cluster was done in a mortar pestle results fine powder. Six pallets were made by cold compaction at three different pressures and with two different ball milling process in Carver Press as shown in Fig. 1. All compacted samples were sintered at 530 °C with holding time of 2 h in a furnace (Nanotech Pvt. Ltd.). During sintering, N_2 atmosphere was maintained to prevent any oxidation. The surface of all the pallets was ground properly using SiC grinding powders followed by polishing in a bain polisher using diamond paste of 1 μm particle size. The particle size of the ball milled powder was compared with a nanoparticle size analyser with dynamic light scattering (Fig. 2).

Density of the samples was evaluated using Archimedes principle in a density metre (acet CY 224C). Microhardness of all samples was measured by Vickers microhardness test (Falcon 500 Innova Test). X-ray diffraction (XRD, Panalytical X'Pert PRO with X'Celerator detector, interval 20–90°) was done to study the phase crystallization happened during the ball milling and sintering process. Thermal analysis was carried out using a TGA/DTA analyser (STA 449F1 Jupiter, NETZSCH

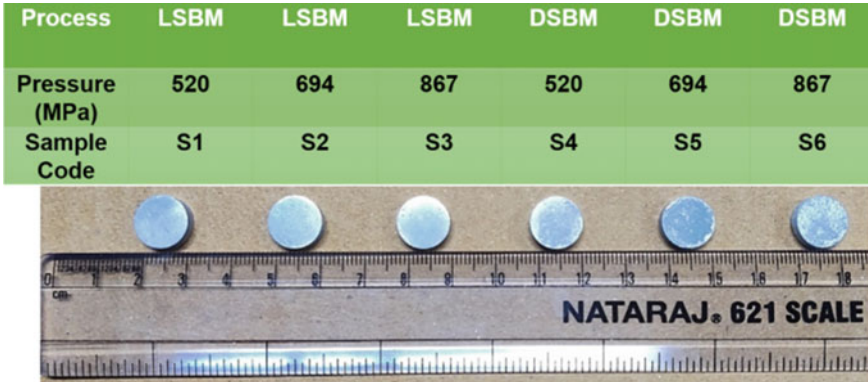


Fig. 1 Images of consolidated samples at different pressures and process with their sample code

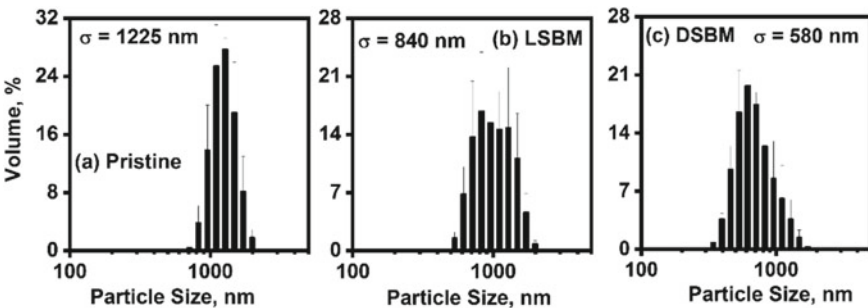


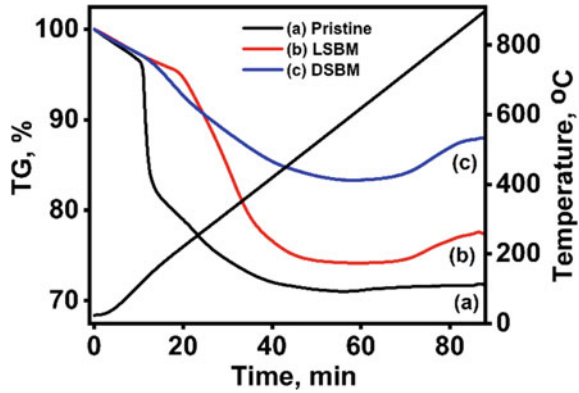
Fig. 2 Comparison of particles size of at different ball milling conditions

instrument). Samples were kept in a pure Al crucible and heated in a flowing N₂ atmosphere at a constant heating rate of 20 °C/min during the measurements.

3 Results and Discussion

The particle size after ball milling with 10 mm balls for 8 h in 200 rpm was found to be ~840 nm. Further grinding of the powder at 600 rpm for 2 h reduced the particle size to 580 nm. The initial size of procured commercial aluminium powder was found to be 1.225 μm. Thus, ball milling resulted in reduction of particle size. Similar result of decreasing particle size with milling time in the range of 8 h to 12 h was reported in literature [7]. It shows the positive effect of adding stearic acid and methanol as a PCA since it impedes excessive cold welding and promotes fracturing of Al particles during HEBM. The particle size distribution of aluminium powders is shown in Fig. 2.

Fig. 3 TGA plot showing weight loss of the Al powder



Variation in particle size distribution considerably affects the Al reactivity. The thermal stability of the pristine and ball milled powder was investigated by thermal gravimetric analysis (TGA). The weight loss of the Al powders was found to decrease with decrease in their particle size, indicating lower mass loss and better oxidation stability (Fig. 3) for the ball milled nanopowders. From the TGA data, the oxidation of the submicron Al powders can provide lots of information on the particle reactivity and composition.

The XRD spectra of the commercial powder, DSBM powder and the cold-pressed DSBM sample was investigated by XRD and all the samples showed all the characteristics peaks of Al. Additionally, no traces of impurities or unwanted phases were found which is evident from the XRD spectra shown in Fig. 4. This leads to conclusion that oxidation did not occur during HEBM and sintering. Further, reduction in grain size is achieved for the DSBM sample which is evident from reduced peak intensities and peaks being slightly broadened at full-width at half-maximum (FWHM).

The results given in Table 2 suggest improvement in density of samples due to change in morphology of Al particles when DSBM is used for ball milling as

Fig. 4 XRD plot of pristine, DSBM Al powder and cold-pressed DSBM sample

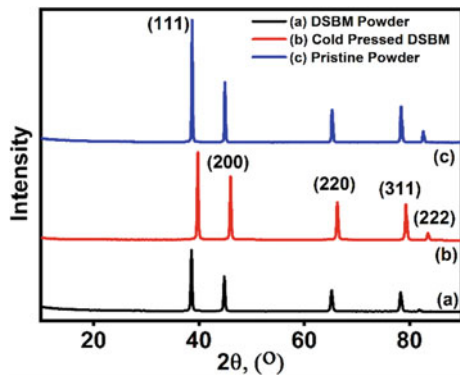


Table 2 Parameters of sintering and density and hardness of the respective ball milled samples

Sample	Pressure (MPa)	Temperature (°C)	Holding time	Density (gm/cc)	Hardness (HV)
S1	520	530 °C	2 h	2.332 ± 0.0050	55.6 ± 1.338
S2	694	530 °C	2 h	2.295 ± 0.003	52.112 ± 4.375
S3	866	530 °C	2 h	2.317 ± 0.0061	51.41 ± 1.443
S4	520	530 °C	2 h	2.283 ± 0.0047	83.75 ± 3.725
S5	694	530 °C	2 h	2.380 ± 0.0005	108.367 ± 2.017
S6	867	530 °C	2 h	2.395 ± 0.0472	111.98 ± 2.328

Bulk Aluminium: Density: 2.7 g/cc; Hardness: 50 – 110 HV

compared to LSBM. The increase in density may be attributed to transformation of larger flake shaped particles to smaller spherical shape particles which has better mobility and lower tendency to form bridges. This inference is made on the basis of results obtained by [7]. The hardness of the samples was also found to be increased when DSBM is used. This is due to fact that when particle size decreases, contact between the particle increases during sintering which favours cold welding between grains. It is also evident that increase in compaction pressure results in increase in density and hardness for the DSBM powder.

4 Conclusions

Comparison of LSBM and DSBM ball milling process was successfully done. Reduction in average particle size was observed when the process changed from LSBM to DSBM. All the characteristics peaks of Al were shown by XRD spectra. A considerable improvement can be seen in the hardness and density when ball milling process was changed to DSBM from LSBM. The hardness got improved by ~118% for sample compacted at 867 MPa. On the other side, density got improved by ~3.4% for the same.

Acknowledgements The authors are grateful to SERB, India, for the research grant in carrying out this work. We are also thankful to our Director for giving permission to publish this work.

References

1. Suryanarayana C (2001) Mechanical alloying and milling. *Prog Mater Sci* 46(1–2):1–184
2. Benjamin JS (1992) Mechanical alloying-history and future potential. *Adv Powder Metall Part Mater* 7:155–155

3. Valiev RZ, Nazarov AA (2009) Bulk nanostructured materials by SPD processing: techniques, microstructures and properties. *Bulk nanostructured materials*. Wiley-VCH, Weinheim, Germany, pp 21–46
4. White RL (1980) The use of mechanical alloying in the manufacture of multifilamentary superconductor wire. Ph.D. Thesis, Stanford University
5. Schwarz RB, Koch CC (1986) Formation of amorphous alloys by the mechanical alloying of crystalline powders of pure metals and powders of intermetallics. *Appl Phys Lett* 49(3):146–148
6. Almotairy SM, Boostani AF, Hassani M, Wei D, Jiang ZY (2020) Effect of hot isostatic pressing on the mechanical properties of aluminium metal matrix nanocomposites produced by dual speed ball milling. *J Market Res* 9(2):1151–1161
7. Toozandehjani M, Matori KA, Ostovan F, Abdul Aziz S, Mamat MS (2017) Effect of milling time on the microstructure, physical and mechanical properties of Al-Al₂O₃ nanocomposite synthesized by ball milling and powder metallurgy. *Materials* 10(11):1232
8. Rikhtegar F, Shabestari SG, Saghafian H (2015) The homogenizing of carbon nanotube dispersion in aluminium matrix nanocomposite using flake powder metallurgy and ball milling methods. *Powder Technol* 280:26–34

Fabrication of Al/Al-Co Composites by Stir Casting Method



Devara Srinu, K. Srinivasarao, and N. R. M. R. Bharagava

1 Introduction

Nowadays, composite materials are used over monolithic materials. There is a continuous curiosity among scientists and researchers to develop a composite material with properties like lightweight, high strength, stiffness, corrosion and wear resistance for structural applications, especially in automobile, aerospace, marine, and chemical industries [1, 2]. The properties of material and microstructure depend on fabrication method, processing parameters, and the quantity of dispersion particulates [3]. To get the desirable properties and uniform dispersion in MMC, wettability between particles and a liquid metal matrix must be strong. In general calcium, lithium, zirconium, and magnesium are added to enhance wettability. Among these, the addition of magnesium furtherly increases solution strengthening of aluminium metal matrix composites (AMMCs) [4, 5].

Mechanical properties of composite materials depend upon the size, shape, nature, and properties of the reinforcement particles in the matrix. Good interfacial bonding between matrix and reinforcement particles plays a vital role in enhancing the mechanical characteristics of composites [6]. Many ceramic hard particles have been significantly employed to enhance aluminium and its alloys, which include SiC, B₄C, CaB₆, TiC, TiO₂, Al₂O₃, and many more, which have been proved to influence the continuous phase of aluminium and its alloys [7, 8]. Liquid phase processing methods are appealing and cost-effective and can produce large-scale production and complex geometry [9].

In the present study, a simple stir casting that falls under the liquid metallurgy technique is adopted for the production of aluminium metal matrix composites in

D. Srinu (✉) · K. Srinivasarao · N. R. M. R. Bharagava
Department of Metallurgical Engineering, Andhra University, Visakhapatnam 530003, India
e-mail: dsdevarasrinu@gmail.com

which aluminium–cobalt reinforcements with different weight percentages were incorporated.

2 Materials and Methods

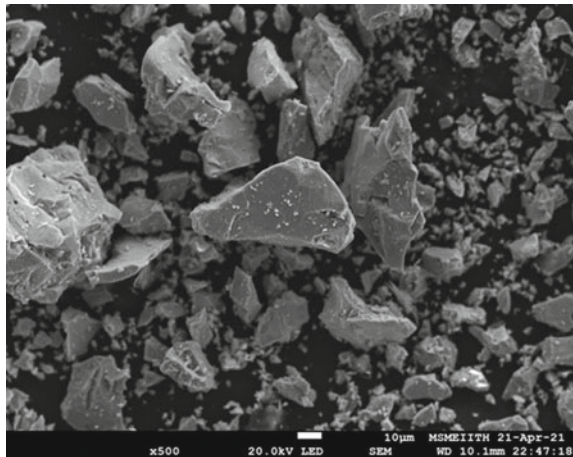
2.1 Materials

Commercial aluminium of purity above 99% was obtained from NALCO, Angul, Odisha. Cobalt of purity above 99% was obtained from Mumbai, India.

2.2 Preparation of Intermetallic Alloy

The masses of aluminium and cobalt were taken 50:50 (atomic wt. %). The quantified aluminium and cobalt are placed into a graphite crucible and heated to a temperature of 1670 °C in an induction vacuum melting furnace until complete melting of the material is achieved. After complete melting, liquid Al–Co alloy is poured into a copper mould to get the desired shape. Solidified intermetallic alloy is converted into powder by using crushing and ball milling followed by sieve analysis. The average particles size of 40 µm is selected for the composite preparation. Figure 1 shows the micrograph of Al–Co intermetallic particulates.

Fig. 1 Micrograph of intermetallic particulates Al–Co



2.3 Fabrication of Composite

The stir-cast technique is employed to synthesize the composite materials with the optimum process parameters for experimentation and study. Figure 2 presents the stir casting set-up schematic diagram. The proportions of the intermetallic material (Al–Co) and pure aluminium are required to produce aluminium—Al–Co composites. Table 1 illustrates the materials used to produce the composite with varied weight percentage ratios.

The schematic of the methodology followed for the composite’s preparation is shown in Fig. 3. The Al–Co reinforcement was heated for one hour at 800 °C to get rid of any moisture and to break down any oxide layers on the surface of the particle reinforcement. The required quantity of pure aluminium was charged in a graphite crucible, and melting was done by induction melting furnace at the temperature of 750 °C above its melting point to ensure the melting of all the material. The preheated Al–Co has been added into the molten metal of aluminium, and stirring was done using a mechanical stirrer to get homogeneity of both continuous and discontinuous phases. Before stirring, 1 g of Mg is added to the molten pool, which enhances the wettability between matrix and reinforcement. The liquid metal was transferred into the preheated grey cast-iron moulds and allowed to solidify.

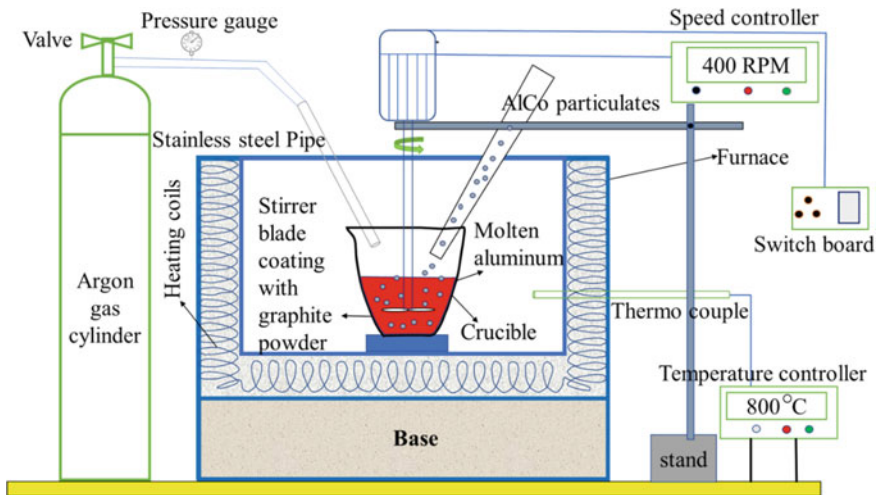
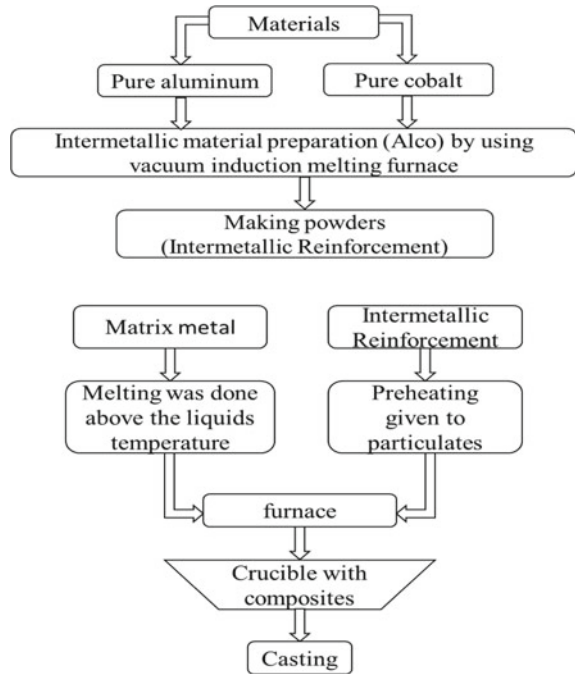


Fig. 2 Schematic diagram of stir casting set-up

Table 1 Materials used to produce the composite with varied weight percentage ratios

Al wt.%	Al–Co wt.%
100	0
97.5	2.5
95	5

Fig. 3 Schematic of the methodology followed for the composite's preparation



2.4 Microstructural and Mechanical Investigation of Al/Al-Co

Investigating microstructures of fabricated composites were carried out using the FESEM (Make: JEOL JSM-7800F). Hardness was measured for the aluminium and prepared composites by using Vickers hardness tester (Model: Lecco LV 700). The load of 1000 g and dwell time of 15 s were maintained during the test, and an average of five readings was taken. The tensile samples are prepared to observe the strengthening behaviour of the composites and base metal, tested by using the universal testing machine (Instron-5967).

3 Results and Discussions

3.1 Microstructures

The SEM microstructures are used for the study of the morphological behaviour of the generated composite materials. It reveals that the distribution of particulates is uniform in the ductile matrix. Figure 4a and b represents Al-2.5 wt.% R and Al-5 wt.% R, respectively.

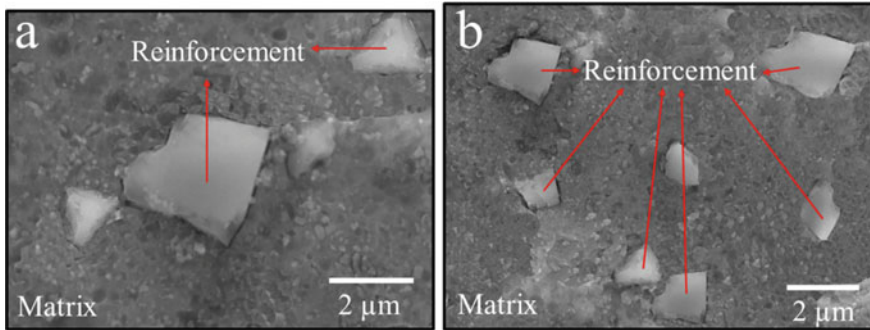


Fig. 4 Microstructures of aluminium composites reinforced with **a** 2.5% R and **b** 5% R

As the amount of reinforcement increases, a greater amount of dispersed phase is observed in the aluminium matrix. Figure 4b represents the Al-5 wt.% R reinforcement content, which is found to be a uniform distribution. In the stir casting process, proper mixing of reinforcement in the matrix is a big task. However, it was identified that less amount of reinforcement content is uniformly distributed in the aluminium metal matrix. Stir casting process parameters also influence the uniform dispersion in the matrix [10].

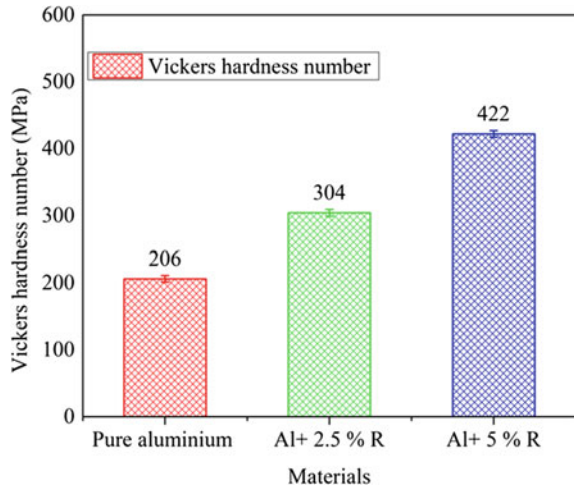
3.2 Hardness

Figure 5 represents the hardness values for developed composites of Al–Al–Co in 0, 2.5, and 5 wt.% of Al–Co particulates. The results show that increasing the hardness values as the increasing the wt.% particle reinforcement. The maximum hardness value was identified et al. –5 wt.% Al–Co composites with Vickers hardness of 422 MPa. The load-bearing capacity of the composite increases with the existence of hard particulates as reinforcement, and these particulates will also restrict the movement of dislocation in the matrix that furtherly leads to a higher hardness of the produced composites [6, 11, 12]. From the results, it is also evident that the minimum hardness values were found for unreinforced material.

3.3 Yield Strength

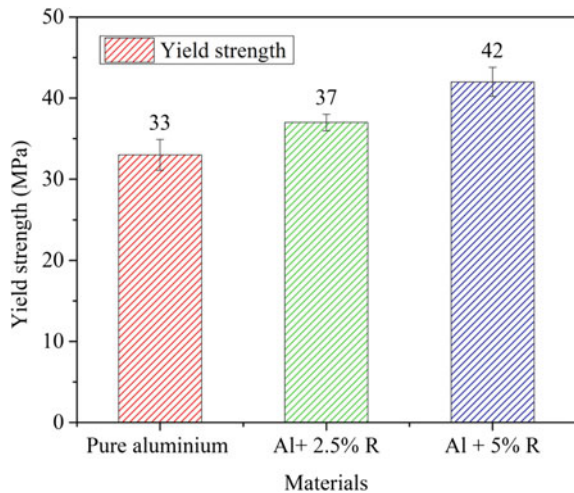
The plots for yield strength of pure Al and its composites are shown in Fig. 6. The enhanced yield strength of produced composites can be attributed to the interaction between the aluminium and dislocations during loading. The reinforcement particles act as a barrier to the movement of dislocations under the load. It has been found that even distribution of reinforcement helps to transfer the load from the matrix

Fig. 5 Progression of the hardness of reinforced aluminium



material to the reinforcement efficiently, which reveals improved yield strength of the composite [13]. From the above, it can be concluded that the increment in yield strength of the composites may be due to the shape, fine size, and distribution of the reinforcement in the matrix [6]. Hence, it was indicated that increasing the intermetallic particles increases the yield strength, it is also evident at 5 weight percentage of intermetallic particulates was shown maximum yield strength this is due to the even distribution of hard intermetallic particles and good wettability between the particulates and matrix.

Fig. 6 Progression of the yield strength of reinforced aluminium



4 Conclusions

In the present experimental study, the stir casting process was successfully implemented to fabricate the desired composites. The findings from the investigation are shown below:

1. The stir casting technique in the liquid metallurgy route is a better method for the fabrication of pure aluminium metal matrix reinforced with the Al-Co intermetallic particulates (AMMCs) to achieve improved mechanical properties.
2. Scanning electron microscopy studies reveal that even distribution of particulates in the aluminium matrix with better bonding between the reinforcement and matrix, the same was confirmed with the mechanical properties as well.
3. The mechanical properties of AMMCs are enhanced by increasing the weight percentage of the Al-Co intermetallic particulates. Hardness and yield strength of Al-5 wt.% R composites are superior when compared to Al-2.5 wt.% R and unreinforced aluminium matrix, and it is also observed that Al-5 wt.% R hardness was increased by 104% and yield strength was increased by 27% when compared to unreinforced matrix, this may be attributed due to uniform distribution of particles.

References

1. Surappa MK (2003) Aluminium matrix composites: challenges and opportunities. *Sadhana* 28(1–2):319–334
2. Ajay Kumar P, Rohatgi P, Weiss D (2020) 50 years of foundry-produced metal matrix composites and future opportunities. *Int J Metalcast* 14(2):291–317
3. Sajjadi SA et al (2012) Fabrication of A356 composite reinforced with micro and nano Al₂O₃ particles by a developed compo casting method and study of its properties. *J Alloy Compd* 511(1):226–231
4. Samal BP, Panigrahi SC, Sarangi B (2013) Use of modified stir casting technique to produce metal matrix composites. *Safety* 10:11
5. Ray S (2009) Expanding frontier of metallic materials for structural. applications. *IIM Metal news* 12(4):12–24
6. Fayomi J et al (2019) Experimental study of ZrB₂-Si₃N₄ on the microstructure, mechanical and electrical properties of high grade AA8011 metal matrix composites. *J Alloy Compd* 790:610–615
7. Selvam JDR, Dinaharan I, Rai RS (2021) 11890 matrix and reinforcement materials for metal matrix composites
8. Kaviyaranan K, et al (2021) Assessment of mechanical and tribological characteristics of A356 reinforced with x wt% CaB₆ composites. *J Inst Eng (India): Ser D* 1–10
9. Pradhan SK et al (2016) A simple stir casting technique for the preparation of in situ Fe-aluminides reinforced Al-matrix composites. *Perspect Sci* 8:529–532
10. Ahamad N et al (2020) Structural and mechanical characterization of stir cast Al-Al₂O₃-TiO₂ hybrid metal matrix composites. *J Compos Mater* 54(21):2985–2997
11. Bhargava NRM et al (1998) Role of cold work and SiC reinforcements on the β' / β precipitation in Al-10 pct Mg alloy. *Metall Mater Trans A* 29(11):2835–2842

12. Fayomi J, Popoola API, Popoola OM et al (2020) Understanding the microstructural evolution, mechanical properties, and tribological behavior of AA8011-reinforced nano-Si₃N₄ for automobile application. *Int J Adv Manuf Technol* 111:53–62
13. Idrisi AH, Mourad A-HI (2019) Conventional stir casting versus ultrasonic assisted stir casting process: mechanical and physical characteristics of AMCs. *J Alloys Compd* 805:502–508

Effect of Low Volume Reinforcement of Graphene/B₄C Nano Particles in Aluminium 6061-T6 Alloy



Saikiran Ammisetty, CH. R. Vikram Kumar, and K. Hemachandra Reddy

1 Introduction

In the present industrial world, aluminium composites are competent with other materials because of their high stiffness, low weight, and exceptional mechanical and tribological properties. Aluminium reinforced composites attain a wide range of acceptance in the fields of aerospace, marine, defence, automobile, sports, etc., due to improved properties [1]. These improvements in properties mainly depend on quantity and type of reinforcement added to the matrix material, processing method, size of particle and processing parameters, etc. Various materials are available for strengthening the aluminium matrix such as carbides, nitrides, ceramics, borides, oxides, etc. Numerous researches were done on aluminium reinforced with SiC, WC, TiB₂, TiC, Al₂O₃, AlN, B₄C, Graphene, etc. Amongst these reinforcing particles, B₄C and graphene are attractive as they possess high melting points, low density, high Young's and elastic modulus, high hardness, good electrical, as well as thermal conductivity, and superior wear resistance [2]. For these reasons, these are widely used in various applications such as cutting tools, ballistic armour, wear resistant, and corrosion resistant applications. The density difference between molten aluminium (2.385 gm/cm³) and reinforced particles (B₄C & Graphene (2.51–2.27 gm/cm³)) was minimum which is desirable during the casting process because it reduces the anomalies in casting like particles sedimentation rate during composite melt solidification [3]. There are numerous methods available for the fabrication of aluminium

S. Ammisetty (✉) · K. H. Reddy
Department of Mechanical Engineering, JNTUACEA, Anantapuramu, India
e-mail: asaikiran301@gmail.com

CH. R. V. Kumar
Department of Mechanical Engineering, N.B.K.R. Institute of Science and Technology, SPSR
Nellore, Vidyannagar, India
e-mail: cvikramkumar@gmail.com

metal matrix composites (AMMCs). Stir casting is one of the most commonly used processing method for producing AMMCs because of its widely accepted advantages like ease of manufacturing, economical in production and maintenance, high production rate, etc. The major challenges in the stir casting technique are the uniform distribution of reinforcement in the aluminium matrix, porosity, and wettability. These are achieved by proper selection of processing parameters such as melting temperature, stirring speed, and stirring time [4]. The tribological behaviour of composites is a complex process due to its dependency on several aspects like mechanical, chemical, and thermal properties of surfaces that were in contact. Numerous studies have been done on wear characterization of aluminium matrix composites in the last two decades due to their potential advantages in the field of automotive applications such as pistons, connecting rods, shafts, and brake discs, etc. [5]. The machining and mechanical properties of B₄C reinforced aluminium composites through powder metallurgy and hot extrusion route were investigated by Karabulut et al. [6]. It was observed that hardness was increased and fracture toughness was decreased with increasing weight fraction of B₄C content in the matrix. The influence of the weight fraction of reinforcement on surface texture, energy consumption, and productivity was also studied. The wear behaviour of aluminium reinforced with Al₂O₃ and SiC was studied by Natrayan et al. [7] and observed that the sliding speed influences more compared to the load and sliding distance. In the recent past, the effect of coatings like metallic or ceramic on reinforced particles was studied. These coatings are mainly used for improving wettability and interfacial strength between primary and secondary phases of composites. It also inhibits the formation of degrading reaction products during the fabrication of composites. Incorporation of these coatings on particles increases the wear resistance of composites compared with the mixing of uncoated particles in the aluminium composites [8–10]. Benel et al. [11] examined the effect of ageing on the wear behaviour of aluminium hybrid composites. The wear resistance was increased with ageing duration and reduces as sliding distance increases in both the cases of as-cast and aged composites. Kumar et al. [11] reported that improvements in mechanical and wear properties of aluminium nitride/zirconium bromide mixed aluminium composites and also examined that the most influencing factor on wear. The impact of particle size on mechanical and wear properties was examined by Raj et al. [12] and revealed that composites with nano-sized particles show better properties than micro particles up to a certain level only. Further addition of nano particles leads to decrement in material properties due to the formation of agglomeration. According to the literature, the majority of hybrid composites were made using micro-sized reinforced particles and only a few utilising nano-sized particles. The purpose of this work is to examine the mechanical properties of low volume-reinforced boron carbide (B₄C) and graphene on aluminium 6061-T6 alloy.

2 Materials and Method

In the present work, commercially available Si-Mg-based aluminium alloy (Al-6061) was used as a matrix material due to its enormous applications in the automotive industry, defence, aerospace, etc. From the results of energy dispersive spectroscopy (EDS), the chemical composition of AA6061 is shown in Table 1. 0.5% of B₄C and 0.5% graphene nanoparticles were selected as reinforcement with a mean particle size of < 100 nm. Particle size distribution and X-Ray diffraction results of nano B₄C are shown in Figs. 1 and 2. Similarly, the particle size distribution of graphene is shown in Fig. 3. In this work, B₄C (0.5 wt%) and graphene (0.5 wt%) were added for reinforcement.

Table 1 Chemical composition of aluminium 6061-T6

Element	Mg	Si	Fe	Cu	Cr
Content (wt%)	1.78	0.55	0.84	1.52	0.82
Element	Zn	Ti	Mn	Others	Al
Content (wt%)	1.48	0.6	0.41	3.39	88.62

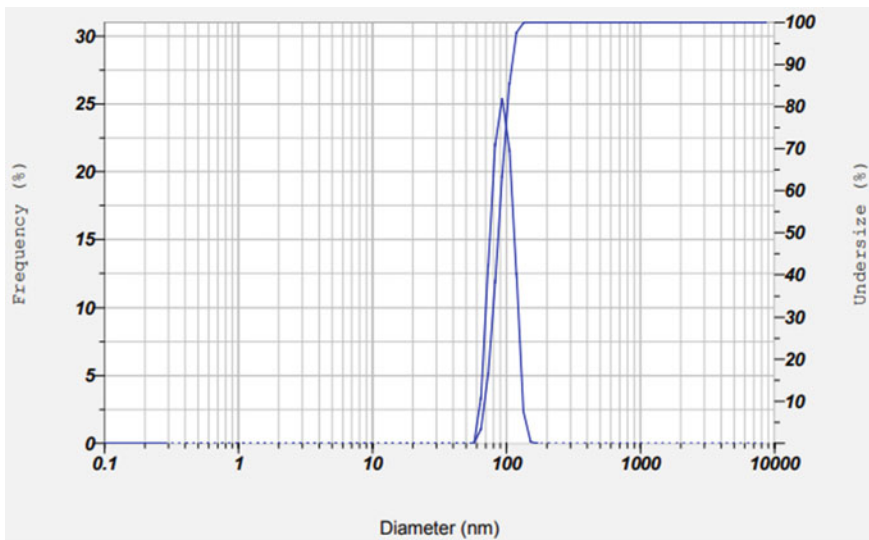


Fig. 1 Particle size distribution of nano B₄C particles

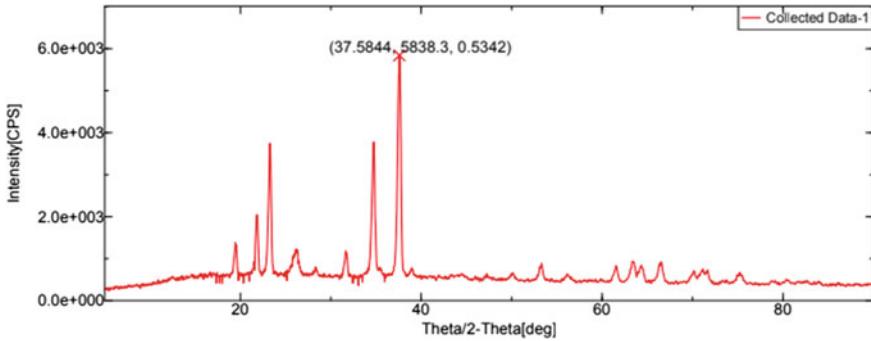


Fig. 2 XRD analysis of nano B₄C particles

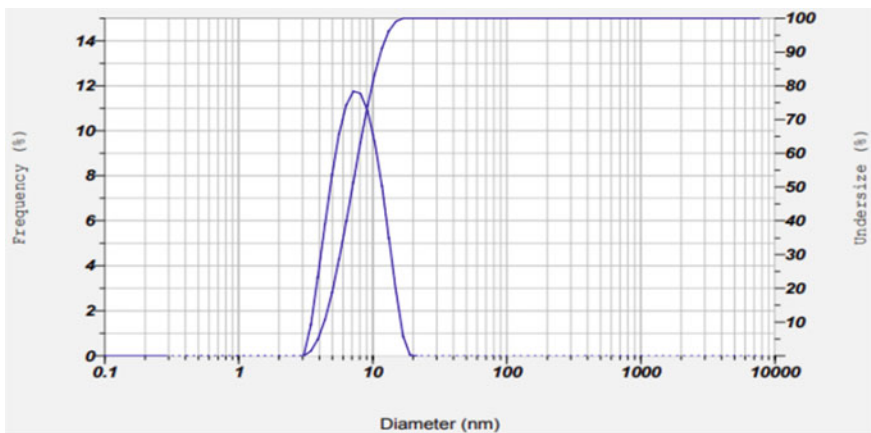


Fig. 3 Particle size distribution of graphene

2.1 Methodology

In the current work, the bottom pouring stir casting technique was used for fabricating aluminium hybrid nanocomposite due to its ease of working and low cost. Initially, AA6061 ingots of size 25 mm diameters were added to the electrical furnace-assisted graphite crucible and allowed to melt at 800 °C for 2 h. After melting of ingots, 3 g of C₂Cl₆ (hexa chloroethane) were added to the molten aluminium to remove the entrapped gasses from the molten metal. Slag was removed before adding the particles into the melt. Reinforcements in the respective proportions, i.e. 0.5% of B₄C and graphene each were mixed with 2 g of potassium hexa fluoro titanate (K₂TiF₆) and then preheated at 400 °C in powder preheater for 2 h so that it is free from foreign particles, moisture content, and also increases the wettability between matrix and reinforcement materials [13]. Later, preheated reinforcement has mixed with the aluminium alloy melt in four steps while rotating the stirrer at a constant speed of

400 rpm. Intermittent reinforcement improves the dispersion of particles inside the matrix, resulting in improved characteristics. The stirrer was swirled in the melt for ten minutes to ensure consistent reinforcement distribution. After agitating the particle-mixed molten liquid for 5 min to settle the particles in the melt, it was poured into a preheated mild steel die with a length of 150 mm and a width of 120 mm and left to solidify naturally for 24 h. The specimens were prepared according to ASTM standards by the wire-EDM machining process. To quantify the improvements in the properties due to reinforcement, the as-casted aluminium alloy was prepared under the same conditions without adding any reinforcement particles into the melt.

3 Experimental Procedure

The mechanical characteristics like hardness, tensile strength, and toughness for fabricated aluminium hybrid nano composite (AHNC) and as-casted specimens were measured. Densities of fabricated samples were also studied.

3.1 Samples Preparation for Mechanical Properties

The hardness test specimens were prepared according to ASTM standards using wire cut electric discharge machine (WCEDM). On the prepared composite specimens Brinell hardness test was performed at a load of 250 kg for 30 s with diamond indenter of 5 mm diameter to find the hardness in terms of Brinell hardness number (BHN). The equation for calculating BHN is shown in Eq. (1).

$$\text{BHN} = \frac{P}{\frac{\pi D}{4} \left(D - \sqrt{D^2 - d^2} \right)} \quad (1)$$

where P = load in kg, D = indenter diameter in mm, d = indentation diameter in mm.

The tensile strength of fabricated AHNC and as-casted specimens were measured at room temperature using a computerized tensometer (KIPL PC2000). The WCEDM equipment was used to prepare the test specimens in accordance with ASTM specifications. The actual tensile testing specimens before experimentation are shown in Fig. 4.

The impact behaviour of casted composites was studied using the Charpy impact test. The dimensions of the test specimen is depicted in Fig. 5.

Density: According to Archimedes's principle the density of as-casted and AHNC specimens was found which implies the weight of specimens in air and liquid with a known density such as water. The density of water at room temperature is taken as 997 kg/m³. The expression for density calculation is given in Eq. (2).

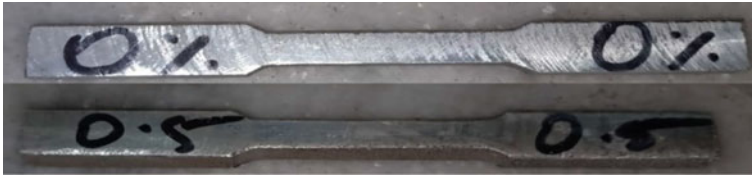


Fig. 4 Tensile testing specimens before testing

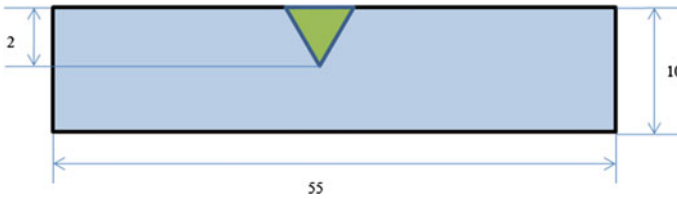


Fig. 5 Impact test specimen with dimensions (mm)

$$\rho = \frac{\text{Weight of specimen in air}}{\text{Weight of specimen in air} - \text{Weight of specimen in water}} \quad (2)$$

4 Results and Discussions

Fabrication of aluminium hybrid nanocomposites containing particles like B_4C and graphene was difficult using the stir casting technique due to lack of wettability between aluminium and reinforced particles [14]. It results in low mechanical and wear properties and non-homogeneous distribution. So to improve the wettability of B_4C and graphene, potassium hexafluoro titanate (K_2TiF_6) was added to the melt. In the present work, mechanical behaviour of aluminium reinforced with 0.5% nano B_4C and 0.5% graphene particles were studied. Densities of fabricated specimens were calculated and the results indicated that AHNC shows lower value than the as-casted specimen due to lesser densities of graphene and B_4C compared to matrix material [15]. The hardness of the as-casted aluminium alloy and AHNC specimens were measured using a Brinell hardness testing machine at various locations and averaged them. The results indicated that compared to as-casted alloy 59.59 BHN, AHNC 69.85 BHN showed better BHN due to the presence of high hardness of ceramic particles in the matrix. A tensile test was carried out to understand the nature of the fabricated composites under loading conditions. From the observed results, AHNC indicated a better strength value than the as-casted specimen, i.e. 149.6 MPa and 65.1 MPa. The difference in tensile strength values is mainly due to the resistance offered by the hard-natured ceramic particles in the AHNC which carries the load transferred by the matrix material and results in improved mechanical

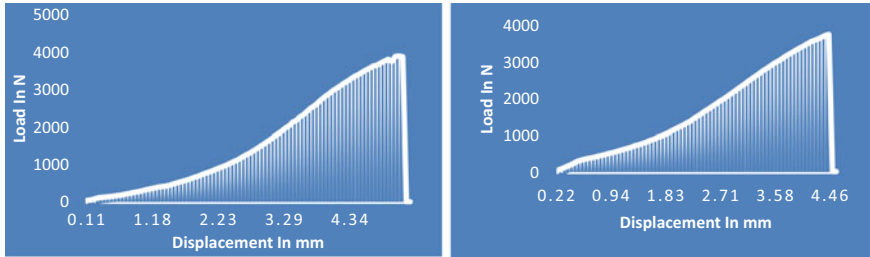


Fig. 6 **a** Load versus displacement of as-casted sample. **b** Load versus displacement of AHNC sample

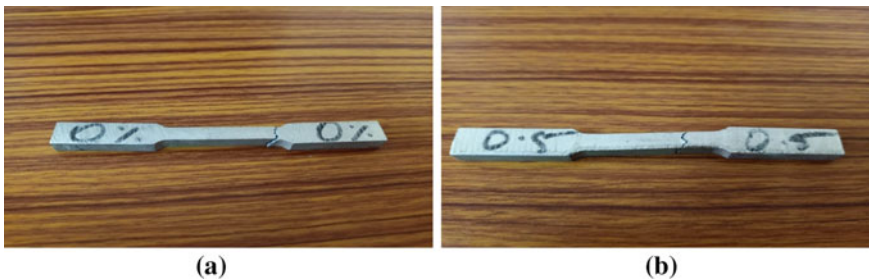


Fig. 7 **a** Tensile tested as-casted sample. **b** Tensile tested AHNC sample

properties. The percentage of elongation was also evaluated for both the composites, and it indicated that AHNC showed a lower value than the as-casted sample due to the presence of reinforced particles. The load vs displacement graph generated during tensile testing and samples after testing are shown in Figs. 6a, b and 7a, b.

The fracture toughness of the casted aluminium composites was measured by using the Charpy impact test, and from the results, it was observed that the toughness of AHNC is higher than the as-casted aluminium alloy. The observed values are 6.47 J for AHNC and 5.88 J for the as-casted specimen. The tested samples are shown in Fig. 8a, b. Comparison of results of prepared nanocomposite and as-cast specimen with previous studies are shown in Table 2.

5 Conclusions

In this paper, aluminium-based hybrid nanocomposites reinforced with low volume nano boron carbide and graphene were fabricated through the stir casting process and its effect on density and mechanical behaviour was investigated. The following conclusions were made from the experimental results:



Fig. 8 **a** As-casted impact tested sample. **b** AHNC impact tested sample

Table 2 Comparison of mechanical properties of previous studies with the present study results

S. No.	Sample	Tensile strength (MPa)	Hardness (BHN)	Density (g/mm ³)	Fracture toughness (J)	% Elongation (mm)	Reference
1	As-casted alloy	65.1	59.59	2.695	5.88	5.16	Present work
2	Al6061-2% B ₄ C micro	–	29.91	2.632	4.6	2.75	Gudipudi Suresh et al. [16]
3	Al6061-1% B ₄ C micro-0.1% graphene	–	60	2.694	–	–	Mahmood Khan et al. [17]
4	Al-0.1% graphene	–	–	–	2.92	–	M Hadad et al. [18]
5	Al7075-0.25 graphene	60	55	–	–	1.7	Ghazanlou et al. [19]
6	Hybrid nanocomposite	149.6	69.85	2.681	6.47	4.40	Present study

- Density of aluminium hybrid nanocomposite decreases with the addition of ceramic particles due to lower density of boron carbide and graphene compared to aluminium.
- Tensile strength of reinforced aluminium nanocomposite was higher than that of the as-casted base matrix material due to the hard nature of added ceramic particles.
- Hardness of fabricated composites was also measured, and an improved hardness value was observed for nanocomposite than the as-casted specimen.
- Fracture toughness of reinforced nanocomposite showed a better value than the as-casted specimen.

References

1. Reddy PS, Kesavan R, Vijaya Ramnath B (2018) Investigation of mechanical properties of aluminium 6061-silicon carbide, boron carbide metal matrix composite. *Silicon* 10(2):495–502. <https://doi.org/10.1007/s12633-016-9479-8>
2. Topcu I, Gulsoy HO, Kadioglu N, Gulluoglu AN (2009) Processing and mechanical properties of B₄C reinforced Al matrix composites. *J Alloys Compd* 482(1–2):516–521. <https://doi.org/10.1016/j.jallcom.2009.04.065>
3. Monikandan VV, Joseph MA, Rajendrakumar PK, Sreejith M (2015) Tribological behavior of liquid metallurgy-processed AA 6061–B₄C composites. *Mater Res Express* 2(1):16507. <https://doi.org/10.1088/2053-1591/2/1/016507>
4. Scholar PG (2013) Production and tribological characterization of stir-cast hybrid composite aluminium 6061 reinforced with SiC and Ti particulates. 2(3):673–687
5. Karabulut Ş, Karakoç H, Çıtak R (2016) Influence of B₄C particle reinforcement on mechanical and machining properties of Al6061/B₄C composites. *Compos Part B Eng* 101:87–98. <https://doi.org/10.1016/j.compositesb.2016.07.006>
6. Natrayan L, Kumar MS (2020) Optimization of wear behaviour on AA6061/Al₂O₃/SiC metal matrix composite using squeeze casting technique-statistical analysis. *Mater Today Proc* 27:306–310. <https://doi.org/10.1016/j.matpr.2019.11.038>
7. Ureña A, Rams J, Escalera MD, Sánchez M (2005) Characterization of interfacial mechanical properties in carbon fiber/aluminium matrix composites by the nanoindentation technique. *Compos Sci Technol* 65(13):2025–2038. <https://doi.org/10.1016/j.compscitech.2005.04.013>
8. Rams J, Campo M, Urena A (2004) Sol-gel coatings to improve processing of aluminium matrix SiC reinforced composite materials. *J Mater Res* 19(7):2109–2116. <https://doi.org/10.1557/JMR.2004.0270>
9. Ureña A, Rams J, Campo M, Sánchez M (2009) Effect of reinforcement coatings on the dry sliding wear behaviour of aluminium/SiC particles/carbon fibers hybrid composites. *Wear* 266(11–12):1128–1136. <https://doi.org/10.1016/j.wear.2009.03.016>
10. Benal MM, Shivanand HK (2007) Effects of reinforcements content and aging durations on wear characteristics of Al (6061) based hybrid composites. *Wear* 262(5–6):759–763. <https://doi.org/10.1016/j.wear.2006.08.022>
11. Kumar NM, Kumaraswamidhas LA (2019) Characterization and tribological analysis on AA 6061 reinforced with AlN and ZrB₂ in situ composites. *J Mater Res Technol* 8(1):969–980. <https://doi.org/10.1016/j.jmrt.2018.07.008>
12. Raj RR, Yoganandh J, Saravanan MSS et al (2021) Effect of graphene addition on the mechanical characteristics of AA7075 aluminium nanocomposites. *Carbon Lett* 31:125–136. <https://doi.org/10.1007/s42823-020-00157-7>
13. Pazhouhanfar Y, Eghbali B (2018) Microstructural characterization and mechanical properties of TiB₂ reinforced Al6061 matrix composites produced using stir casting process. *Mater Sci Eng: A* 710:172–180. <https://doi.org/10.1016/j.msea.2017.10.087>
14. Gao X, Yue H, Guo E, Zhang S, Wang B, Guan E, Song S, Zhang H (2018) Preparation and tribological properties of homogeneously dispersed graphene-reinforced aluminium matrix composites. *Mater Sci Technol*. <https://doi.org/10.1080/02670836.2018.1446869>
15. Asghar Z, Latif MA, Rafi-ud-Din, Nazar Z, Ali F, Basit A, Badshah S, Subhani T (2018) Effect of distribution of B₄C on the mechanical behaviour of Al-6061/B₄C composite. *Powder Metall* 61(4):293–300. <https://doi.org/10.1080/00325899.2018.1501890>
16. Gudipudi S, Nagamuthu S, Subbian KS, Chilakalapalli SPR (2020) Enhanced mechanical properties of AA6061-B₄C composites developed by a novel ultra-sonic assisted stir casting. *Eng Sci Technol Int J* S221509861932350X. <https://doi.org/10.1016/j.jestech.2020.01.010>
17. Khan M, Din RU, Basit MA, Wadood A, Husain SW, Akhtar S, Aune RE (2021) Study of microstructure and mechanical behaviour of aluminium alloy hybrid composite with boron carbide and graphene nanoplatelets. *Mater Chem Phys* 271:124936. <https://doi.org/10.1016/j.matchemphys.2021.124936>. ISSN 0254-0584

18. Hadad M, Babazade A, Safarabadi M (2020) Investigation and comparison of the effect of graphene nanoplates and carbon nanotubes on the improvement of mechanical properties in the stir casting process of aluminum matrix nanocomposites. *Int J Adv Manuf Technol* 109(9–12):2535–2547. <https://doi.org/10.1007/s00170-020-05838-1>
19. Ghazanlou SI, Eghbali B (2021) Fabrication and characterization of GNPs and CNTs reinforced Al7075 matrix composites through the stir casting process. *Int J Miner Metall Mater* 28(7):1204–1214. <https://doi.org/10.1007/s12613-020-2101-5>

Evaluation of Chemical and Mechanical Properties of Al–Si–Mg Composite for Use in Boat Engine Bed



N. Mathimurugan , R. Subramanian , S. Ajith Balaa, R. Manoj, and C. Sathish

1 Introduction

The body of medium-sized fishermen boat is made of Glass fibre, which has good mechanical as well as corrosive properties [1]. But the engine bed used is made of mild steel, which is highly prone to corrosion because of the surrounding environment. As a result the lifespan of the engine bed is greatly reduced, which is very much less than 1 year on an average. Thus, a better material which is suitable to withstand corrosion as well as the loading conditions is needed [2]. Various corrosion resistant materials are available in abundance such as aluminium, stainless steel, magnesium, etc., taking into account the cost of the material and manufacturing feasibility, aluminium is selected as prime material to replace the existing mild steel. Magnesium is profoundly known to be an excellent corrosion resistant material [3]. Thus, a new composition has been carried out using aluminium as base metal and adding Mg in proportions of 4% and 12% to aluminium. Finally, five different materials, namely A413, A356, A413+4% Mg and A413+12% Mg are compared using decision matrix analysis taking into consideration the total deformation under extreme loading conditions, factor of safety and corrosive resistant properties. Total deformation and factor of safety are found using ANSYS Workbench 18.1, and for corrosion properties, the materials are tested using salt spray test [4]. In this paper, the objective is to find suitable material which will prevent corrosion and withstand the dynamic loading conditions.

N. Mathimurugan (✉) · R. Subramanian · S. A. Balaa · R. Manoj · C. Sathish
Department of Mechanical Engineering, PSG College of Technology, Coimbatore, India
e-mail: nma.mech@psgtech.ac.in

© The Author(s), under exclusive license to Springer Nature Singapore Pte Ltd. 2023
B. Bhattacharyya et al. (eds.), *Advances in Micro and Nano Manufacturing and Surface Engineering*, Lecture Notes in Mechanical Engineering,
https://doi.org/10.1007/978-981-19-4571-7_28

309

2 Case Study

Based on real-time survey conducted in Nagapattinam fishermen association, the following problems were identified. The images added below are taken in real time in order to compare the corrosion effect on engine bed. Also, based on our case study, it is found that the average lifespan of these is approximately 1 year. This it has been proposed to replace the existing mild steel with suitable aluminium composition.

The above Fig. 1 illustrates how the engine is mounted on the engine bed and the way in which engine bed is fixed to the boat. As seen, the engine can be swivelled in clockwise and anti-clockwise direction with the help of the lever. Figure 2 illustrates a new engine bed which is yet to be used. When it is used for some time, the paint sheds off and the engine bed is more prone to corrosion.

Although, sea water enters through a provision in the bed, which gets trapped inside the engine bed and accelerates the corrosion process. When it is not lubricated, it becomes difficult to steer the engine because of low clearance and results in higher friction leading to wearing the material. This in turn enlarges the gap and allows more water to get trapped in between, fastening the corrosion process.

Figures 3 and 4 illustrate the bottom view of a new engine bed. After some time, as water is clogged inside the engine bed, the corrosion process increases and as a

Fig. 1 Boat engine



Fig. 2 Engine bed



Fig. 3 Before corrosion**Fig. 4** After corrosion

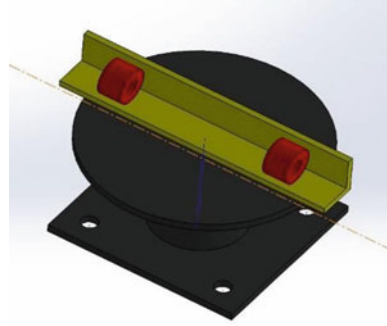
result in failure of the engine bed. Three distinctive colours can be seen in the engine bed:

- Light yellow indicates high corrosion because of the availability of high oxygen
- Dark brown, which is just above the light yellow indicates atmospheric corrosion
- Spots of light orange colour above dark brown indicate pitting corrosion.

3 CAD Modelling

The engine bed component is reverse engineered for structural analysis. Materials and dimensions of each parts were measured then the CAD model shown in Fig. 5 which is generated using the measurements with the help of SOLIDWORKS 2021, and the design is analysed using ANSYS Workbench.

Fig. 5 Engine bed CAD model



4 Forces Acting on the Engine Bed

The engine bed, which is attached to the rear of the boat experiences horizontal and vertical forces [5]. The forces acting are calculated by considering various factors such as static, dynamic loads and also inertial force of sea water [6].

4.1 Horizontal Force

$$F_t = P \times A$$

$$P = 1/2 \times \rho \times (v_b^2 - v_0^2),$$

where v_b = velocity of the boat and v_0 = velocity of the fluid A = Propeller swept area = πr^2

$$\text{Density of water } (\rho) = 1000 \text{ kg/m}^3$$

$$\text{Average speed of boat } (v_b) = 20 \text{ km/hr} = 5.55 \text{ m/s}$$

$$\text{Speed of fluid } (v_0) = 0 \text{ m/s (Worst case scenario)}$$

$$\text{Radius of propeller } (r) = 0.15 \text{ m}$$

$$F_t = 1/2 \times 1000 \times (5.5^2 - 0^2) \times (3.14 \times 0.15^2)$$

$$F_t = F_h = 1087.328 \text{ N}$$

4.2 Vertical Force

Engine weight = 50 kg (**for 8 hp engine**)

Miscellaneous = 35 kg

Net weight = 85 kg = **850 N**

$F_v = 850 \text{ N}$

Considering the dynamic loading conditions, factor of safety is taken as 2. Thus, $F_v = 1700 \text{ N}$.

5 ANSYS Input Parameters

5.1 Input Parameters

After calculating the forces acting on the engine bed, it is analysed using ANSYS Workbench 18.1. The main reason for using Workbench is its user-friendly interface and less pre-requisites required when compared with other platforms.

- **Mesh size:** 1 mm (Tetrahedral)

5.2 Boundary Conditions

To set the boundary conditions for the simulations, bottom face is fixed which is shown in Fig. 6a and the loading conditions are given at the bushes, and Fig. 6b shows the vertical loading condition and Fig. 6c shows vertical loading conditions, respectively.

- | | |
|--------------------|----------------------|
| • Fixed support | : Base plate |
| • Horizontal force | : 1087.2 N (at bush) |
| • Vertical force | : 1700 N (at bush) |

6 Aluminium A413

Aluminium A413, due to its presence of eutectic silicon, offers a good combination of casting, mechanical and thermal properties and thus exhibits excellent fluidity while melting and resistance to hot cracking [7]. It is used in wide variety of variety of products that are casted and used in highly corrosive environments [8].

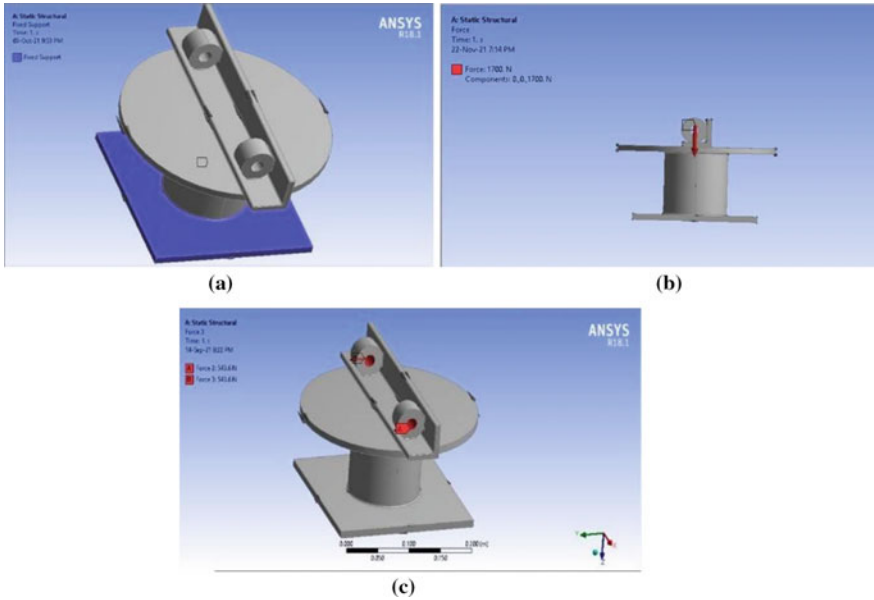


Fig. 6 a Fixed support, b vertical load and c horizontal load

Table 1 A413 properties of material

Properties	A413
Modulus of elasticity (E)	71,000 MPa
Poisson’s ratio	0.33
Ultimate tensile strength	295 MPa
Yield strength	150 MPa
Density	2660 m ³

6.1 Material Properties

The material properties of A413 is listed on Table 1.

6.2 Total Deformation

Total deformation is used to determine the maximum deformation that takes place for the given load for this composition. The maximum deformation is found to be 0.018 mm as shown in the Fig. 7c. Factor of safety details are shown in the Fig. 7a, b, respectively.

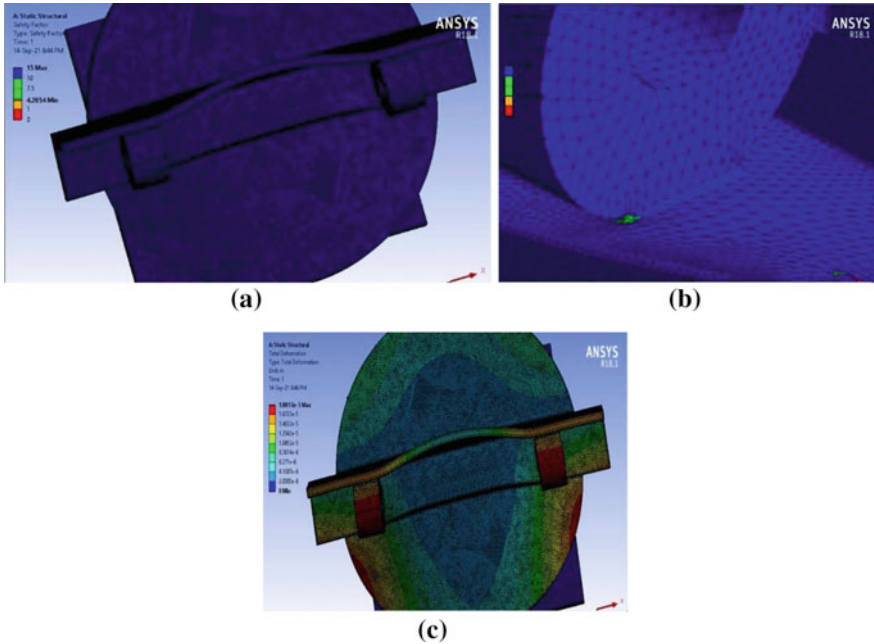


Fig. 7 a, b A413—factor of safety and c A413—total deformation

Factor of safety is used to determine whether the stress developed as a result of applied load is safe within the ultimate stress. Higher is the factor of safety, safer is the design. Minimum FOS obtained is 4.2054, whereas maximum obtained is 15.

Since, FOS should be greater than or equal to 1.5, and this material properties satisfy the loading conditions and are safe for this use.

7 Mild Steel

Mild steel containing a small percentage of carbon, solid and tough but not readily tempered. Mild steel, also otherwise called plain-carbon steel and low-carbon steel, is presently the most well-known type of steel since its price is moderately low while it provides material properties that are satisfactory for some applications [3, 9].

7.1 Material Properties

The material properties of mild steel is listed on Table 2.

Table 2 Mild steel material properties

Properties	Mild steel
Modulus of elasticity (E)	210,000 MPa
Poisson's ratio	0.301
Ultimate tensile strength	450 MPa
Yield strength	250 MPa
Density	7850 m ³

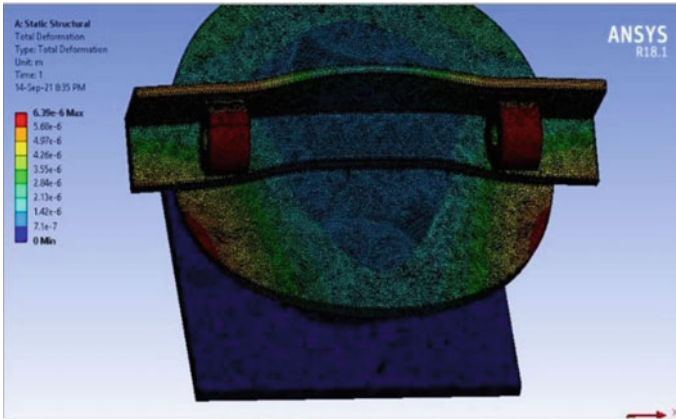


Fig. 8 Mild steel—total deformation

7.2 Total Deformation

Total deformation is used to determine the maximum deformation that takes place for the given load (Fig. 8). For this composition, the maximum deformation is found to be 0.0063 mm.

7.3 Factor of Safety

Static structural analysis is carried out for mild steel and A413 using ANSYS Workbench, and the results such as total deformation and factor of safety shown in Fig. 9 for the given loading conditions were obtained, and the results has been listed in the below Table 3.

Static structural analysis is carried out for mild steel and A413 using ANSYS Workbench, and the results such as total deformation and factor of safety for the given loading conditions were obtained.

Fig. 9 Mild steel—factor of safety**Table 3** Result A413 and mild steel

	A413	Mild steel
Total deformation (m)	1.8×10^{-5}	6.39×10^{-6}
Factor of safety	4.2	7.2
Yield strength (MPa)	150	250

Table 4 Result A356, 4%mg and 12% mg

	4% Mg	12% Mg	A356
Total deformation (m)	4.99×10^{-5}	4.02×10^{-5}	1.84×10^{-5}
Factor of safety	3.67	0.99	4.74
Yield strength (MPa)	132	54	165

Similarly, with a same procedure, the analysis is carried out for 4%Mg in A413, and 12% Mg in A413 and A356 and the results have been listed in the below Table 4.

8 Corrosion Test

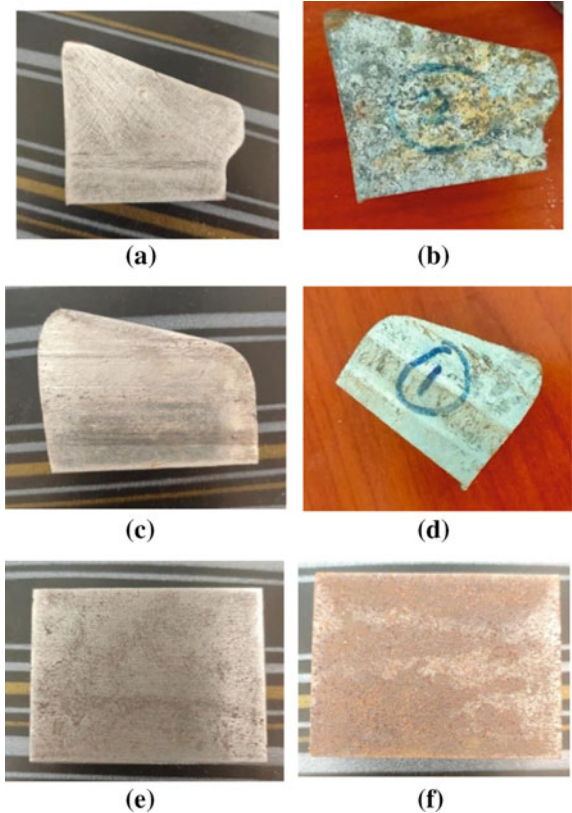
There are many studies of the use of aluminium alloys in order to reduce the weight of marine boat components. In this case, one of the important matters is the corrosion problem. We have to take into consideration that boats are running in severe saline environment. In the area where salt for deicing is scattered in winter time and coastal area where marine salty air exists, it is very important to investigate whether these are fit for use in this area. We, therefore, attempted to get some basic data to investigate the durability of mild steel which is currently used material for boat engine bed, and

our alternative aluminium alloys especially A413 and A356 were tested and for this purpose, we employed the accelerated corrosion test using salt spray test apparatus with 5% NaCl solution which is main component of sea water. We also examine the corrosion resistance of mild steel in the same test to compare with aluminium alloys. For the corrosion test, procedure ASTM B117 standard is used.

8.1 Observation

After every 24 hour, the specimens were taken out and the surfaces were examined, and it is found that the mild steel in Fig. 10e and f shown a red dots formation at the end of 24 h and red rust at the end of 48 h, and similarly for A356 (Fig. 10a and b), it is examined for 24th and 48th hours, and it is found that there is no significant change in the surface during first 24 h but there is a black corrosion formation observed at the end of 48 h. At last, A413 (Fig. 10c and d) is observed under similar time frames, and there is no corrosion layer formation even at the end of 48 h.

Fig. 10 a A356 before corrosion, b A413 after corrosion, c A413 before corrosion, d A413 after corrosion, e mild steel before corrosion and f mild steel after corrosion



8.2 Corrosion Rate

$$\text{Corrosion rate} = \frac{(\text{weightloss in grams})\text{mm/hr}}{A \times d \times t} \text{ (i)}$$

A Area of specimen (mm²)

d Metal density of specimen (g/mm³)

t Time of exposure in corrosive environment (Hours)

8.3 Finding Corrosion Rate for A413

$$W1 = 58.070 \text{ g}$$

$$W2 = 58.020 \text{ g}$$

$$\begin{aligned} \text{Density} &= 2.66 \times 10^{-2} \text{ g/mm}^3 \text{ Area} = 4960 \text{ mm}^2 \\ &= \frac{(58.070 - 58.020) \times 534 \times 1000}{4960 \times 2.66 \times 48} \text{ (substitute in (i))} \\ &= 4.2149 \times 10^{-2} \text{ mm/hr} \end{aligned}$$

8.4 Result

In this chapter, the corrosion test is studied under sea environment using salt spray accelerated test, and firm that weights before and after corrosion were taken and corrosion rate is determined (Table 5). It is clear that A413 has a low corrosion rate of 4.21×10^{-2} mm/hr when compared to mild steel (10.39×10^{-2}) and A356 (6.82×10^{-2}), respectively.

Table 5 Corrosion test result

Name	Area mm ²	Observation 1: 24 h	Observation 2: 48 h	Weight before test (W1)g	Weight after test (W2) g	Corrosion rate (C.R) mm/hr
Mild steel	6546	Red dots	Red rust	246.920	246.440	10.39×10^{-2}
A413	4961.13	No sign	No sign	58.070	58.020	4.21×10^{-2}
A356	5010.49	No sign	Black corrosion	47.400	47.280	6.82×10^{-2}

Table 6 Decision matrix analysis

Material	Corrosion resistance	Structural safety factor	Weight	Total
Mild steel	4	10	4	18
A356	7	7	10	24
A413	10	6	10	26

9 Decision Matrix Analysis

Decision matrix is a table used in evaluating possible alternative to a course of samples, here the materials A413, A356 and mild steel are taken as samples, and corrosion resistance, safety factor and weight (less weight more fuel efficient) are taken as parameters. The properties of a materials are rated between 1 and 10, material with most desirable properties is given as 10 and one with least as 1 (Table 6).

10 Conclusion

In this paper, suitable material for boat engine bed is selected using its corrosion resistance of the material and its structural strength using factor of safety analysis using ANSYS, finally from the decision matrix analysis, it is concluded that A413 have highest score since it has most desirable properties, so A413 is a much suitable material for the boat engine bed.

References

1. Angadi B, Reddy A, Bhavi I, Chappar S (2018) Finite element analysis of hypereutectic aluminium silicon alloys
2. Agnihotri R, Dagar S. Mechanical properties of Al-Si C metal matrix composites fabricated by stir casting route
3. Dasu P. Static and fatigue analysis of aluminum alloy wheel under a radial load have been done using FEA package
4. Ojha A (2018) Continuum simulation of heat transfer and solidification behavior of AlSi10Mg in direct metal laser sintering process, IOP conference series: materials science engineering, vol 338, p 012052
5. Arunkumar S (2017) Comparative investigation on modal analysis of LM25 aluminium alloy with other aluminium alloys using finite element analysis software. IOP conference series: materials science engineering, vol 183, p 012011
6. Biswas P, Mandal D (2011) Micromechanical response of Al-Mg²Si composites using approximated representative volume elements (RVEs) model. Mater Res Express. MRX-118193.R1
7. Zhai YB (2016) Two kinds of Al based functionally gradient composite tubes reinforced by primary Si particles alone and primary Si/in situ Mg₂Si particles by centrifugal casting
8. Kolhe RG (Aug 2020) Static, modal and thermal analysis of engine block. Int J Eng Res Technol (IJERT) 9(08)

9. Panda BK, Sahoo S (July 2020) Thermo-mechanical modeling and validation of stress field during laser powder bed fusion of AlSi10Mg built part. 9(08)
10. Karasoglu M, Karaoglu S, Sinan T, Tekin T. A research on effect of process parameters on mechanical properties of B₄C reinforced aluminum matrix composites fabricated by mechanical milling and hot press sintering route
11. Boysal A, Rahnejat H. Torsional vibration analysis of a multi-body single cylinder internal combustion engine model. Department of Mechanical and Manufacturing Engineering, University of Bradford, UK
12. AHIRRAO NS. Dynamics and vibration measurements in engines, 2nd international conference on materials manufacturing and design engineering

Realizing the Application Potential of Graphene-Modified Bionanocomposites for Prosthesis and Implant Applications



Devendra Kumar Singh and Rajesh Kumar Verma

1 Introduction

The biomedical sector has been proliferating in developing various unique polymer materials for the last two decades. Due to exceptional mechanical features and biocompatibility, the polymer base biomaterial widely replaces traditional materials such as metal and alloys. The supplement of the carbon derivatives gives a new direction to achieve exceptional material characteristics. Graphene is observed as a unique material with a long list of superlatives to its terminology in this series. It is also known for being the thinnest material and the strongest ever measured. Graphene/graphene derivative nanocomposites have recently gained popularity in the areas of biology along with various biomedical applications. Drugs, nucleic acids, antibodies, and other compounds have all been combined with graphene and its derivatives. Due to their large specific surface area, strong elasticity and flexibility, good biocompatibility, and remarkable mechanical strength, these substances could be used as nanocomposite carriers or scaffold material. Graphene-based biomaterials have sparked a lot of scientific and technological interest among nanomaterials utilized in biological applications in the recent years and hold a lot of potential as antibacterial agents [1, 2], biosensors application [3], photothermal therapies (PTTs) [4], an important agent in bioimaging [5], as a tissue engineering, and stem cell modules [6, 7]. Since 2004, a surfeit work of literature focusing on graphene-based materials has emerged. Based on the previous studies about graphene in the biomaterial field, graphene incorporated with different polymers is the new development in biomaterials. It contributes to low cost, easy availability, lightweight, and favorable properties. This review primarily concentrates on UHMWPE as a polymer matrix

D. K. Singh · R. K. Verma (✉)

Materials and Morphology Laboratory, Department of Mechanical Engineering, Madan Mohan Malaviya University of Technology, Gorakhpur 273010, India
e-mail: rkvme@mmmut.ac.in

because of its superior use and excellent properties, making it a gold standard in today's era and a standard polymer for biomaterial applications and manufacturing industries. Graphene is combined with multiple polymer matrices for improved properties [8–10]. In the recent years, there has been an increase in the studies on the fabrication, mechanical, and biological examinations of these innovative new materials. The primary bearing ingredient for use in artificial joints is UHMWPE. Nonetheless, the durability of these implants is compromised by an osteolytic immune response triggered by submicron-sized wear debris produced by the UHMWPE material. The occurrence of joint replacement due to damage or some hazardous medical conditions in the young and old population has recently increased dramatically. This paper will focus on graphene and its variants as nanofiller materials and UHMWPE as a matrix material. The associated research has recently started in 2004 [11].

The data for Fig. 1 were obtained from the Scopus library using the keyword “graphene biomaterial.” Figure 1 shows the novelty and importance of this theme in the modern research community, underlined by the significant increase in publications from 2011 to 2021. The first study was reported in 2004, and the investigation continues by eminent scholars at a slower pace until 2011. Renowned research and development were observed from the year 2011 till today. Figure 2 shows the publications in UHMWPE-based graphene nanofiller biomaterials (Scopus). It can be easily pointed out that around 43% of studies concerning UHMWPE/graphene derivatives was observed in the recent years, which was earlier about 14% in 2014–2017. The chart clearly shows the current trend of development in UHMWPE/graphene/graphene-derivative polymeric biomaterial.

Therefore, more and more related works will be carried out in the foreseeable future. It is a need of time to present an extensive review of current findings and accomplishments in this field that can guide future studies along with their application and discusses the part of graphene and its derivatives in polymeric (UHMWPE) biomaterials.

Fig. 1 Number of publications versus year plot (2004–2021) for graphene biomaterials

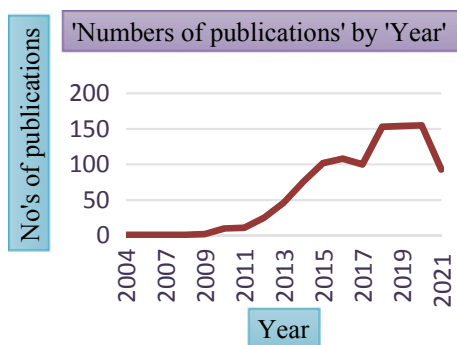
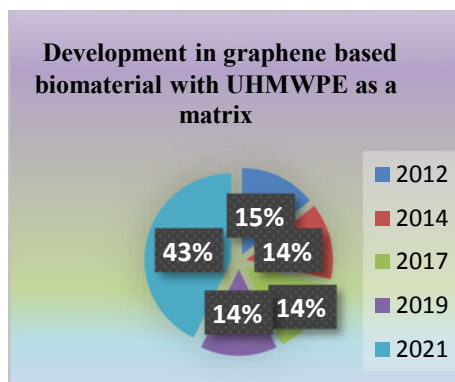


Fig. 2 Development in graphene-based biomaterial with UHMWPE as a matrix



2 Graphene and Their Derivatives

In 2004, Andre Geim and Nosovelov used the Scotch tape method to extract single-layer graphene from graphite [12] by mechanically cleaving a natural graphite crystal.

Graphene is a primary carbon allotrope form that consists of a one-atom-thick 2D sheet of sp² hybridized carbon atoms closely packed into six rings to form a lattice structure like a honeycomb [13]. Due to its superior quality and unique behavior with different environments and materials, it has attracted the attention of a large group of the scientific community.

2.1 *The Following are the Three Main Approaches to Synthesis Graphene*

- Mechanical cleavage from pure graphite.
- Plasma or chemical exfoliation from pure graphite.
- Chemical vapor deposition (CVD).

Figure 3 illustrates the widely explored carbon nanomaterials in recent studies, and different forms of graphene/graphene-derived derivatives, respectively. Graphene is sometimes preferred over other carbon nanostructures because of its exceptional qualities, including flexibility and transparency. More recently, there have been attempts to use graphene-based materials for research in biomedical applications (Table 1).

Apart from the above-discussed derivatives, many more graphene derivatives are on the verge of development such as graphene ribbons, graphene nanodots, etc. The graphene and its derivatives are produced via effective techniques, as summarized in Fig. 4, and their different applications are presented in Fig. 5.

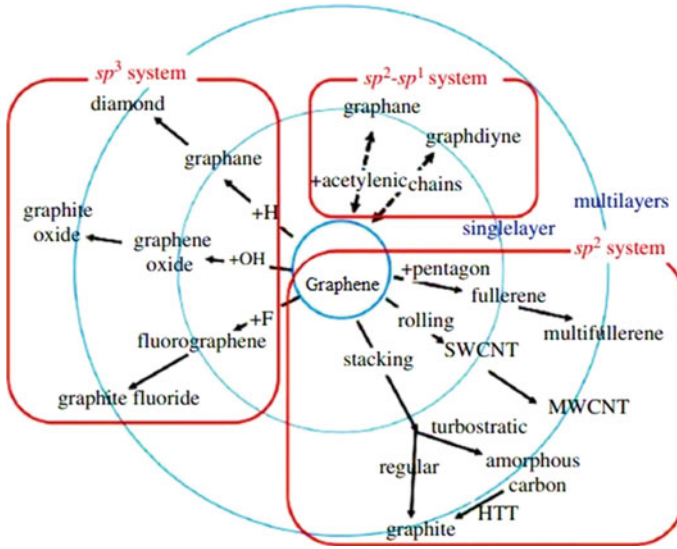


Fig. 3 Graphene/graphene derivatives [14]

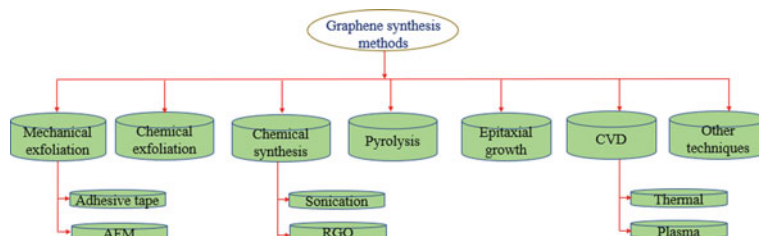
Table 1 Brief description of different forms of graphene/processing methods and applications

Derivative [Ref]	Process/Route	Application
Graphene oxide (GO) [13, 15–17]	<ol style="list-style-type: none"> 1. Staudenmaier, Hofmann, Brodie and hummers/improved hummer’s method 2. Exfoliation 3. There are numerous versions of these methods, with new ones being developed to get better results and lower costs 	Hydrogen storage, ion conductors, nanofiltration membranes. Flexible electronics, solar cells, chemical sensors, biomineralization, so on
Reduce graphene oxide (RGO) [18–24]	<ol style="list-style-type: none"> 1. Thermal treatment 2. Photocatalyzed reactions 3. Electrochemical reduction 4. Green, reducing agent (Vitamin C, sugars, amino acids, and even microorganisms) 5. Improved Tour’s method (improved mechanical and electrical properties) 	Lubricating efficiency improvement, drug delivery application, biosensing application. Electronic device development, etc.
GNNPs [25, 26]	<ol style="list-style-type: none"> 1. Micromechanical cleavage of bulk graphite 2. Plasma exfoliation (f-GNNPs) (Exfoliation of GO- > polystyrene–polyacrylamide (PS–PAM) copolymer graft on graphene sheet) 	Bioimaging, nanomedicine, disease diagnosis

(continued)

Table 1 (continued)

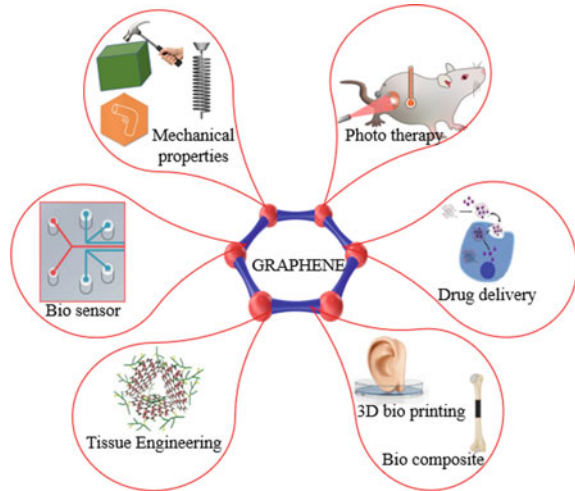
Derivative [Ref]	Process/Route	Application
Graphane [27–29]	Graphane, with the CH composition, is the fully hydrogenated graphene derivative 1. Graphene is exposed to low-pressure and temperature argon-diluted hydrogen plasma	Nanoelectronics and hydrogen-fuel technologies, application in biotechnology
Graphone [30–32]	Graphone is a semi-hydrogenated graphene derivative	Magnetism, organic ferroelectrics, molecular packing, spintronics
Fluorographene [33, 34]	Fluorographene was synthesized by fluorinating graphene and mechanical or chemically exfoliating graphite fluoride	Electronics and energy technologies, sensing and bioimaging
Graphyne, graphdiyne [35, 36]	Organic syntheses (Modern acetylene chemistry and new organometallic synthetic methodologies based on dehydrobenzo annulene framework)	Nanocomposites, nanoelectronics
CNTs, SWNTs, MWCNTs [37–40]	1. CVD 2. Electric arc method, and 3. Laser deposition method 4. Plasma enhanced chemical vapor deposition Apart from this, there are many more methods for functionalized CNTs synthesis	Antibacterial, antifungal, drug delivery, nanoprobes and sensors, biocomposites, etc.

**Fig. 4** Significant techniques for graphene and their derivatives synthesis

3 Synthesis and Characteristics of Graphene/UHMWPE Polymeric Biomaterials

In this paper, the attention is made on polymer-based graphene/graphene derivatives biomaterials. Numerous studies have been published in this field in recent years due to the extreme demand for polymeric biomaterials because of availability and supporting favorable properties for biomaterials application.

Fig. 5 Application of graphene in the biomedical field



3.1 Synthesis

Tai et al. demonstrated the application of UHMWPE/GO nanocomposite for tribological application. They have observed that when (1 wt.%) GO nanosheets obtained by oxidation–exfoliation of natural graphite is incorporated in UHMWPE matrix, and the wear resistance gets improved. It gets further improvement with an increase in GO content (3%). Modified Hummers method was adopted for GO synthesis followed by ultrasonication of 1 h, and after drying, it is hot pressed to produce a block of $70 \times 70 \times 1 \text{ mm}^3$. With a GO load of 3wt.%, a 40% reduction of wear rate is observed; thus, the wear resistance ability of graphene oxide is observed [41].

Further, Aliyu et al. studied tribological characterization on UHMWPE/GNPs nanocomposite coating for bearing application. Aluminum surfaces are protected for tears and wear during dry and boundary lubrication conditions. The wear analysis findings show that UHMWPE/ GNPs (1 wt.%) coated sample is much better than the reference sample without any coating [42]. The recent study by Vinoth et al. in 2021 adopted machine learning and an evolutionary algorithm to generate an acceptable composite material in hip joint replacement for acetabular. Experimental results, including MWCNT, graphene, and carbon fiber, were utilized as a library. The concept was applied to create higher-performance composites using genetic algorithms as objective optimization functions in single and multi-target designs [43]. Vinoth et al. further adopted the ANN/GA approach for tribological properties optimization of weight fraction of UHMWPE nanocomposites. The geometry of the various nanoparticles concerning tribological properties is used as an input parameter. The friction coefficient and specific wear rates were the output parameters employed in ANN modeling. Genetic algorithms (GA) are employed to perform optimization [44]. Liu et al. described an octa-screw extrusion technique for increasing the wear resistance of UHMWPE/graphene nanocomposites. Uniform dispersion of

nanofiller was observed. When compared to pure UHMWPE, an 18% increase in yield strength, a more excellent anti-wear characteristic, a 67% rise in crystallinity, and an increase in decomposition temperature by 4% were concluded [45]. Saad et al. findings revealed that UHMWPE/PAN/HA/GNP nanocomposite synthesized by 5% short fibers polyacrylonitrile (PAN), GNP (0.3, 0.8 and 1.3) %, and HAp by following the process of sonication and vacuum drying and then hydraulic pressing at 180°C and 12 MPa pressure improves mechanical and antibacterial properties [46]. Mindivan et al. and Çolak et al. both elaborated the development of UHMWPE/RGO composite through liquid phase ultrasonic mixing followed by hot press molding. Both the groups adopted the green route of synthesis for RGO by using Vitamin C. Mindivan et al. preferred dry sliding conditions with the Al₂O₃ counterpart. Çolak et al., on the other side, chose the water-lubricated state of sliding between UHMWPE/RGO and Al₂O₃ counterpart. Both groups observed improvement in tribological behavior. The optimum filler content of 0.7 wt% and 1.0 wt. % was followed by Çolak et al. and Mindivan et al., respectively [47, 48]. Lu et al. recently studied the irradiated UHMWPE/GO nanocomposites. In conjunction with GO's irradiation cross-linking technology, the crystallinity and melting point can be increased, and the friction and wear rate of the material decreased. The reduction in average coefficient of friction (COF) and wear rate was about 0.1035 and $4.78 \times 10^{-9} \text{ g N}^{-1} \text{ m}^{-1}$, respectively [49]. According to Chih et al., coating techniques based on graphene materials and graphene/PE composites may be used to enhance the tribological properties of UHMWPE. A GNP/PE composite coating reduces the COF by 10%. The surface electrical resistivity of the produced layer (graphene/PE) decreases as the consolidation temperature rises from 175 to 245 °C, without compromising surface mechanical properties or tribology [50].

Chen et al. demonstrated the characterization and design of polymer (UHMWPE) surface porous composite. The composite is developed with NaCl and GO by hot pressing. The modified UHMWPE/GO/NaCl porous composite's mechanical and tribological aspects were studied in water-lubricated conditions. 1 wt.% GO and 10% NaCl fillers are added to the UHMWPE matrix. Sedimentation technique was used to produce good dispersion of GO in saturated NaCl with UHMWPE Matrix [51].

3.2 Characterization of Graphene/UHMWPE Polymeric Biomaterials

Tai et al. observed GO sheets' thickness and surface morphology using a multi-mode atomic force microscope (AFM). They noticed a 1 nm GO sheet on the surface of a silicon wafer, which is consistent with the thickness of a single-layer GO sheet. The surface of the UHMWPE composite is analyzed using SEM to verify the morphological characteristics of the materials. The fracture surface shows river-like fracture patterns after the crack propagation. The microhardness of the GO/UHMWPE

composite is enhanced by adding GO. This effect is evidenced by the increasing GO content [41].

Aliyu et al. by visual observation of the disc counterface after the wear tests (by optical profilometer), suggested the counterface did not show signs of wear after six tests. Also, the SEM micrograph of the wear track of UHMWPE/1 wt-% GNPs coating for variable sliding speed suggests the two types of wear mechanism, peeling and adhesive wear [42]. Liu et al. elaborated the characteristics of the developed G-UHMWPE composite by tensile, nanoindentation, friction/wear, DSC, TGA, and TEM, including water contact angle test and cell culture. Microscopy investigations show that the graphene filler is not accumulating and is dispersed uniformly, confirming the octa-screw extruder's outstanding compounding capabilities. The hardness and hydrophilicity of the nanocomposites improved with no evidence of cytotoxicity [45]. SEM image of RGO reinforcement in UHMWPE was studied by Mindivan et al. to find the effect as reinforcement in UHMWPE (under dry wear condition). Plastic deformation could be seen on the virgin UHMWPE worn surface in the low magnification SEM micrographs, which is characteristic of adhesive wear. In the high magnification photograph, fatigue wear was prominent [47]. Çolak et al., on the other hand, studied the RGO-UHMWPE composite (under water-lubricated condition) SEM photographs of the surfaces of developed biocomposites with varying concentrations of RGO, as well as an EDS elemental map of carbon and oxygen. The surface of UHMWPE/RGO-0.7 was reasonably flat; however, there have been some irregular regions. The images of biocomposite revealed that RGO was incorporated into the UHMWPE matrix, resulting in high interfacial bonding strength between RGO and UHMWPE [48]. Lu et al. recently observed the FTIR and DSC for the developed GO-UHMWPE composite and found that for R/GO-UHMWPE, vibration peaks of C–O and C–OH can be seen at $1050\text{--}1250\text{ cm}^{-1}$. Under irradiation cross-linking treatment for R-UHMWPE, the oxidation process promotes the creation of oxygen-containing groups such as aldehyde, ketone, acid, and ester. Meanwhile, at $3100\text{--}3500\text{ cm}^{-1}$, prominent peaks of the O–H bond will develop, revealing the interaction of free radicals with oxygen. The average COF of GO/UHMWPE nanocomposites submerged in SBF solution for six months is enhanced due to increased crystallinity following a long-term immersion treatment, as confirmed by the DSC [49].

Chen et al. observed that in the friction process with NaCl dissolution, new porous are built on the surface of the developed composite. The nature of the micro holes formed due to NaCl dissolution can be well seen in the micrographic scan (See Fig. 6). Both improvements in anti-friction and anti-wear properties are concluded through this study [51].

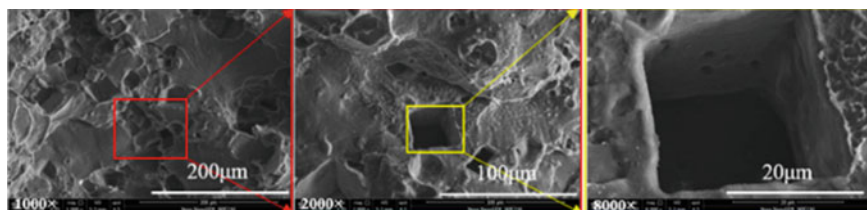


Fig. 6 Cross-sectional microscan of UHMWPE/GO/NaCl developed composite

In addition to the graphene/UHMWPE bionanocomposites types discussed. UHMWPE polymeric biomaterials are increasing daily due to their varied application and scope of future research in this field (Table 2) illustrate the same.

4 Conclusions

Present work describes an extensive literature review on graphene-modified UHMWPE bionanocomposites. It has been observed that graphene and its derivatives have become exciting areas of investigation for the biomedical component. However, graphene-based nanomaterials exhibit unique and compelling characteristics. Several fascinating and surprising biological advances in this approach have recently been made in biomedical applications. This field is currently undergoing an advanced phase of development. Several significant issues must be dealt with before this sector is wholly marketable and requires appropriate guidance. Interdisciplinary strategies combining physics, chemistry, biology, and materials and metallurgy science will be vital in achieving graphene and its derivatives in biomedical applications, from the laboratory to the actual clinical utility.

A practical, multi-disciplinary collective methodology needs to speed up the mechanistic knowledge of graphene-based biomaterials and their varied application. Other than graphene, CNTs (graphene derived), GNPs, GO, and RGO (pristine and biofunctionalized), the investigation of additional graphene variants as biological materials might be an exciting future research area, including green route synthesized GO and RGO. Apart from the biomedical sector, graphene/derivatives find its exciting use in a variety of functions such as solar cells, storage setup, development of electronics devices, different types of gas sensing devices, membrane development and filtration use.

Table 2 Graphene/graphene-modified bionanocomposites (UHMWPE-based)

Reference	Graphene/graphene derivatives (wt.%)	Bionanocomposites	Synthesis technique	Modulus	Hardness	COF/wear resistance (Wr)	Application
[52]	Fluorinated graphene (FG) (0, 0.1, 0.3, 0.5, and 1 wt.%)	UHMWPE/FG	Ultrasonic dispersion (in ethanol), and liquid thermoforming method	–	25% & 64% improved @0.1 and 1 wt.% FG, respectively	43% decrease in wear rate @1 wt.% FG COF reduced; Wr improved	Artificial joint replacement material
[53]	GNP (0.1, 0.5 and 1 wt%)	UHMWPE-10 wt% HAp)/GNP	Solvent mixing and ultrasonication (ethanol), hot pressing	861 ± 93 MPa (improved) @ 1 wt.% GNP	–	(Improved except for 1 wt.% GNP) 54% and 82% reduction in COF and wear	Biomedical application (biocomposites)
[54]	GNPs (0, 0.1, 0.5 and 1 wt%)	UHMWPE/GNPs	Ultrasonication (acetone) hot compression technique	–	–	COF decreases with an increase in GNP, Wr improved	Lubricating surface, bearing use
[55]	GO (0–2 wt.%) (0.1, 0.3, 0.5, 0.7, 1 and 2 wt%)	UHMWPE/GO	Ultrasonication in ethanol, ball milling, hot pressing	15% improvement	Improved	–	Biomedical, aerospace, automobile
[56]	modified graphene (*mGO) (≤3 wt% mGO)	60% HDPE–40% UHMWPE) /*mGO * (mPE (maleated polyethylene) grafted mGO)	Melt-extrusion (220°C, 60 rpm for 10 min)	40% improvement (up to 908 MPa)	–	–	Bone tissue applications, implant

(continued)

Table 2 (continued)

Reference	Graphene/graphene derivatives (wt.%)	Bionanocomposites	Synthesis technique	Modulus	Hardness	COF/wear resistance (Wt)	Application
[57]	0.5 wt%GO + 0.5 wt% ND + 10 wt%SCF	UHMWPE /GO /ND /SCF hybrid composite	Mechanical blinding-compression molding	–	–	No significant change reported	Tribological application
[58]	CNT (0.05, 0.5, 1, and 2)	UHMWPE/CNT	Ultrasonication (deionized water) -centrifugal mixing-hot pressed	–	–	20% (improvement)@0.05wt.% of CNT Wr improved	Biomedical, pickers, bumpers, linings
[59]	MWCNT (0.1 wt%, 0.5 wt% and 1.0 wt%)	UHMWPE/MWCNT	Sonication (in ethanol)-Hot pressing	–	A slight increase	Lowest @ 1.0 wt% MWCNT COF lubricated < dry condition	Implants

References





1. Kumar P, Huo P, Zhang R, Liu B (2019) Antibacterial properties of graphene-based nanomaterials. *Nanomaterials* 9:1–32
2. Zou X, Zhang L, Wang Z, et al (2016) Mechanisms of the antimicrobial activities of graphene materials
3. Jiang WS, Xin W, Xun S et al (2017) Reduced graphene oxide-based optical sensor for detecting specific protein. *Sens Actuators, B Chem* 249:142–148
4. Gao S, Zhang L, Wang G et al (2016) Hybrid graphene/Au activatable theranostic agent for multimodalities imaging guided enhanced photothermal therapy. *Biomaterials* 79:36–45
5. Wang R, Guo Z, Liu Y et al (2021) Concentration-dependent emissive lignin-derived graphene quantum dots for bioimaging and anti-counterfeiting. *Diam Relat Mater* 117:108482
6. Kenry LWC, Loh KP, Lim CT (2018) When stem cells meet graphene: opportunities and challenges in regenerative medicine. *Biomaterials* 155:236–250
7. Bai RG, Ninan N, Muthoosamy K, Manickam S (2018) Graphene: a versatile platform for nanotheranostics and tissue engineering. *Prog Mater Sci* 91:24–69
8. Graziano A, Jaffer S, Sain M (2019) Graphene oxide modification for enhancing high-density polyethylene properties: a comparison between solvent reaction and melt mixing. *J Polym Eng* 39:85–93
9. Martínez-Morlanes MJ, Pascual FJ, Guerin G, Puértolas JA (2021) Influence of processing conditions on microstructural, mechanical and tribological properties of graphene nanoplatelet reinforced UHMWPE. *J Mech Behav Biomed Mater* 115
10. Aliyu IK, Mohammed AS, Al-Qutub A (2019) Tribological performance of ultra high molecular weight polyethylene nanocomposites reinforced with graphene nanoplatelets. *Polym Compos* 40:E1301–E1311
11. Sukhanova A, Devy J, Venteo L, et al (2004) Biocompatible fluorescent nanocrystals for immunolabeling of membrane proteins and cells. *Anal Biochem* 324:60–67
12. Novoselov KS, Geim AK, Morozov SV, et al (2004) Electric field effect in atomically thin carbon films. *Science* 306:666–669
13. Ege D, Kamali AR, Boccaccini AR (2017) Graphene oxide/polymer-based biomaterials. *Adv Eng Mater* 19:1–22
14. Inagaki M, Kang F (2014) Graphene derivatives: graphane, fluorographene, graphene oxide, graphyne and graphdiyne. *J Mater Chem A* 2:13193–13206
15. Marcano DC, Kosynkin DV, Berlin JM, et al (2010) Improved synthesis of graphene oxide. *ACS Nano* 4:4806–4814
16. Hummers WS, Offeman RE (1958) Preparation of graphitic oxide. *J Am Chem Soc* 80:1339
17. Park S, Ruoff RS (2009) Chemical methods for the production of graphenes. *Nat Nanotechnol* 4:217–224
18. Pei S, Cheng HM (2012) The reduction of graphene oxide. *Carbon N Y* 50:3210–3228
19. Williams G, Seger B, Kamat PV (2008) UV-assisted photocatalytic reduction of graphene oxide. *ACS Nano* 2:1487–1491
20. Chua CK, Pumera M (2014) Chemical reduction of graphene oxide: a synthetic chemistry viewpoint. *Chem Soc Rev* 43:291–312
21. Stankovich S, Dikin DA, Piner RD, et al (2007) Synthesis of graphene-based nanosheets via chemical reduction of exfoliated graphite oxide. *Carbon N Y* 45:1558–1565
22. Yang S, Lohe MR, Müllen K, Feng X (2016) New-generation graphene from electrochemical approaches: production and applications. *Adv Mater* 28:6213–6221
23. De Silva KKH, Huang HH, Joshi RK, Yoshimura M (2017) Chemical reduction of graphene oxide using green reductants. *Carbon N Y* 119:190–199
24. Benzait Z, Chen P, Trabzon L (2021) Enhanced synthesis method of graphene oxide. *Nanoscale Adv* 3:223–230
25. Shen J, Hu Y, Li C et al (2009) Synthesis of amphiphilic graphene nanoplatelets. *Small* 5:82–85
26. Nieto A, Lahiri D, Agarwal A (2012) Synthesis and properties of bulk graphene nanoplatelets consolidated by spark plasma sintering. *Carbon N Y* 50:4068–4077

27. Sofo JO, Chaudhari AS, Barber GD (2007) Graphane: a two-dimensional hydrocarbon. *Phys Rev B—Condens Matter Mater Phys* 75:1–4
28. Savchenko A (2006) Transforming graphene. *Dev Cell* 10:589–590
29. Boukhvalov DW, Katsnelson MI, Lichtenstein AI (2008) Hydrogen on graphene: electronic structure, total energy, structural distortions and magnetism from first-principles calculations. *Phys Rev B—Condens Matter Mater Phys* 77:1–7
30. Zhou J, Wang Q, Sun Q et al (2009) Ferromagnetism in semihydrogenated graphene sheet. *Nano Lett* 9:3867–3870
31. Boukhvalov DW (2010) Stable antiferromagnetic graphone. *Phys E Low-Dimensional Syst Nanostruct* 43:199–201
32. Peng Q, Dearden AK, Chen XJ et al (2015) Peculiar pressure effect on Poisson ratio of graphone as a strain damper. *Nanoscale* 7:9975–9979
33. Nair RR, Ren W, Jalil R et al (2010) Fluorographene: a two-dimensional counterpart of Teflon. *Small* 6:2877–2884
34. Robinson JT, Burgess JS, Junkermeier CE et al (2010) Properties of fluorinated graphene films. *Nano Lett* 10:3001–3005
35. Haley MM (2008) Synthesis and properties of annulenic subunits of graphyne and graphdiyne nanoarchitectures. *Pure Appl Chem* 80:519–532
36. Kausar A (2021) Ingenuities of graphyne and graphdiyne with polymers: design insights to high performance nanocomposite. *Polym Technol Mater* 60:1149–1165
37. Temizel-Sekeryan S, Wu F, Hicks AL (2021) Global scale life cycle environmental impacts of single- and multi-walled carbon nanotube synthesis processes. *Int J Life Cycle Assess* 26:656–672
38. Xu B, Li T, Liu X et al (2007) Growth of well-aligned carbon nanotubes in a plasma system using ferrocene solution in ethanol. *Thin Solid Films* 515:6726–6729
39. Sinha N, Ma J, Yeow JTW (2006) Carbon nanotube-based sensors. *J Nanosci Nanotechnol* 6:573–590
40. Harris PJF (2007) Solid state growth mechanisms for carbon nanotubes. *Carbon N Y* 45:229–239
41. Tai Z, Chen Y, An Y et al (2012) Tribological behavior of UHMWPE reinforced with graphene oxide nanosheets. *Tribol Lett* 46:55–63
42. Aliyu IK, Samad MA, Al-Qutub A (2021) Tribological characterization of a bearing coated with UHMWPE/GNPs nanocomposite coating. *Surf Eng* 37:60–69
43. Vinoth A, Dey S, Datta S (2021) Designing UHMWPE hybrid composites using machine learning and metaheuristic algorithms. *Compos Struct* 267:113898
44. Vinoth A, Nirmal KN, Khedar R, Datta S (2021) Optimizing the tribological properties of UHMWPE nanocomposites-an artificial intelligence based approach. In: *Trends in mechanical and biomedical design*. Springer Singapore, Singapore, pp 831–843
45. Liu CY, Ishigami A, Kurose T, Ito H (2021) Wear resistance of graphene reinforced ultra-high molecular weight polyethylene nanocomposites prepared by octa-screw extrusion process. *Compos Part B Eng* 215:108810
46. Saad NA, Obaid MN (2020) Enhanced the antibacterial and mechanical properties of UHMWPE by addition sort fibers of polyacrylonitrile PAN, graphene nanoplate (GNP) and hydroxyapatite (HAp)
47. Mindivan F (2019) Dry wear studies on reduced graphene oxide filled uhmwpe composites. *SERBIATRIB '19 16th Int Conf Tribol*
48. Çolak A, Göktaş M, Mindivan F (2020) Effect of reduced graphene oxide amount on the tribological properties of UHMWPE biocomposites under water-lubricated conditions. *SN Appl Sci* 2
49. Lu P, Ni Z, Chen G, Wu M (2021) Influence of SBF-induced degradation on surface and tribological properties of irradiated GO/UHMWPE nanocomposites. *Iran Polym J (English Ed)* 30:247–255
50. Chih A, Ansón-Casaos A, Puértolas JA (2017) Frictional and mechanical behaviour of graphene/UHMWPE composite coatings. *Tribol Int* 116:295–302

51. Chen X, Zhang S, Zhang L, et al (2021) Design and characterization of the surface porous UHMWPE composite reinforced by graphene oxide. *Polymers (Basel)* 13:1–14
52. Xu L, Zheng Y, Yan Z, et al (2016) Applied surface science preparation, tribological properties and biocompatibility of fluorinated graphene/ultrahigh molecular weight polyethylene composite materials. *370*:201–208
53. Taromsari SM, Salari M, Bagheri R, et al (2019) Optimizing tribological, tensile & in-vitro biofunctional properties of UHMWPE based nanocomposites with simultaneous incorporation of graphene nanoplatelets (GNP) & hydroxyapatite (HAp) via a facile approach for biomedical applications. *Compos Part B* 175:107181
54. Lahiri D, Hec F, Thiesse M, Durygin A (2014) Tribology international nanotribological behavior of graphene nanoplatelet reinforced ultra high molecular weight polyethylene composites. *Tribology Int* 70:165–169
55. Joffe R, Tipper JL, Emami N (2015) Ultra high molecular weight polyethylene/graphene oxide nanocomposites: thermal, mechanical and wettability characterisation 78
56. Bhusari SA, Sharma V, Bose S, Basu B (2019) HDPE/UHMWPE hybrid nanocomposites with surface functionalized graphene oxide towards improved strength and cytocompatibility. *J R Soc Interface* 16
57. Belotti LP, Vadivel HS, Emami N (2019) Tribological performance of hygrothermally aged UHMWPE hybrid composites. *Tribol Int* 138:150–156
58. Fang J, Dong L, Dong W, et al (2015) Freeze-drying method prepared UHMWPE/CNTs composites with optimized micromorphologies and improved tribological performance. *41885*:1–7
59. Baena J, Peng Z (2018) Dispersion state of multi-walled carbon nanotubes in the UHMWPE matrix: effects on the tribological and mechanical response. *Polym Test* 71:125–136

Sliding Wear Behavior of Cast, Cold Extruded, and Precipitation-Hardened Al/TiC_p Metal Matrix Composite



P. N. Siddappa , B. P. Shivakumar , M. Mruthunjaya ,
and K. S. Anil Kumar 

1 Introduction

Wear is the gradual removal of materials at specimen surfaces. Causes of wear can be erosion or corrosion. Tribology is the study of wear and related to processes of friction and lubrication. In the present research work, Magana makes wear tester was employed to conduct the wear behavior with various parameters like load, sliding distance, and constant velocity. As shown in Fig. 1, generally, wear test specimen is held firmly and loaded perpendicularly against a rotating disc wear tester. The wear tests were conducted using the Magnum make wear test rig (Fig. 1) following the ASTM G99 standard. For as-cast composite and extruded specimens with various weight percentages, wear test pins with 6 mm diameter and a height of 40 mm were machined. Each tested pin's end surface should be free of burrs and knife edges to avoid damage during the sliding on the solid disc surface. The pin contact face of the pin was smoothed with 1000 grit abrasive emery paper before being cleaned with cleaning agent. The surface was checked for flatness and perpendicularity to ensure full area of the pin samples tip and the disc surface.

Oil hardened non-shrinking (OHNS) steel with high hardness and high strength superior wear resistance rotating disc is used. The revolving surface was ground for a few minutes with 800 grit SiC paper to evacuate the accumulated particles and then wipe with cleaning agent. Wear tests were performed using a test rig (made by Magnum) at room temperature under normal environment. The composite specimen was tested by sliding it on a rotating disc with a track radius of 50 mm. At a normal load of 10, 20, and 30 N and a sliding velocity of 2 m/s, a number of tests were carried out for various weight fractions of reinforcement composites for sliding distances

P. N. Siddappa (✉) · B. P. Shivakumar · M. Mruthunjaya · K. S. Anil Kumar
Department of Mechanical Engineering, JSS Academy of Technical Education,
Bangalore 560060, India
e-mail: siddappa.pn@gmail.com; siddappapn@jssateb.ac.in

Fig. 1 Wear test rig

ranging from 1000 to 3000 m in increment of 1000 m. Weight loss was calculated by dividing the weight loss by a sliding distance and calculating the rate of wear by knowing the weight of the pin before and after every trial using an electronic weighing machine. For all of the trials, frictional force readings were directly noted from the digital display on wear testing rig [1–4] (Table 1).

Table 1 Specification of a pin-on-disc wear test rig

Parameters	Min	Max	Remarks
Pin-on-disc wear test rig	3 mm	12 mm	Diameter
Ball diameter	10 mm	12.7 mm	Different holders
Disc diameter	–	150 mm	
Disc thickness	–	8 mm	Hardened steel EN-32 and HRC 60
Wear track diameter	20 mm	145 mm	–
Disc rotation	200 RPM	2000 RPM	–
Normal load	5 N	200 N	In steps of 5 N

2 Literature Review

Literature survey carried out on MMCs, extrusion process, material properties and their characterization. The investigation results are briefed in the following paragraphs.

Murthy Y. et al. discovered that Al6061-BN composites have a lower wear rate than aluminum alloy. The wear rate of both aluminum alloy and composites increases as the sliding velocity and load increase, but the wear rate of composites is lower when compared to base alloy. Fractography was performed on the worn surface to determine the wear mechanisms [5].

Gur, A. K., et al. used the plasma transferred arc (PTA) welding method to coat the surface of AISI 430 stainless steel with a hyper-eutectic FeCrC and pure B₄C powders. The weight loss due to wear was assessed using the criterion of “the smaller, the better.” The sliding distance was found to be the most significant cause of wear among all input parameters. A linear regression equation was also developed to estimate the weight loss between the input data and the levels used [6].

H. M. Magid et al. have investigated the mechanical properties of the extruded LM6/TiC aluminum composite which was prepared by liquid route with 5% of weight fraction reinforcement of TiC particulates. The extrudability and mechanical properties of this composite (LM6/TiC) are evaluated before and after extrusion theoretically and practically. The results revealed by the experiment exhibit that mechanical properties are better after extrusion like hardness, UTS, stiffness, and wear resistance. Heat treatment enhanced the strength of greater than 15% compared with base matrix LM6. This enhancement is due to the high intervention and bonding strength between the matrix and reinforcement. This metal forming process results in fine grain size after the method [7].

Dhanalakshmi Sathishkumar et al. analyzed the result of various extrusion ratios (i.e., 4:1, 8:1, and 15:1) at slug temperatures in the range 350 °C to 550 °C an increment of 50 °C for the hot extrusion process of Al2014-SiC sample using FEM analysis. Experimental hot extrusion was also conducted on the composite at a slug temperature of 450 °C for all the extrusion ratios. Three extrusion ratios, viz. 4:1, 8:1, and 15:1, depict that the maximum grain refinement takes place at extrusion ratio 8:1. However, higher extrusion ratio of 15:1 has revealed in the presence of hot shortness and surface cracks. Also found that the extrusion ratio has highest effect on the propagation of surface cracks. The conclusion of this work helped in arriving at the optimum extrusion ratio and billet temperature to conduct further extrusions [8].

P. Dhanasekaran et al. found that TiC reinforced with Al, the tensile and tear behavior of 6063 alloys and SEM exhibits the distribution of reinforcement in the matrix. It was seen that, by accumulation of TiC particles into the alloy, hardness, dry wear properties, and volatility were improved. Increasing the reinforcement weight fraction, the wear rate of composited declines, which upgrades the hardness [9].

S. Venkatesan et al. did the experimental relative investigation of Al/TiC and TiB₂ MMC with fluctuating weight fraction. They also analyzed the mechanical

and wear behavior of the above composite material. They found that increasing the wt. % of TiC enhances yield strength, UTS, Young's modulus and diminishes the ductility. Addition of weight % of titanium boride improves the frictional coefficient and tensile strength [10].

The impact of the forming method and SiC particle size on the properties of Al-SiC composite was studied by M. Zakeria et al. Powder metallurgy is used to create the composite. A composite was created using three different forming methods: hot press, pressure less, and hot extrusion, as well as two different SiC particle sizes. Optical microscopy was used to examine the microstructure. The hot-pressed specimens had the highest relative density. Hardness, yielding point, and UTS were all influenced the most by a higher reinforcement content with smaller particles. With a SiC mesh size of 1000, Al-20 percent SiC achieved maximum hardness (6.57 GPa) and UTS 212 MPa. At higher reinforcement contents, there is a significant difference between HP and the extrusion process. The yielding points of the extrusion specimens are better than hot press specimens [11].

Rupa Dasgupta et al. were explored the impact of the properties achieved in cast Al2014-based MMCs made with SiC scatterings through the extrusion under improved condition. Obtained properties have been analyzed between the cast and extruded. The mechanical, physical, and wear properties are improved between them. Endeavors have been made to break down the got outcomes through little examinations on the composite specimens [12].

J. B. Fruhaufa et al. used three different powder metallurgy techniques to make Ti + TiCp composites: extrusion, hot isostatic pressing (HIP), and sintering. TiC particles have been found to successfully reinforce Ti matrix metal. EBSD was used to characterize the microstructures and textures. The mean of tensile tests was used to calculate the tensile properties. The mechanical properties of Ti/TiC did not deteriorate. The microstructural characteristics and mechanical properties of specimens are compared [13].

C. S. Ramesh et al. used liquid metallurgy to make Al6061-based composites. They used SiC, alumina, and cerium oxide as reinforcements, with particle sizes ranging from 20 to 30 microns, 20 to 25 microns, and 5 microns, respectively. Cast and extruded matrix alloys, as well as their composites, were subjected to hardness, microstructure studies, and wear tests. The wear rate of composites decreases as the fraction of reinforcement in the matrix alloy increases. The presence of a good bond between the matrix and reinforcement is the most important factor affecting extruded composites' wear resistance [14].

A. E. Karantzalis et al. created Al/TiC metal matrix composites using a novel course that allows solid Al to nucleate on the TiC reinforcement, resulting in line as-cast grain sizes. During solidification, it was observed that solid nucleation causes broad grain refinement and the engulfment of numerous particles into developing essential Al grains. Through the removal of porosity from the casting stage, extrusion improves the composites strength and ductility [15].

It is observed from the literature review that exhaustive research was done on aluminum alloy-based MMCs, but not appreciable amount of work has been done till date on the synthesis and characterization of cold extruded of Al6061 MMC

reinforced with TiC particulate. It is also observed that most of the researchers were chosen powder metallurgy route to fabricate the composite rather than choosing stir casting technique. Many researchers showed that the behavior of the composite also depends on the manufacturing route, and hence, an attempt is made to develop extruded Al6061-TiCp MMCs with varying weight percent of TiC using stir casting technique.

The main objective of the present investigation is to synthesize and characterize the effect of cold extrusion on Al/TiC MMCs. Al/TiC composite specimens were produced by reinforcing TiC particles of size 28 microns into the matrix alloy with different fractions from 3 to 12% in steps of 3% by stir casting technique. The cast composites were further subjected to secondary manufacturing process which are cold extruded and cold extruded with age-hardened specimens. This study aims to achieve MMC composites with improved the mechanical and wear properties.

3 Wear Behavior

Pin-on-disc wear test rig was used to investigate the effect of cold extrusion and weight percent of TiC particles on the wear behavior of Al-TiC composites. Series of wear tests were examined at a constant speed of 1000 rpm for three different loads of 10 N, 20 N, and 30 N and sliding distances 1000 m, 2000 m, and 3000 m. For each sliding distance, the load was kept constant and the wear rate was measured for different weight fractions. The experimental procedure repeated for all the loads at each sliding distance. To improve the wear resistance, the composites were extruded and also heat treated and again wear tests were conducted for extruded as well as extruded precipitation-hardened composites. Table 2 shows the wear rate recorded for all the cases considered for Al6061/TiC MMCs [16, 17].

3.1 Hardness Test

The Brinell hardness tester was used to test the hardness of the all composite test specimens, and the results were given in Table 3. The hardness of the composite specimen is found to be directly related to the porosity of the composite specimen based on the results obtained. The composite is squeezed during the cold extrusion process, resulting in strain hardening and the elimination of porosity, resulting in increased hardness. In all of the composites, the hardness increased as the reinforcement increased. The hardness of the age-hardened composite is found to be higher than that of extruded composites for all weight fractions, according to the results [18, 19].

Table 2 Wear test results for Al6061/TiC particle composites for different conditions

Exp. No.	Sliding distance (m)	Load (N)	Wt. % of TiC in Al-6061	Wear rate 10 ⁻⁶ g/m				
				Cast composite	Extruded composite	Extruded composites with precipitation hardening		
1		10	0	6.5	4.5	3.9		
2			3	5.8	3.8	3.3		
3			6	5.1	2.9	2.3		
4			1000	20	9	3.9	2.3	1.9
5					12	3	1.9	1.2
6					0	7.6	6.5	5.9
7	3	7	5.8		5.3			
8	6	6.5	4.8		4.2			
9	9	6.1	3.8		3.2			
10	12	3	7.8	13.2				
11		0	8.6	7.667	5.667			
12		30	3	7.667	6.667	4.667		
13			6	6.33	5.667	3.3		
14			9	5.8	4.667	2		
15			12	4.9	3.2	1.7		
1	2000	10	0	7.21	6.1	5.6		
2			3	6.5	5.9	4.8		
3			6	5.52	4.5	3.9		
4			9	4.6	3.9	2.92		
5			12	3.8	3.2	2.2		
6		20	30	0	8.2	6.9	5.1	
7				3	7.5	6.1	4.5	
8				6	7.1	5.3	3.3	
9				9	6.6	4.9	2.92	
10				12	5.8	4.6	2.2	
11			10	0	9.8	8.8	7.37	
12				3	8.2	7.233	6.161	
13				6	7.333	6.4	5.33	
14				9	6.833	5.8	4.1	
15				12	5.667	4.9	3.9	
1		10	0	8.9	7.1	6.1		
2			3	7.9	6.6	5.5		

(continued)

Table 2 (continued)

Exp. No.	Sliding distance (m)	Load (N)	Wt. % of TiC in Al-6061	Wear rate 10 ⁻⁶ g/m		
				Cast composite	Extruded composite	Extruded composites with precipitation hardening
3			6	6.8	5.3	4.3
4			9	6.6	4.9	3.92
5			12	5.8	4.3	2.9
6	3000	20	0	10.1	8.2	6.7
7			3	9.31	7.81	5.7
8			6	8.2	6.1	4.1
9			9	7.3	5.5	3.8
10			12	7.4	4.8	3.6
11				30	0	12.1
12	3	11.2			9.233	7.161
13	6	9.633			8.1	6.33
14	9	9.833			7.6	5.21
15	12	9.01			6.9	4.9

Table 3 Results obtained from hardness test of Al/TiC composites

% of TiC in composites	BHN		
	As-cast	Extruded	Extruded with age hardened
Al-alloy	44.88	51.87	70.0
Al-3%	47.46	53.05	75.37
Al-6%	50.31	54.27	87.39
Al-9%	56.81	71.56	90.81
Al-12%	64.60	98.28	104.49

4 Results and Discussion

4.1 Effect of TiC Reinforcement on Wear Rate

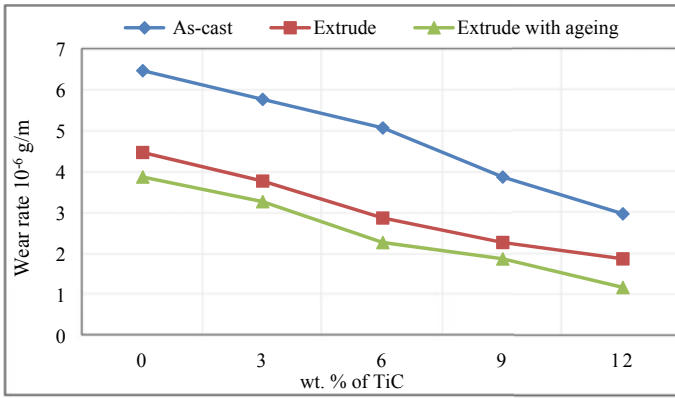
Figure 2 shows that, the variation of wear rate with the different weight percent of reinforcement for 10 N, 20 N and 30 N at a sliding distance of 1000 m. It is observed from Fig. 2a, wear rate keeps decreased with the increase of reinforcement for all the cases considered such as, as-cast, extruded, and extruded with precipitation hardening composites for the applied load of 10 N. Further, it reveals that the wear rate is less for the extruded sample compared to the as-cast one at all the weight fractions

and it is further less in the case of precipitation-hardened extruded composite. The addition of TiC particulates enhances the hardness of the samples, which leads to enhanced wear resistance of the samples. Figure 2b, c shows similar trends for 20 N and 30 N applied loads, respectively, for all the weight fractions of reinforcements [4, 20].

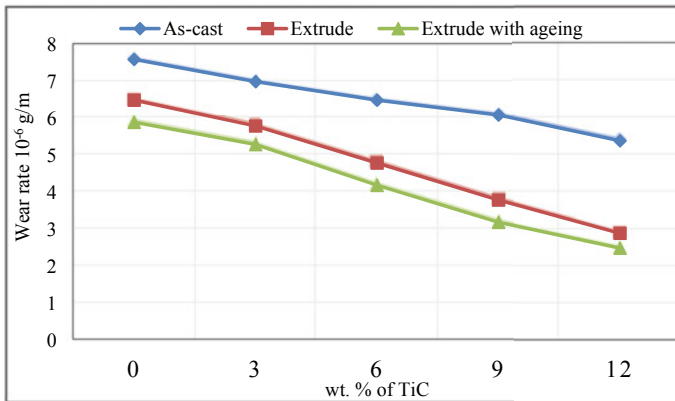
Figures 3 and 4 show the wear rate variation with TiC particle reinforcement for sliding distances of 2000 m and 3000 m, correspondingly. For the sliding distances of 2000 m and 3000 m, a similar pattern was observed in all cases. The findings show that at first rubbing, the TiC particulate acts as a wear barrier and load-bearing material. It also restricts the plastic deformation, preventing the Al matrix from adhering to the rotating disc's contact surface. The addition of TiC particulates improves hardness, which can be contributed to enhanced wear resistance. On the other hand, composite material's lower porosity could help it resist crack propagation. It also acts as a barrier against plastic deformation, preventing the Al matrix from adhering to the rotating disc's contact surface. The addition of TiC particulates improves the composites' hardness, which can be attributed to the composites' improved wear resistance. On the other hand, the composite material's lower porosity could help it resist crack propagation. Delimitation is caused by cracks that are aligned with other cracks. The porosity level precipitation hardened during compression flow metal through die is reduced during the extrusion process, increasing both hardness and wear rate [21].

4.2 Effect of Sliding Distance on the Wear Rate

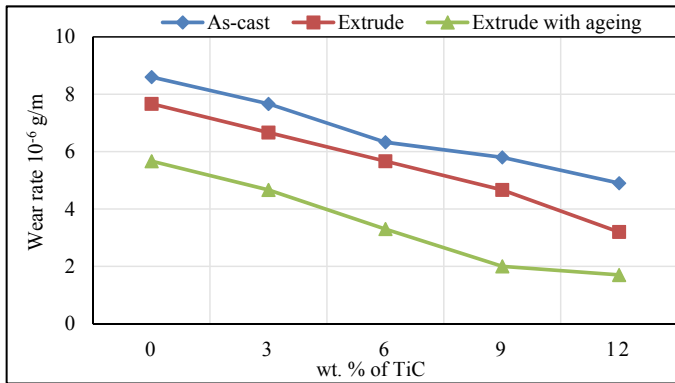
Figures 5, 6, and 7 show the variation of wear rate on different sliding distance at different weight percentages of TiC and loading conditions (10, 20, and 30 N) for as-cast, extruded, and precipitation-hardened composites. The wear rate increases linearly with increasing wear path distance in all of the trails. The wear rate for extruded and precipitation-hardened conditions shows lower values compared to as-cast and extruder conditions. The higher wear rate at a higher sliding distance could be attributed to the increase in temperature between the interfaces of the pin and disc. In addition to TiC, the drastic reduction of wear rate was observed in all of the experiments due to the higher hardness of the composites reinforced with TiC. After the wear test, a thick layer of Al stuck on the counter-surface. The layer (Fig. 8) continuously increased in thickness during the wear test, reached its maximum thickness, and then detached itself from the sliding surface and wear debris. The adhesion and removal of base metal on the surface of the disc depending on the load, sliding speed and even the amount of reinforcement additions. Owing to the coefficient of friction, heat is developed between the interfaces, which results in better compaction and detaching. The higher hardness of the TiC particles protects the matrix alloy from further wear, and hence, these specimens show a lower wear rate [16, 17, 20, 22].



(a)

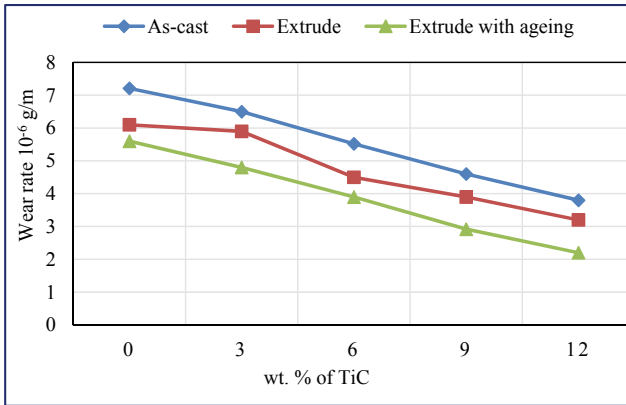


(b)

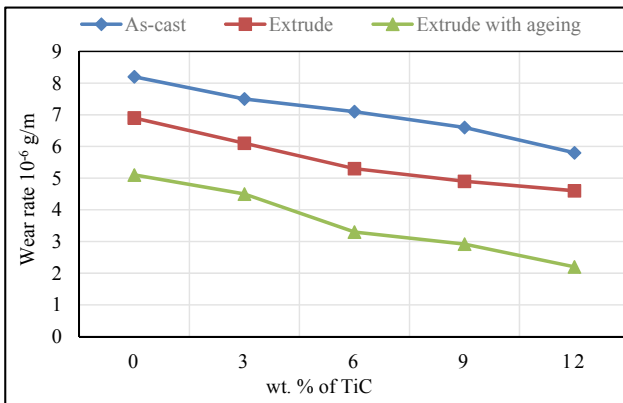


(c)

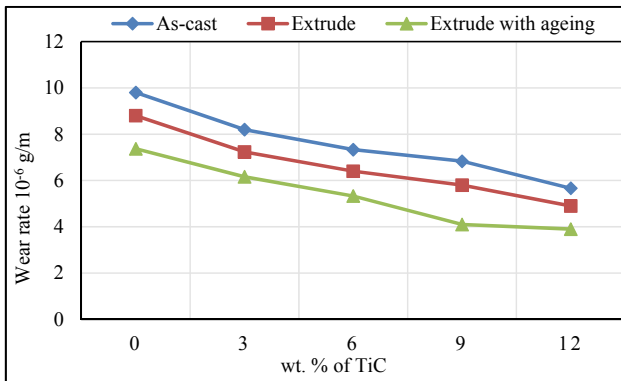
Fig. 2 Variation of wear rate with weight fraction of TiC particles for a constant sliding distance of 1000 m at an applied load of **a** 10 N, **b** 20 N and **c** 30 N



(a)

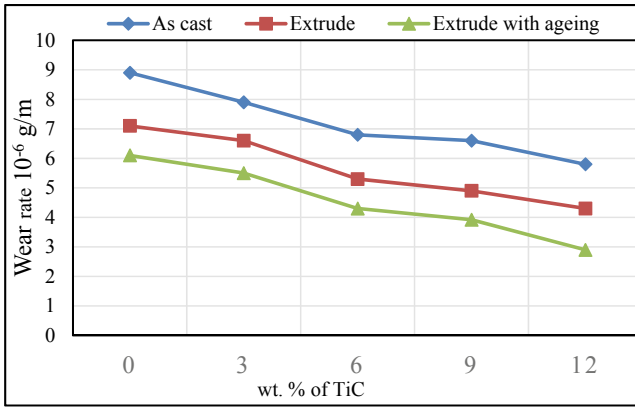


(b)

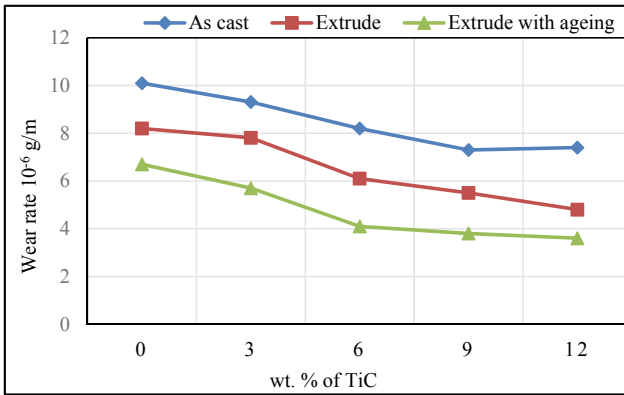


(c)

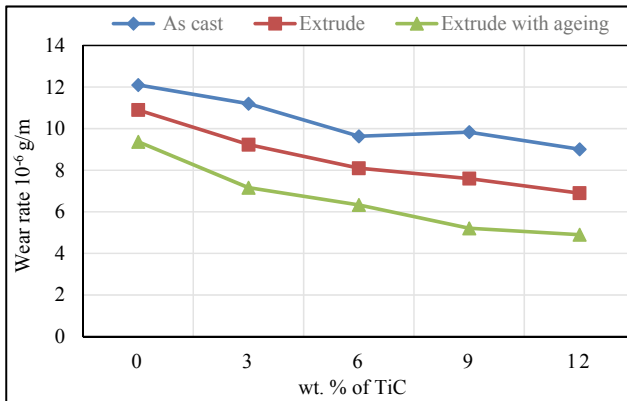
Fig. 3 Variation of wear rate with weight fraction of TiC particles for a constant sliding distance of 2000 m at an applied load of **a** 10 N, **b** 20 N and **c** 30 N



(a)

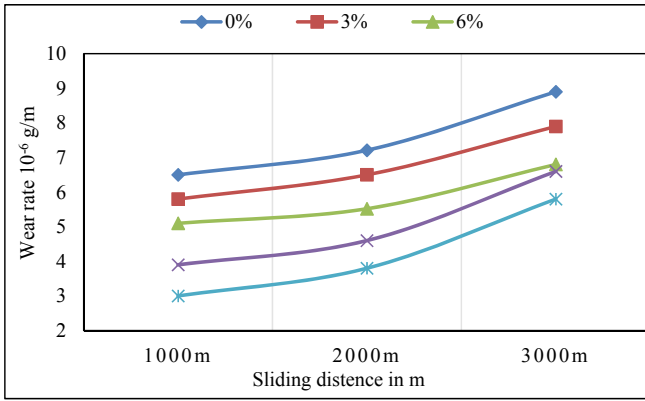


(b)

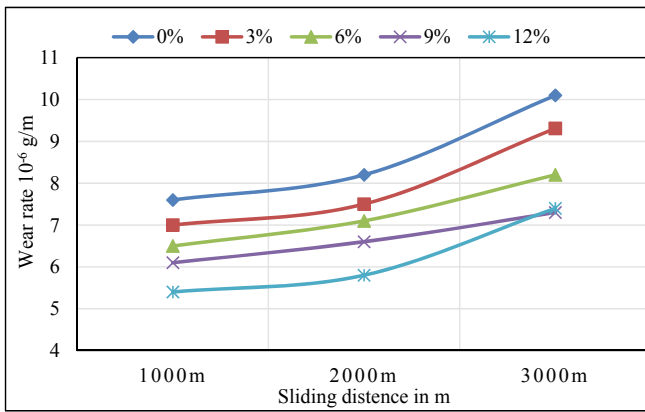


(c)

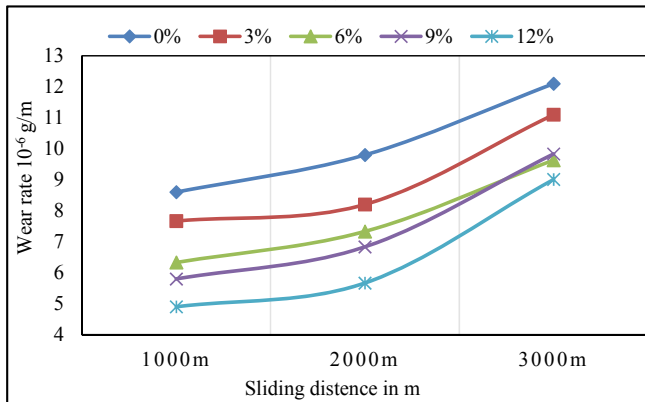
Fig. 4 Variation of wear rate with weight fraction of TiC particles for a constant sliding distance of 3000 m at an applied load of **a** 10 N, **b** 20 N and **c** 30 N



(a)

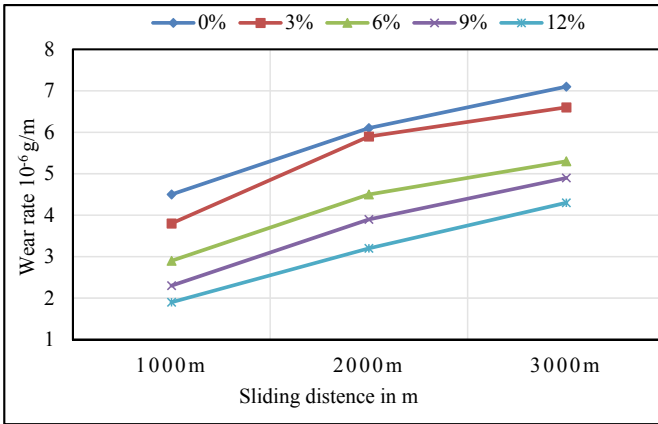


(b)

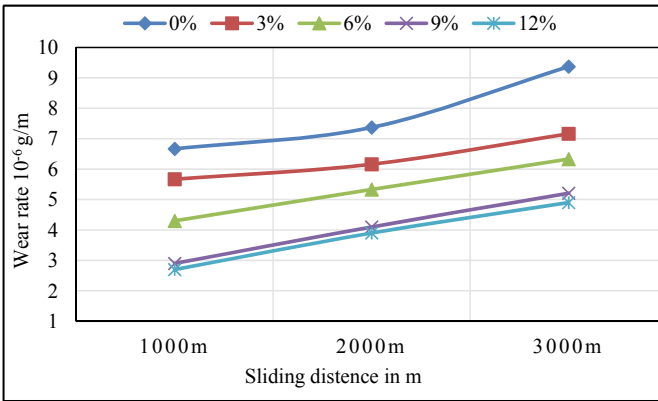


(c)

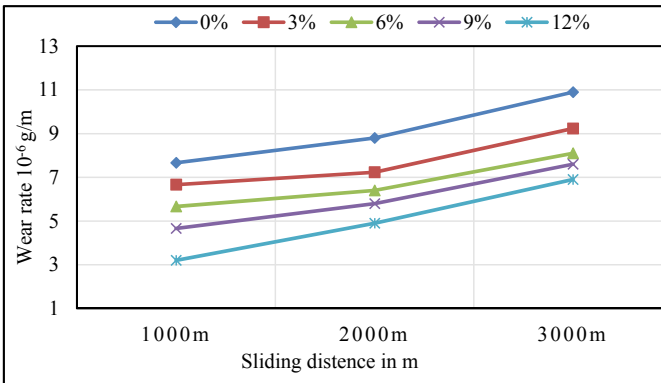
Fig. 5 Variation of wear rate of as-cast composite with sliding distance at normal load **a** 10 N **b** 20 N **c** 30 N



(a)

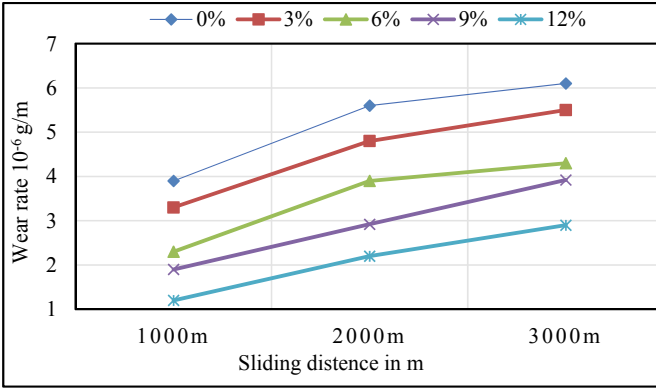


(b)

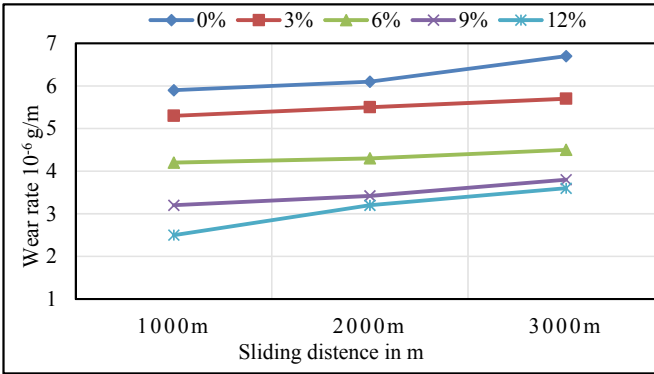


(c)

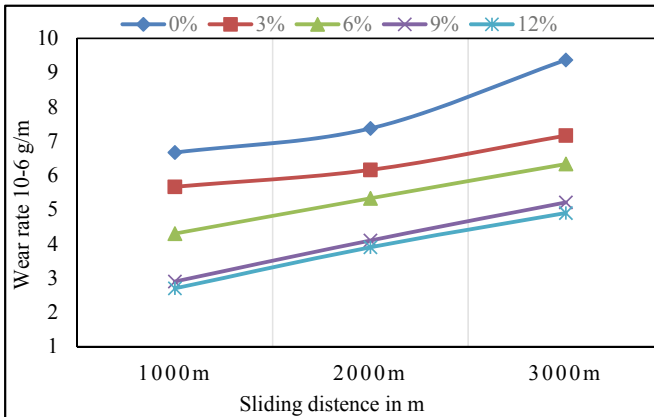
Fig. 6 Variation of wear rate of extruded composite with sliding distance at normal load **a** 10 N **b** 20 N **c** 30 N



(a)



(b)



(c)

Fig. 7 Variation of wear rate of extruded composite (precipitation hardened) with sliding distance at load **a** 10 N **b** 20 N **c** 30 N

Fig. 8 Thick layer of Al stuck on the contact surface of the pin



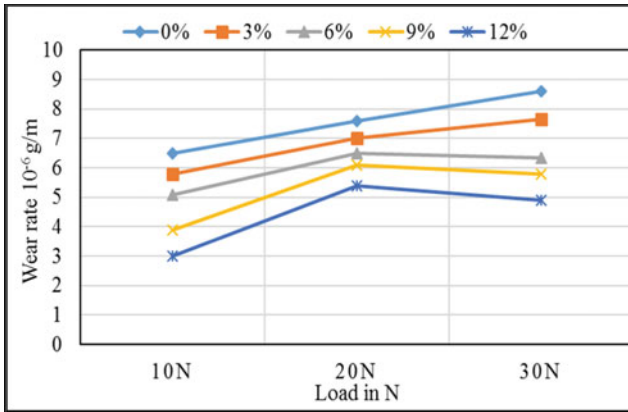
4.3 Effect of Normal Load on Wear Rate

Figures 9, 10, and 11 shows the effect of normal load on the wear loss of Al/TiC composites in as-cast, extruded, and precipitation-hardened conditions for all weight percentages of composites. Regardless of the condition, the wear rate of the composite improved linearly with the addition of normal load.

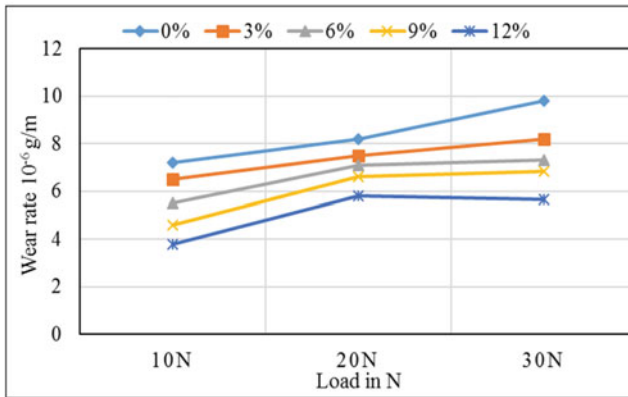
When load increases wear rate increases can be endorsed that at higher loads, there is a tendency of large plastic deformation which induced wear debris, tends to higher wear rate. As a result, it can be concluded that TiC reinforcement in matrix metal improves wear resistance significantly. Agglomeration in the Al6061 extruded with precipitation-hardened composite, which leads to poor interfacial adhesion between the TiC particles and the matrix alloy, may have caused this increase in wear rate for a higher weight fraction of TiC (12 wt. %) [19, 23–26].

5 Conclusion

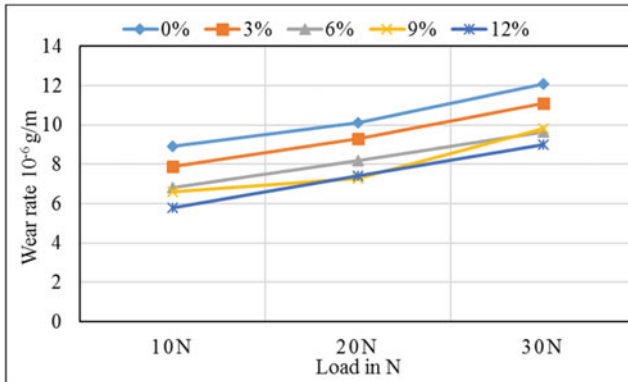
The presence of TiC particles increases the hardness of the MMC, which can be endorsed to the composites' enhanced wear behavior; the wear rate is lower for extruded composites than as-cast composites at all weight fractions, and it is even lower for precipitation-hardened extruded composites.



(a)

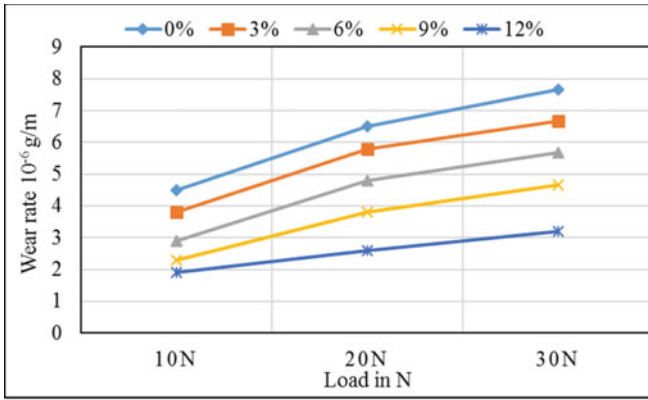


(b)

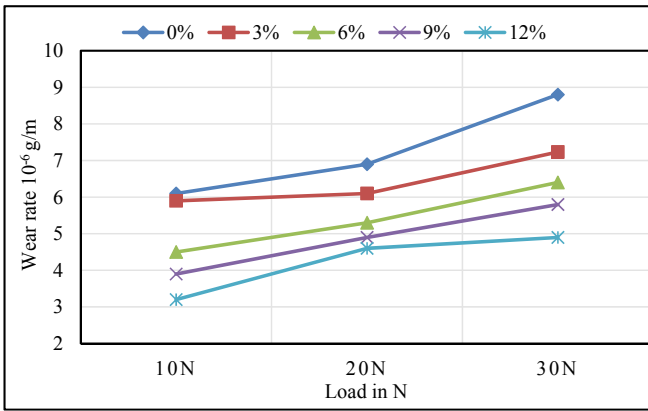


(c)

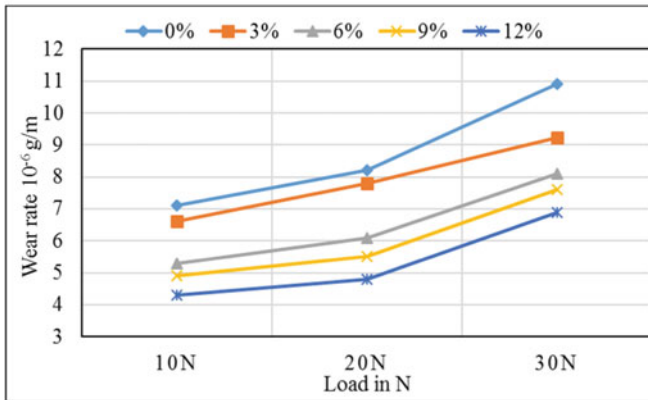
Fig. 9 Variation of wear rate with the increase of normal load for different weight fraction of as-cast composite at sliding distance **a** 1000 m **b** 2000 m **c** 3000 m



(a)

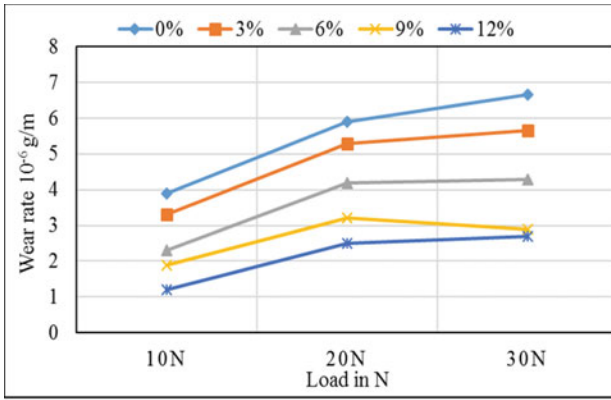


(b)

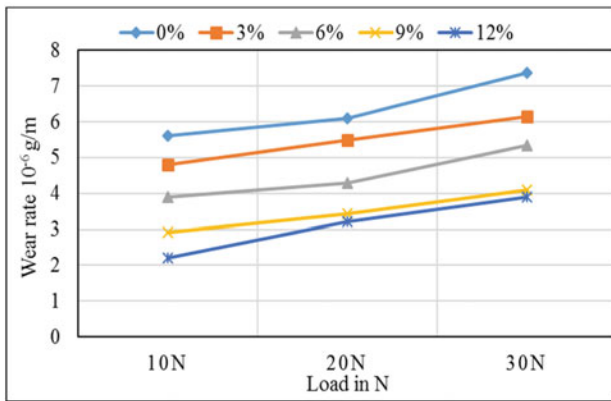


(c)

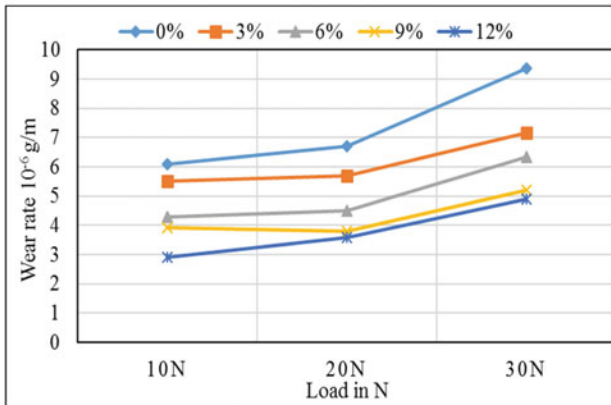
Fig. 10 Variation of wear rate with the increase of normal load for different weight fractions of the extruded composite at sliding distance **a** 1000 m **b** 2000 m **c** 3000 m



(a)



(b)



(c)

Fig. 11 Variation of wear rate with an increase of normal loads for different weight fractions of extruded composite with aging at sliding distance **a** 1000 m **b** 2000 m **c** 3000 m

The wear rate of the as-cast composites decreases as the reinforcement TiC particulates increase, while it decreases in extruded composites. At all weight fractions of reinforcements, the rate of wear increased with the increase of tracking distance and applied loads.

For the applied load of 10 N, the wear rate decreases as reinforcement increases for all trails considered, such as-cast, extruded, and extruded with precipitation hardening composites. Furthermore, the wear rate of the extruded composite is lesser than that of the as-cast composite at all weight fractions, and it is even lower in the case of precipitation-hardened composites.

In all cases, the wear rate increases linearly as the wear track distance increases. When compared to as-cast and extruder conditions, the wear rate for extruded and precipitation-hardened conditions is lower. The increased temperature between the pin and disc interfaces could explain the higher wear rate at greater sliding distances. In addition to TiC, the higher hardness of the composites reinforced with TiC resulted in a significant reduction in wear rate in all of the experiments.

A thick layer of Al stuck on the counter-surface. The layer continuously increased in thickness during the wear test, reached its maximum thickness, and then detached itself from the sliding surface and wear debris. This extrusion process reduces the porosity level precipitation hardened during compression flow metal through die thus increasing both hardness and wear rate.

References

1. Siddappa PN, Shivakumar BP, Yogesha KB, Mruthunjaya M, Girish DP (2020) The effect of TiC particulate reinforcement on dry sliding wear behavior of Al-based composites. *Mater Today: Proc*
2. Siddappa PN, Shivakumar BP, Yogesha KB (2021) Synthesis and characterization of cold extruded Al/TiC metal matrix composite produced by stir casting technique. *Mater Today: Proc*
3. *Advances in mechanism and machine science* (2019) Springer science and business media LLC
4. Girish BM, Shivakumar BP, Hanamantraygouda MB, Satish BM (2020) Wear behaviour of hot forged SiC reinforced aluminium 6061 composite materials. *Aust J Mech Eng*
5. Mukesh Y, Bharathesh T, Keshavamurthy R, Girish H. Impact of extrusion procession wear behavior of boron nitride reinforced aluminum 6061-based composites
6. Gur AK, Icen B, Shankar S, Mohanraj T (2021) Examination of B₄C–FeCrC composite layer during dry sliding using statistical method. *Surf Rev Lett (SRL)* 28(05):1–11
7. Magid HM, Kadhim KJ, Hawas MN (2017) Exploration the extrudability of aluminum matrix composite (LM6/TiC) through modeling, simulation and experimental process. *J Fundam Appl Sci* 9(7S):1493–1507
8. Sathishkumar D, Sivakumar P, Sundaram KS, Anand S (2017) Finite element analysis and experimental study on the effect of extrusion ratio during hot extrusion process of aluminium matrix composites. *Defence Sci J* 67(4):428–436
9. Danashekaran P, Ravishankar M, Sathishkumar S, Velavan N (2011) Tensile test and wear behaviour of titanium carbide reinforced with Al6063 MMC. *Int Res Innovative Res Sci*
10. Venkatesan S, Xavior (April 2015) Comparative analysis of aluminium MMC reinforced with TiC and TiB₂ using stir casting process. *Int J Sci Res Eng Stud (IJSRES)* 2(4):61–65

11. Zakeria M, Vakili-Ahrari Rudi A (2013) Effect of shaping methods on the mechanical properties of Al-SiC composite. *Mater Res* 16(5):1169–1174
12. Dasgupta R, Dasgupta R (2013) Effect of extrusion on the microstructure and properties of 2014-based particulate composites. *Int J Microstruct Mater Prop* 8(4/5):313–324
13. Fruhaufa JB (2012) Microstructural and mechanical comparison of Ti+ 15% TiCp composites prepared by free sintering, HIP and extrusion. *Mater Sci Eng A* 554:22–32
14. Ramesh CS, Hiriania A, Harishanand KS, Noronha NP (2012) A review on hot extrusion of metal matrix composites (MMC's). *Int J Eng Sci* 1(10):30–35
15. Karantzalis AE, Wyatt S, Kennedy AR (1997) The mechanical properties of Al-TiC metal matrix composites fabricated by a flux-casting technique. *Mater Sci Eng: A* 237(2):200–206
16. *Advances in Materials and Metallurgy* (2019) Springer science and business media LLC
17. *Industrial lubrication and tribology* (2012) 64(6)
18. Pauschitz A (2009) On the scratch behaviour of self-lubricating WSe₂ films. *Wear*
19. Qi W (2003) Microstructure and tribological behavior of a peak aged Cu-Cr-Zr alloy. *Mater Sci Eng A*
20. Shivakumar BP, Hanamantraygouda MB, Prashanth L, Yogesha KB, Siddappa PN, Mrityunjaya M (2019) Chapter 387 effect of SiC particulate on dry sliding wear behaviour of Al based forged metal matrix composites. Springer Science and Business Media LLC
21. Das S, Mondal DP, Sawla S, Dixit S (2002) High stress abrasive wear mechanism of LM13-SiC composite under varying experimental conditions. *Metall Mater Trans A*, 9. Gautam RK. Tribological behavior of Cu-CrSiC. p in si
22. Ramesh CS (2011) Friction and wear behaviour of cast Al 6063 based in situ metal matrix composites. *Wear*
23. Nagara M, Auradi V, Kori SA (2014) Dry sliding wear behavior of graphite particulate reinforced Al6061 alloy composite materials. *Appl Mech Mater*
24. Gopalakrishnan S (March 2012) Production and wear characterisation of AA 6061 matrix titanium carbide particulate reinforced composite by enhanced stir casting method. *Compos Part B*
25. Modi OP (15 June 2007) High-stress abrasive wear response of 0.2% carbon dual phase steel: effects of microstructural features and experimental conditions. *Mater Sci Eng A*
26. Chelladurai SJS, Murugesan T, Rajamani T, Anand S, Asok SJP, Kumaravel S (2019) Investigation on mechanical properties and tribological behaviour of stir cast LM13 aluminium alloy based particulate hybrid composites. *Materialwissenschaft und Werkstofftechnik*